CORRECTIONS

page no.	line no.	wrong	correct
4	10	cencerely	sincerely
10	12	bondary	boundary
15	26	rotating	this rotating
20	6	Fig.1.6	Fig.1.5
22	9	r.p.m.	rev/min
26	eq(1.17)	ν	ν^2
26	21	fullly	fully
28	24	r.p.m.	rev/min
32	Fig.1.14	secindary	secondary
45	23	Reynolds	a Reynolds
46	Fig.1.21	Z	X
53	5	methods	method
53	13	checked	checks
54	8	shew	show
57	18	these	this
57	21	equations	equations for
58	4	developmens	developments
58	8	momentom	momentum
60	3	are	have
60	21	stess	stress
61	6	as	as a
69	18	apprximation	approximation
84	4	the	that the
84	7	influence	influence that
86	4	cinditions	conditions
87	4	proceeds	proceed
88	7	flows	flow
89	14	Genral	General
90	Fig.4.1	SCREAN	SCREEN
95	26	tength	tenth
101	10	an	a
105	Fig.4.12	FRECUANCY	FREQUENCY
108	10	weere	were
116	19	in are shown	are shown in
133	16	centripetal	centripetal
135	13	Skiaderessis	Skiadaressis
152	6	Stevenson	Stephenson
154	21	decreased.	decreased, and is displaced away from the symmetry line for the cases III and IV due to strong body forces effect.
154	24	U/W_m=22%	U/W_m=17%
154	25	V/W_m=15%	V/W_m=19%
154	29	is increased.	is increased. The maximum dimensionless temperature is displaced away from the symmetry line for case IV.
166	21	not	also
166	25	50%	18%
166	26	60%	26%
204	16	these trend are	this trend is
227		HUMPHREY	HUMPHREYS
233	26	SPLDING	SPALDING
237	25	dimenssionless	dimensionless

TURBULENT FLOW IN CURVED AND ROTATING TUBES

BY

MOHSEN MOHAMED ENAYET

Thesis Submitted For The Degree Of

Doctor Of Philosophy

In The Faculty Of Engineering

University Of London

And

For The Diploma Of Membership

Of Imperial College

Fluid Section

Mechanical Engineering Department

Imperial College Of Science And Technology

LONDON SW7 2BX

April 1983

ABSTRACT

The body forces imposed on flows in pipes induce secondary flows in planes perpendicular to the axes, resulting in non-symmetrical axial-velocity and temperature profiles which modify the resistance to the flow and the rate of heat transfer. Two different test-cases have been studied: the first being the flow in a rotating pipe, of circular cross section, about an axis parallel to the centre line; the second being the isothermal flow in 90 degree bends with mild and strong curvature.

For the rotating pipe flow, a computer code using a finite-difference method has been developed to solve the conservation equations governing three-dimensional turbulent flow including the effects of body force and heat transfer. Two different turbulence models have been used: the first model is based on transport equations for the kinetic energy of turbulence k and its rate of dissipation ε, which are solved simultaneously with the mean flow momentum, continuity and enthalpy equations. This model has been applied to developing pipe flows. The second model is based on a set of algebraic Reynolds stress and heat flux equations which have been applied to the prediction of fully-developed flows. The results obtained have been compared where possible with available experimental data.

The flow in the 90 degree bend has been investigated experimentally and numerically. A water rig with a 90 degree bend of circular cross-section was constructed with a ratio of radius of curvature to pipe diameter equal to 2.8. The axial velocity contours with developing flow were measured using a laser Doppler anemometer

for both laminar and turbulent flows. The wall static pressure distribution has also been measured. Experimental results have also been obtained for turbulent flow in a square cross section duct with a 90 degree bend in which the ratio of radius of curvature to cross-sectional width has been 7. Another computer program has been developed to solve the flow in curved pipes, using two solution procedures. A so-called "parabolic" calculation procedure has been used for mildly curved pipes. For the case of strongly curved ducts, a so-called "partially-parabolic" calculation procedure was found to be necessary.

The principal results of the research are:

1- Computer codes intended for practical calculations of laminar and turbulent flow with heat transfer in

   a) tubes rotating about a parallel axis

   b) tube bend of arbitrary curvature.

2- Velocity data for laminar and turbulent flow in pipe bends suitable for calibration and testing calculation methods.

ACKNOWLEDGEMENTS

I wish to express my deep gratitude to my supervisor Dr. M.M. Gibson for his help, advice and encouragement. I am also indebted to Dr. Y. Yianneskis and Dr. A. Taylor for helping me in the experimental work and for the useful and helpful discussions. I offer my thanks to Professor J.H. Whitelaw for the opportunity to work in the fluid mechanics group, and for the valuable advice in numerous discussions. I thank the CEGB Central Electricity Research Laboratories, London, England for supporting this research by a contract for around three year period. I cencerely appreciate a further two year grant from the Egyptian Education Bureau, London. Finally, I wish to thank all those who provided me with help and encouragement during the present study.

LIST OF CONTENTS

	page
ABSTRACT	2
ACKNOWLEDGEMENTS	4
LIST OF CONTENTS	5
1. INTRODUCTION	9
1.1 The Problem Ccnsidered	9
1.2 Previcus Work On The Flow Through Ducts Rotating About A Parallel Axis	11
1.2.1 Analytical Solutions	13
A) Laminar Flow	13
B) Turbulent Flow	18
1.2.2 Experimental Work	18
A) Laminar Flow Measurements	18
B) Turbulent Flow Measurements	22
1.2.3 Numerical Solutions	26
A) Laminar Flow	26
B) Turbulent Flow	28
1.2.4 Ccncluding Remarks	31
1.3 Previous Work On The Flow Through Curved Ducts Of Circular Cross-Section	31
1.3.1 Thecretical Studies	31
A) Laminar Flow	31
B) Turbulent Flow	33
1.3.2 Experimental Work	34
A) Laminar Flow	34
B) Turbulent Flow	37
1.3.3 Numerical Solutions	38
A) Laminar Flow	38
B) Turbulent Flow	42
1.3.4 Concluding Remarks	42
1.4 Previous Work On The Flow Through Curved Ducts Of Rectangular Cross-Section	45
1.4.1 Theoretical Studies	45
1.4.2 Experimental Work	45
A) Laminar Flow Measurements	45
B) Turbulent Flow Measurements	47
1.4.3 Numerical Solutions	50
A) Laminar Flow	50
B) Turbulent Flow	51
1.5 Present Contributions	53
1.6 Layout Of The Thesis	54

	page
2. MATHEMATICAL DESCRIPTION OF THE FLOW	56
2.1 The Governing Differential Equations	56
2.2 Mathematical Modelling Of Turbulence	57
2.3 The k-ε Turbulence Model	59
2.3.1 Wall Influence	60
2.3.2 Evaluation Of The Model Constants	62
2.4 Reynolds Stress Equation Modelling	64
2.4.1 Wall Effects In The Pressure-Strain Terms	66
2.5 Algebraic Model	68
2.6 Heat Flux Model	68
2.6.1 The Choice Of The Heat Flux Model Constants	71
3. NUMERICAL METHODS OF SOLUTION	73
3.1 Introduction	73
3.2 "Partially-Parabolic" Calculation Procedure	75
3.2.1 The Partially-Parabolic Solution Procedure	81
3.2.2 The Boundary Conditions	83
3.3 "Parabolic" Calculation Procedure	83
3.3.1 The Parabolic Solution Procedure	86
3.4 Concluding Remarks	86
4. EXPERIMENTAL INVESTIGATION	88
4.1 Introduction	88
4.2 Description Of The Rig	89
4.2.1 General Layout	89
4.2.2 The Test Sections	93
4.3 Laser Doppler Velocimetry	95
4.3.1 Doppler Signal Generation And Interpretation	99
4.3.2 The Laser Doppler Velocimeter Control Volume	101
4.3.3 Control Volume Displacement Correction	103
4.3.4 Doppler Signal Processing	104
4.4 Scope And Accuracy Of The Measurements	106

page

4.5 Results And Discussion For Circular Cross-Section Bend 108
4.5.1 Flow Visualization 108
4.5.2 Laminar Flow Measurements 108
4.5.3 Turbulent Flow Measurements 116
4.5.4 Closure 124

4.6 Results And Discussion For Square Cross-Section Bend 124

5. PREDICTION OF FLOW THROUGH ROTATING DUCTS 133

5.1 Laminar Flow 133
5.1.1 Laminar Isothermal Flow 133
5.1.2 Laminar Flow With Heat Transfer 135

5.2 Turbulent Flow 137
5.2.1 Isothermal Turbulent Flow With The k-ε Model 137
5.2.2 Isothermal Turbulent Flow With Algebraic Model 147
5.2.3 Turbulent Flow With Heat Transfer Using The k-ε Model 152
5.2.4 Turbulent Flow With Heat Transfer Using The Algebraic Heat Flux Model 162

5.3 Concluding Remarks 171

6. PREDICTION OF FLOW THROUGH BENDS OF CIRCULAR CROSS-SECTION 185

6.1 Introduction 185

6.2 Laminar Flow 186
6.2.1 Laminar Flow In A Mildly-Curved Duct 186
6.2.2 Laminar Flow In A Stongly-Curved Duct 189

6.3 k-ε Model Predictions Of Turbulent Flow In Strongly-Curved Ducts 210

6.4 Concluding Remarks 217

7. CONCLUSIONS AND SUGGESTIONS FOR FUTURE RESEARCH 224

7.1 Conclusions 224

7.2 Suggestions For Future Work 225

LIST OF REFERENCES 227

NOMENCLATURE 234

APPENDIX A1. THE GOVERNING DIFFERENTIAL EQUATIONS 240
A1.1 Introduction 240
A1.2 The (r,θ,z) Coordinate System 240
A1.3 The (r,θ,ϕ) Coordinate System 243

page

APPENDIX A2. ALGEBRAIC REYNOLDS STRESS AND HEAT FLUX MODEL EQUATIONS FOR THE FLOW IN A TUBE ROTATING ABOUT A PARALLEL AXIS 246

APPENDIX A3. ALGEBRAIC REYNOLDS STRESS AND HEAT FLUX MODEL EQUATIONS FOR THE FLOW IN BENDS 254

APPENDIX A4. ALGEBRAIC REYNOLDS STRESS AND HEAT FLUX MODELS APPLIED TO STATIONARY PIPE FLOW 260

APPENDIX A5. THE DETERMINATION OF THE LASER BEAM PATH THROUGH A DUCT OF CIRCULAR CROSS-SECTION 267
A5.1 Bend Cross-Section 267
A5.2 Straight Pipe Cross-Section 271

APPENDIX A6. PUBLICATIONS 275

CHAPTER 1

INTRODUCTION

1.1 The Problem Considered

When the flow in pipes is subjected to a body force a secondary flow in the plane perpendicular to its centre line will be induced. This secondary flow modifies the flow behaviour so as to increase the resistance to flow and the rate of heat transfer. Many important types of flow in engineering applications are subjected to body forces, such as flow in pipes with gravitational effects, flow in bends and flow in rotating pipes.

The present study describes two types of flow in pipes with body forces; the first is the flow with heat transfer in circular cross-section ducts rotating about an axis parallel to its centre line. The second type of flow is isothermal flow in 90° bends with both circular and rectangular cross-sections.

The increasing demand for efficient cooling techniques for rotating machinery indicates the practical significance of the problem of heat transfer and fluid flow in the entry region of a heated tube which revolves about a displaced and parallel axis. As service conditions become more arduous, more accurate understanding and prediction of heat transefer in such passages become more important. The power output from electrical generators is partially restricted by the permissible operating temperature of the insulation which surrounds the armature windings. To prevent thermal break-down of the insulation there are clear advantages to be obtained by circulating a suitable coolant along passages located within the rotor conductors.

Gas cooling, notably by hydrogen, has been adequate for generators of moderate power output, but designs involving water cooling have become more attractive and suitable for machines rated in excess of about 500 MW (Anon, 1968). For generators nominally rated at 1000 MW, water cooling can produce an improvement of 0.5% in the effeciency.

As a fluid flows through a straight duct and into a bend the pressure, which -in the straight section- is uniform across the flow, must adjust in the bend to counter centrifugal forces. The pressure is greatest at the outer wall farthest from the centre of curvature and least at the inner wall and the cross-stream pressure gradient in the bend has two well known effects on the flow. At the bend inlet the boundary layer on the outer wall experiences the effects of a positive streamwise pressure gradient which may in a tight bend be strong enough to produce local separation; conversely, the inner wall boundary layer is accelerated. The reverse occurs at the pipe exit where local pressure gradients of the opposite sign appear as the flow adjusts to uniform pressure conditions downstream. Inside the bend, the presence of side wall boundary layers ensures that the conditions for radial equilibrium cannot be satisfied exactly over the entire field. The slow-moving fluid in these layers is forced inwards towards the centre of curvature, and continuity ensures that the high speed fluid near the axis is driven outwards. The result is a secondary flow superimposed on the main flow.

If the bend is of circular cross section, the effect of the secondary flow is to displace the region of maximum velocity from the centre towards the outer wall. If, however, the boundary layers are thin and the secondary flow is weak the velocity distribution in the inviscid central core approximates to that of a free vortex with

velocity increasing towards the centre of curvature. The effects of longitudinal curvature on the boundary layers on the inner and outer walls also tend to counteract the effects of pressure-driven secondary flow. In the inner boundary layer the shear stress is reduced by curvature and the boundary layer grows relatively slowly. In the outer boundary layer the shear stress is increased and the layer is retarded and thickened. The effects of curvature on the turbulence in turbulent boundary layer flow are an order of magnitude greater and may be large enough to counteract the effects of secondary flow and to play a significant role in determining the flow structure, (Bradshaw, 1973).

The presence and origin of secondary flow in bends have been known and understood although obvious measurement difficulties associated with probe explorations have hindered detailed investigation and have largely restricted experiments to flow visualization studies and overall pressure loss measurements. The total friction loss of energy near the wall of the pipe increases due to secondary flow. This increase in resistance is rather small when the curvature of the pipe is small, but may be considerable if it is sufficiently curved.

1.2 Previous Work On The Flow Through Ducts Rotating About A Parallel Axis

In recent years a number of theoretical, numerical and experimental studies have been undertaken on flow and heat transfer in tubes which rotate about an axis parallel to the centre line of the tube with uniform angular velocity Ω. The arrangement and notation are shown in Fig.1.1.

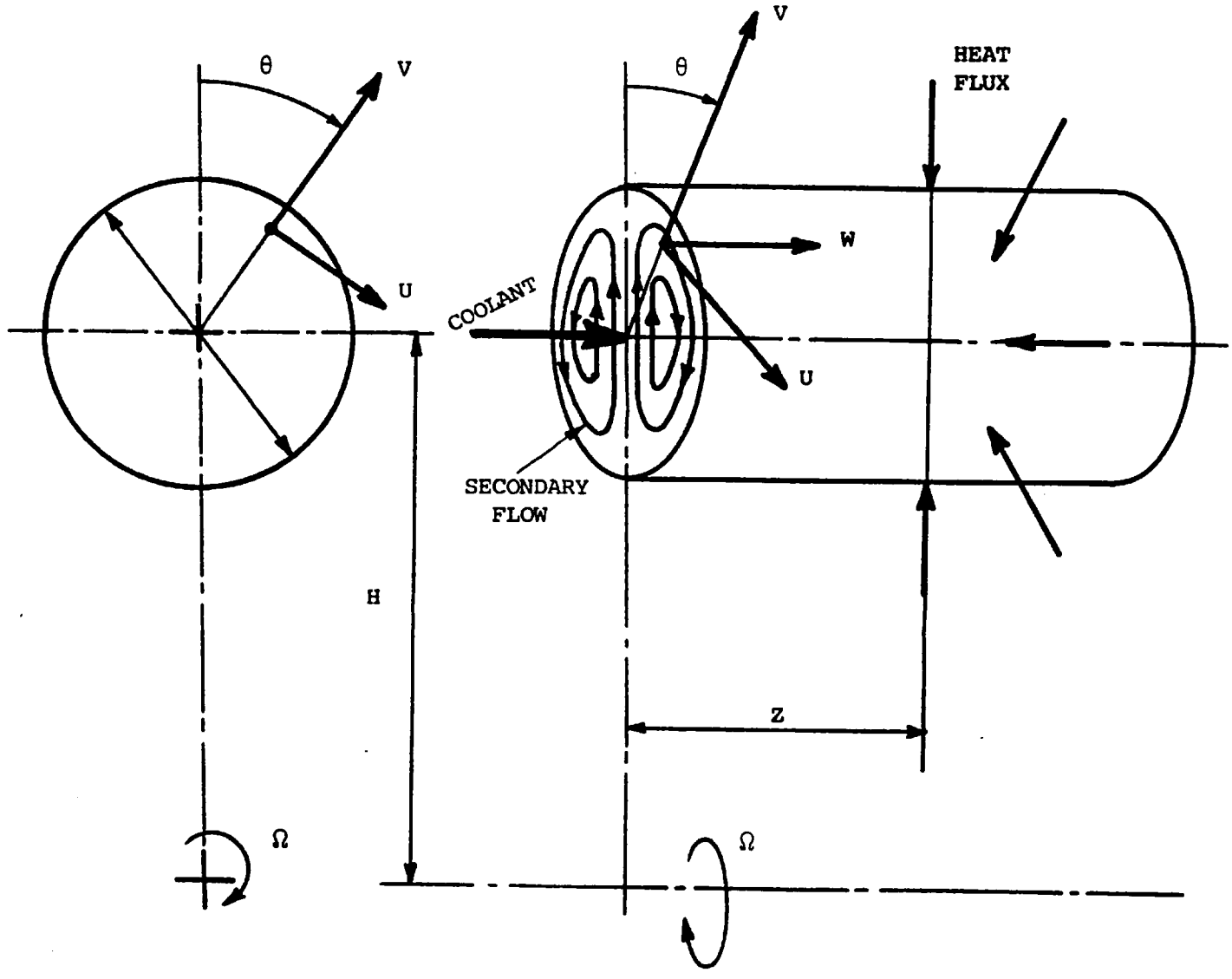


Fig.1.1 Flow through a rotating duct about a parallel axis.

1.2.1 Analytical Solutions

A) Laminar Flow:

I- Isothermal Flow:

Morris (1965a) studied isothermal fully-developed case using the cylindrical polar co-ordinate system with reference to rotating frame. The momentum and continuity equations used are as follows:

$$V(\partial V/\partial r) + U(\partial V/r\partial\theta) + W(\partial V/\partial z) - U^2/r = -(\partial p/\partial r)/\rho + \nu\{\nabla^2 V - V/r^2 - 2(\partial U/r\partial\theta)/r\} + 2U.\Omega + (r+H.\cos\theta).\Omega^2 \quad (1.1)$$

$$V(\partial U/\partial r) + U(\partial U/r\partial\theta) + W(\partial U/\partial z) + U.V/r = -(\partial p/r\partial\theta)/\rho + \nu\{\nabla^2 U+2(\partial V/r\partial\theta)/r - U/r^2\} - 2U.\Omega - H.\sin\theta.\Omega^2 \quad (1.2)$$

$$V(\partial W/\partial r) + U(\partial W/r\partial\theta) + W(\partial W/\partial z) = -(\partial p/\partial z)/\rho + \nu.\nabla^2 W \quad (1.3)$$

$$\partial(rV)/\partial r + \partial U/\partial\theta + \partial(rW)/\partial z = 0 \quad (1.4)$$

where: $\nabla^2 = (\partial^2/\partial r^2) + (\partial/\partial r)/r + (\partial^2/\partial\theta^2)/r^2 + (\partial^2/\partial z^2)$

and ν is the kinematic viscosity.

The continuity equation may be satisfied by defining a dimensionless stream function Ψ, by the following relationship:

$$U = \nu(\partial\Psi/\partial\theta)/r \quad \text{and} \quad V = -\nu(\partial\Psi/\partial r) \quad (1.5)$$

Elimination of the pressure terms in equations (1.1 and 1.2) eliminates the dependency of Ψ, and hence the secondary flow, on rotational speed. Thus secondary flow is not induced, and the pressure distribution must take the form:

$$P = \gamma z + p(r,\theta) \tag{1.6}$$

where γ is the axial pressure gradient, and $p(r,\theta)$ is obtained from equations (1.1 and 1.2) thus:

$$p(r,\theta) = \rho.\Omega^2.r^2/2 + H.r.\rho.\Omega^2.\cos\theta + A \tag{1.7}$$

where A is some arbitrary constant.

Thus the modification to flow conditions as a consequence of rotation is made manifest solely as a pressure distribution in the (r,θ) plane which is superimposed on the pressure field present with zero rotation.

II- Flow With Heat Transfer:

Morris (1965b) continued his study to see the influence of rotation on the fully-developed flow with heat transfer. The geometry used was a rotating vertical cylindrical tube similar to that shown in Fig.1.1. While the tube rotates, fluid is pumped through in an upward direction and the tube wall is subjected to a uniform temperature gradient. The conservation equations (1.1 to 1.4) were solved using a series expansion in ascending powers of the rotational Rayleigh number, defined as:

$$Ra_r = \beta.\Omega^2.\tau.H.r_o^4/(\alpha.\nu) \tag{1.8}$$

where: β is the coefficient of expansion, α is the thermal diffusivity and τ is the axial temperature gradient.

The terms containing Ω in equations (1.1 and 1.2) produce "centrifugal-buoyancy" effects when fluid temperature gradients are present, and the fluid density must vary with temperature. Morris assumed that this variation is small, however, to be ignored in all terms except the buoyancy force in the momentum equations. It was

assumed that the wall material is of high thermal conductivity so that any circumferential temperature variations could be ignored. The resulting solution was an approximate one and valid only for low rates of heating. It was shown that rotation produces secondary flow in the plane perpendicular to the axis resulting in non-symmetrical axial-velocity and temperature profiles and changes in the resistance to flow and rate of heat transfer. It was shown that the resistance coefficient C_f and the Nusselt number Nu were greater than the values obtained with stationary tube. It was also shown that the percentage increase in resistance was greater than the corresponding increase in heat transfer. In this type of flow three components of convection may be identified. Circulation of the fluid through the tube is maintained by an axial pressure gradient, so that forced convection results in a constant value of Nu. Owing to gravitational buoyancy in the axial direction, this Nu was modified, the magnitude of the alterations being characterized by the gravitational Rayleigh number, defined as:

$$Ra_g = \beta . \tau . g . r_o^4 / (\alpha . \nu) \qquad (1.9)$$

where g is the gravitational acceleration.

Rotational buoyancy due to centrifugal and Coriolis forces causes convection currents across the tube section, and Nu was modified again. The centrifugal buoyancy was seen to depend on the product of Ra_r and Reynolds number, defined as:

$$Re = -r_o^3 (\partial p/\partial z)/(4\nu^2 . \rho) \qquad (1.10)$$

Another attempt has been made, by Mori and Nakayama (1967), to solve the fully-developed case for rotating pipe with large angular velocity by assuming secondary flow due to buoyancy. Flow and

temperature fields were analyzed by dividing the fields into a core region, where the effect of the secondary flow is predominant as shown in Fig.1.2, and a thin boundary layer along the wall. In addition to the axial pressure gradient, there exists the pressure distribution in the cross section due to the body force. The pressure distribution in the core region is in balance with the body force, and the secondary flow was regarded as being uniform. However, in the boundary layer, the force balance between the body force and the pressure gradient in the cross section breaks down so that the difference between these forces causes a secondary flow along the pipe wall. When the secondary flow is set up, some of the work done by the axial pressure gradient is transferred to the secondary flow, and dissipation by viscous diffusion near the wall. The specific relation for the flow in a rotating pipe is obtained from the momentum eqation in the circumferential direction which expresses force balance between the body force in the strong centrifugal field and viscous resistance against the secondary flow at the pipe wall. The resistance coefficient ratio C_f/C_{fo} (where $C_{fo}=64/Re$ for a Poisieulle profile for stationary pipe flow) and the Nusselt number ratio Nu/Nu_o (where $Nu_o=48/11$ for constant temperature gradient for stationary pipe flow) were obtained as functions of Prandtl number Pr and $Re.Ra_r$. They are proportional to $(Re.Ra_r)^{1/3}$ in the region of large values of $Re.Ra_r$, when the Coriolis' effect is disregarded. It was shown that the effect of Coriolis' force appears through the non-dimensional parameter J, which was defined as follows:

$$J = 2r_o^2 . \Omega / \nu \qquad (1.11)$$

and the corrections due to Coriolis' effect were applied to C_f/C_{fo} and Nu/Nu_o as shown in Fig.1.3.

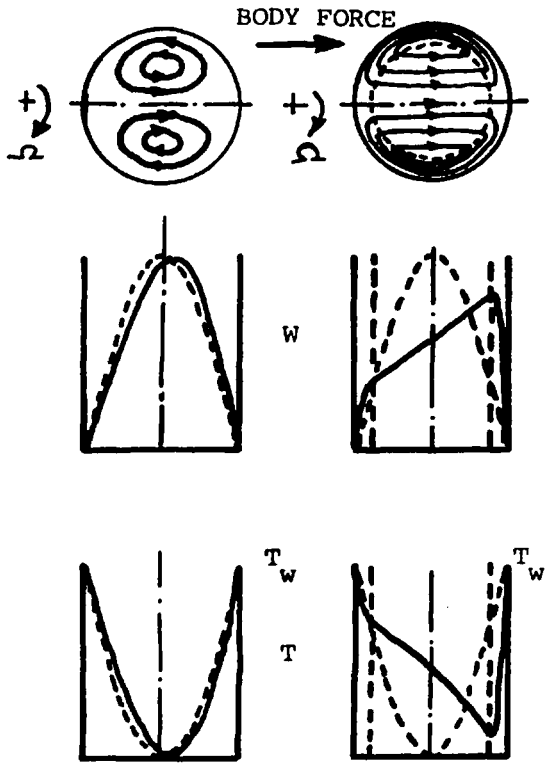


Fig.1.2 Flow and temperature fields under the effect of secondary flow.

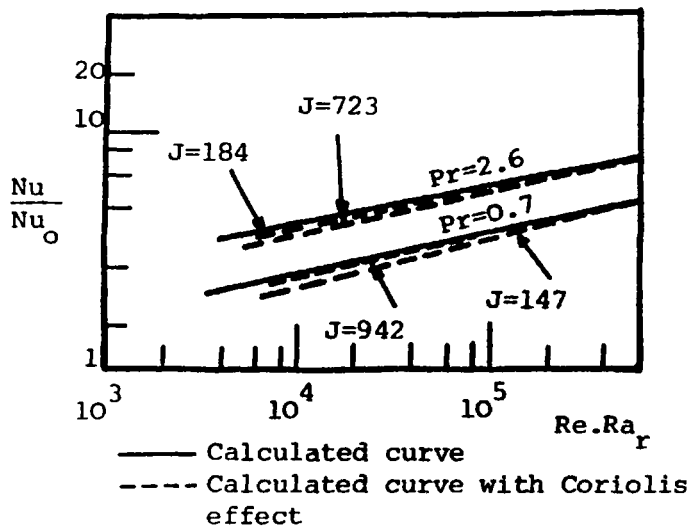
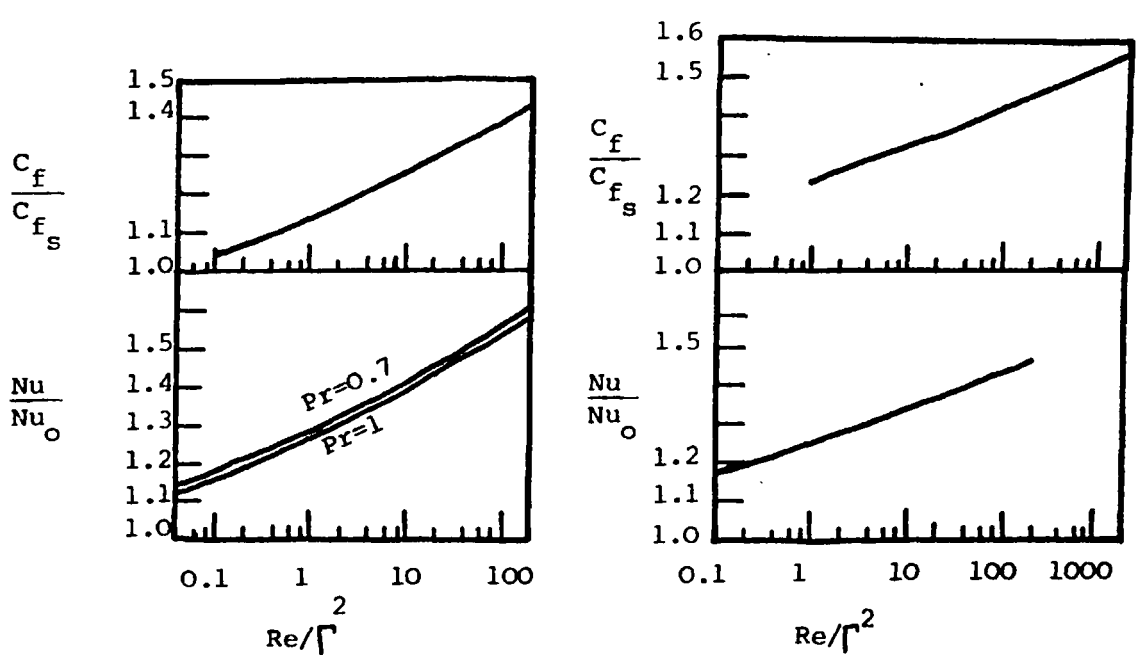


Fig.1.3 Effect of Coriolis force for rotating laminar pipe flow.

(From: MORI and NAKAYAMA, 1967)



(a) For gases

(b) For liquids

Fig.1.4 Nusselt number and resistance coefficient ratios for rotating turbulent pipe flow. (From: NAKAYAMA, 1968).

B) Turbulent Flow:

Heat transfer in turbulent fully-developed flow with constant heat flux was studied by Nakayama (1968). The same analysis used for laminar flow by Mori and Nakayama (1967) was carried out for turbulent flow. The increases in C_f and Nu due to secondary flow were obtained in terms of $Re/\Gamma^{m/2}$, where Γ is the ratio of the inertia force to the body force. It was found that various parameters appearing in different secondary flow problems could generally be expressed by $Re/\Gamma^{m/2}$ in either laminar flow (where m=1) or turbulent flow (where m=4 for gases and m=5 for liquids for the type of flow considered here). The increases in C_f and Nu in turbulent flow due to rotation, as shown in Fig.1.4, were not so remarkable as those encountered in laminar flow. The effect of Coriolis force was expressed in terms of the ratio of Coriolis force to body force. However, this effect in turbulent flow was so small that it was neglected in the analysis. It was shown that the effect of secondary flow increases remarkably with increasing angular velocity, if the other factors are kept constant, and decreases with increasing mean velocity.

1.2.2 Experimental Work

Most of the experimental work carried out for rotating pipes has been done using rigs similar to that shown in Fig.1.5. Heat transfer measurements are available for different flow conditions and test section geometries.

A) Laminar Flow Measurements:

Morris (1968 and 1969) studied the influence of rotationally induced buoyancy on heat transfer in rotating tubes. Data for both

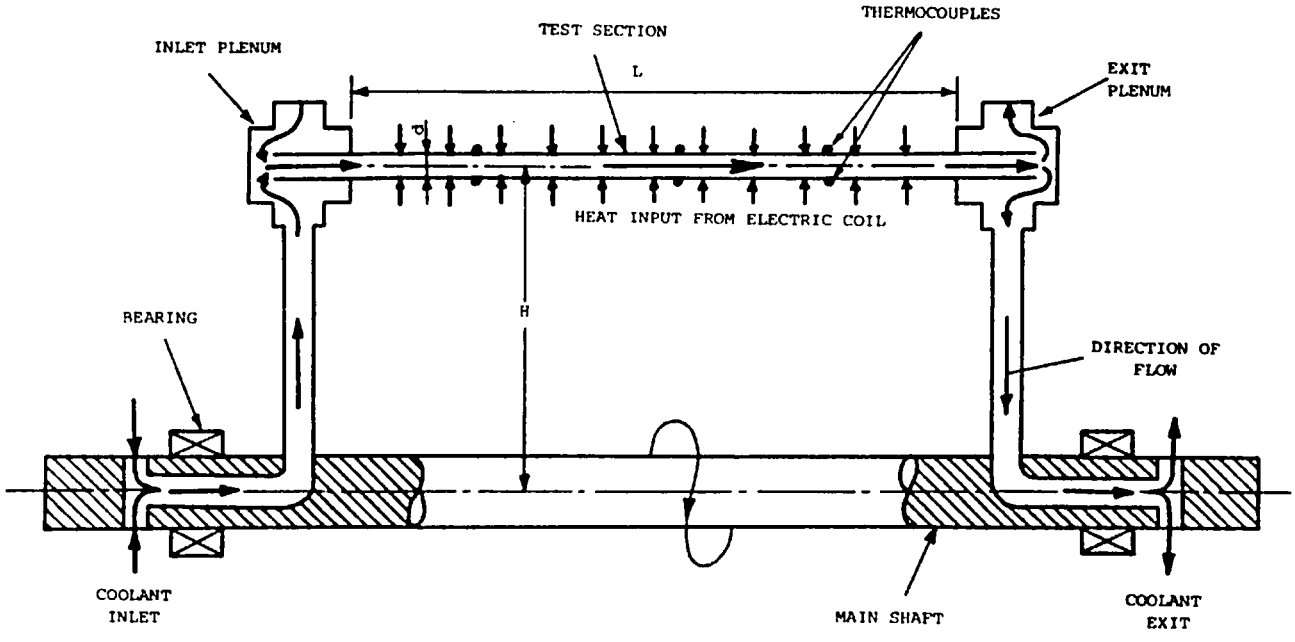


Fig.1.5 Schematic layout of the parallel rotating pipe flow apparatus.

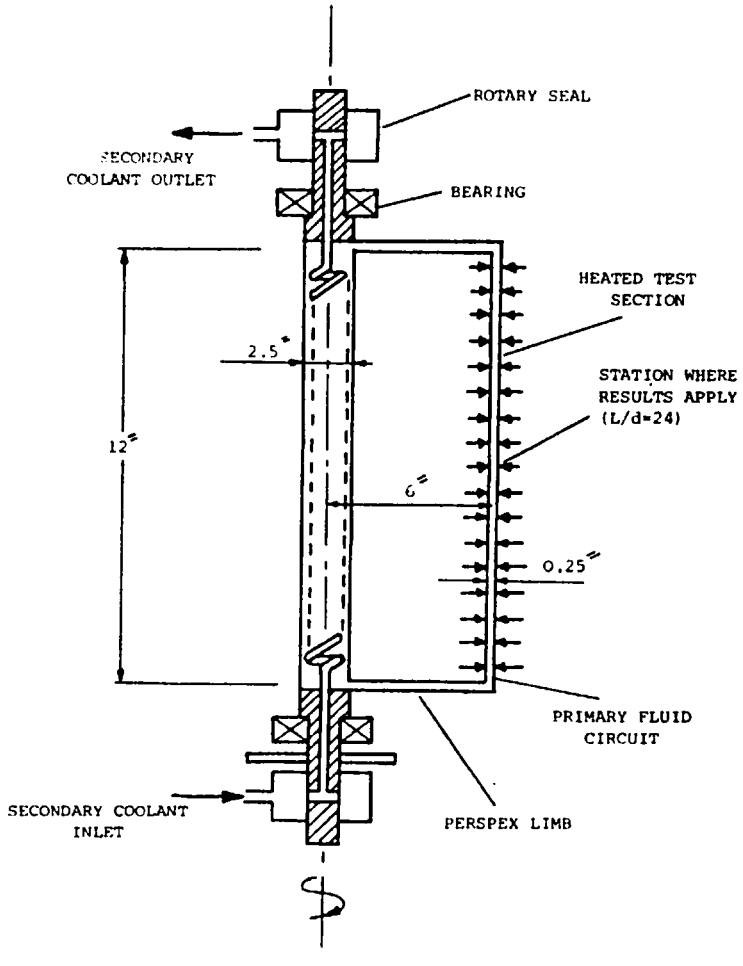


Fig.1.6 Schematic layout of rotating thermosyphon test loop.
(From: MORRIS, 1968)

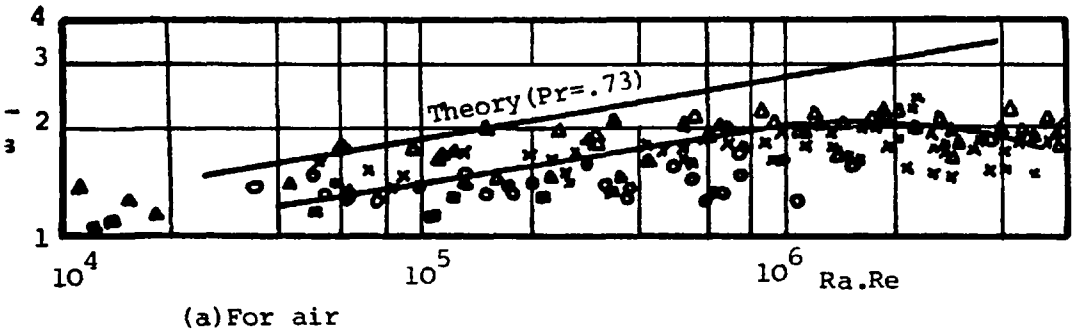
water and glycerol were obtained using a rotating thermosyphon apparatus as shown in Fig.1.6. Experiments showed much greater sensitivity to rotation than was suggested by theoretical studies.

Morris and Woods (1974) obtained data for fully-developed air flow in rotating pipes with uniform heat flux through the wall. The apparatus used was similar to that shown in Fig.1.6, and the experiments were carried out using two different test sections. Data for air and data for water taken from Morris (1964) and used in this paper, are shown in Fig.1.7. Morris and Woods (1977) continued this work, using the same apparatus and test sections. They studied the effect of rotation on heat transfer in the entrance region of the rotating test sections. Each test section was electrically heated and the axial wall temperature distribution was measured. The heater power was measured with a conventional wattmeter. The external convective loss varies with speed of rotation, and was estimated from a series of heat loss calibrations. The conduction loss at each end of the test section was estimated from knowledge of the tube wall temperature distribution together with details of the cross sectional dimensions and the material used. The local heat flux distribution along the tube was determined by dividing the test section into a number of segments and performing an energy balance on each segment. The effect of rotation on wall temperature and heat transfer are depicted in Fig.1.8. The authors concluded that the mean Nusselt number Nu_m is a function of both Re and rotational Reynolds number J defined as:

$$J = \Omega . r_o^2/(2\nu) \qquad (1.12)$$

= Coriolis force/viscous force.

Two separate equations were needed to correlate the data obtained



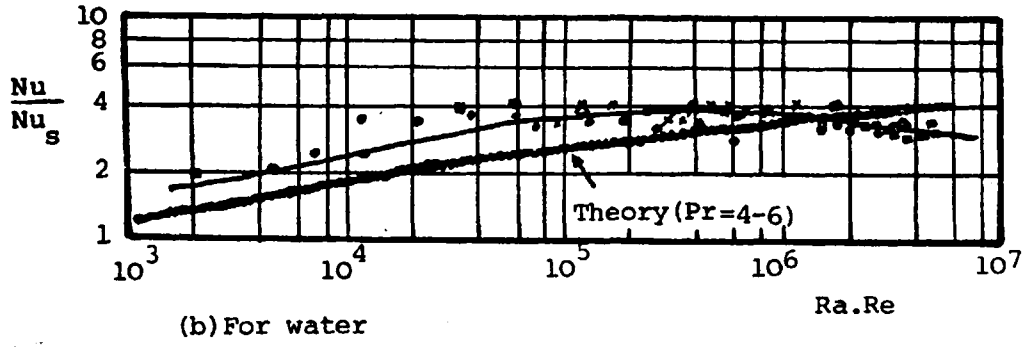
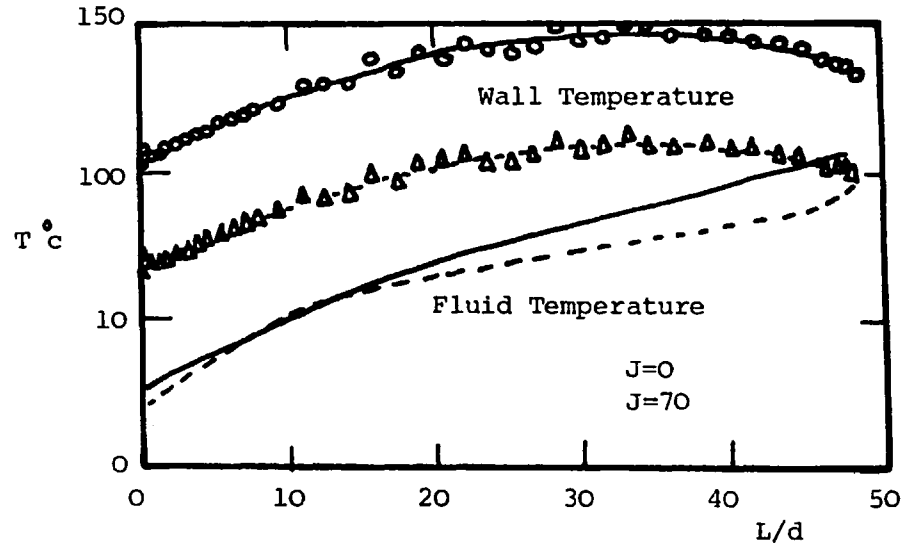
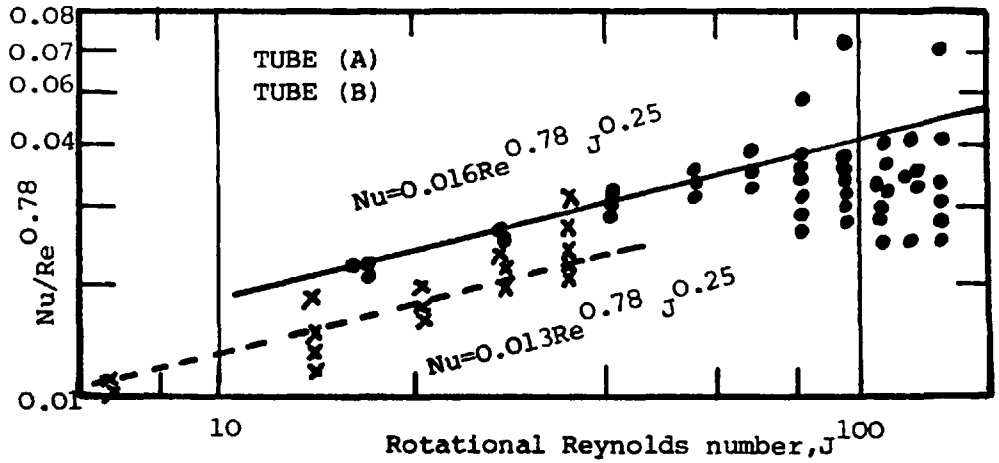


Fig.1.7 Comparison of experimental data with predictions.
(From: MORRIS and WOODS, 1974)



(a) Temperature distributions for test section (A)
(Re=1300, Nominal heat flux=0.05 KW/m)



(b) Comparison of laminar flow data with proposed correlations

Fig.1.8 Results of MORRIS and WOODS (1977)

with the two rotating geometries used. Wide scatter was evident implying a complex interaction between Coriolis force and centrifugal buoyancy.

B) Turbulent Flow Measurements:

The influence of rotation on heat transfer to turbulent air flow in the entrance region of a tube was studied by Barrow et al (1967). The test section length-to-diameter ratio was small (L/d=12 and H/d=6). Reynolds number of 5000, 10 000, 15 000 and 20 000 were used with rotational speeds of 0, 200 and 500 r.p.m. These speeds corresponded to a tube centre line acceleration ratio ranging between 0-42.6g. Results showed that for a given speed of rotation the increase in heat transfer over that achieved under non-rotating conditions was greater at lower Re. The increase in heat transfer had been raised because of two effects. First, the entry swirl, which was characterized by the Rossby number defined as:

$$Ro = W_m/(H.\ \Omega) \qquad (1.13)$$

This swirl caused a step-like change in the heat transfer. Secondly, centrifugal buoyancy causes further increase in heat transfer, the amount of change being characterized by the slope of the (Nu-Ra_g) curves. In the entry region it appeared that the inlet swirl was the more dominant term. No attempts to fit a correlating equation to the data were made because the complex interaction between upstream geometry, flow conditions, and rotary geometry would not give generally applicable results.

Humphreys (1968) extended the work done by Barrow et al (1976). The effects due to swirling flow at the inlet to the test section caused by rotation were reduced by flow straighteners. The results

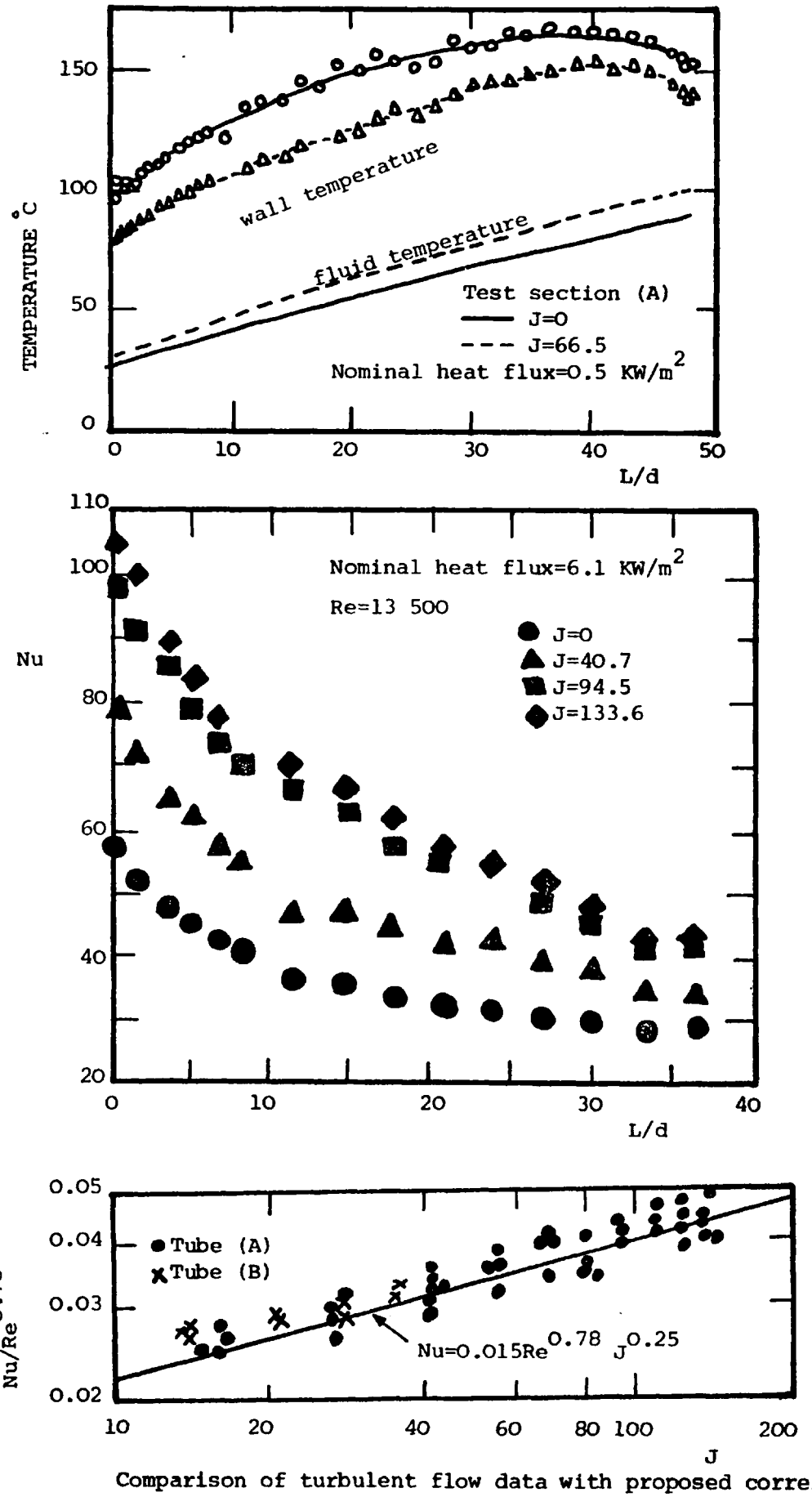
showed Nu to be reduced when straightners were used.

Morris and Woods (1977) showed that buoyancy affects only the centrifugal terms and not the Coriolis terms. They concluded that the effects of rotation may be taken into account in terms of J, as defined in equation (1.12). Physically, this means that Coriolis-induced secondary flow increases radial mixing with consequential benefit to the heat transfer mechanism. For flows in two test sections the authors concluded that Nu_m was a function of both Re and J, as shown in Fig.1.9, and that one equation correlated all data to within ±12%.

Recently, Stephenson (1982) studied air flow with heat transfer in rotating ducts under conditions found in the cooling system of the rotors of large turbogenerators. A rig similar to that shown in Fig.1.5 was used. A tenth order polynominal expression was fitted to the measured wall temperatures, from which the axial variation of air temperature and heat input into the air were calculated. The axial heat loss was calculated from the tube dimensions, and the radial loss from preliminary experiments with zero flow rate. The local values of Nu were calculated, and the mean Nusselt number for the first quarter of the test section (described as "inlet value") was also found. The pressure rise due to rotation was allowed for in calculating the overall pressure loss coefficient, which was defined as follows:

$$C_T = (2.\Delta P + \rho.\Omega^2.H^2)/(\rho.W_m^2) \qquad (1.14)$$

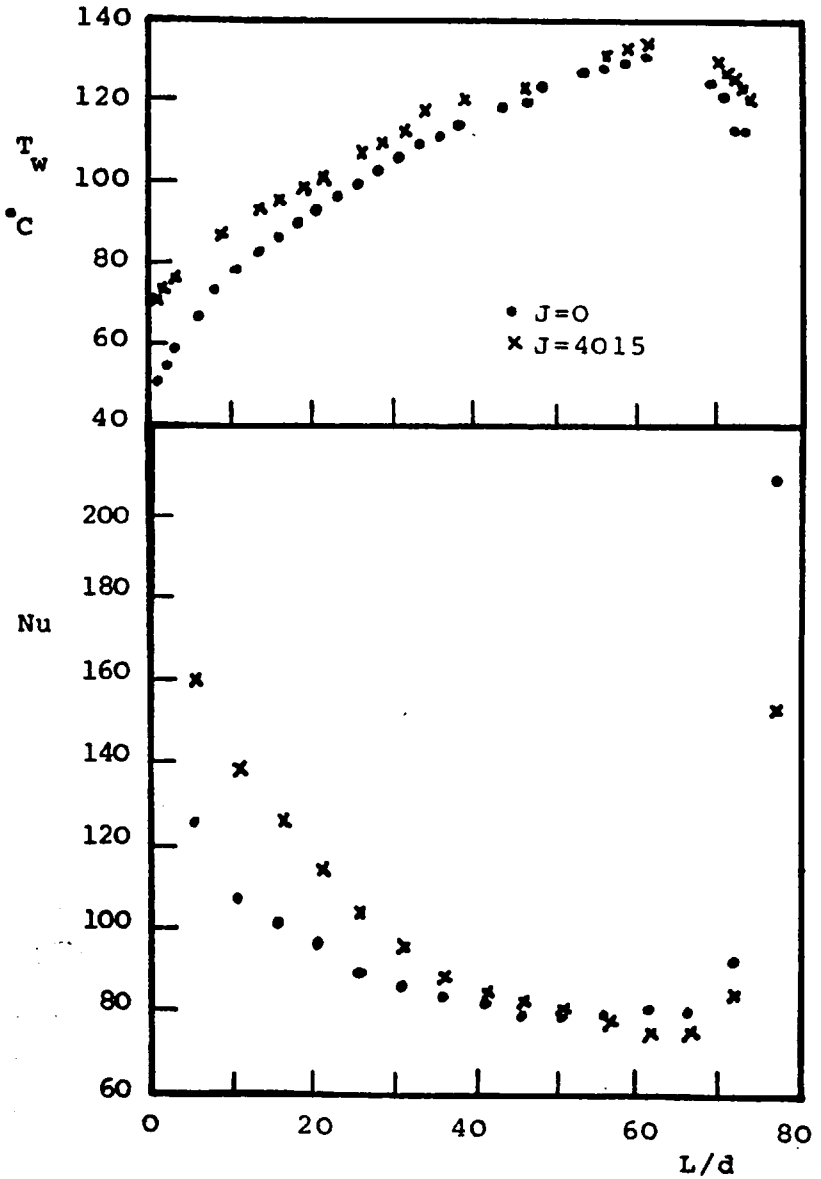
The results are shown in Fig.1.10. The tests covered values of Re between 5500 and 33 000, J between 600 and 4000, swirl number Sw between 0.4 and 19 and rotational Grashof number Gr_r between 1700 and 740 000. The eccentricity parameter ε was 0.0397 and test section was

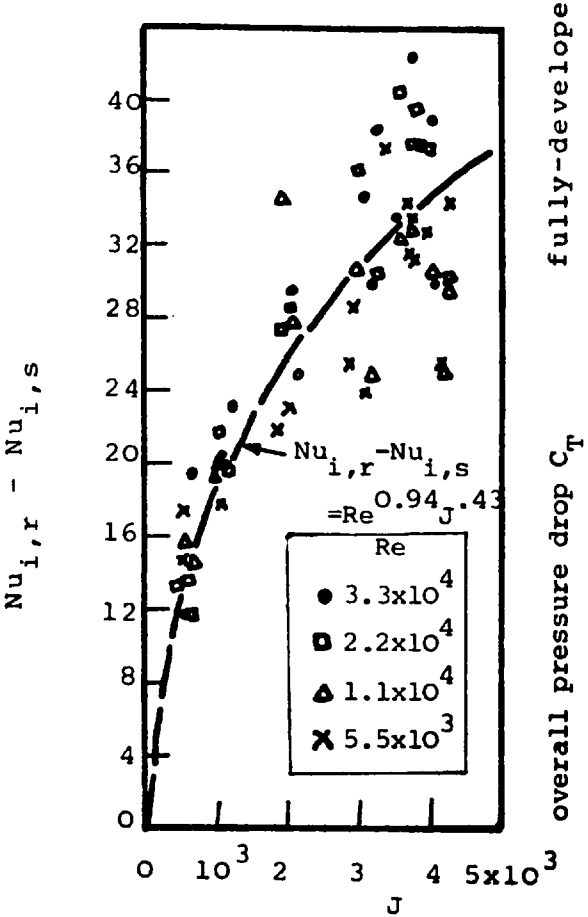


Comparison of turbulent flow data with proposed correlation

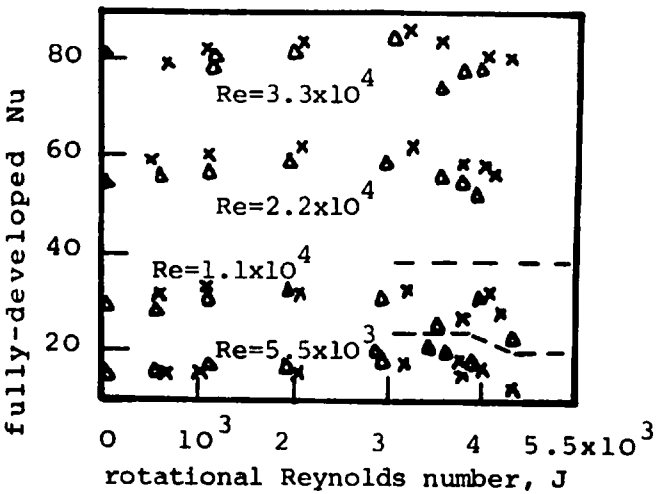
Fig.1.9 Turbulent flow in rotating pipes.

(From: MORRIS and WOODS, 1977)





increase in mean Nusselt number for inlet region as function of rotational Reynolds number.



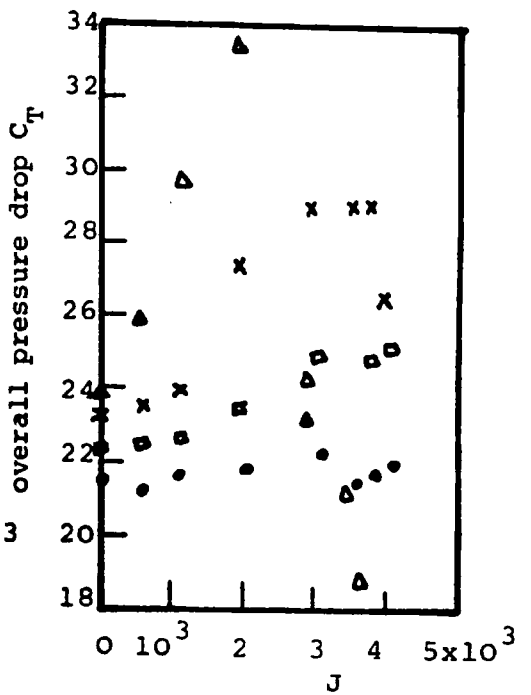


Fig.1.10 Experimental results of rotating pipes (From: STEPHENSON, 1982).

77.2 diameters long. The dimensionless groups used in this paper were:

$$J = \Omega d^2/\nu \tag{1.15}$$

$$Sw = \Omega.H/W_m \tag{1.16}$$

$$Gr_r = \beta.\Omega^2.\tau.H.d^4/\nu \tag{1.17}$$

$$\epsilon = d/H \tag{1.18}$$

Tests showed that the increase in heat transfer were greatest in the developing flow region and for lower flow rates. The overall pressure-loss coefficient increased with increasing rotation. However, at high rotational speeds and low flow rates it decreased with increasing rotation. Measurements of heat transfer and pressure drop did not show a significant variation with maximum test section temperature. The only exceptions were for low flow rates and high rotational speeds. This results showed that rotational buoyancy was not important, so that the dominant effect was of inlet swirl induced by rotation, combined with Coriolis accelerations.

1.2.3 Numerical Solutions

A) Laminar Flow

The first attempt to solve the flow through a rotating duct using a finite difference method was made by Morris and Woods (1971, 1974). The calculations were limited to fullly-developed laminar flow. The motion of the fluid was referred to a cylindrical polar co-ordinate frame (r,θ,z) rotating with the duct as shown in Fig.1.1. To reduce the conservation equations to a tractable form the following assumptions were made:

a) The flow was laminar and steady.

b) All the fluid properties were constant, except ρ which varies

with temperature T according to

$$\rho/\rho_o = 1-\beta(T-T_o) \qquad (1.19)$$

where subscription "o" referes to a reference datum.

c) The thermal conductivity of the tube material was high enough to smooth out circumferential variations in wall temperature.

d) Variable density was accounted for in the body force terms only (the Boussinesq approximation).

e) The heat flux at the wall was uniform.

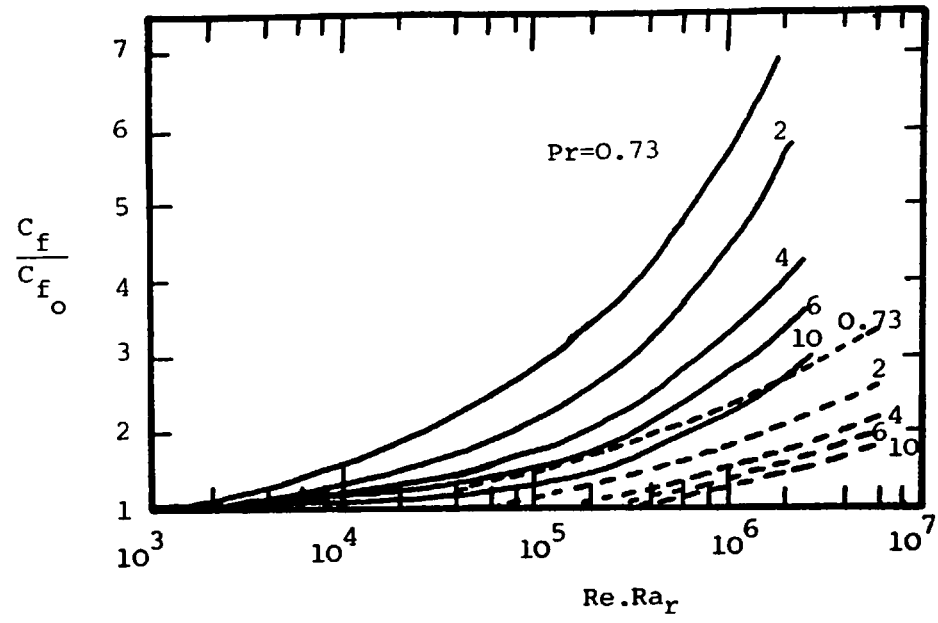
A set of two-dimensional elliptic equations was solved numerically and the results were compared with experimental data. It was concluded that the influence of Coriolis acceleration characterized by J, as defined in equation (1.12), had little effect on the solution, and it was neglected. It was demonstrated that both Nu and C_f increased with eccentricity. The largest increases occurred for fluids of high Prandtl number. For $d/H > 0.2$ it was found that the effect of eccentricity could be neglected. The results were compared with the experiments, and the predicted improvement in heat transfer was about 25% greater than the "best fit" line drawn as shown in Fig.1.7 for air. For $Re.Ra_r > 10^6$ the predicted result sustained improvement in the heat transfer, while the measurements did not. For water the comparison was made for fluid Prandtl numbers between 4 and 6. The experimental results tended to confirm the predicted trends over a large portion of the experimental range covered. The analysis tended to underestimate the increase in heat transfer by about 35% in the range $10^3 \leq Re.Ra_r \leq 5x10^5$. Again in the vicinity of $Re.Ra_r=10^6$, the increase in heat transfer leveled off and subsequently declined in a manner similar to that found with air. The authors did not take into account the temperature dependence of viscosity. For air the

viscosity increases with temperature, so that the secondary flow in the near-wall region might be suppressed in relation to the theoretical prediction, a result which could account partially for the observed overestimation. The converse argument appllies to the water data. The theoretical analysis treated a fully-developed flow, when investigating convection in stationary ducts the length of the test section may be arranged to approach the fully-developed flow. This is not easily accomplished if the duct is rotating. Futher the entry region will itself be related to the rotational speed as well as the usual Re. The predictions are shown in Fig.1.11.

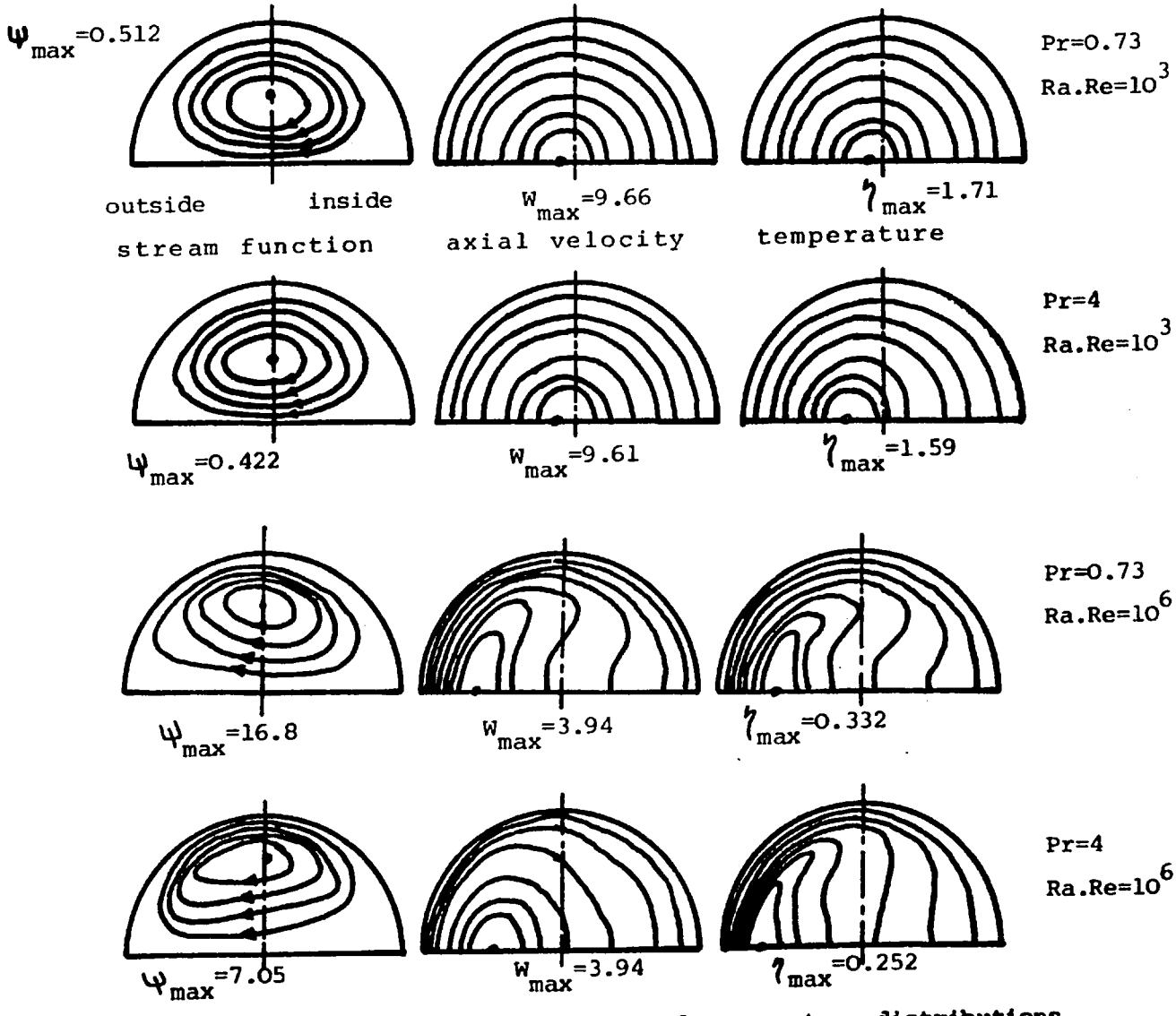
Skiadaressis and Spalding (1976) assumed, in their analysis, that downstream effects of the flow are not transmitted upstream; so that the flow may be described by parabolic transport equations (the implications of this assumption will be discussed later in chapter 3). It was concluded that a secondary flow is generated, as a result of the interaction of density gradients with centrifugal forces. The effect of Coriolis force for the range of Re and rotational speeds considered was negligible. The results are shown in Fig.1.12a.

B) Turbulent Flow:

Majumdar et al (1976) used the same solution procedure as Skiadaressis and Spalding (1976) for laminar flow to predict turbulent flow using the k-ε turbulence model. Predictions for fully-developed flow were obtained for two values of Reynolds number (Re=10 000 and 20 000) and a rotation speed range from 0-4000 r.p.m. It was concluded that the increase of heat transfer was relatively smaller than in the laminar case. The effects of Coriolis force were neglected for the range of Re and rotational speeds considered. The

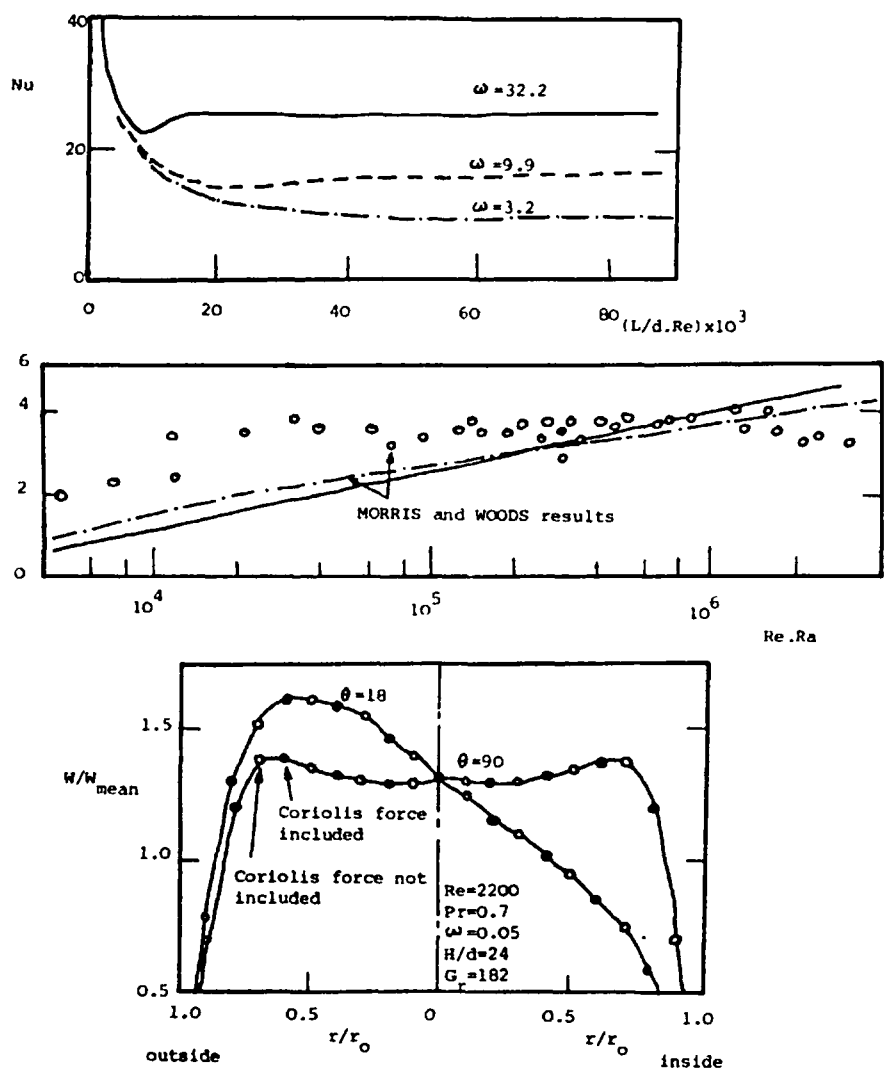


Variation of friction coefficient with Ra.Re product



Influence of Prandtl number on velocity and temperature distributions

Fig.1.11 MORRIS and WOODS (1974) predictions. ($J=10^9$, $\varepsilon=0$).



The effect of Coriolis force for fully-developed flow.

Fig.1.12a Laminar heat transfer in rotating ducts.
(From: Skiadaressis and Spalding, 1976).

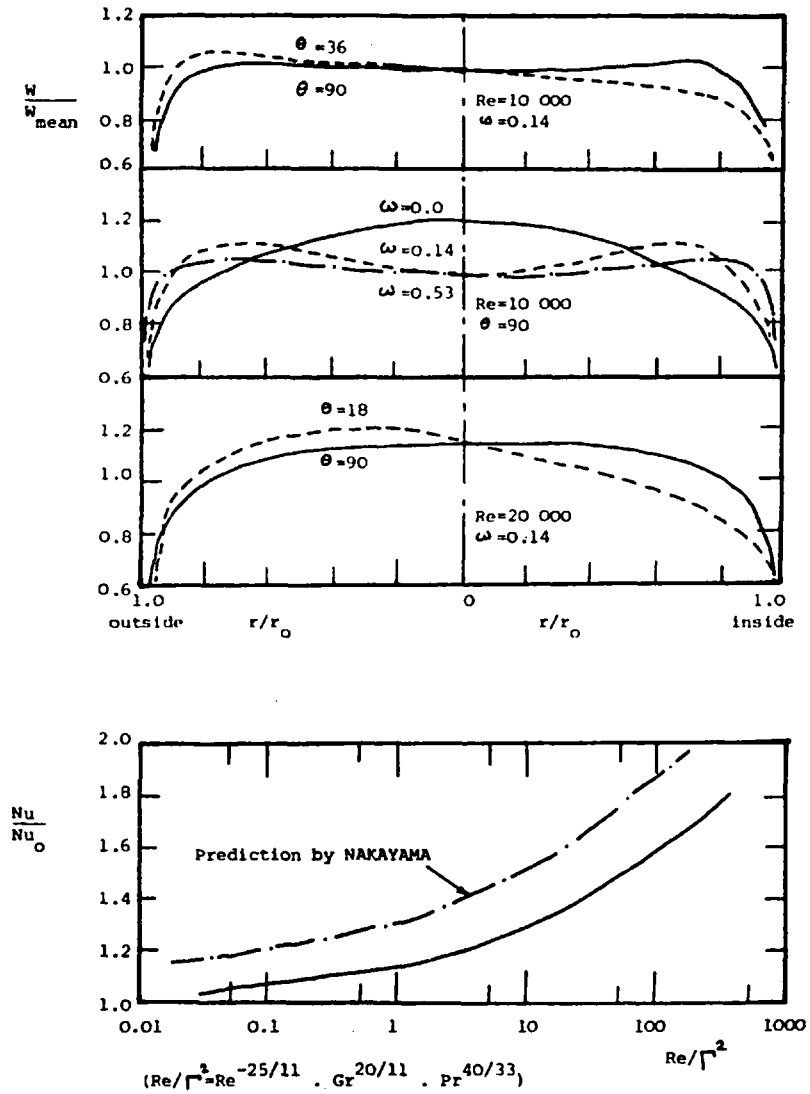


Fig.1.12b Turbulent heat transfer in rotating ducts.
(From: Majumdar, Morris, Skiadaressis and Spalding, 1976).

results are shown in Fig.1.12b.

1.2.4 Concluding Remarks:

The above review reveals discrepancies between theoretical predictions and experimental data for parallel rotating duct flow. The discrepancy at the inlet part of the rotating pipe is mainly due to the difficulty in specifying the exact inlet conditions for theoretical calculation. Thus the effect of inlet swirl has not been taken into account in the theoretical studies and uniform inlet axial velocity and temperature profiles have always been assumed. In addition, the temperature dependence of viscosity has been neglected in the calculations with consequential effects on the predictions at high Reynolds number. For turbullent flow, more advanced turbulence models may well be required in order to deal with the complications introduced by rotation.

1.3 Previous Work On The Flow Through Curved Ducts Of Circular Cross-Section

1.3.1 Theoretical Studies

A) Laminar Flow:

The first theoretical studies of bend flow appear to have been made by Dean (1927, 1929), who pointed out that dynamical similarity of the flow depends on the Dean number:

$$K = Re\sqrt{r_o/R} \qquad (1.20)$$

where r_o and R are pipe radius and radius of curvature respectively as shown in Fig.1.13. Dean analysed the secondary flow and calculated the resistance to the main flow in bends for small values of K.

Barua (1963) studied the flow through bends for large values of

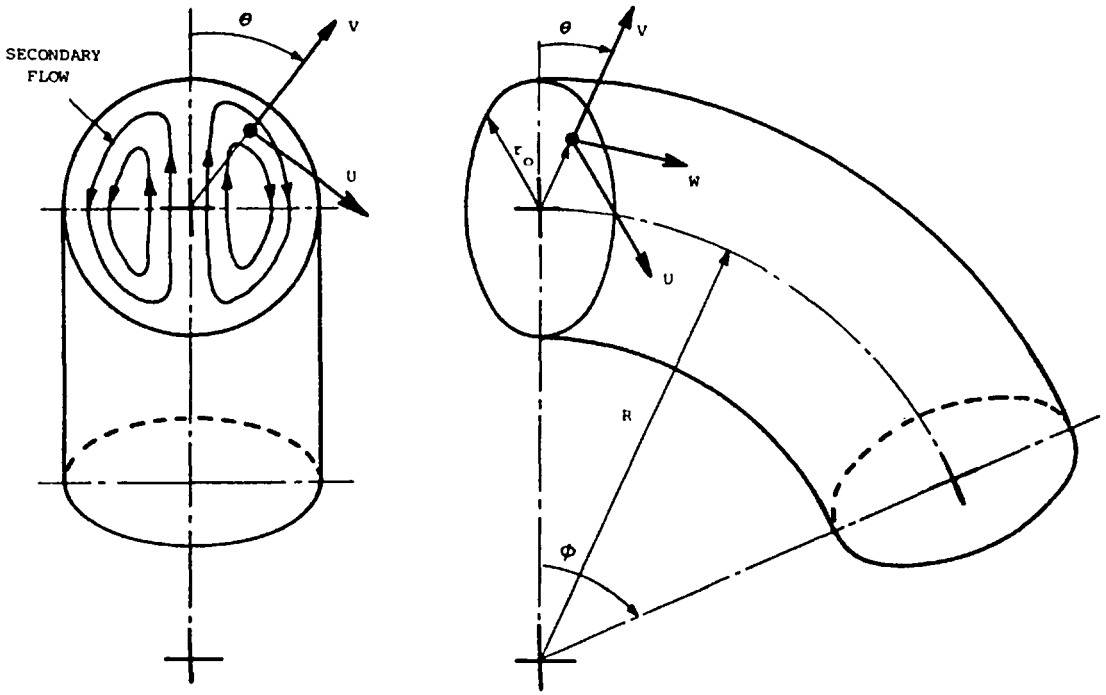
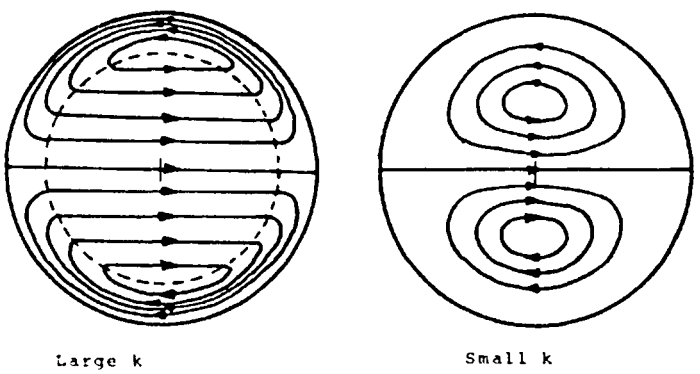


Fig.1.13 Flow through circular curved ducts.



Flow pattern of the secindary flow

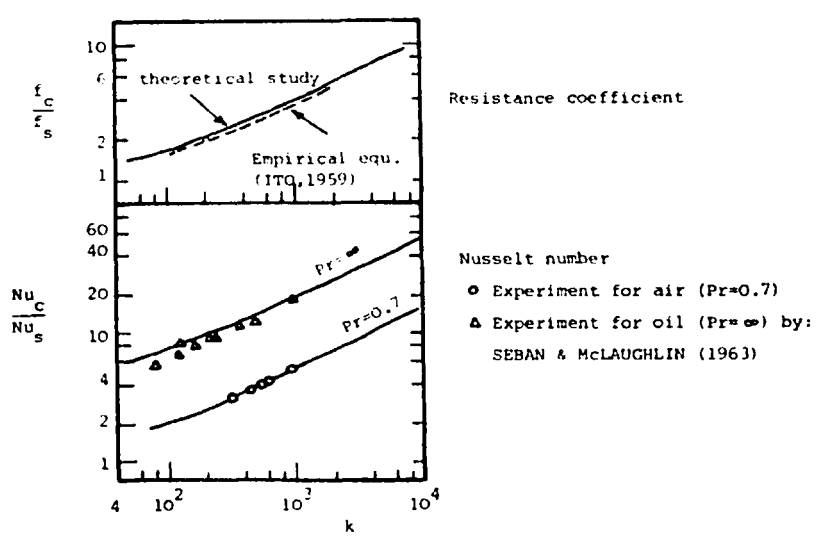


Fig.1.14 Effect of curvature and heat transfer on laminar flow in bends.

(From: MORI and NAKAYAMA, 1965)

K. He assumed that the flow consists of two zones, a potential core moving slowly outward surrounded by an inward moving boundary-layer adjacent to the wall. The ressult is to increase the resistance coefficient C_f of the bend relative to the coefficient C_{fo} of the same pipe if it were straight. The ratio C_f/C_{fo} was found to be proportional to K, and an equation was obtained for the range $30 < K < 2000$ which gave good agreement with the observed results. An arbitrary distribution of velocity was assumed in the boundary-layer, which satisfied the boundary conditions at the wall and at the edge of the boundary-layer, and also satisfied the boundary-layer momentum integral equation.

Mori and Nakayama (1965) studied the case of fully-developed flow using the same concept as Barua (1963). This study gave satisfactory results for resistance coefficient and heat transfer for uniform heat flux at large K. The ratio of Nu for bend flow to that for straight flow was obtained as a function of K and Pr, as shown in Fig.1.14. As K increases, the effect of curvature on flow resistance and heat transfer increases, but the Nu ratio approaches an asymptotic value with increasing Pr. The same assumption was used by Ito (1969) and for quantitative comparison a closer approximation was made and a formula for the friction factor was derived.

B) Turbulent Flow:

Mori and Nakayama (1967) studied the effect of curvature on heat transfer in fully-developed flow with constant heat flux, using Barua's method (1963). Local shear stresses and local heat fluxes at the wall were given on the basis of reducing C_{fo} and Nu_o formula for straight pipes to the local relation of friction and heat transfer.

When the formula for straight pipes were given as

$$C_{fo} \propto Re^{-1/m} \tag{1.21}$$

$$Nu_o \propto Re^{(m-1)/m} \tag{1.22}$$

It was shown that the dynamical similarity and also the similarity for heat transfer in curved pipes depend upon $Re(r_o/R)^{m/2}$. The resistance coefficient and the Nusselt number for curved pipes were obtained by putting m=4 for gases and m=5 for liquids to give Nusselt number in good agreement with experimental data for air for R/r_o=40 and 18.7. The results are shown in Fig.1.15.

1.3.2 Experimental Work

A) Laminar Flow:

Friction and heat transfer were measured by McLaughin and Seban (1963) for oil flow with constant-heat-fux in tube coils having ratio of coil to tube diameter of 17 and 104. The friction factors corresponded to the results of Ito (1959) and were predictable when, for heated flow, the fluid properties were evaluated at the mean film temperature. The heat-transfer coefficient varied during the initial developing flow, but except for certain anomalous runs, the entry effect terminated and asymptotic coefficients could be estimated.

Measurements were made for fully developed air flow in a curved pipe of R/r_o=40 by Mori and Nakayama (1965). Velocity and temperature profiles were obtained consistent with the results of boundary-layer calculations. Nusselt number values calculated from the experimental data were shown to agree with those predicted as shown in Fig.1.14.

Brian et al (1971) conducted experimental and theoretical studies of the heat transfer in helically coiled tubes. It was shown that at

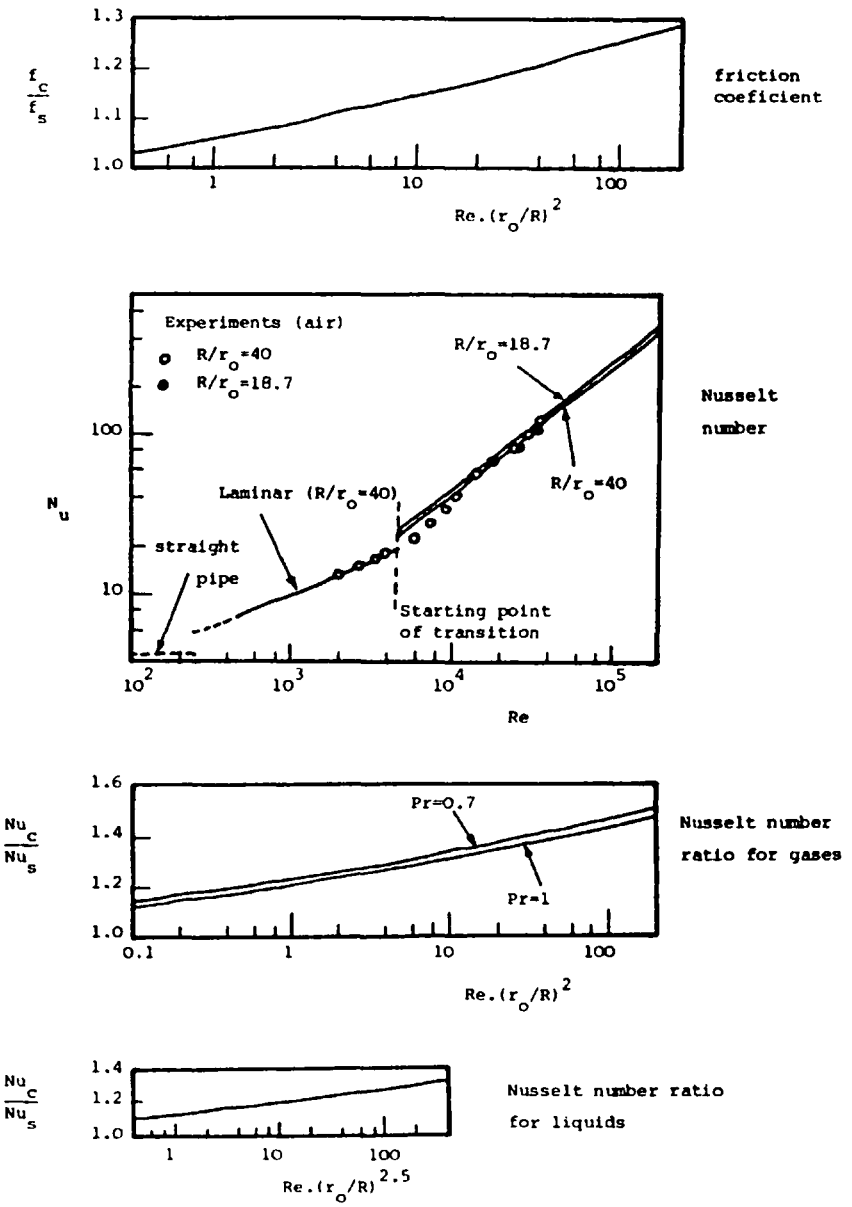


Fig.1.15 Forced convective heat transfer in curved pipes for turbulent flow. (From: MORI and NAKAYAMA, 1967).

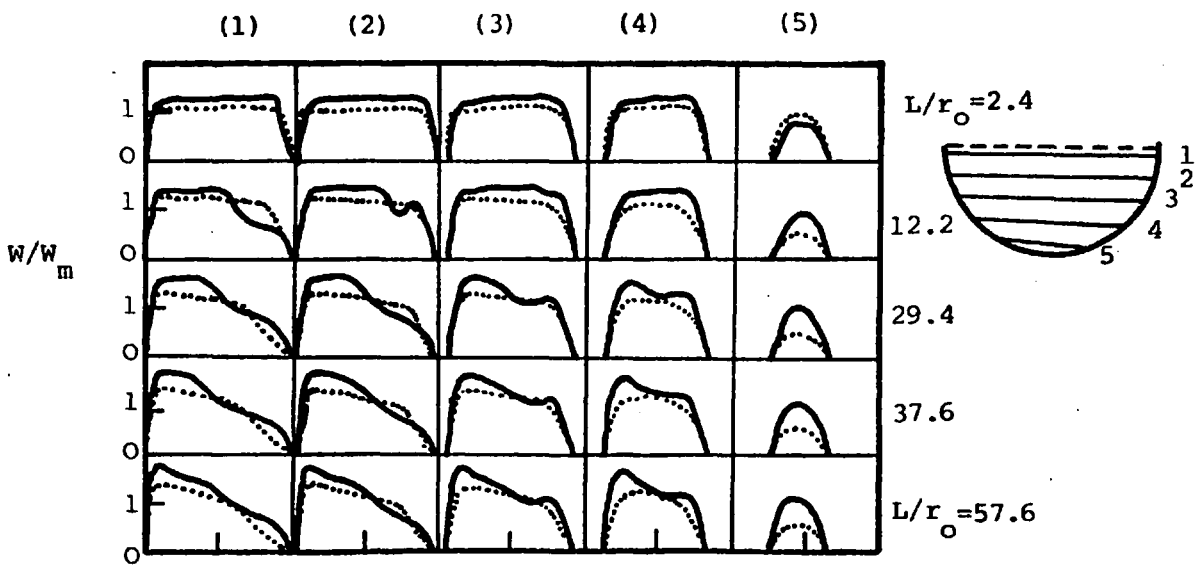


Fig.1.16 Comparison between measured axial velicity (From: AGRAWAL, TALBOT and GONG, 1978) and prediction (of YAO and BERGER ....., 1975) for laminar flow in bends.

very short distance from the start of the heat transfer zone, the thermal boundary layer was too thin to be affected by the secondary flow field, which reaches its maximum intensity at some distance away from the tube wall. Near the tube inlet the ratio of heat transfer coefficient in a coiled tube to that in a straight tube varied as a function of $(K)^{1/6}$, while for greater axial distances, this ratio increased progressively and reached a value corresponding to a function of $(K)^{1/2}$ for fully developed region. The local heat transfer coefficient changed cyclicly with increasing axial distance. These oscillations were damped out as the region of fully developed temperature field was approached. The oscillations arose because the fluid core was not well mixed even for high Dean numbers. A correlation for the asymptotic value of Nu, as a function of K and Pr, was shown to be applicable for values of K between 5 and 175.

Hummel et al (1975) studied the two-dimensional flow and pressure field in the central plane of a 90 degree bend of $R/r_o=4$ and Re of 944. The test section was a circular bend made from a Pyrex tube. The flow at the inlet was fully developed. The non-intrusive photochromic tracer technique was used to visualize the motion of fluid elements in the central plane of the bend. The identification of fluid elements in the central plane was achieved by introducing traces vertically in the plane of the bend and then making use of the flow symmetry in the upper and lower half of the bend. Optical distortion at the walls of the round glass tube was eliminated by using a liquid both inside and outside the pipe with the same refractive index as glass. The liquid used was a mixture of methyl benzoate and Imperial Oil Varsol DX-3135 in equal parts by volume.

An investigation was carried out by Agrawal et al (1978) into the

development of flow in 180 degree bend with uniform inlet axial velocity. Two semi-circular pipes of radius ratio 20 and 7 were used, and the experiments covered a Dean number range from 138 to 679. The axial velocity and the component of secondary velocity parallel to the plane of curvature of the pipe were measured by laser Doppler anemometry. The circulating liquid employed was a mixture of glycerine and water, in proportions chosen to match closely the index of refraction of Plexiglas. Exact matching was not possible, so that corrections were needed in processing the data, but approximate matching was required to ensure that the laser beams intersected within the flow. It was observed that, in the upstream region where the boundary layers were thin compared with the pipe radius, the axial velocity within the irrotational core first developed to form a vortex-like flow. In the downstream region, characterized by viscous layers of thickness comparable with the pipe radius, there appeared to be three-dimensional separation at the inner wall. There was also an indication of an additional vortex structure embedded within the secondary motion. The experimental axial velocity profiles were compared with those obtained by theoretical analysis. The quantitative agreement between theory and experiments was found to be poor. The results are shown in Fig.1.16.

B) Turbulent Flow:

Ito (1959) studied the effect of curvature on the friction factor for smooth bends. A wide range of bends was used with radius ratios from R/r_o=16.4 up to 648. All The results collapsed satisfactorily on a single curve for fully-developed flow, and empirical formulae were deduced from the results. Friction and heat transfer were measured by McLaughin and Seban (1963) for water flow in tube coils having ratios

of coil-to-tube diameter of 17 and 104 for Re up to 65 000, with nominally constant heat flux. Mori and Nakayama (1967) measured Nu, velocity and temperature distributions for air flow through the curved pipes of R/r_o=40 and 18.7. Theoretical predictions agreed well with the data. Measurements of total pressure and yaw relative to the pipe axis of flow in various bends attached to the end of a long straight pipe were given by Rowe (1970) for $Re=2.36 \times 10^5$. The behaviour of the induced secondary flow was studied in detail. The results are shown in Fig.1.17.

1.3.3 Numerical Solutions

A) Laminar Flow:

Brian et al (1971) studied the heat transfer for flow in helically coiled tubes, with $r_o/R \ll 1.0$. The results were limited to Dean numbers greater than 100. A finite-difference solution was presented, for fully-developed flow subjected to axially uniform wall heat flux and peripherally uniform wall temperature, by Akiyama and Cheng (1971). The effect of Pr on heat transfer was clarified. It was shown that all heat transfer results for $Pr \geq 1.0$ could be correlated by a single curve with reasonable tolerance. The results were compared with other experimental and theoretical data. The numerical results showed that the perturbation method diverges quickly with the increasing K. It was shown that the boundary layer calculation method predicted incorrect Prandtl number effects, and that it was valid only near Pr=1.0.

Kalb and Seader (1972 and 1974) studied fully-developed flow with uniform axial heat flux and peripherally uniform wall temperature. The solutions were presented for K range from 1 to 2000, Pr from 0.005

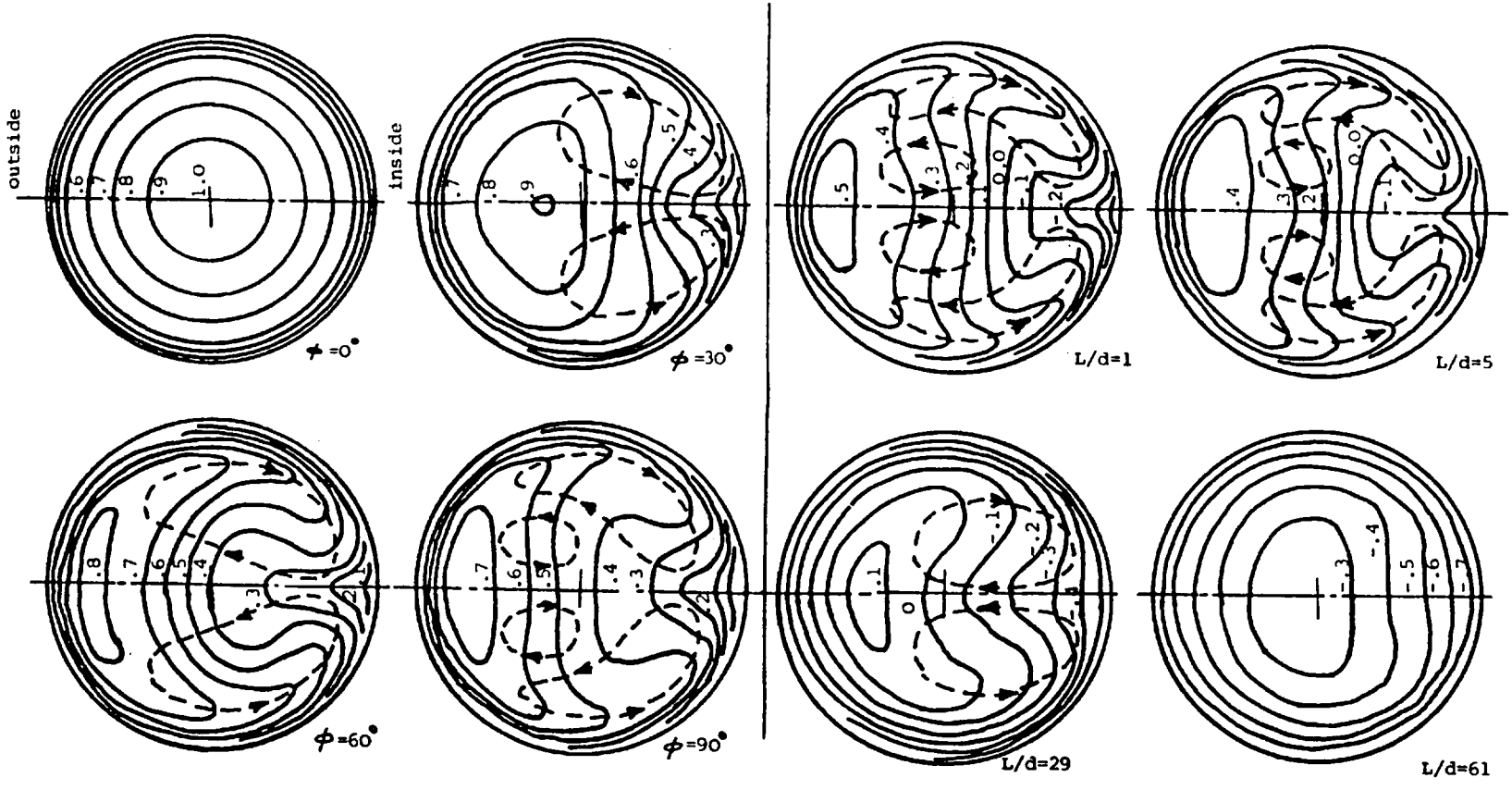
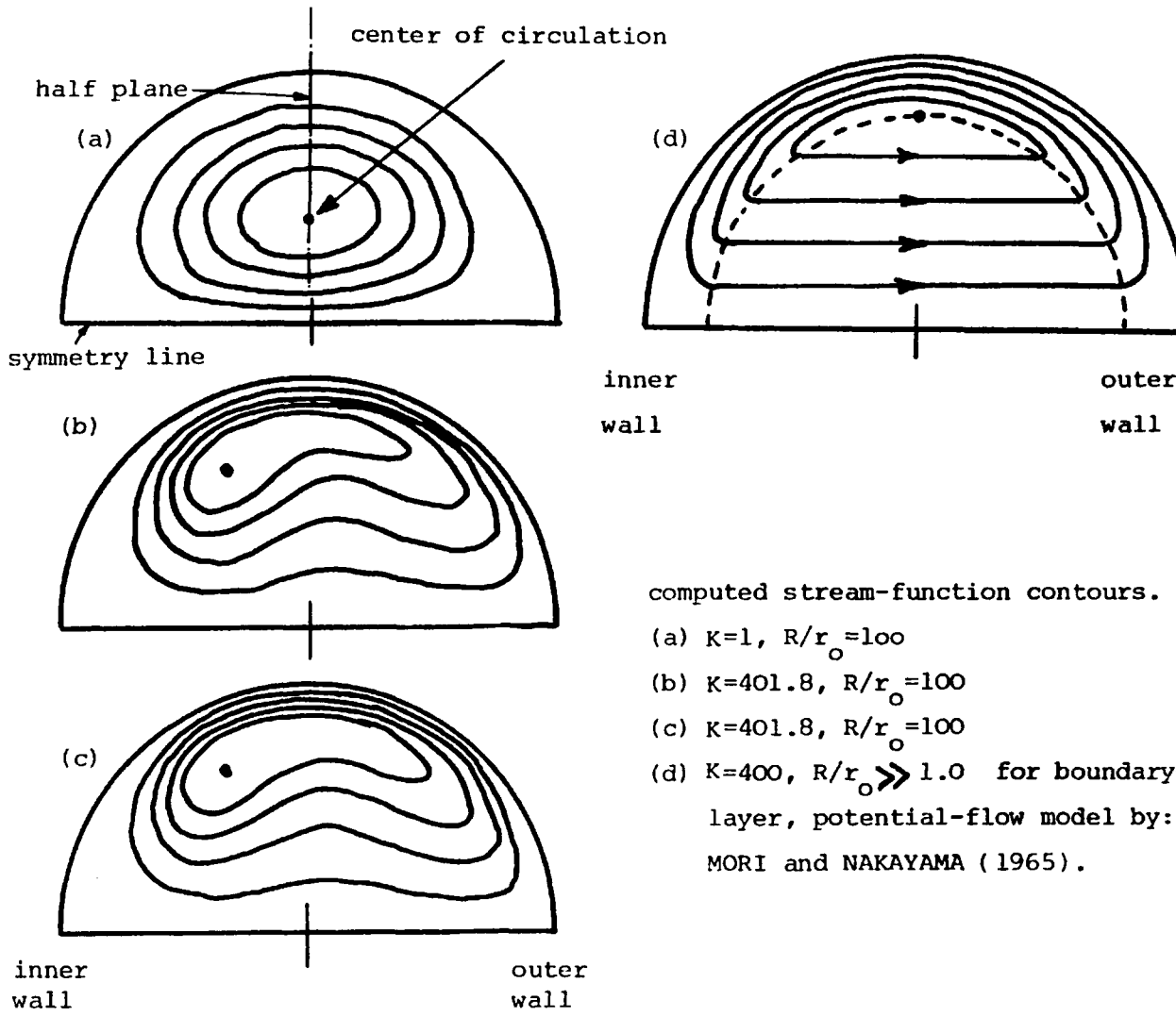


Fig.1.17 Contours of measured total pressure $(P-P_o)/\frac{1}{2}\rho W_{max}^2$, in a 180 degree pipe bend and at various distances (pipe diameters) in a straight section downstream of the bend. Dashed lines show the estimated secondary flow pattern. (From: ROWE, 1970).

to 1600 and R/r_o from 10 to 100. It was concluded that Nu could be correlated as a function of K and Pr only, but when the peripheral variation of Nu was considered, the curvature ratio entered as an additional parameter.

Austin and Seader (1973) studied isothermal fully-developed flow in bends for values of K between 1 and 1000, and values of the curvature ratio between 5 and 100. As shown in Fig.1.18 at K=1 and R/r_o=100, the centre of the secondary vortex lies somewhat closer to the symmetry line than to the upper wall. As K was increased, concave regions developed from the formation of dimples in the streamlines, which also departed from their symmetrical nature in the half plane. In addition, the vortex centre shifted toward the upper wall and toward the inside wall. When K was held constant while the curvature ratio was reduced, the nature of the secondary flow was slightly altered. The results were compared with those obtained using Mori and Nakayama's assumption of uniform secondary flow outward in the central-core region as shown in Fig.1.18. Tow calculations of the location of the centre of the secondary-flow circulation differed significantly. The friction factor for the curved tube was obtained and a slight dependence on the curvature ratio was noticed.

Greenspan (1973) studied the flow in bends for R/r_o=31.9 and values of K ranging from 0 to 5000. A finite difference method was used to calculate the behaviour of isothermal fully-developed flow. A calculation procedure for three dimensional laminar flow described by parabolic equations was used by Patankar et al (1974) to predict the velocity and temperature fields in helically coiled pipes. Predictions were presented for developing and fully developed flow. Only large curvature ratios $R/r_o \geq 15$ were considered. Elliptic



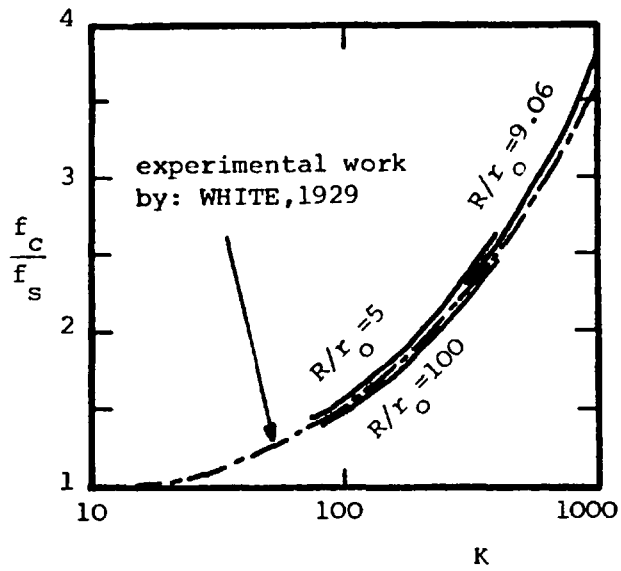
computed stream-function contours.

(a) K=1, R/r_o=100

(b) K=401.8, R/r_o=100

(c) K=401.8, R/r_o=100

(d) K=400, $R/r_o \gg 1.0$ for boundary-layer, potential-flow model by: MORI and NAKAYAMA (1965).



Friction in curved tubes.

Fig.1.18 Numerical results of AUSTIN and SEADER (1973).

equations in toroidal coordinates (r,θ,ϕ) have been solved numerically for isothermal flow in a 90^{o} bend of small radius by Humphrey (1978). The calculations showed that the cross-stream flow in a strongly curved pipes was as large as 80% of the bulk average velocity at 40^{o} and 90^{o} as shown in Fig.1.19.

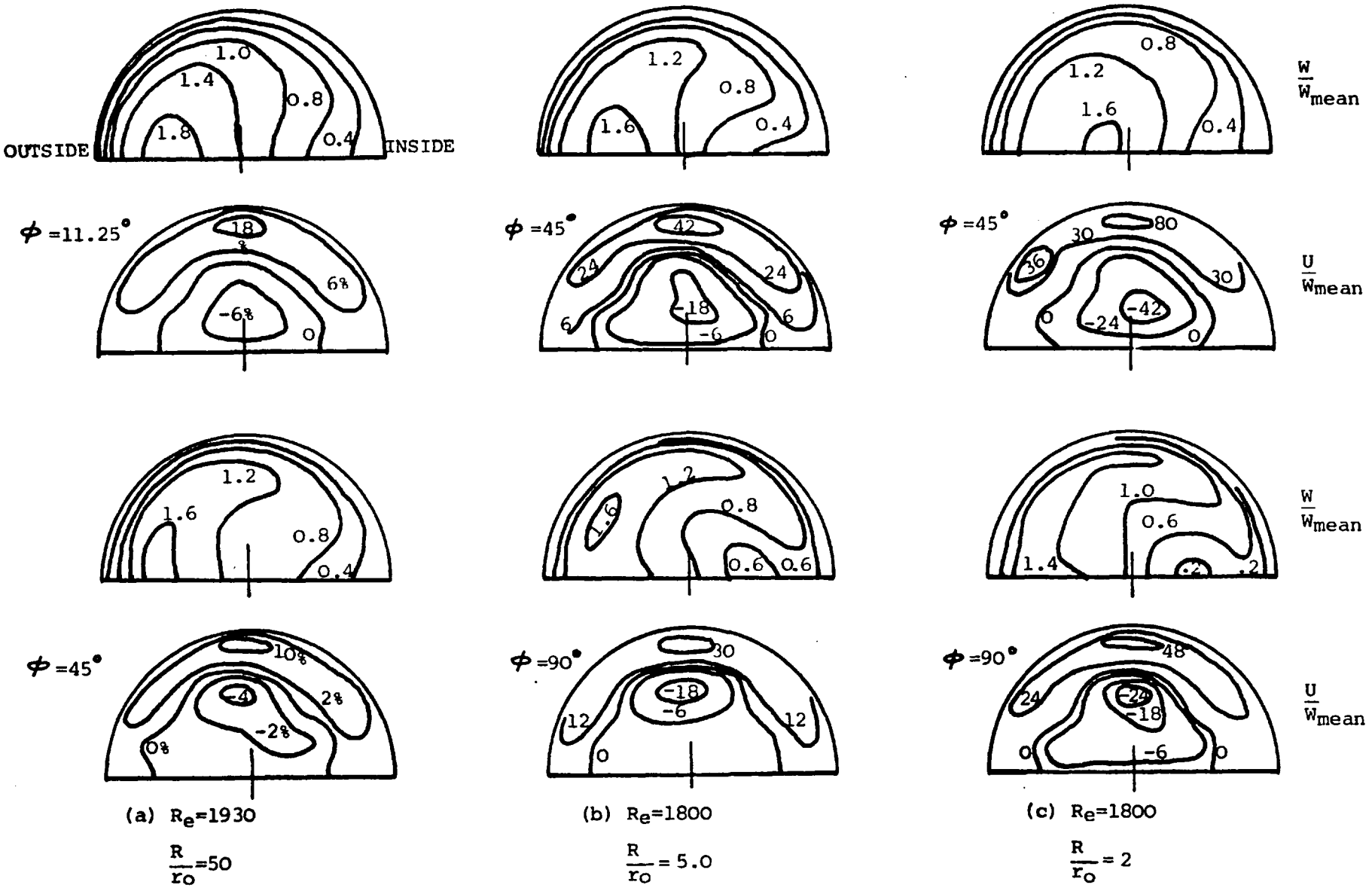
B) Turbulent Flow:

A finite-difference procedure was employed to predict the development of turbulent flow in bends by Patankar et al (1974) and Pratap (1975) using the k-ε turbulence model. The predicted velocity contours for developing flow in a 180^{o} bend were compared with the experimental data. Fully-developed velocity profiles of the flow in long helically-wound pipes were presented and compared with experimental measurements as shown in Fig.1.20.

1.3.4 Concluding Remarks:

Most of the theoretical studies of bend flow have been based on the assumption that the main secondary flow consists of a core region moving uniformly outwards surrounded by an inward moving boundary layer. The results obtained have been limited to fully-developed flow at high Dean numbers; they also differ significantly from the numerical predictions, particularly for larger values of K.

Boundary-layer type approximations to the Navier-Stokes equations break down when the bend is strongly curved. While the flow in mildly curved bends can be treated satisfactorily, and with considerable saving in computer storage and time, by the use of parabolic differential equations, strongly curved flows require the solution of the full, elliptic, equations of motion or, as a compromise, treatment



(a) R_e=1930

$\frac{R}{r_o}$=50

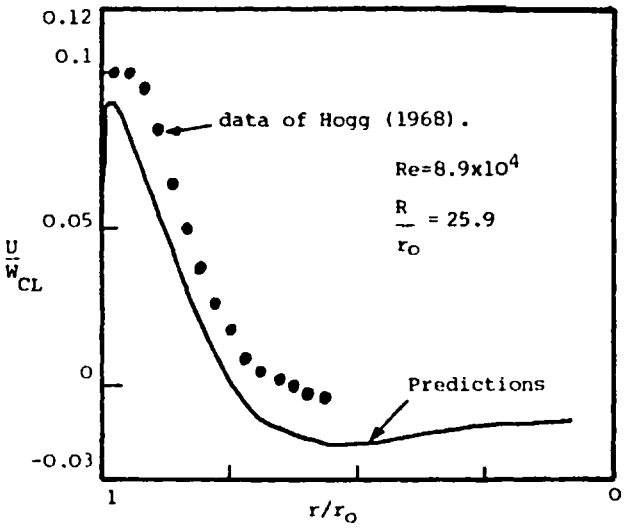
(b) R_e=1800

$\frac{R}{r_o}$= 5.0

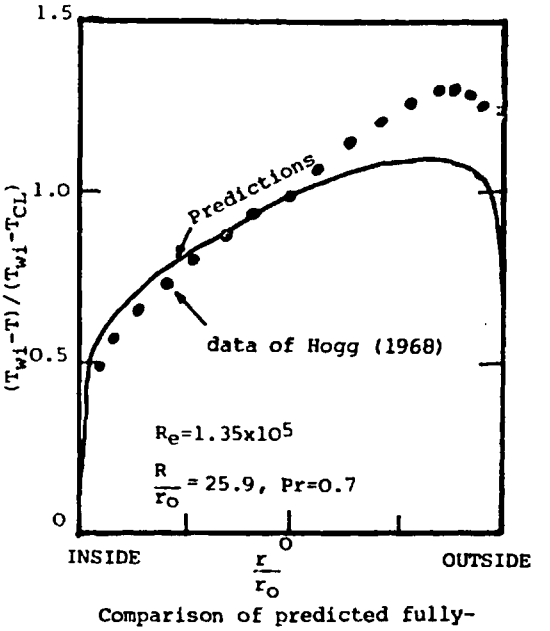
(c) R_e=1800

$\frac{R}{r_o}$= 2

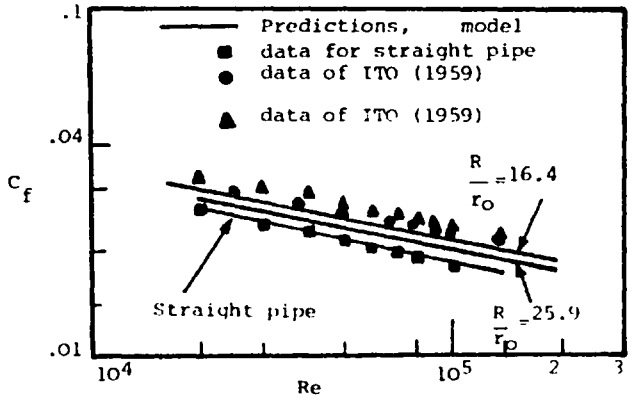
Fig.1.19 Contours of longitudinal (W) and tangential (U) velocities in developing curved pipe flow. (HUMPHREY 1978)



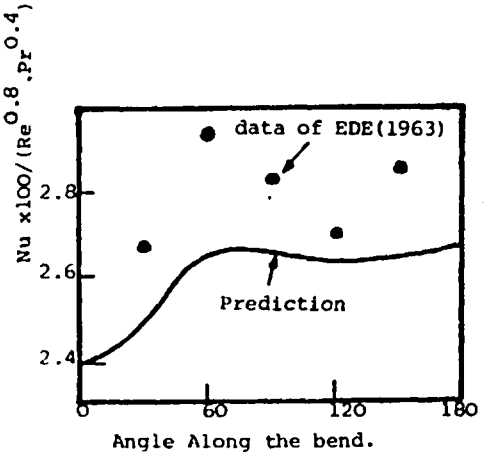
Comparison of fully-developed secondary velocity profile along the vertical diameter.



Comparison of predicted fully-developed temperature profiles with experimental data.



Comparison of fully-developed friction factors with experimental data.



Angle Along the bend.

Development of Nusselt Number for flow in a 180 degree bend,

$\frac{R}{r_o} = 22$, $R_e = 3.99 \times 10^4$, Pr=10.3

Fig.1.20 Turbulent flow and heat transfer in curved ducts.

(From: PRATAP 1975).

by the so-called "partially parabolic" method to be described later.

1.4 Previous Work On The Flow Through Curved Ducts Of Rectangular Cross-Section

1.4.1 Theoretical Studies

Mori et al (1971) studied fully-developed laminar flow in a bend of square cross-section with constant heat flux, shown in Fig.1.21, in which secondary flows were generated by centrifugal forces. The intensity of the secondary flow increased with the increase of K, and it was possible to consider the existence of the secondary flow boundary layer for the range of the large K when the effect of curvature of the channel cannot be neglected. The flow velocity and temperature fields were divided into two regions, the core and the boundary layer region, and analytical results were obtained. Values of C_f and Nu were significantly increased by the effects of secondary flow. Analytical and experimental results were compared, and it was found that they was in good agreement.

1.4.2 Experimental Work

A) Laminar Flow:

Humphrey (1977) and Humphrey et al (1977) studied laminar flow in strongly curved square duct. The axial velocity component was measured for the water flow in a 90° bend fitted with downstream and upstream straight sections. The experiments were carried out at Reynolds number based on the hydraulic diameter and bulk velocity of 790 (corresponding to K=368). Flow visualization was used to identify qualitatively the chatacteristics of the flow and laser-Doppler anemometry to quantify the velocity field. The results confirmed that the location of maximum velocity moves from the centre of the duct

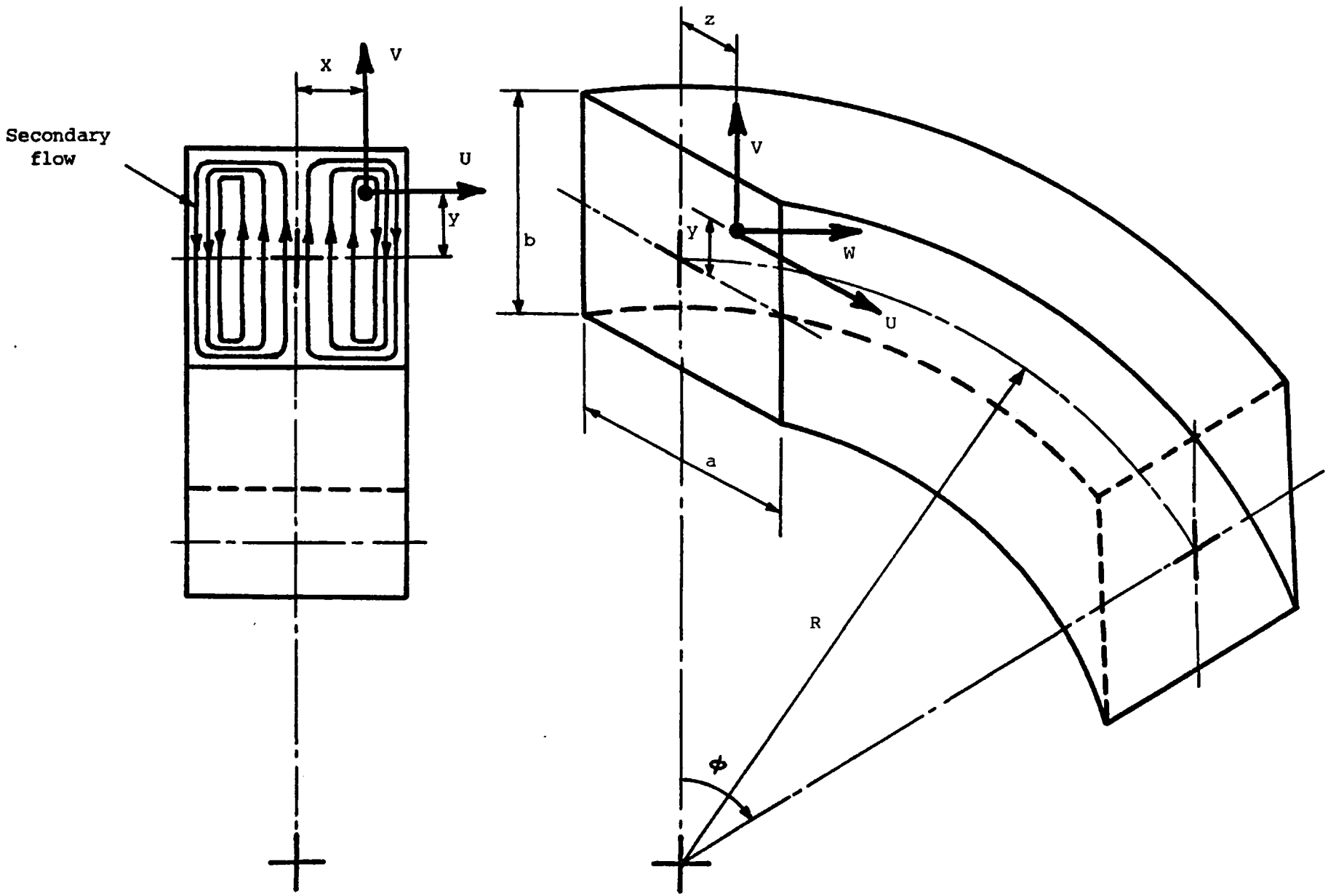


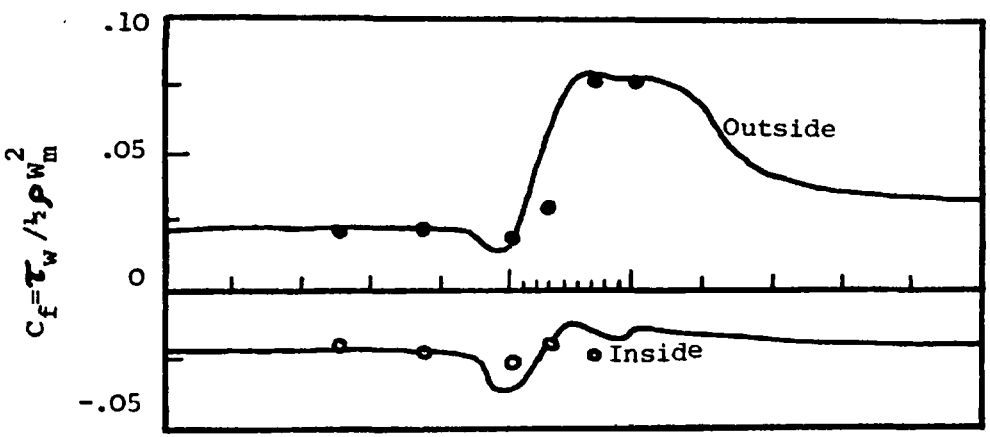
Fig.1.21 Flow through rectangular curved ducts.

towards the outer wall and, in the 90^{o} plane, is located around 85% of the duct width from the inner wall. The principal results are shown in Fig.1.22.

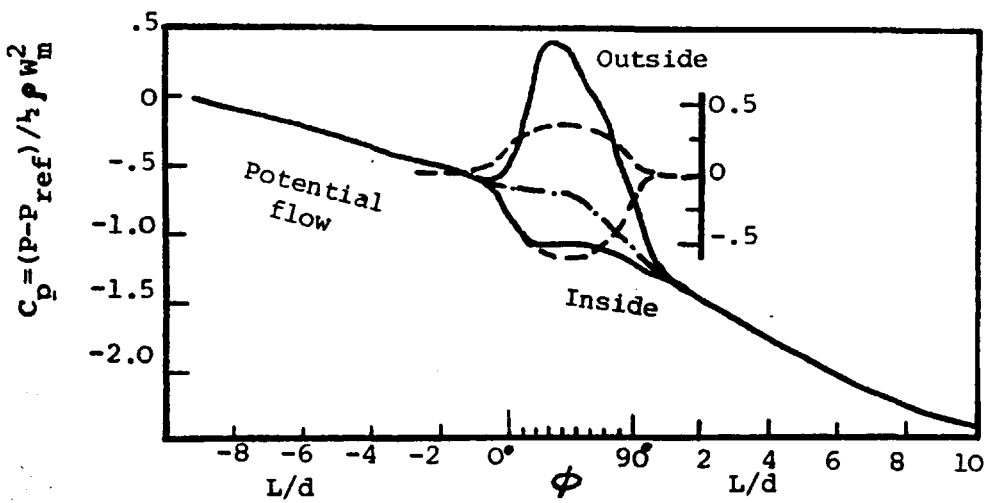
The same test section was used for experiments with thin boundary layers at the inlet (approximately 25% of the hydraulic diameter) by Taylor et al (1980). The maximum cross-stream component measured was 60% of the bulk velocity. The axial velocity contours showed that large velocities were found progressively nearer to the outer radius of the bend and along the sidewalls. The principal results are shown in Fig.1.23.

B) Turbulent Flow:

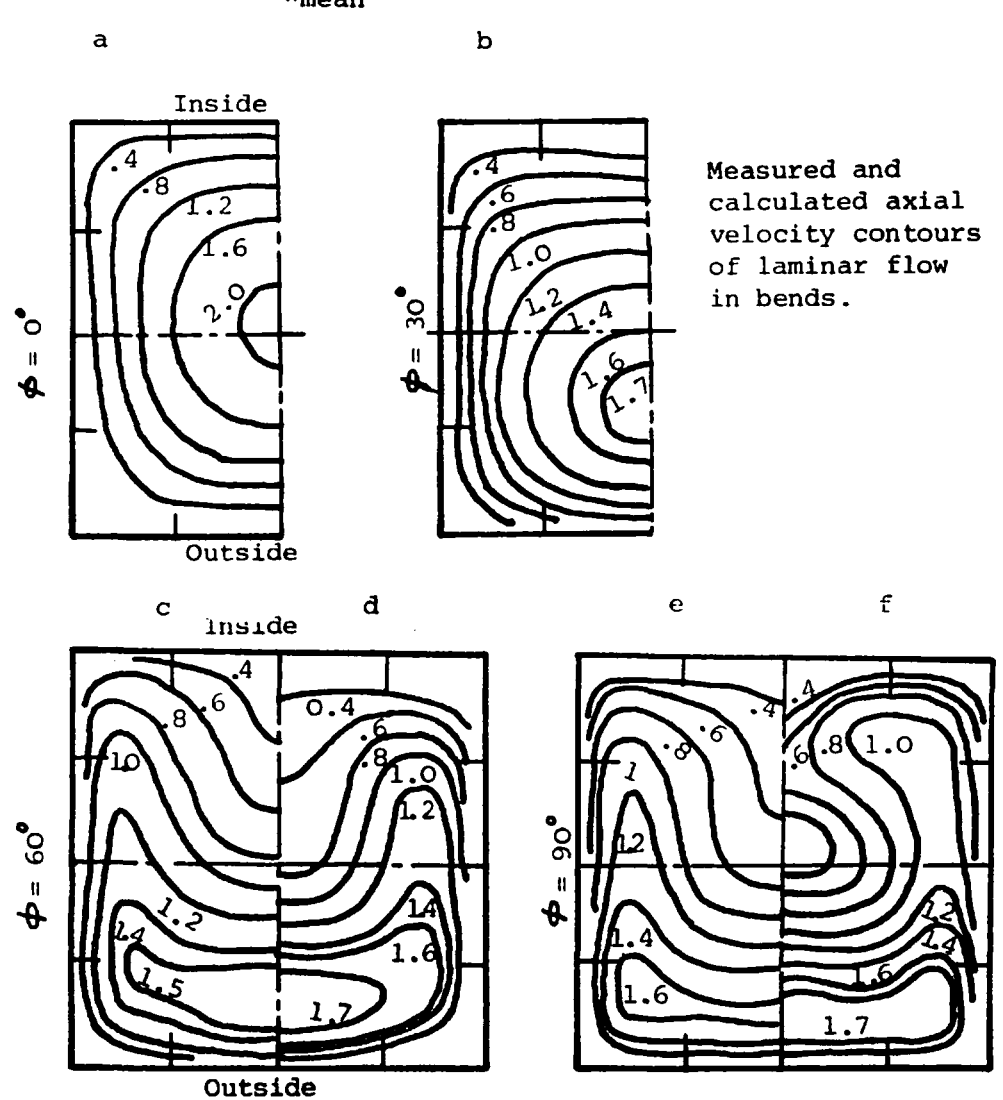
Humphrey and Whitelaw (1978), Humphrey (1977) and Humphrey et al (1981) reported the results of laser-Doppler measurements in the developing flow in the same square-section bend with smooth walls at a Reynolds number of $4x10^{4}$. Measurements of the longitudinal and radial components of mean velocity and corresponding components of the Reynolds-stress tensor were obtained in various cross-stream planes. The secondary mean velocities, driven mainly by the pressure field, attained values of up to 28% of the bulk velocity, and were largely responsible for the convection of Reynolds stresses in the cross-stream plane. Production of turbulent kinetic energy predominated close to the outer-radius wall and regions with negative production were identified. Thus, at a bend angle of 90^{o} and near the inner-radius wall, $\overline{uv}(\partial U/\partial r)$ was positive and represented a negative contribution to the generation of turbulent kinetic energy. This result is in accord with the stabilizing effect of curvature near the inner wall.



Measured and computed friction coefficient at the centre line of the inside and outside curved walls.



Computed pressure coefficient at the centre-line.

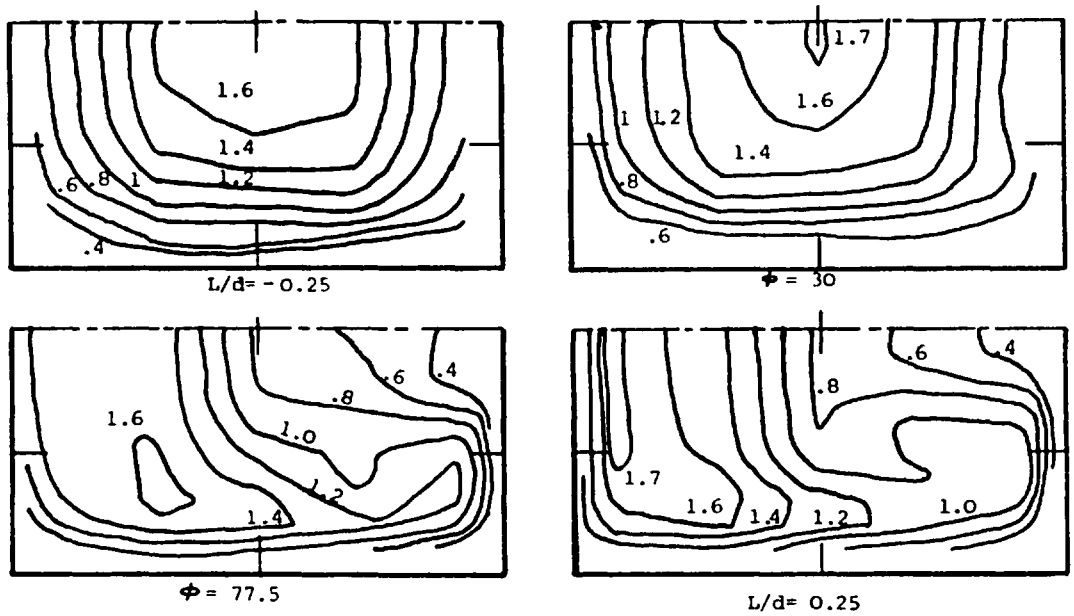


Measured and calculated axial velocity contours of laminar flow in bends.

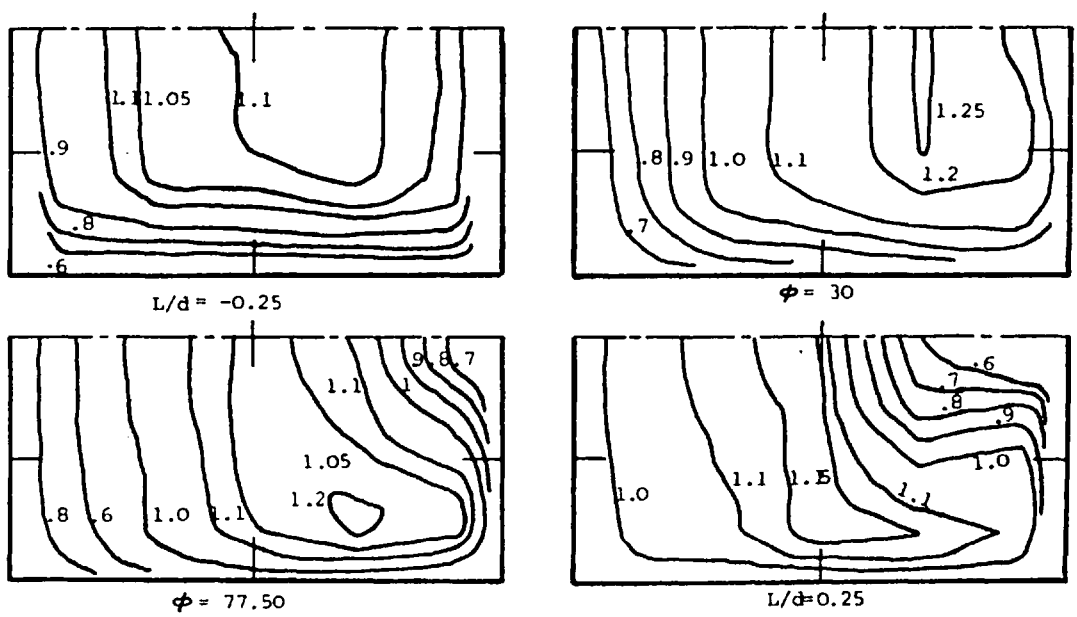
measured: d,f

calculated: a,b,c,e

Fig.1.22 Laminar flow in square duct of strong curvature. (HUMPHREY, TAYLOR and WHITELAW, 1977).



Laminar flow: axial velocity contours (W/W_m)



Turbulent flow: axial velocity contours (W/W_m)

Fig.1.23 Measurements of laminar and turbulent flow in a curved duct with thin inlet boundary layers. (From: TAYLOR, WHITELAW and YIANNESKIS, 1980).

Using the same test section Taylor et al (1980) studied the flow with thin inlet boundary layers (approximately 15% of the hydraulic diameter). The maximum cross-stream velocity component measured was 40% of the bulk velocity. Contours of the streamwise velocity showed that large velocities moved towards the inner radius under the action of pressure gradients until about 60° around the bend where the influence of the strengthening secondary motion became evident. Turbulence level and shear stress measurements were also presented. The results are shown in Fig.1.23.

1.4.3 Numerical Solutions

A) Laminar Flow:

The three-dimensional flow of a viscous fluid in a duct has been analyzed by Ghia and Sokhey (1977). A mathematical model was formulated using a three-dimensional approximation to the Navier-Stokes equations. Solutions were obtained for a number of duct geometries and flow parameters: R/d ranging from 3 to 100 and K varying between 55 and 350. Detailed results for developing flow in rectangular bends were obtained and the effect of longitudinal curvature on secondary flow was also analyzed.

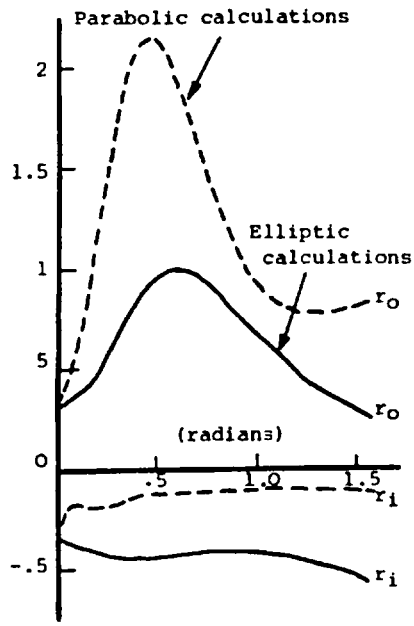
A numerical solution was compared with experimental data by Humphrey (1977) and Humphrey et al (1977). Calculated values of the three velocity components were obtained by solving the Navier-Stokes equations in cylindrical co-ordinates. The results exhibited the same trends as the experimental data with reasonable quantitative agreement, even though the number of grid nodes used for the finite-difference solution of the differential equations was limited by the computer time and storage available. The region of

recirculation observed experimentally appeared also in the calculations. The magnitudes of the various terms in the equations were examined to determine the extent to which details of the flow could be represented by reduced forms of Navier-Stokes equations. The implications of the so-called "partially-parabolic" equations and potential- and rotational-flow analysis of an ideal fluid were examined. The results are shown in Fig.1.22.

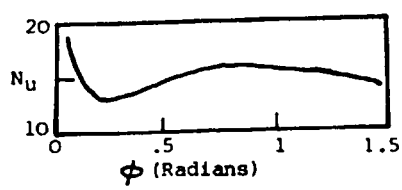
A study of heat transfer in a 90 degree bend was presented by Humphrey and Yee (1979), based on fully elliptic forms of the transport equations. The effects of duct geometry on heat transfer were examined by considering the role of secondary motion during the developing period of the flow. Attention was given to varying initial conditions of velocity and temperature at the entrance section to the duct, as well as to the duct geometry, and an assessment was made of the relative contributions of individual duct walls to heat transfer in the flow. In general, the heat transfer increased with K, with the largest rates occuring through the duct side walls and outer curved wall. The results are shown in Fig.1.24.

B) Turbulent Flow

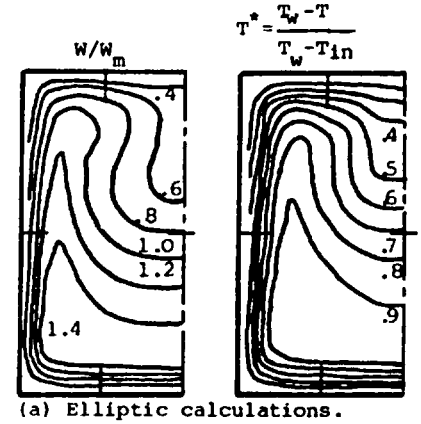
Humphrey et al (1981) made laser-Doppler measurements in the flow in a square duct with strong curvature and compared the results with previously cited experimental work. In spite of the complex mean flow and Reynolds stress distributions, the cross-stream flow was controlled mainly by the centrifugal force-radial pressure gradient imbalance. As a consequence, calculated mean velocities obtained from the numerical solution of elliptic differential equations were not strongly dependent on the two-equation turbulence model used since



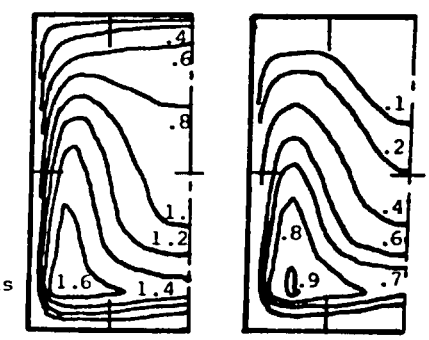
Calculation of pressure at inner and outer walls



Variation of Nusselt number

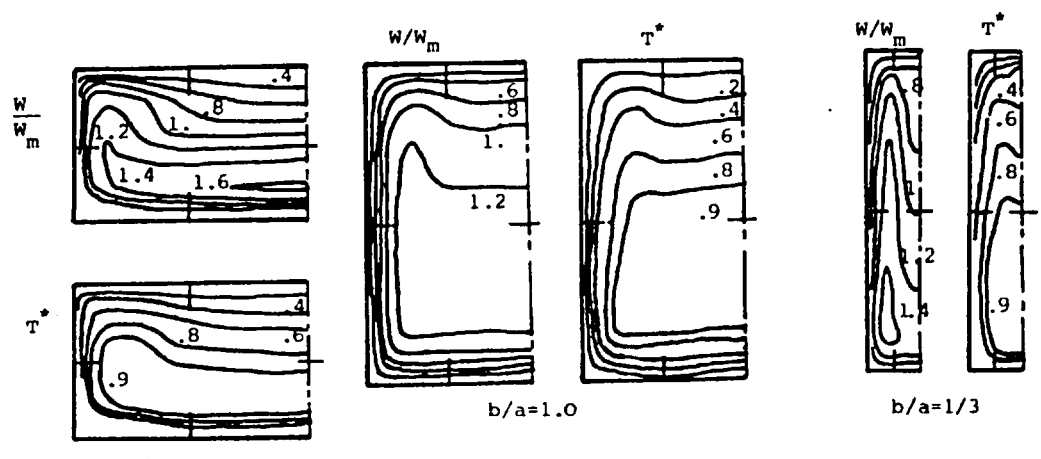


(a) Elliptic calculations.



(b) Parabolic calculations.

Longitudinal velocity and temperature (b/a=1, $\frac{R}{DH}$=2.3, R_e=740, k=368, T_{in}=300°K, T_w=350°k).



Longitudinal velocity and temperature at ϕ=90 for different aspect ratios (Re=790, k=368, T_{in}=300°k, T_w=350°k and R/DH=2.3)

Fig.1.24 Laminar flow and heat transfer in strongly curved rectangular ducts. (From: HUMPHREY and YEE, 1979).

numerical errors were considerable.

1.5 **Present Contributions**

a) Objective

The main objective of the work has been to devise an accurate and ecconomical computer methods for the calculation of laminar and turbulent flow with heat trnsfer in tubes rotating about a parallel axis, and to verify numerical predictions by comparison with experimental data.

b) Principal Results Of The Work

(I) Theoretical And Computational

An existing "TEACH" computer code for duct flows has been modified for circular cross section, the effects of rotation, and turbulent flow with heat transfer. Numerical accuracy checked have been carried out for stationary laminar pipe flow. Predictions for laminar flow in rotating tubes have been compared with the results of theoretical analyses and with the limited amount of experimental data currently available. Turbulent flow predictions, based on two closure methods, have been compared with experimental data supplied by the Central Electricity Board and with the very limited number of published measurements.

Because the data from rotating flow are so sparse, and lack the detail needed for proper validation of the method, the same methods have been applied to the calculation of laminar and turbulent flow in pipe bends. The effects of curvature are similar in many ways to the effects of rotation and are much better documented in detail. The calculation method produces results in fair agreement with the data, which have also been

augmented in the course of the present work.

The result is a tested computer code which is generally applicable to the calculation of these two types of flow and which is capable of future development for different geometries and turbulence models.

A simplified second-order turbulence closure has been developed for rotating tube flow. Calculations for fully developed flow shew significant differences in results obtained with this and with a two-equation eddy-viscosity model.

(II) Experimental

Laser Doppler measurements of mean flow and turbulence quantities have been made in water flow through two 90 degree bends. The results, which are intended for use in the validation of turbulence models and calculation methods, are a significant addition to the limited quantity of data currently available for this purpose.

1.6 Layout Of The Thesis

The remaining sections of the thesis describe the present work in more detail. The partial-differential equations governing the flows are described in Chapter 2 with the turbulence models used for closure. Chapter 3 deals with the numerical methods used, and the experimental program is described in Chapter 4. The experimental data obtained are presented for the strongly curved, 90^{o} circular bend and the mildly curved, 90^{o} square bend. The application of the numerical procedures to compute laminar and turbulent flows for rotating ducts is explained in Chapter 5, and for circular cross-section bends in

Chapter 6. The results of the computations are presented and compared with experimental data. Chapter 7 summarizes the main contributions of the present study, the conclusions arrived at and suggestions for future work. The last part of the thesis contains a list of references, a list of symbols and six appendices. The appendices provide supplementary details regarding the governing differential equations, turbulence models, the application of the Reynolds stress and heat flux models to stationary circular pipe flow, the correction method used for determining the the position of the measuring point in the cross section of the circular bend, and two published papers about flow in 90 degree bends.

CHAPTER 2

MATHEMATICAL DESCRIPTION OF THE FLOW

2.1 The Governing Differential Equations

For a Newtonian fluid of uniform density ρ and kinetic viscosity ν, the conservation equations of mass, momentum and energy, which govern the instantaneous turbulent motion, can be expressed as

Mass: $$\partial \hat{U}_i / \partial X_j = 0 \tag{2.1}$$

Momentum: $$(\partial \hat{U}_i / \partial t) + \partial(\hat{U}_i \hat{U}_j)/\partial X_j = -(\partial P/\partial X_i)/\rho + \nu(\partial^2 \hat{U}_i / \partial X_j^2) \tag{2.2}$$

Energy: $$(\partial \hat{\Phi}/\partial t) + \partial(\hat{U}_i \hat{\Phi})/\partial X_j = S_\Phi + \Gamma_{\Phi j}(\partial^2 \hat{\Phi}/\partial X_j^2) \tag{2.3}$$

where $\Gamma_{\Phi j}$ is the kinematic diffusivity of the scalar Φ and S_Φ is the generation of Φ per unit volume.

The mathematical expression of the instantaneous variables, as suggested by Osborne Reynolds, can be put in the form:

$$\hat{U}_i = U_i + u_i \tag{2.4}$$

$$\hat{\Phi} = \Phi + \phi \tag{2.5}$$

where U and Φ are the time-averaged values and u and ϕ are the fluctuating values of the velocity component $\hat{U}$ and $\hat{\Phi}$ respectively.

Theoretically, it should be possible to predict turbulent flow directly by solving the unsteady set of equations (2.1) to (2.3). Such a solution would yield all the details of the instantaneous turbulence motion and the time mean motion. In practice, the

analytical solution is not possible, because the equations are non-linear, simultaneous and partial differential. Numerical solution is not practically possible, because the turbulence is three-dimensional with some of the important processes taking place at very small distances and very small times, (Hinze 1959, Bradshaw 1972, Launder and Spalding 1972). Even if the expense of the small time steps could be tolerated, the computational storage requirement would far exceed the capacity of the largest existing computers. Fortunately, engineers are interested in the time averaged properties of turbulence, thus, time-averaging equations (2.1), (2.2) and (2.3) could be expressed as:

$$\partial U_i / \partial X_j = 0 \tag{2.6}$$

$$\partial (U_i U_j)/\partial X_j = -(\partial P/\partial X_i)/\rho + \frac{\partial}{\partial X_j} \{ \nu (\partial U_i/\partial X_j) - \overline{u_i u_j} \} \tag{2.7}$$

$$\partial (\Phi U_j)/\partial X_j = S_\phi + \frac{\partial}{\partial X_j} \{ \Gamma (\partial \phi/\partial X_j) - \overline{u_j \phi} \} \tag{2.8}$$

The new terms $\overline{u_i u_j}$ and $\overline{u_j \phi}$ are the turbulent or Reynolds stress and turbulent scalar flux in direction X_j respectively. These correlations introduce additional unknown in each equation. In order to solve these set of equations (2.6) to (2.8), additional equations or expressions are required to evaluate $\overline{u_i u_j}$ and $\overline{u_j \phi}$.

2.2 Mathematical Modelling Of Turbulence

In principle, one can deduce further differential equations $\overline{u_i u_j}$ and $\overline{u_j \phi}$, but these contain further correlations of higher order, so that closure cannot be achieved in this way. To close the system of time averaged equations, an appropriate "level of closure" must be chosen, and the still unknown correlations must be approximated in

terms of known quantities, or neglected if they are not important. This process is known as "Turbulence Modelling".

Many researches have been made concerning turbulence models and their developmens, extensive reviews are available in many references, such as in Launder and Spalding (1972), Rodi (1973), Reynolds (1976) and Rodi (1980). A convenient classification of turbulence models uses the number of additional partial differential equations to be solved with continuity and momentom equations. For zero-, one- and two-equation models $\overline{u_i u_j}$ is approximated using Bossinesq's suggestion (1877):

$$-\overline{u_i u_j} = \nu_t\{(\partial U_i/\partial X_j)+(\partial U_j/\partial X_i)\} - (2k/3).\delta_{ij} \qquad (2.9)$$

where ν_t is the kinematic turbulent, or eddy, viscosity, and k is the turbulent kinetic energy (where $k=\overline{u_j^2}/2$).

As an analogy to the turbulent viscosity concept, the turbulent heat or mass transport is often assumed to be related to the gradient of the transported quantity (Rodi 1980):

$$-\overline{u_j \Phi} = \Gamma_t.(\partial \Phi/\partial X_j) \qquad (2.10)$$

where Γ_t is the turbulent diffusivity of Φ. In practice, it is often the ratio of turbulent viscosity and turbulent Prandtl or Schmidt number σ_t that is used in describing the scalar fluxes

$$\Gamma_t = \nu_t/\sigma_t \qquad (2.11)$$

Zero-equation models express ν_t as a product of length scale l which is prescribed in algebraic form, and a characteristic velocity scale, which is equal to $l\left|\partial U/\partial y\right|$

$$\nu_t = l^2\left|\partial U/\partial y\right| \qquad (2.12)$$

On the other hand, $\sqrt{k}$ is chosen as velocity scale for

one-equation models, where k is to be found by solving its transport equation, thus the expression of ν_t yields

$$\nu_t = l.\sqrt{k} \tag{2.13}$$

For two-equation models an additional partial differential equation for the length scale or a related variable is introduced.

Only the two models of turbulence used in the present study will be explained in the following sections; the resultant governing differential equations of the cases considered here are given in detail in Appendices A1, A2 and A3.

2.3 The k-ε Turbulence Model

For high Reynolds numbers, the length scale is expressed as following (Launder and Spalding 1972, Rodi 1980):

$$l = C_\mu.k.\sqrt{k}/\varepsilon \tag{2.14}$$

where ε is the rate of dissipation of the turbulence energy and C_μ is an empirical constant. The turbulent viscosity is expressed as:

$$\nu_t = C_\mu .k^2/\varepsilon \tag{2.15}$$

The partial-differential equations governing the transport of k and ε, as described in Launder and Spalding (1974), are expressed as:

$$Dk/Dt= \partial\{(\nu_{eff}/\sigma_k)(\partial k/\partial X_j)\}/\partial X_j + \nu_t\{(\partial U_i/\partial X_j)+(\partial U_j/\partial X_i)\}(\partial U_i/\partial X_j)-\varepsilon \tag{2.16}$$

$$D\varepsilon/Dt= \partial\{(\nu_{eff}/\sigma_\varepsilon)(\partial \varepsilon/\partial X_j)\}/\partial X_j + C_{\varepsilon 1}\, t(\varepsilon/k)\{(\partial U_i/\partial X_j)+(\partial U_j/\partial X_i)\}(\partial U_i/\partial X_j)- C_{\varepsilon 2}\varepsilon^2/k \tag{2.17}$$

where: $\nu_{eff} = \nu + \nu_t$ (2.18)

and: σ_k, σ_ε, $C_{\varepsilon 1}$ and $C_{\varepsilon 2}$ are empirical constants.

2.3.1 Wall Influence

Close to solid walls, there are regions where the local Reynolds number of turbulence ($k^2/\nu\varepsilon$) is so small that viscous stresses are important effects predominate over turbulent ones. The variations of flow properties are much steeper than that in the central region of the flow, thus necessitating an extremely fine finite-difference grid for accurate computation. There are two methods of accounting for this region in numerical methods for computing turbulent flow: equations (2.16) and (2.17) valid for high Reynolds number turbulence may be modified for low Reynolds number conditions or numerical solution for the flow away from the wall may be fitted to the "law of the wall". The second method permits real savings in computer time and storage, and has been used for this reason. The logarithmic velocity-profile is:

$$u^+ = (1/\kappa).\ln(y^+) + B = (1/\kappa).\ln(E.y^+) \qquad (2.19)$$

where:

$$u^+ = U/u_\tau = \text{local mean velocity/friction velocity}$$
$$= U/\sqrt{(\tau_w/\rho)} \qquad (2.20)$$

$$y^+ = y.u_\tau/\nu \qquad (2.21)$$

and κ is the Von Karman constant, and E or B are integration constants which depend on the magnitude of the variation of shear stess across the layer, and on the roughness of the wall. These constants are determined experimentally and there are slight variations in these quantities as reported in the literature. κ and B were given by Clauser (1956) as 0.41 and 4.9 respectively.

At the near-wall region, where local equilibrium prevails and the

shear stress can be considered uniform, the following relation for shear stress can be obtained

$$u_\tau^2 = \tau_w/\rho = k\sqrt{C_\mu} \qquad (2.22)$$

From equations (2.22) and (2.19) the shear stress can be expressed as:

$$\tau_w/\rho = \kappa.(C_\mu)^{1/4}.\sqrt{(k)}.U/\ln(E.y^+) \qquad (2.23)$$

Equation (2.22) is used as boundary condition for k at the grid node adjacent to the wall, and the boundary condition for ε is expressed as follows:

$$\varepsilon = u_\tau^3/(y.\kappa) \qquad (2.24)$$

More details are given by Launder and Spalding (1972) and Rodi (1980).

The near-wall variation of temperature is also assumed to be logarithmic, the expression being:

$$T^+ = \sigma_t\{u^+ + P\{\sigma/\sigma_t\}\} \qquad (2.25)$$

where:

$$T^+ = \rho.u_\tau.C_p.(T_w-T)/\dot{q}_w'' \qquad (2.26)$$

C_p is the specific heat of the fluid at constant pressure and

$\dot{q}_w''$ is the wall heat transfer rate per unit area.

$P\{\sigma/\sigma_t\}$ is a function of laminar and turbulent Prandtl numbers of the fluid, and represents the additional resistance caused by the laminar sublayer to the transport of heat. There are many forms of P-function, but here in this work the empirical form by Jayatillaka (1966), which is valid for smooth wall, has been used. This form is expressed as:

$$P\{\sigma/\sigma_t\} = 9.24\{(\sigma/\sigma_t)^{0.75}-1\} \qquad (2.27)$$

2.3.2 Evaluation Of The Model Constants

The value of $C_{\varepsilon 2}$, which appears in equation (2.17), can be deduced from experimental data on the decay of homogeneous turbulence behind a grid, where diffusion and production are zero (Launder and Spalding, 1972). $C_{\varepsilon 2}$ lies between 1.8 and 2.0.

Local equilibrium shear layer measurements show that the ratio of shear stress $\overline{u_1 u_2}$ and k is nearly constant and approximately equal to 0.3 (Rodi 1980). For this type of flow where the energy production rate P is equal to the dissipation rate ε, equations (2.15 and 2.16) give $C_\mu=(\overline{u_1 u_2}/k)^2$, $C_\mu=0.09$.

In near-wall tubulent flows, P is approximately equal to ε, and the convection of ε is small, accordingly one may arrive at the result (Rodi 1980):

$$C_{\varepsilon 1} = C_{\varepsilon 2} - \kappa^2/(\sigma_\varepsilon \sqrt{C_\mu}) \qquad (2.28)$$

Equation (2.28) gives the value of $C_{\varepsilon 1}$ if the other constants are known. According to the recommendations of Launder et al (1972), Rodi (1980), made after extensive examination of free turbulent flows, the constants take the values shown in table (2.1).

For turbulent heat transfer calculations, the thermal diffusivity in the temperature equation for laminar flow is replaced by its effective (molecular + turbulent) equivalent, the turbulent contribution being obtained from the eddy viscosity by assuming a uniform turbulent Prandtl number $\sigma_t=0.9$.

C_μ	$C_{\varepsilon 1}$	$C_{\varepsilon 2}$	σ_k	σ_ε
0.09	1.44	1.92	1.0	1.3

Table 2.1 The values of the constants used in the k-ε model.

Type of flow	$\overline{u_1^2}/k$	$\overline{u_2^2}/k$	$\overline{u_3^2}/k$	$\overline{-u_1 u_2}/k$
Plane homogeneous shear layer (Champagne et al 1970)	0.97	0.54	0.49	0.33
Near wall turbulence a consensus of data (Launder et al 1975)	1.17	0.59	0.24	0.24

Table 2.2 Reynolds stresses in plane equilibrium shear flow.

C_1	C_2	C_{1w}	C_{2w}	C_{1T}	C_{2T}	C_{1Tw}	C_{2Tw}	C'_T
1.8	0.6	0.5	0.3	3.0	0.33	0.5	0	1.6

Table 2.3 The algebraic Reynolds stress and heat flux models constants.

2.4 Reynolds Stress Equation Modelling

The simple k-ε model described above gives good results for stationary tube flow with axial symmetry, but is limited in its application to more complex flows. For flow in rotating tube the rate of turbulent energy production is affected by the appearance of secondary flow while terms involving the angular velocity appear as sources in the individual Reynolds stress equations, as shown in Appendix A2, affecting the partition of energy between components, directly influencing the shear stresses, and hence invalidating the assumption of the k-ε model that the eddy viscosity is isotropic. With respect to heat transfer it has been pointed out that the conventional turbulent Prandtl number approach is grossly inadequate to predict turbulent heat fluxes in other than the cross-stream direction (Bremhorst et al 1981). The measurements made by Quarmby and Quirk (1974) in tube flow with assymetrical heating, a situation in some ways analogous to the flows through rotating tubes considered here, reveal tangential eddy diffusivities many times larger than those in the radial direction.

In our view, a more satisfactory method is to approach the problem through the transport equations for the Reynolds stresses and turbulent heat fluxes. A brief account of a proposed Reynolds stress model will be given, omitting most of the algebraic detail, given by, for example, Launder (1971), Rodi (1972) and (1980).

The transport equations for the Reynolds stresses may be obtained from Navier-Stokes equations by multiplying the equation for (u_i+U_i) by u_j and the equation for (u_j+U_j) by u_i, adding the results and averaging. The Reynolds number is assumed to be high enough for the

fine-scale turbulent motion to be isotopic (Kolmogorov 1942), and viscous diffusion to be negligibly small. The turbulent energy dissipation rate ε is then distributed equally among components $\overline{u_i^2}$ and all the viscous terms disappear from shear stress equations. With these assumptions, the transport equations for the Reynolds stresses may be written, as reported by Rodi (1970), as following:

$$\underbrace{u_k \cdot \partial(\overline{u_i u_j})/\partial X_k}_{\text{Convection}} + \underbrace{\frac{\partial}{\partial X_k}\{\overline{u_i u_j u_k} - \nu \cdot \partial(\overline{u_i u_j})/\partial X_k + \overline{(\delta_{ik} u_i + \delta_{jk} u_j) \cdot p/\rho}\}}_{\text{Diffusion}}$$

$$= \underbrace{-(\overline{u_j u_k} \cdot \partial U_i/\partial X_k + \overline{u_i u_k} \cdot \partial U_j/\partial X_k)}_{\text{Stress Production } P_{ij}}$$

$$\underbrace{- 2\delta_{ij} \cdot \varepsilon/3}_{\text{Dissipation}}$$

$$\underbrace{+\overline{\{(\partial u_i/\partial X_j) + (\partial u_j/\partial X_i)\} \cdot p/\rho}}_{\text{Redistribution or Pressure-strain}} \qquad (2.29)$$

where p is the fluctuation of static pressure about its mean value.

The last term in equation (2.29) is the mean product of fluctuating pressure and the fluctuating strain fields, and is called the pressure-strain term. Its effect on normal stress components is to diminish the difference between them (Hinze 1959). The explicit appearance of the fluctuating part of the pressure in the correlation is eliminated (Chou 1945) by taking the divergence of the equation for the fluctuating velocity u_i, thus obtaining a Poisson equation for p. This Poisson equation suggested that two distinct types of interaction

contributed to the pressure-strain correlation; one involving only fluctuating quantities, and the other resulting from the interaction of the turbulence field with the mean rate of strain. In modeling the former most workers have made use of Rotta's hypothesis (1951), that for flows with negligible mean strain, the rate of return of anistropic turbulence to isotropy is proportional to the anisotropy. If the characteristic decay time is taken as (k/ε), the wholly turbulent contribution to the pressure strain may then be written as:

$$\overline{\{(\partial u_i/\partial X_j + \partial u_j/\partial X_i).p/\rho\}_1} = \underbrace{-C_1(\varepsilon/k)(u_i u_j - 2\delta_{ij}k/\varepsilon)}_{\Phi_{ij1}} \qquad (2.30)$$

where C_1 is a coefficient to be evaluated by reference to the experimental data.

With the assumption of small departures from homogeneity, Launder et al (1975) concluded that the rapid part of pressure strain simple form produced could be approximated by:

$$\overline{\{(\partial u_i/\partial X_j + \partial u_j/\partial X_i).p/\rho\}_2} = \underbrace{-C_2(P_{ij} - 2P\delta_{ij}/3)}_{\Phi_{ij2}} \qquad (2.31)$$

where P_{ij} and P are the rates of production of $\overline{u_i u_j}$ and k respectively and the coefficients C_2 is supposed to be constants for high Reynolds number. Following the recommendation of Gibson and Launder (1978) and Samaraweera (1978), C_1 and C_2 are taken as 1.8 and 0.6 respectively.

2.4.1 Wall Effects In The Pressure-Strain Terms

Experiments, as shown in Table (2.2), show that near a wall the streamwise normal stress component is appreciably larger and the

transverse component much smaller, than in typical free shear layers.

The effect of a wall on turbulence must be included in modelling the wall region. Gibson and Launder (1978) added a wall correction, obtained by generalizing Shir's (1973) proposal, to their model. The wall effects modify the fluctuting pressure field so as to impede the transfer of energy from the streamwise direction to that normal to the wall. The relative magnitude of the shear stress is also reduced. By introducing the unit vector n_i normal to the surface and the position vector r_i, Shir (1973) advanced the following near-wall addition to Φ_{ij1} producing generally the desired behaviour:

$$\Phi_{ij1w}=C_{1w}(\varepsilon/k)(\overline{u_k u_m}n_k.n_m\delta_{ij}-\tfrac{3}{2}\overline{u_k u_i}n_k.n_j-\tfrac{3}{2}\overline{u_j u_k}n_k.n_i).f(l/n_i r_i) \qquad (2.32)$$

where the wall-damping function f takes the values unity and zero in wall and free shear flows respectively. Launder et al (1975) suggested the following expression:

$$f \propto (l/y) \qquad (2.33)$$

where l is the length scale of energy-containing eddies and can be taken as $(k^{3/2}/\varepsilon)$ or $(|\overline{u_1 u_2}|^{3/2}/\varepsilon)$, with appropriate normalisation to unity value near the wall.

Gibson and Launder (1978) applied the idea expressed by (2.29) to the mean-strain component Φ_{ij2} as follows:

$$\Phi_{ij2}=C_{2w}\{\Phi_{km2}(n_k.n_m)\delta_{ij}-(\tfrac{3}{2})\Phi_{ik2}(n_k.n_i)-(\tfrac{3}{2})\Phi_{jk2}(n_k.n_j)\}.f \qquad (2.34)$$

where C_{1w} and C_{2w} are constants, chosen to give the right stress levels in the uniform-stress layer close to a plane wall, are taken as 0.5 and 0.3 respectively.

For the case of a round pipe, the effect of near-wall terms should be more clear in positions away from the wall, especially for the fully-developed case, as is shown by Lawn's (1971) measurements that there is substantial anisotropy in the stresses near the axis of the pipe. Equation (2.34) was extended, by Samaraweera (1978), to the case of circular pipe, and he derived an expression for the wall-damping function f. In this study, the case of fully-developed pipe flow has been considered for stationary and rotating pipes, the effect of f on the results will be shown later.

2.5 Algebraic Model

In order to obtain an algebraic expression for the Reynolds stresses, the triple correlation whose gradient represents turbulent transport of $\overline{u_i u_j}$ must be modelled. Rodi (1972) proposed the use of the following relationship for $\overline{u_i u_j}$ transport:

$$\text{Transport of } (\overline{u_i u_j}) = (\text{Transport of } k).(\overline{u_i u_j})/k$$

$$= (P-\varepsilon).(\overline{u_i u_j})/k \qquad (2.35)$$

The same assumption was used by Rodi (1976), Gibson and Launder (1976) and Gibson (1978) for different types of flows. Equations (2.29) and (2.35) may then be combined to yield a formula for the Reynolds stresses. This formula together with the k and ε equations form a complete turbulence model. The application of this model to fully-developed pipe flow for stationary pipe, rotating pipe and curved bends will be described later in Appendices A2, A3 and A4.

2.6 Heat Flux Model

The transport equations for the heat fluxes are obtained by

multiplying the equation for the instantaneous temperature (T+t) by u_i and that for (U_i+u_i) by t. The resulting equations are added and averaged to yield the following equations for $\overline{u_i t}$ given by Launder (1973):

$$\underbrace{u_k \cdot \partial(\overline{u_i t})/\partial X_k}_{\text{Convection}} - \underbrace{\frac{\partial}{\partial X_k}\{\overline{u_i t u_k} + \delta_{ik}\cdot\overline{pt/\rho} - \Gamma\overline{u_i(\partial t/\partial X_k)} - \nu\,\overline{t(\partial u_i/\partial X_k)}\}}_{\text{Diffusive transport}}$$

$$= \underbrace{-(\overline{u_i u_k}\cdot\partial T/\partial X_k + \overline{u_k t}\cdot\partial U_i/\partial X_k)}_{\text{Mean-field generation}}$$

$$\underbrace{-\overline{(\Gamma+\nu)(\partial t/\partial X_k).(\partial u_i/\partial X_k)}}_{\text{Dissipation}} + \underbrace{\overline{(\partial t/\partial X_i).p/\rho}}_{\text{Pressure scrambling}} \qquad (2.36)$$

where T and t represent the mean and fluctuating temperatures respectively. At high Reynolds number the dissipation rate is approximately equal to zero, assuming that the small scale eddies are isotropic (Launder 1975). The second term to be modelled is the pressure-temperature gradient correlation $\overline{(\partial t/\partial X_i).p/\rho}$ which is the counterpart of the pressure-strain correlation in the stress equation. This term provides the mechanism which limits the growth of the heat fluxes. Launder (1975) suggested the following apprximation:

$$\overline{(\partial t/\partial X_i).p/\rho} = \underbrace{-C_{1T}\cdot\overline{u_i t}.(\varepsilon/k)}_{\phi_{iT1}} \underbrace{- C_{2T}\cdot P_{iT}}_{\phi_{iT2}} + S_{iT} \qquad (2.37)$$

where S_{iT} is a surface integral included for near-wall regions, and C_{1T} and C_{2T} are constants. P_{iT} represents the part of the production rate of $\overline{u_i t}$ which contains a component of mean strain, i.e.:

$$P_{iT} = -\overline{u_k t}.(\partial U_i/\partial X_k) \qquad (2.38)$$

The near-wall effect is introduced in S_{iT} term in equation (2.37). The turbulent and mean-strain parts can be identified and modelled in a similar manner to that of the wall effects on the pressure-strain correlation. As suggested by Gibson and Launder (1978), the wall effect can be written as:

$$S_{iT} = \underbrace{-C_{1Tw}(\overline{u_k t})(n_i.n_k)(\varepsilon/k).f}_{\Phi_{iTw1}} + \underbrace{C_{2Tw}(C_{2T}.P_{kT})(n_i.n_k).f}_{\Phi_{iTw2}} \qquad (2.39)$$

where C_{1Tw} and C_{2Tw} are constants, and may be fixed, as well as C_{1T} and C_{2T}, by reference to heat transfer data for high Reynolds number turbulent flow.

The transport terms are treated by the technique known as algebraic heat-flux modelling. Gibson and Launder (1976) assumed the following approximation, in a precisely parallel way to the Reynolds stress equation:

$$\text{Transport of } (\overline{u_i t}) \simeq \{\text{Transport of } \sqrt{(k.\overline{t^2})}\ \}.(\overline{u_i t})/\sqrt{(k.\overline{t^2})}$$

$$= (P-\varepsilon).(\overline{u_i t})/2k + (P_T-\varepsilon_T).(\overline{u_i t})/(2\overline{t^2}) \qquad (2.40)$$

where P_T and ε_T denote the rates of production and destruction of the temperature fluctuations respectively, and were assumed nearly in balance. Thus, equation (2.40) simplifies to:

$$\text{Transport of } (\overline{u_i t}) = (P-\varepsilon).(\overline{u_i t})/2k \qquad (2.41)$$

The dissipation rate of $\overline{t^2}$ was assumed to be proportional to $\overline{t^2}.(\varepsilon/k)$,

so that when mean flow and turbulent transport are negligible,

$$\overline{t^2} = -C_T'(\overline{u_k t})(k/\varepsilon)(\partial T/\partial X_k) \qquad (2.42)$$

where C_T' is a constant.

The corresponding heat flux model equations, for the cases studied in this work, will be shown in Appendices A2, A3 and A4.

2.6.1 The Choice Of The Heat Flux Model Constants

This model contains several constants to be chosen by reference to experimental data. C_{1T} and C_{2T} are evaluated by reference to turbulent Prandtl number values typical of free and wall flows. For local equilibrium in plane flow, shear stress and vertical heat flux can be put as follows:

$$-\overline{u_3 u_2} = \beta(k/\varepsilon).\overline{u_2^2}.(\partial U_1/\partial X_3) \qquad (2.46)$$

$$-\overline{u_2 t} = \eta(k/\varepsilon).\overline{u_2^2}.(\partial T/\partial X_3) \qquad (2.47)$$

where:

$$\beta = \{1-C_2+(3/2).C_2.C_{2w}.f\}/\{C_1+(3/2).C_{1w}.f\} \qquad (2.48)$$

$$\eta = 1/(C_{1T}+C_{1Tw}.f) \qquad (2.49)$$

It is convenient to denote the ratio of the turbulent exchange coefficients by turbulent Prandtl number as:

$$\sigma_t = \beta/\eta = \{1-C_2+(3/2).C_2.C_{2w}.f\}(C_{1T}+C_{1Tw}.f)/\{C_1+(3/2).C_{1w}.f\} \qquad (2.50)$$

Substitution of C_{1T}=3.0 and C_{1Tw}=0.5 together with the other constants already specified produces values of σ_t=0.67 and 0.92 for free and wall flow respectively. The coefficient C_T' is chosen by

reference to the decay of temperature fluctuations behind a grid, and Launder (1975) suggested that its value to be approximately 1.6. The calculations for curved and buoyant flow show that the wall modification involving the mean strain rate appears to exercise little influence and so, in the absence of more definite information, C_{2Tw} is set to zero (Gibson 1978). The constants used here in the algebraic Reynolds stress and heat flux models are shown in Table 2.3.

CHAPTER 3

NUMERICAL METHODS OF SOLUTION

3.1 Introduction

From the computational point of view, the numerical solution method depends on the type of equations describing the flow: some flows can be described by parabolic equations and some others, governed by elliptic equations, can be treated by approximate marching methods. A general numerical, marching procedure is used for the calculation of flows in which physical influences are almost exerted in only one direction; as for example, in a boundary layer. Such flows are described by parabolic differential equations. For flows described by elliptic differential equations, perturbations at any point in the flow domain can influence conditions at any other point. The mechanisms of these interactions are usually: convection (downstream transmission along stream line), conduction, diffusion and viscous action (propagation in all directions by molecular inter-mixing), and pressure transmission. Flows with recirculation are clear examples of this type of flow, governed by elliptic differential equations which require iterative solution methods. For flows without recirculation so that convection operates mainly in the downstream direction, but with significant curvature of the streamlines (e.g. flows in strongly-curved ducts) causing pressure transmission from downstream regions to upstream ones, the solution procedure was described by Spalding (1975) as "Partially-Parabolic". This procedure has been adapted by Pratap (1975) for prediction of flow in strongly-curved ducts.

The present work is concerned with "partially-parabolic" and

"parabolic" solution procedures, applied to equations written in cylindrical polar coordinates. The two solution procedures used were similar in many aspects, but differed in the way in which they calculated the pressure field. The partially-parabolic procedure employed a single pressure field common to all the three momentum-equations, while in the parabolic method, two separate pressure fields were calculated, one for the solution of the lateral momentum equations and the other for the longitudinal momentum equation.

A calculation procedure suitable for parabolic equations has been described in detail by Spalding (1974) and Pratap (1975); the "partially-parabolic" method has been described by Pratap (1975), Spalding (1975) and Majumdar and Spalding (1977). Only the main features will be mentioned here.

These methods were embodied in a modified version of the basic "TEACH" computer code (Ideriah and Gosman 1976). The basic program had first to be adapted to cylindrical polar coordinates (r,θ,z) for the rotating pipe flow, and additional modifications had to be made for the effect of longitudinal curvature in toroidal coordinates (r,θ,ϕ) for curved pipes.

Algebraic finite-difference equations were derived by a combination of formal integration and approximation (applied for continuity, momentum and energy equations 2.1, 2.2 and 2.3) over a small control volumes across the flow field. The algebraic set of equations obtained was then solved as will be shown later.

3.2 "Partially-Parabolic" Calculation Procedure

The first step is to construct a finite-difference grid, consisting of orthogonal, intersecting lines, arranged over the flow domain along directions parallel to the toroidal coordinate axes (r,θ,ϕ) for the flow through circular bends. The spacing of the grid lines can be varied to locate more grid nodes in regions of steep variations of the flow variables. Scalar properties such as pressure, temperature, viscosity etc. are calculated at the grid nodes, while the velocity-components are calculated at points midway between adjacent grid nodes, as shown in Fig.3.1. In this "staggered grid" system, velocity-components are conveniently located for calculating the convective fluxes of flow properties stored at the grid nodes. The pressures are located so as to make it easy to calculate the pressure gradients that affect the velocity components. As shown in Fig.3.1, the "control volumes", which represent regions over which the partial-differential equations (2.3) are integrated to obtain their finite-differences form, are different for each flow variable. The integration is performed with a few assumptions regarding the variation of Φ over the grid spacing. For convection in the lateral directions, the value of Φ is assumed to vary linearly between grid nodes. However, this value is modified if the convective flux is much larger compared to the diffusive flux in the same direction. This modification, called the "high-lateral-flux modification" removes certain numerical difficulties (Patankar and Spalding, 1972). In the axial direction, the value of ϕ, which is convected, is assumed to be equal to its upstream value Φ_U. The variation of the upstream value of Φ in the lateral plane (r,θ) is assumed to be stepwise. For diffusion in the lateral plane, Φ is assumed to be linear; but is

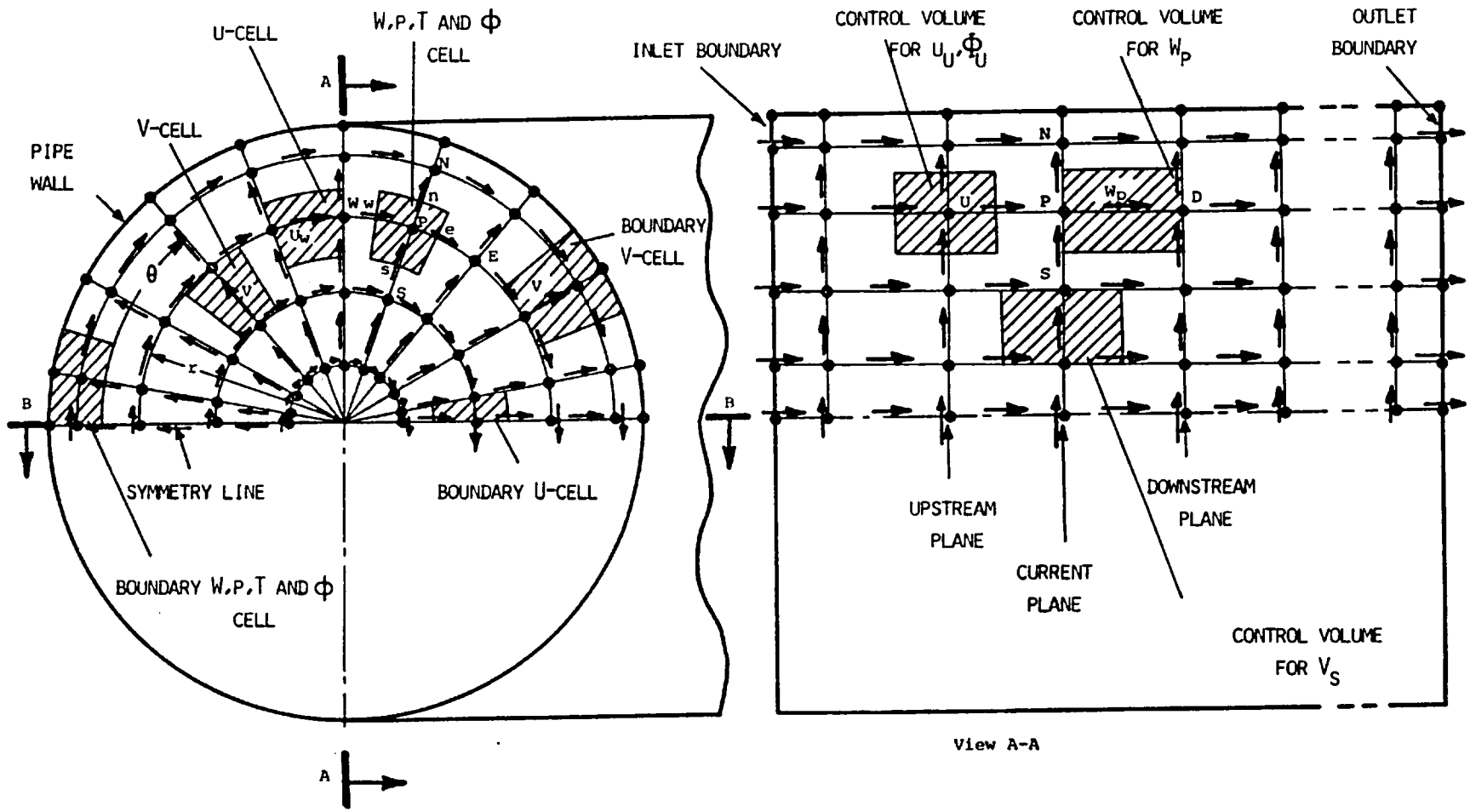


Fig.3.1a Computationsl grid in detail. (For curved ducts).

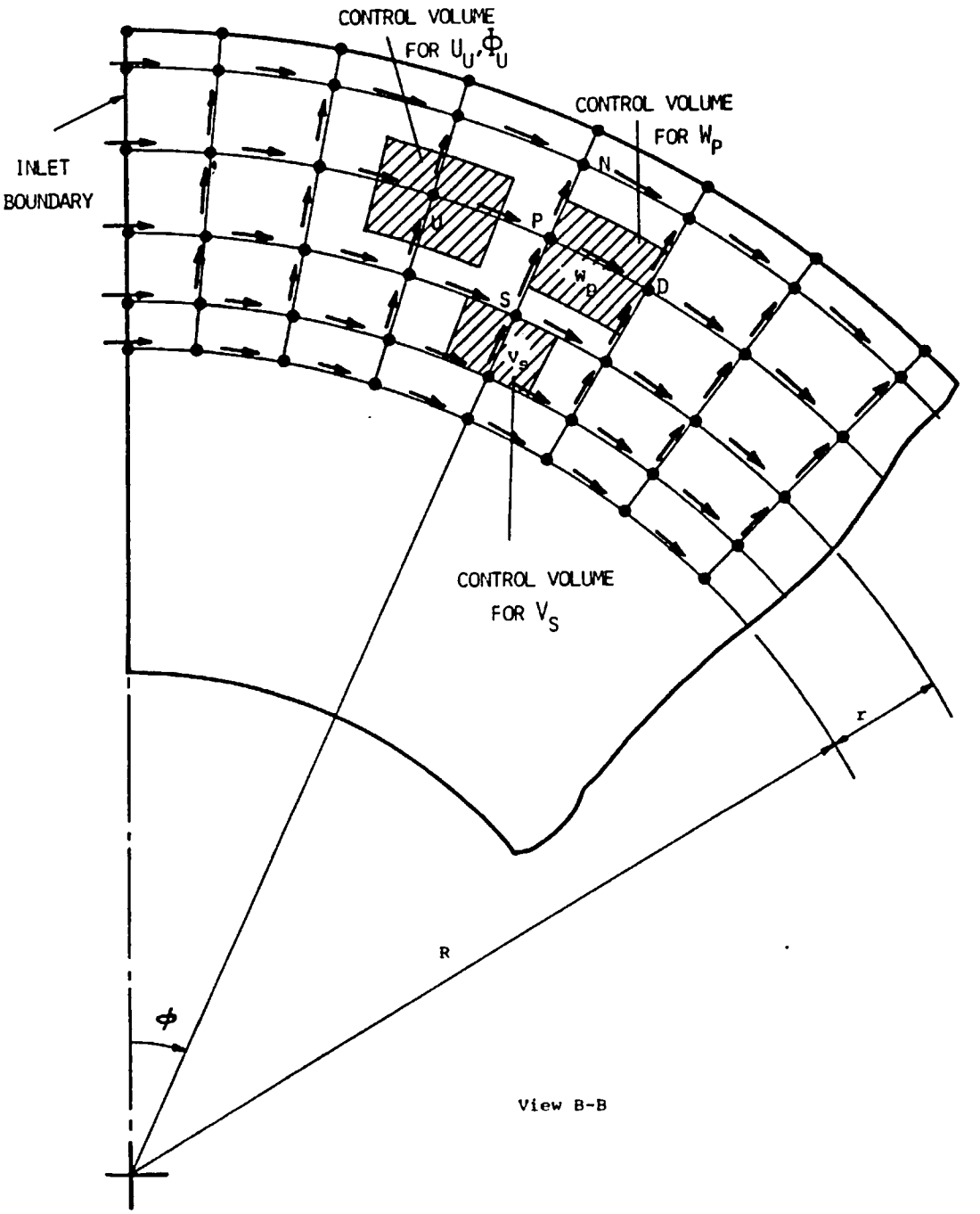


Fig.3.1b Computational grid in detail. (for curved ducts).

also altered later, by the high-lateral-flux modification.

The integrated form of equation (2.3) may be expressed as:

$$\Sigma \left\{ \int_{A} (U_i \Phi - \Gamma_{\Phi j} . \partial\Phi/\partial X_j).dA \right\} + \int_{vol} S_\Phi.dV = 0 \qquad (3.1)$$

where the summation represents the combined flux due to convection and diffusion at the six faces of the control volume, where A is surface area and i stands for east, west, north, south and upstream nodes surrounding the grid node considered p. The integral of the second term in equation (3.1) is expressed in linearized form as:

$$\int_{vol} S_\Phi.dV = Su + Sp.\Phi_p \qquad (3.2)$$

This linearization has been found to promote stability, especially when S_Φ is itself a function of Φ, as shown in the treatment of k equation. The source term, (P- ε), in equation (A1.4) has been put in the finite-difference equation as a function of k as follows:

$$S_k = P - \varepsilon = P - C_\mu.k^2/\nu_t \qquad (3.3)$$

$$= Su + Sp.k \qquad (3.4)$$

where: Su=P and $Sp=-C_\mu.k/\nu_t$

The resultant finite-difference equation has the form:

$$(\sum_i A_i - Sp).\Phi_p = \sum_i (A_i.\Phi_i) + Su \qquad (3.5)$$

where A is positive quantity.

One such equation (3.5) exists for every scalar variable at every grid node. For velocities, similar equations apply but the control volumes are displaced, as shown in Fig.3.2, necessitating minor changes to the coefficient expression A. The finite-difference

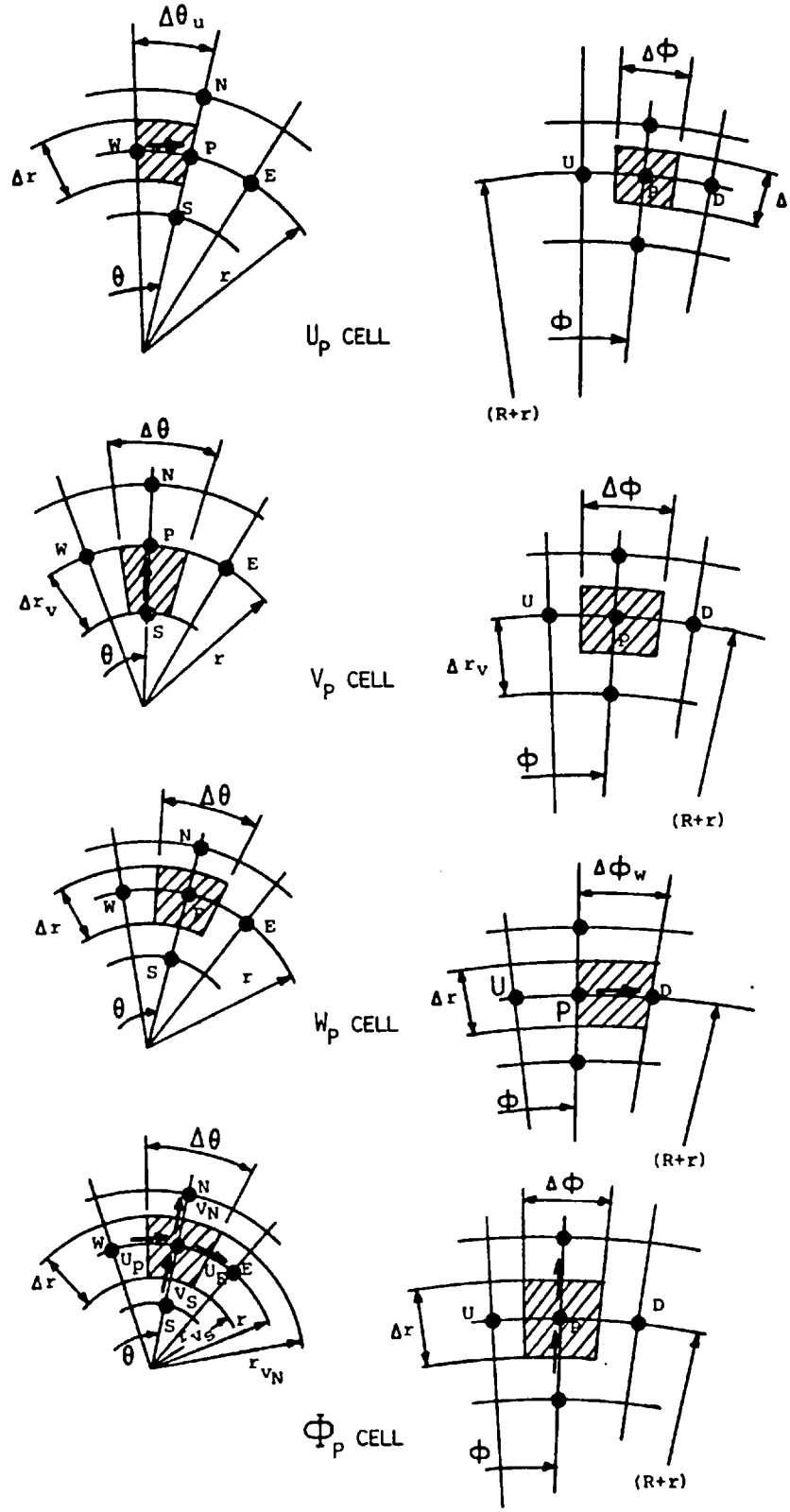


Fig.3.2 Control volumes in detail.

equations for the velocity components can be written as:

$$\left(\sum_i A_i - Sp\right).U_p = \sum_i (A_i U_i) + Su + D_p^U(p_p - p_W) \tag{3.6}$$

$$\left(\sum_i A_i - Sp\right).V_p = \sum_i (A_i V_i) + Su + D_p^V(p_p - p_S) \tag{3.7}$$

$$\left(\sum_i A_i - Sp\right).W_p = \sum_i (A_i W_i) + Su + D_p^W(p_D - p_p) \tag{3.8}$$

where p's are the pressures at different nodes and D's are areas.

The continuity equation can be expressed as following, by making a mass balance over the Φ control volume:

$$U_p.a_w + V_p.a_s + W_U.a_U - U_E.a_e - V_N.a_n - W_p.a_D = 0 \tag{3.9}$$

where:

$$a_w = \Delta r.\Delta\phi.\sqrt{R^2+(r-r.\Delta\theta/2)^2+2(r-r.\Delta\theta/2).R.\cos\theta} \tag{3.10}$$

$$a_e = \Delta r.\Delta\phi.\sqrt{R^2+(r+r.\Delta\theta/2)^2+2(r+r.\Delta\theta/2).R.\cos\theta} \tag{3.11}$$

$$a_U = a_D = r.\Delta\theta.\Delta r \tag{3.12}$$

$$a_n = r_{V_N}.\Delta\theta.\sqrt{R^2+r_{V_N}^2+2r_{V_N}.R.\cos\theta} \tag{3.13}$$

$$a_s = r_{V_S}.\Delta\theta.\sqrt{R^2+r_{V_S}^2+2r_{V_S}.R.\cos\theta} \tag{3.14}$$

Starting with the continuity equation (3.9), one can derive the pressure correction equation:

$$p'_p \sum_j A_j = A_w p'_W + A_s p'_s + A_e p'_E + A_n p'_N + Su \tag{3.15}$$

where:

$$Su = a_w U_p + a_s V_p + a_U W_p - a_e U_E - a_n V_N - a_D W_p \qquad (3.16)$$

and j stands for east, west, north, upstream and downstream nodes. The coefficients A's of the equations of Φ, U, V, W and p' are shown in Table (3.1).

3.2.1 The Partially Parabolic Solution Procedure

The finite-difference equations are solved by an iterative procedure. All variables, except the pressure, are stored in two-dimensional arrays and are evaluated, over cross-stream planes, by marching in the predominant flow direction. The sequence of calculation steps is as follows:

1) The three-dimensional pressure field is first assigned guessed values
2) A march through the flow domain is initiated; and, from the inlet distribution of velocity components, their distribution at the next downstream location are calculated. The pressure gradients are evaluated from the guessed pressure field ; the coefficients in the equations are evaluated on the basis of flow properties at the upstream station. The finite-difference equations are solved by a tridiagonal matrix algorithm, along lines in the lateral directions.
3) The newly calculated distribution of velocity components are checked for satisfaction of mass continuity at all the grid locations in the cross stream plane. The pressure and velocity fields are then corrected by solving a pressure-correction equation so as to remove errors in mass continuity.
4) The equation for property Φ is solved so as to provide

variable and equation number	coefficient					
	A_E	A_W	A_N	A_S	A_U	A_D
U_p (3.6)	$(a.\nu)_e/r\Delta\theta$ $-(1-f_e)(U.a)_e$	$(a.\nu)_w/r\Delta\theta$ $+f_w.(U.a)_w$	$(a.\nu)_n/\Delta r$ $-(V.a)_n/2$	$(a.\nu)_s/\Delta r$ $+(V.a)_s/2$	$(W.a)_U$	0
V_p (3.7)	$(a.\nu)_e/r\Delta\theta$ $-(U.a)_e/2$	$(a.\nu)_w/r\Delta\theta$ $+(U.a)_w/2$	$(a.\nu)_n/\Delta r$ $-(1-f_n)(V.a)_n$	$(a.\nu)_s/\Delta r$ $+f_s.(V.a)_s$	$(W.a)_U$	0
W_p (3.8)	$(a.\nu)_e/r\Delta\theta$ $-(U.a)_e$	$(a.\nu)_w/r\Delta\theta$ $+(U.a)_w$	$(a.\nu)_n/\Delta r$ $-(V.a)_n$	$(a.\nu)_s/\Delta r$ $+(V.a)_s$	$(W.a)_U$	0
T_p (3.5)	$(a.\nu)_e/r\Delta\theta$ $-(U.a)_e/2$	$(a.\nu)_w/r\Delta\theta$ $+(U.a)_w/2$	$(a.\nu)_n/\Delta r$ $-(V.a)_n/2$	$(a.\nu)_s/\Delta r$ $+(V.a)_s/2$	$(W.a)_U$	0
k_p (3.5)	$(a.\nu/\sigma_k)_e/r\Delta\theta$ $-(U.a)_e/2$	$(a.\nu/\sigma_k)_w/r\Delta\theta$ $+(U.a)_w/2$	$(a.\nu/\sigma_k)_n/\Delta r$ $-(V.a)_n/2$	$(a.\nu/\sigma_k)_s/\Delta r$ $+(V.a)_s/2$	$(W.a)_U$	0
ε_p (3.5)	$(a.\nu/\sigma_\varepsilon)_e/r\Delta\theta$ $-(U.a)_e/2$	$(a.\nu/\sigma_\varepsilon)_w/r\Delta\theta$ $+(U.a)_w/2$	$(a.\nu/\sigma_\varepsilon)_n/\Delta r$ $-(V.a)_n/2$	$(a.\nu/\sigma_\varepsilon)_s/\Delta r$ $+(V.a)_s/2$	$(W.a)_U$	0
p'_p (3.15)	$a_e.D_E^U$	$a_w.D_p^U$	$a_n.D_N^V$	$a_s.D_p^V$	$a_U.D_U^W$	$a_D.D_p^W$

Table 3.1 The finite-difference equation coefficients "A" for the flow through bends. (f's stands for the weighting factor and a's are areas)

distribution appropriate to the new downstream axial station.

5) Another new downstream axial station is chosen and the momentum, continuity and ϕ equations are solved as described above. This step-wise march is continued until the end of the flow domain is reached. By the end of one complete marching sweep, a new three-dimensional distribution of pressure is obtained.

6) Steps 2, 3, 4 and 5 are then repeated until the pressure corrections, or the continuity errors which give rise to them, become smaller than a preassigned value.

3.2.2 The Boundary Conditions

The boundary conditions are such that either the value of the variable at the boundary is specified, or a prescription of the gradient of the variable normal to the boundary is made. For example, the velocities are zero at a stationary wall, but at planes of symmetry, their gradients normal to the boundary are zero. The incorporation of boundary conditions into the calculation procedure is achieved by modifying either the source terms or the exchange coefficients in the finite-difference equations for the near-boundary variables. At boundaries where the velocities are fixed, the gradients of the pressure-corrections normal to that boundary are equal to zero; and if the values of the pressure themselves are prescribed; the corrections to the pressure at that boundary are put to zero. As for other variables, the incorporation of either condition is straightforward.

3.3 "Parabolic" Calculation Procedure

For the flow described by parabolic equations a calculation

procedure is used, in which the pressure field is stored in a two-dimensional array, as well as other variables, and all variables are calculated in one single sweep through the flow domain.

In this procedure we consider the influences travel only from upstream to downstream and not vice versa. Thus, diffusion and pressure transmission are assumed to be negligible along the predominant flow direction; and convection exerts influence considered only along the flow direction. The difference between the parabolic and partially-parabolic methods is that, in the parabolic case, the pressure field in the longitudinal momentum equation is simplified and is represented by a value $\overline{P}$ which is constant over a cross-sectional plane for confined flow. The use of a $\overline{P}$ field permits a "once-through" marching procedure through the flow domain and does not introduce large errors in the solution for small forward steps and with no strong curvature in the stream lines.

The finite difference grid, the location of the flow variables and the definition of the control volume are the same as those explained before, except that the axial velocity component is placed directly at the grid nodes where the pressure is stored. The control volumes slightly differ in (r,z) plane as shown in Fig.3.3.

The finite-difference equations are derived in the same way as explained for the partially-parabolic procedure except for the axial momentum equation which becomes:

$$\left(\sum_i A_i - Sp \right).W_p = \sum_i (A_i W_i) + Su - D^W(\partial\overline{P}/\partial z) \qquad (3.17)$$

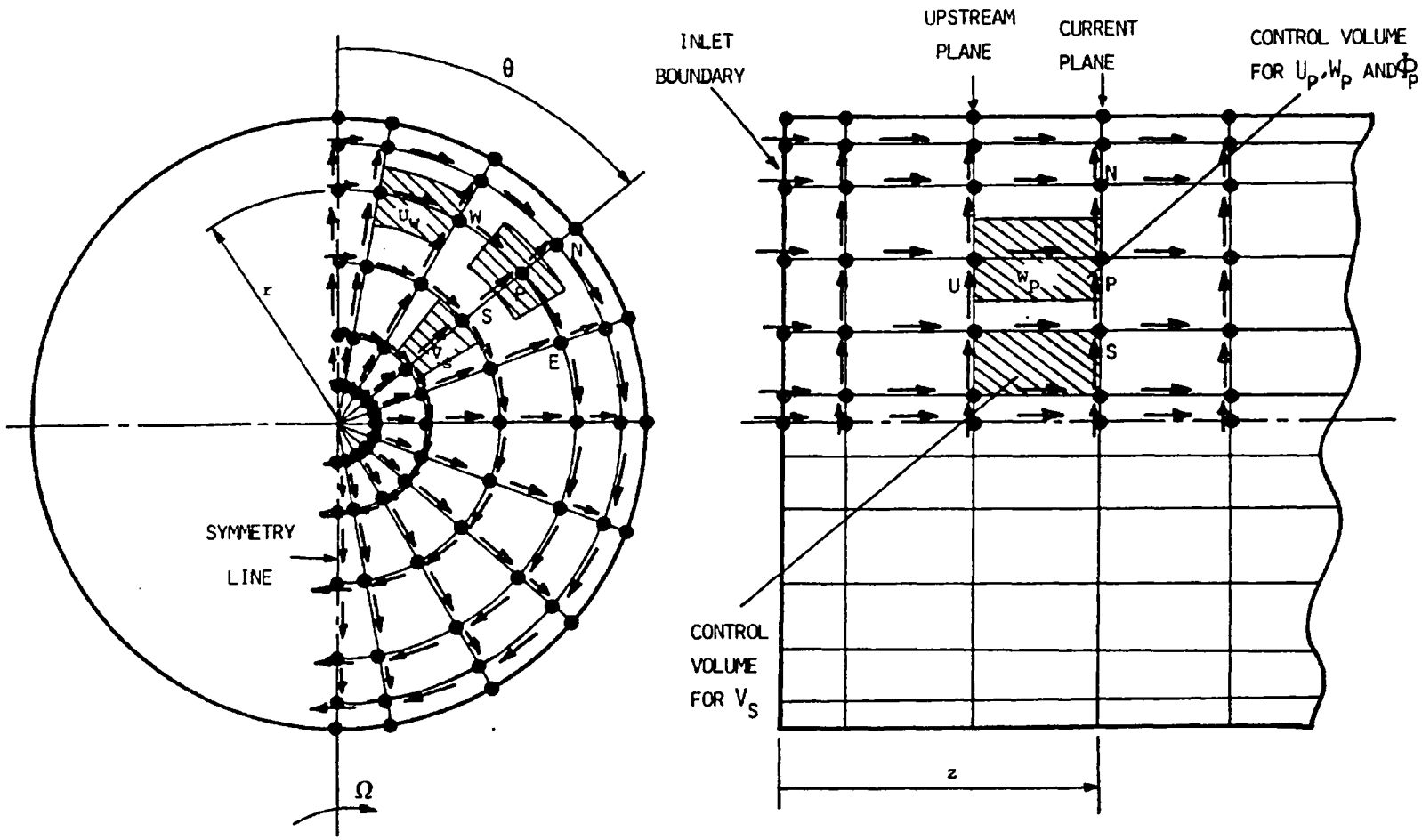


Fig.3.3 Location of variables and control volumes for rotating ducts.

3.3.1 The Parabolic Solution Procedure

Finite-difference forms of the differential equations of motion are solved by "marching" from an upstream station, where the flow cinditions are known, to successive stations downstream. The main steps are:

1) At a given section z, the velocity field and the gradient $\partial\overline{P}/\partial z$ are estimated
2) The axial-velocity distribution is calculated.
3) The axial-velocity and $\partial\overline{P}/\partial z$ are corrected using the continuity condition.
4) The pressure field $P(r,\theta)$ is estimated.
5) Lateral velocity components U and V are calculated.
6) The pressure field is corrected to satisfy locally the continuity condition, and improved values of U and V are calculated.
7) The temperature field is calculated.
8) A forward step is taken to the new downstream station, $z+\Delta z$, and calculation steps 1 to 7 are repeated.

The process is repeated until the end-plane of the flow domain is reached.

3.4 Concluding Remarks

In this chapter, the two calculation procedures used in the present work have been described. The two procedures are based on the same finite-differace method and share several important features. The calculation procedures are general and flexible, and may be applied to the calculation of various similar flows with different boundary conditions.

From the computational point of view, it is seen that the method

used for solving parabolic equations, used here for parallel rotating ducts and mildly curved pipes, employs a marching technique and in one sweep the problem can be solved and iterations are not required. But this can proceeds only with relatively small forward steps, particularly in the enterance region. In this method all the variables are stored in two-dimensional arrays. The "partially-parabolic" method, used here for strongly curved pipes, permits the use of larger forward steps but several iterations are required to obtain converged stable solutions. These iterations are used to update the three-dimensional guessed pressure field in order to obtain the actual pressure field required. The results of the calculations by both methods and the computational details will be presented in Chapters 5 and 6.

CHAPTER 4

EXPERIMENTAL INVESTIGATION

4.1 Introduction

The flow in bends is similar in some respects to the flow through parallel rotating ducts. For both types of flow, centrifugal forces, due to curvature in bends and due to rotation in rotating ducts, affect the flow field, and the same type of secondary flows is obtained. The aim of this experimental work is to provide data for the development and evaluation of numerical prediction methods in bends as well as to obtain data for use in checking the calculation method used for similar type of flow through rotating ducts where detailed measurements are unobtainable.

The present Chapter presents the measurements of velocities in bends. Two test-sections were used:

a) The first test-section was a 90° bend of circular cross-section with ratio of centre line radius of curvature to pipe diameter was 2.8. The maximum obtainable Reynolds number, based on flow rate and pipe bore, was 43 000. Three sets of measurements were obtained: in laminar flow at Re=500 and 1093 and in turbulent flow at Re=43 000. The measurements were made in cross-stream planes set at 30°, 60° and 75° to the bend entry plane and at one and six diameters downstream of the bend exit plane.

b) The second test-section was a 90° bend with square cross-section with ratio of centre line radius of curvature to duct width was 7.0. The maximum obtainable Reynolds number, based on flow rate and duct width, was 35 200. Turbulent flow measurements were obtained in the 45° and 90° planes.

The instrumentation consisted of a forward-scatter fringe-mode laser Doppler anemometer with a frequency-tracking processing system. This system is described in detail in section 4.3. The flow was first checked carefully for symmetry at each station and in the entry length.

The present experimental work is an extension of that reported in Humphrey et al (1977 and 1981) and Taylor et al (1980) on the flow in curved ducts of rectangular cross-section. The entry flow has thin boundary layers, and in this respect differs from the fully-developed flow studied by Rowe (1970), while the bend of circular cross-section, is considerably tighter than those employed for the developing laminar flow measurements reported by Agrawal et al (1978).

4.2 Description Of The Rig

4.2.1 General Layout

The test sections used in the present investigation were set up in two water rigs which were similar to that described by Taylor et al (1980). A diagram of the present experimental apparatus for the circular cross-section bend is shown in Fig.4.1; Fig.4.2 shows the overall view of the apparatus. The closed circuit water system consisted of a sump tank from which water was pumped into a constant head tank from which it flowed by gravity into a large plenum chamber, then through a contraction with a honeycomb, the test section, flowmeters, and to the sump. The flow rate was monitored by means of two flowrators (Type: Fischer-Parter series 10A3500), one for turbulent flow and one for laminar flow, with standard accuracy of ±2% of maximum flow. The flow system was operated for the conditions shown in Table 4.1.

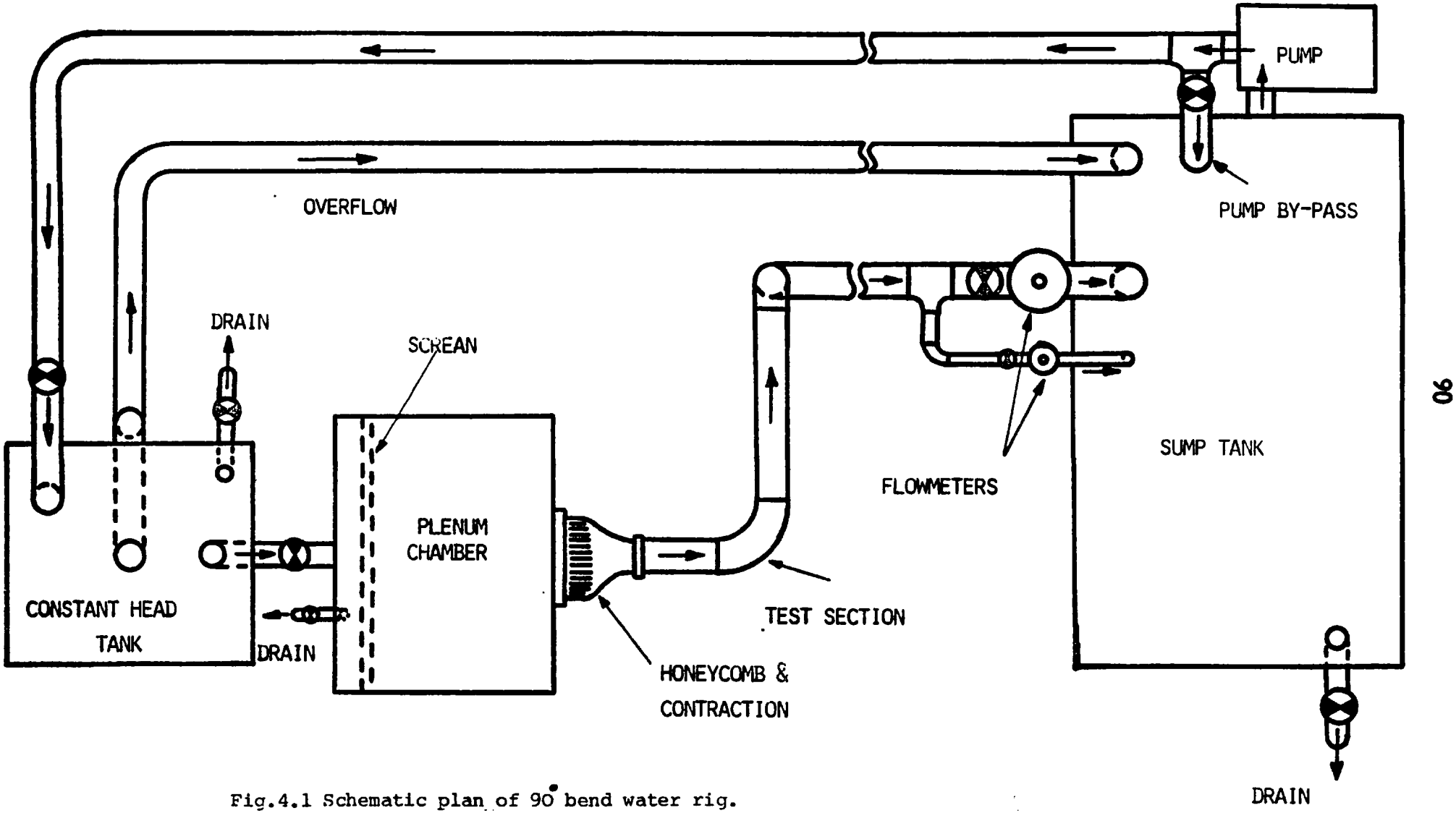
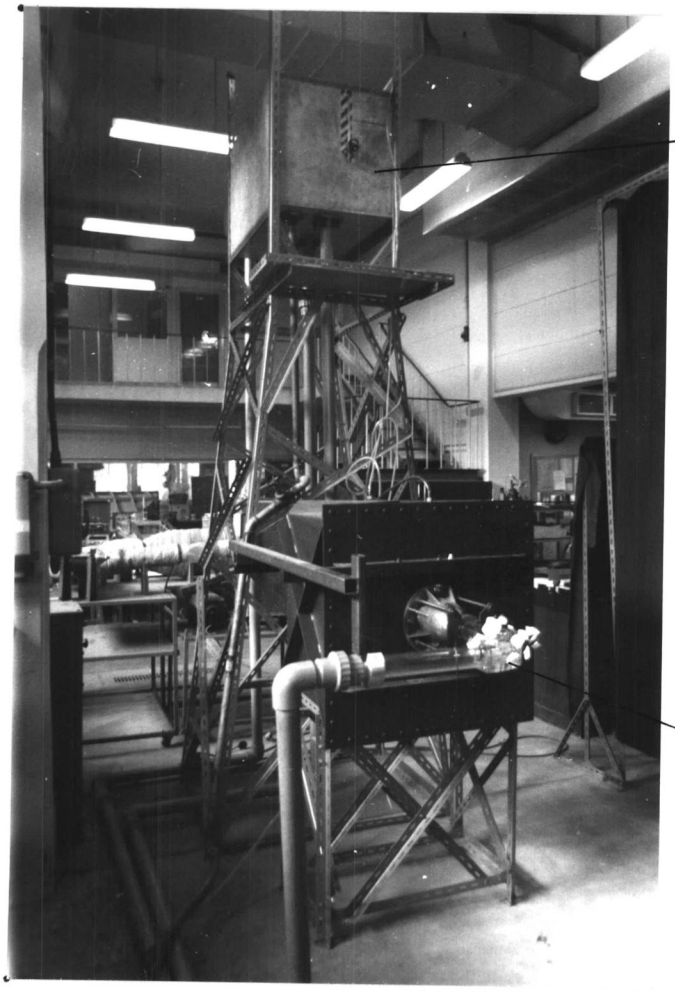


Fig.4.1 Schematic plan of 90° bend water rig.



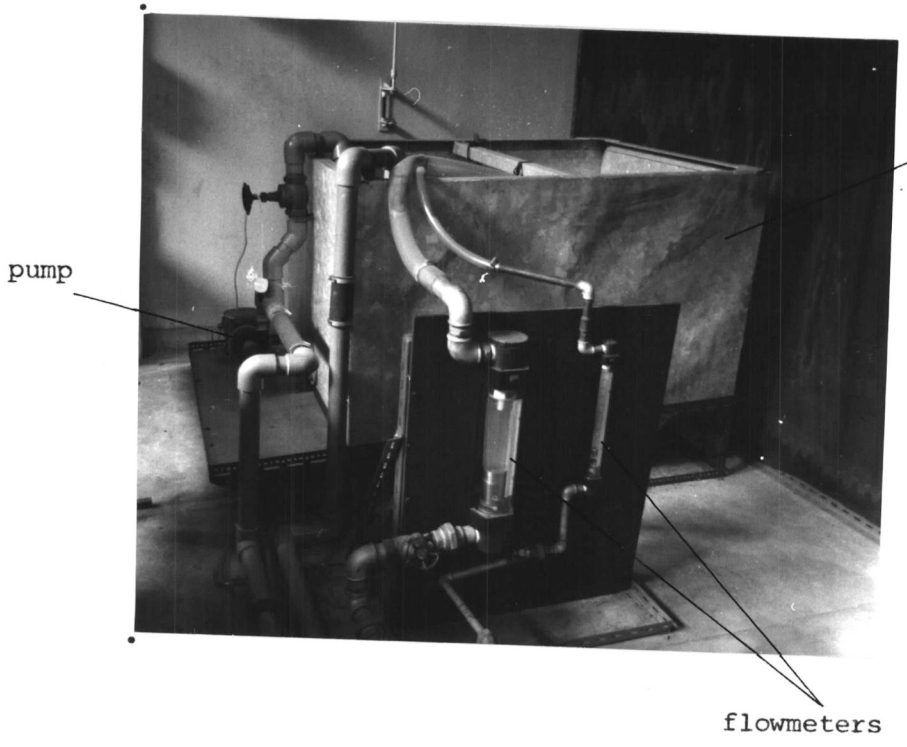


Fig.4.2 Overall-views of the rig.

Flow	$\dot{m}$ (kg/s)	W (m/s)	Re
laminar	0.019	0.0105	500
laminar	0.042	0.0230	1 093
turbulent	1.660	0.9200	43 000

Table 4.1 Laminar and turbulent flow conditions for circular cross-section bend.

Focal length of imaging lenss (f)	300 mm
Half-angle of beam intersection in air (Ψ)	9.11
Half-angle of beam intersection in water (Ψ_L)	6.84
Fringe separation (line-pair spacing) (Δx)	1.9 m
Number of fringes in measuring volume	84
Intersection volume diameter calculated at $1/e^2$ intensity (2z)	0.167 mm
intersection volume length calculated at $1/e^2$ intensity (2y)	1.931 mm
Photomultiplier pinhole diameter (D_{ph})	0.5 mm
Transfer constant	0.5 MHz/m.s
Laser beam wavelength (λ)	0.6328

Table 4.2 Optical characteristics of the lasser Doppler anemometer.

ϕ^o	$(\dot{m}_2 - \dot{m}_1)/\dot{m}_1$		
	Re=500	Re=1093	Re=43000
30	-3.84%	+1.55%	-1.06%
60	-2.48%	+0.34%	-0.55%
75	-5.18%	+2.40%	+0.73%

Table 4.3 The difference between calculated mean flow rate using velocity measurements ($\dot{m}_2$) and flowmeter reading ($\dot{m}_1$).

The working fluid used was water, because high Reynolds number flows are difficult to obtain with viscous fluids of the desired refractive index matching the perspex walls of the bend. For the circular cross-section bend the consequent change in refractive index across the perspex/water interface effectively limits the measurements to the streamwise component of velocity only.

The plenum chamber was connected to the test section by a smooth contraction entrance of circular cross-section and area ratio 8:1, made of fibreglass and containing impregnated paper honeycomb placed in the large end of the contraction. Two metal screens were placed within the plenum chamber. preliminary measurements showed that after passing through the honeycomb and gradual contraction, the flow entering the test section was steady and symmetrical.

Another similar water rig of smaller dimensions was used for the square cross-section bend.

4.2.2 The Test Sections

Fig.4.3 shows the geometry and dimensions of the 90° test bend of circular cross-section. The internal diameter d was 48 mm and the radius of curvature R meaured to the axis was 134.4 mm (R/d=2.8). The bend was machined accurately as suggested by Agrawal et al (1978) from two halves of a rectangular perspex block split in the plane of symmetry. This method was adopted because of the near impossibility of bending a tube to this radius while still maintaining accurate circularity of the cross section. The effects of refraction on the the path of the laser beam must, however, be taken into consideration. A method for the calculation of these effects, in the complex three dimensional view, is given by Enayet et al (1981). In the present

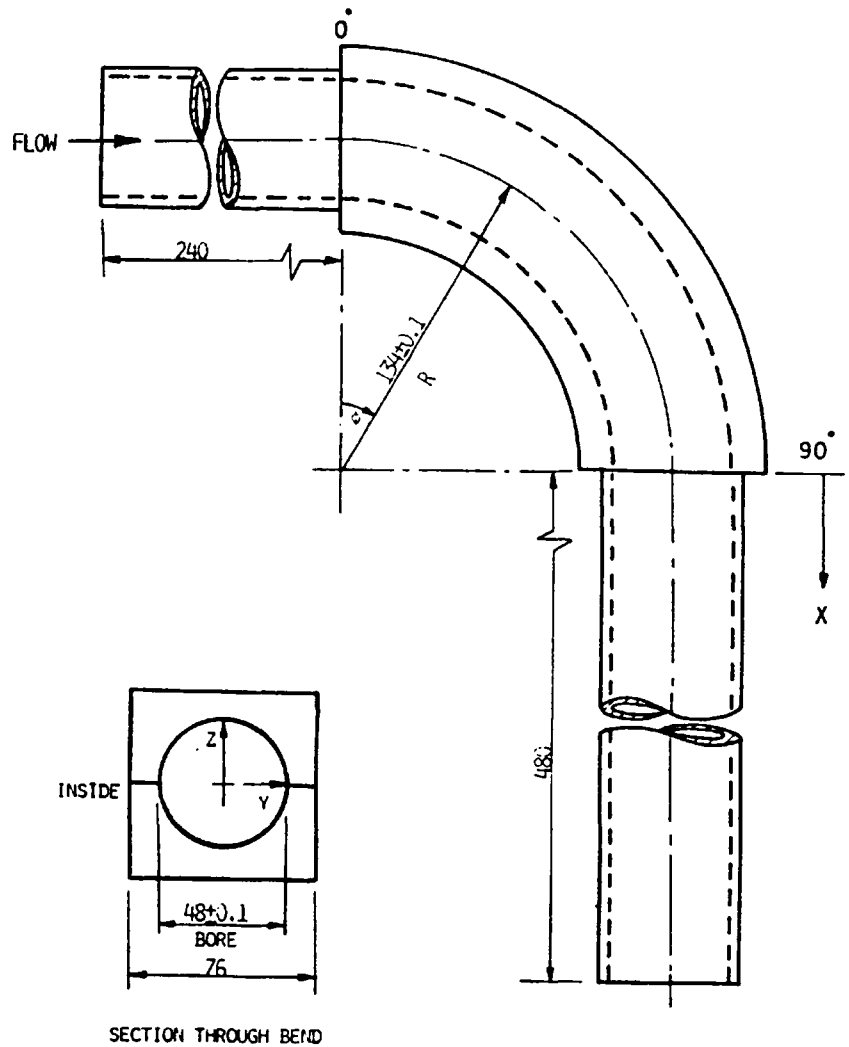


Fig.4.3 Bend dimensions and nomenclature,(dimensions in mm).

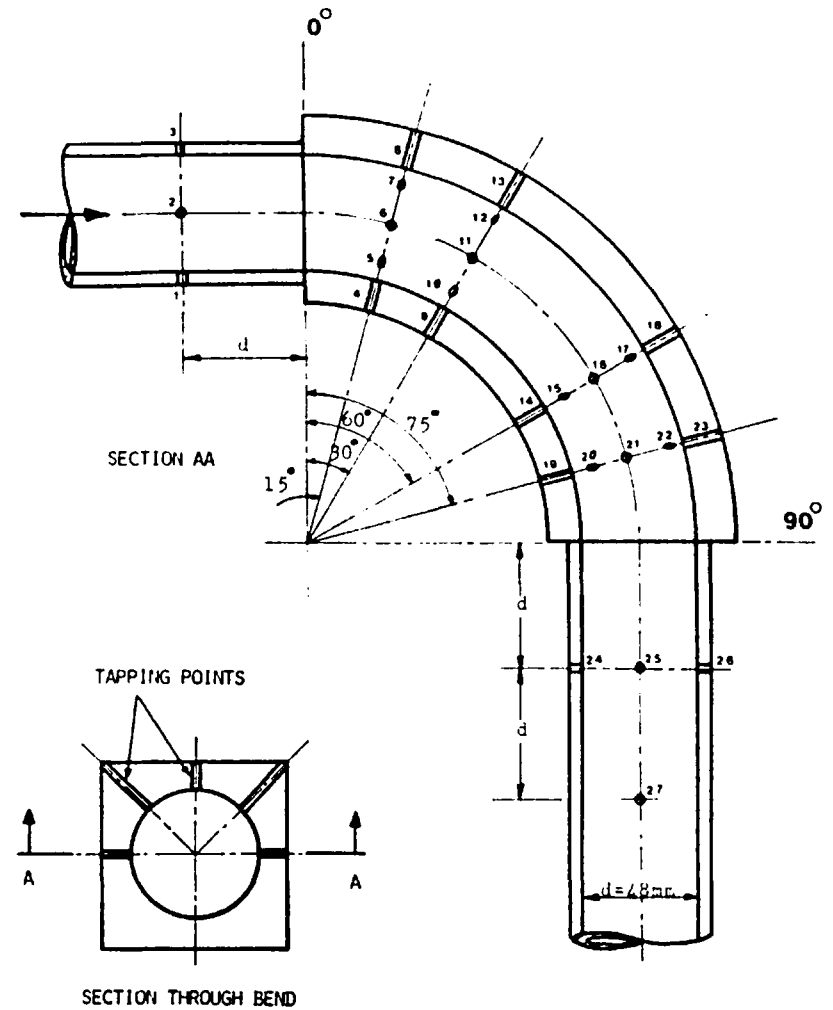


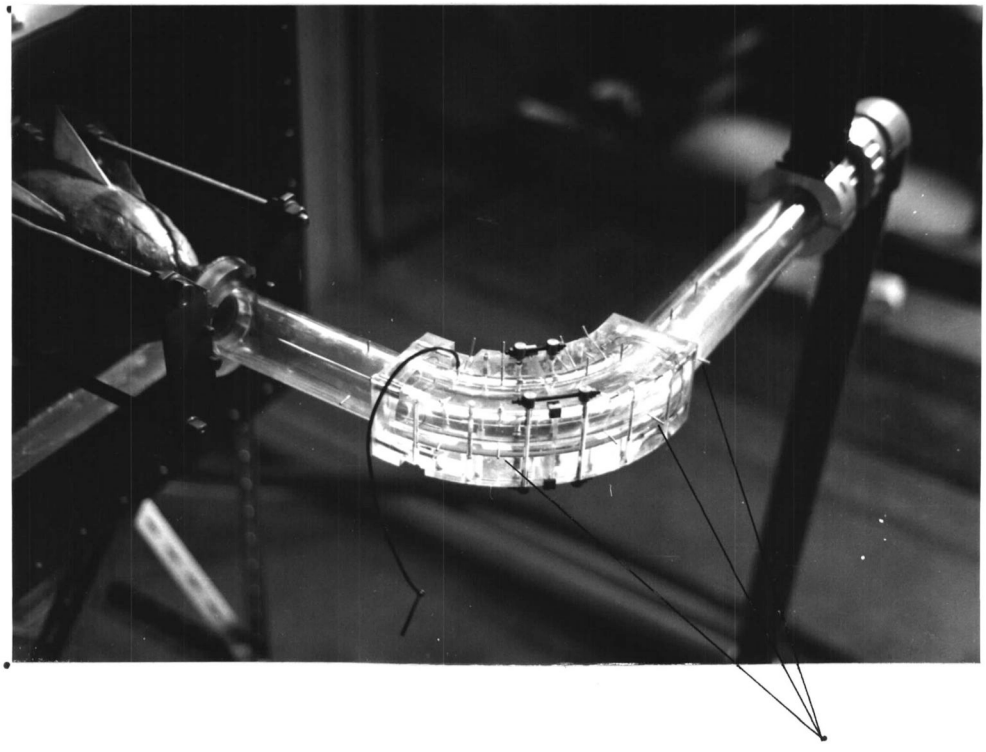
Fig.4.4 Pressure tapping locations.

study a simplified two dimensional analysis was used. This will be discussed later. The bend was fixed in the horizontal plane and fitted with a short straight tube 24 cm long at the inlet and another straight length of 48 cm downstream. Wall pressure measurements were obtained by means of pressure tappings let into the walls of the test section, as shown in Fig.4.4. Pressure measurements were made with a water micromanometer. In laminar flow the pressure differences of water were too small for reliable measurements. Views of the details of the test section are shown in Fig.4.5.

The other test section used consisted of a 90° square cross-section bend of mean radius 280 mm and of radius to duct width ratio 7.0, as shown in Fig.4.6. A short upstream straight duct (length/width=7.5) is fitted to get thin inlet boundary layers in the bend and 2 metres straight duct at downstream of the bend was also fitted.

4.3 Laser Doppler Velocimetry

The optical arrangement used in this investigation is shown in Fig.4.7 and the principal characteristics of the anemometer are given in Table 4.2. The anemometer unit consisted of a 5 mW helium- neon laser which provided light focussed on to a diffraction grating, collimated in order to reduce spherical aberration, and focussed to form the scattering volume within the bend. Forward scattered light collected by the objective lense was focussed on a pinhole in front of an EMI9658 photomultiplier. The mirror shown in Fig.4.7 which is used to turn the optical axis through 90 degrees was optically flat within one tength of the wavelength of light. The photomultiplier output is processsed using a Cambridge Consultants CC01 frequency-tracking



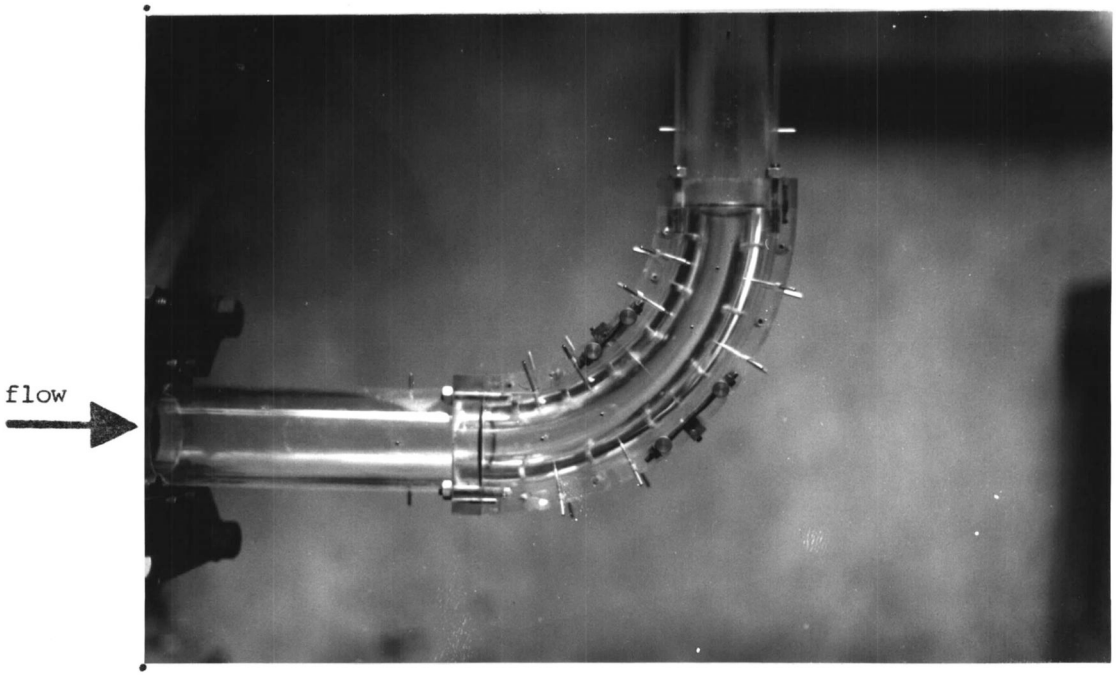


Fig.4.5 Views of the test section.

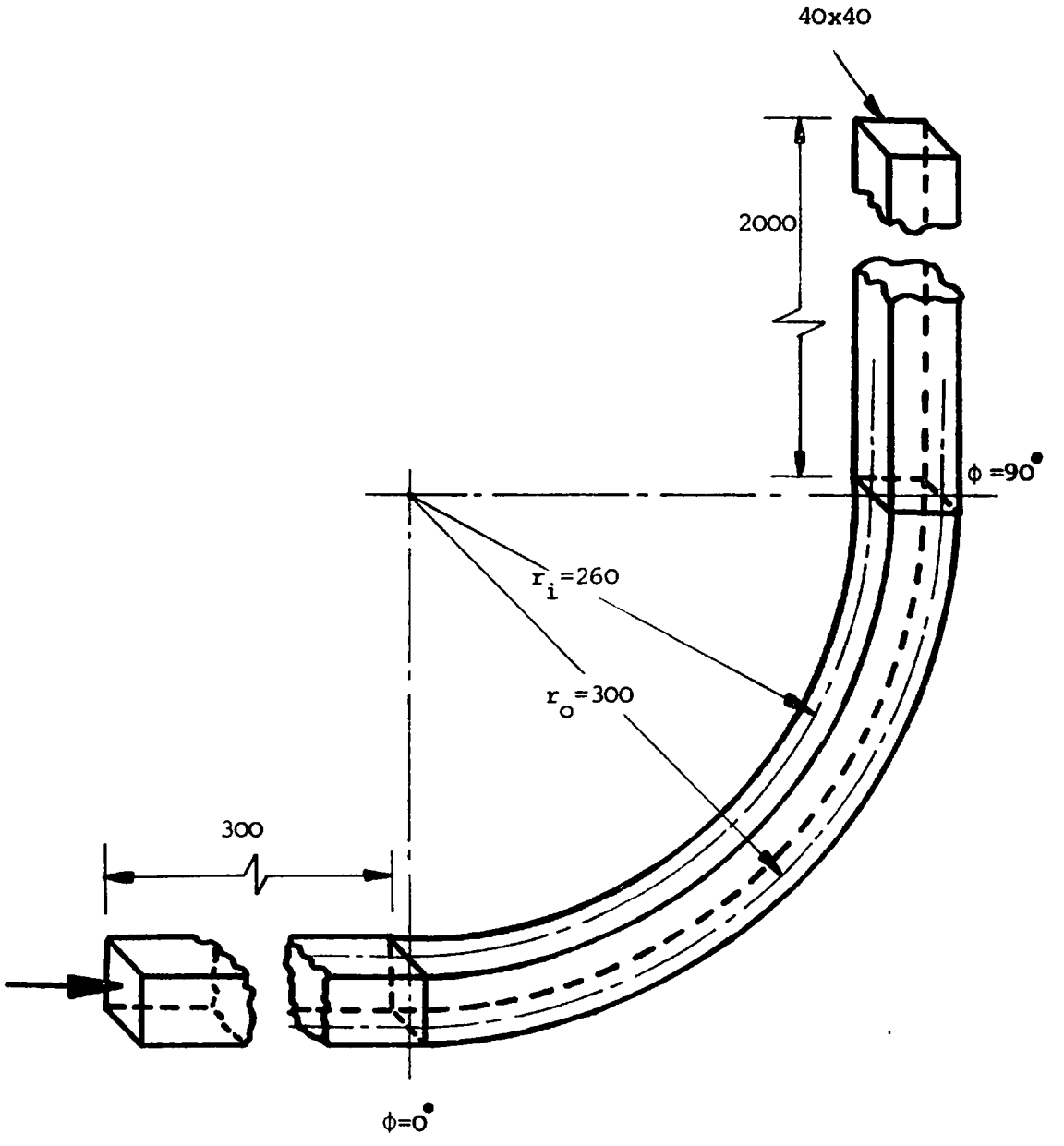


Fig.4.6 Square cross-section bend geometry (dimensions in mm).

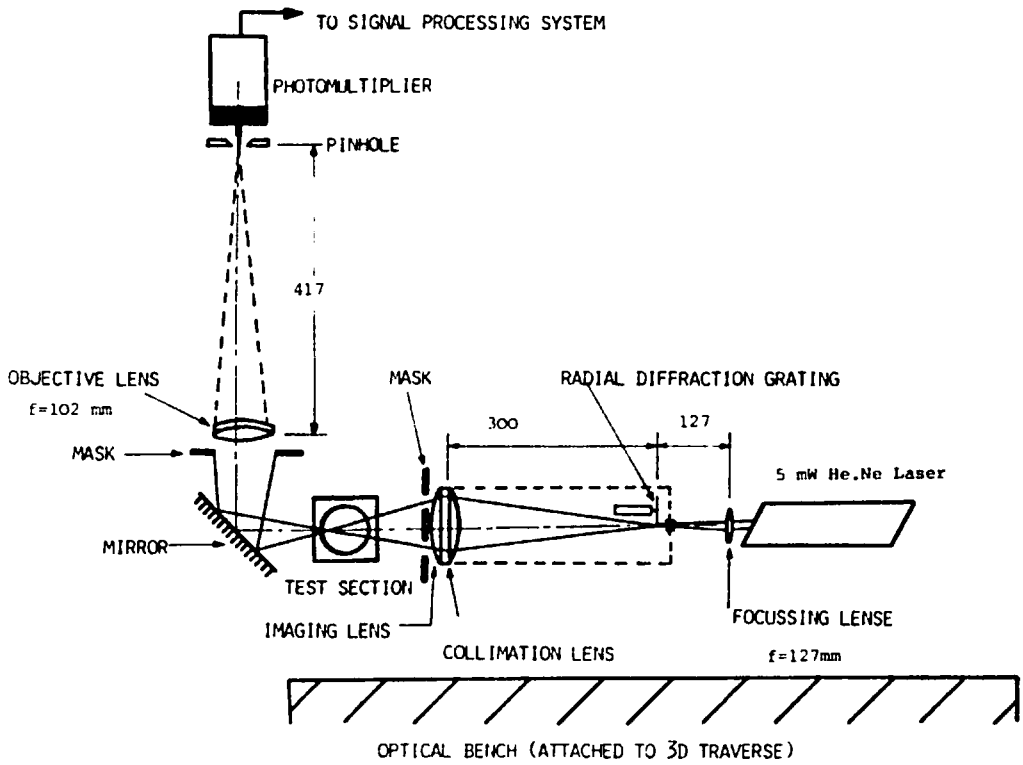


Fig.4.7 Details of the optical arrangement.

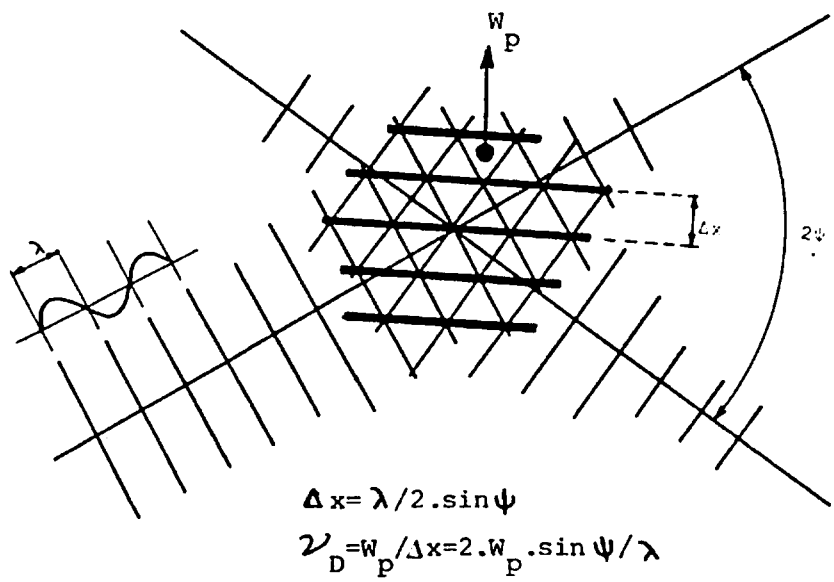


Fig.4.8 Interference fringe mode.

demodulator. More details are reported by Durst et al (1976).

All the optical system components were mounted on an optical bench which in turn was fixed to a three dimensional traversing arrangement. The entire optical system could be traversed relative to the test section while keeping the components aligned at all times.

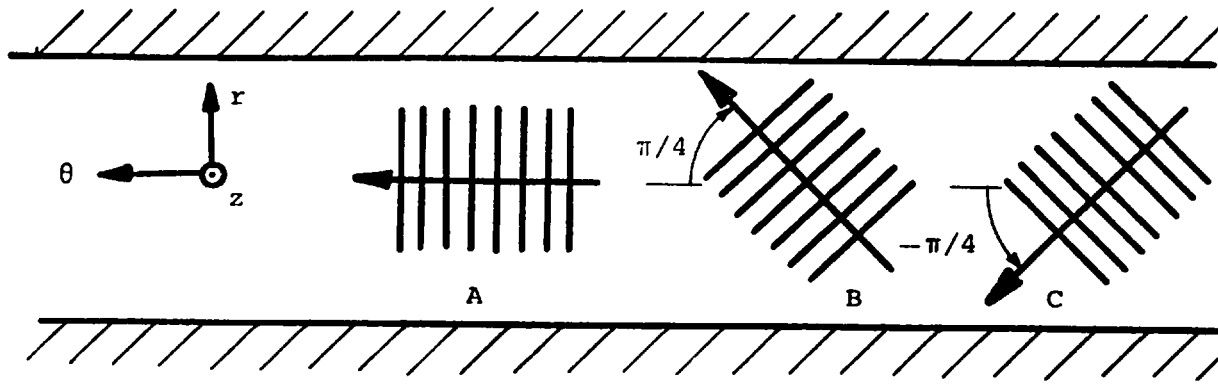
4.3.1 Doppler Signal Generation And Interpretation

When two light beams with wavelength λ intersect at an angle 2Ψ, an interference pattern of stationary fringes parallel to the bisector of the two beams is formed. A particle moving through the fringe pattern with instantaneous velocity component W_p (normal to the bisector of the angle 2Ψ) as shown in Fig.4.8, will scatter varying intensity light. The Doppler shifted frequency is given as follows:

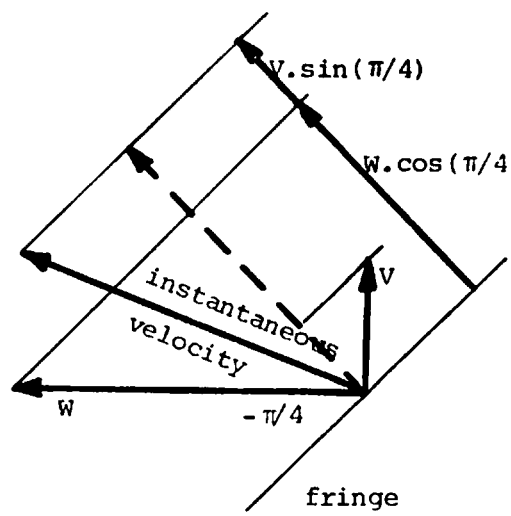
$$\nu_D = 2.W_p .\sin\Psi/\lambda \qquad (4.1)$$

For the square bend, in addition, the optical system can be adjusted for measuring both streamwise and transverse components of velocity, using an optical axis adaptor to rotate the plane of the incident laser beams. When measuring the axial velocity component W the incident beams of the anemometer are arranged to lie in (r,θ) plane. For transverse velocity component V in z direction, measurements are made with the fringe system orientated in such a way that the normal to the fringe is inclined successively at angles of 0, 45 and -45 degrees to the axial direction as shown in Fig.4.9. The velocity components are derived from the measured Doppler frequencies using the following equations derived by Melling and Whitelaw (1976):

$$W = (\nu_D)_0/K \qquad (4.2)$$

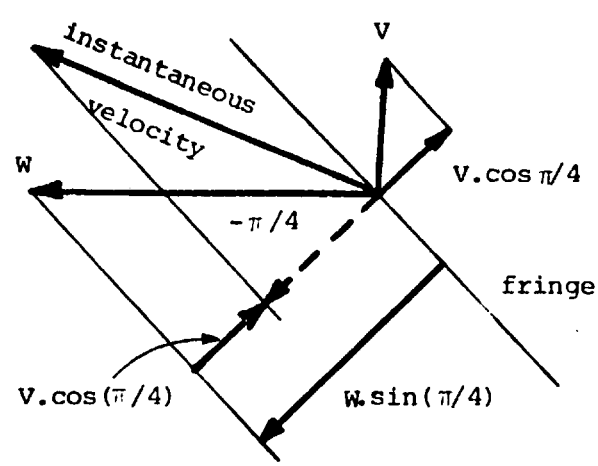


(a)



(b)

velocity component
normal to fringe
$=W.\cos(\pi/4)+V.\sin(\pi/4)$



(c)

velocity component
normal to fringe
$=W\sin(\pi/4)-V\cos(\pi/4)$

Fig.4.9 (a) Orientation of fringes for sensitivity to two velocity components.
(b) Vector diagram for case B.
(c) Vector diagram for case C.

$$w = (\tilde{v}_D)_0/K \tag{4.3}$$

$$V = \{(v_D)_{45} - (v_D)_{-45}\}/(K.\sqrt{2}) \tag{4.4}$$

$$v = \sqrt{\{(\tilde{v}_D)^2_{45} + (\tilde{v}_D)^2_{-45} - (\tilde{v}_D)^2_0\}}\ /K \tag{4.5}$$

$$\overline{w.v} = \{(\tilde{v}_D)^2_{45} - (\tilde{v}_D)^2_{-45}\}/(2.K^2) \tag{4.6}$$

where: $K = 2.\sin\Psi/\lambda$ (4.7)

and $(v_D)_0$, $(v_D)_{45}$ and $(v_D)_{-45}$ are the frequencies at 0, 45 and -45 degrees respectively. W, V and v represent local mean values, while w, v and $\tilde{v}$ are the corresponding fluctuating values.

4.3.2 The Laser Doppler Velocimeter Control Volume

Fig.4.10 shows an laser Doppler velocimeter operating in the fringe mode. Two beams are focused at the measuring point P by the lens L_1 of focal lenth f. The intensity distribution of the fringe pattern, which is formed at their crossing region, is an ellipsoid. The dimensions of the ellipsoid are dependent on the arrangement of the optical components which observe the Doppler signal and transmit it to the photomultiplier. Considering a pinhole diameter D_{ph} and a light-collecting lens magnification M, the diameter of the control volume and the number of fringes that can be viewed by the pinhole are given by:

$$d_{ph} = D_{ph}/M \tag{4.8}$$

$$N_{fr} = d_{ph}/\Delta x \tag{4.9}$$

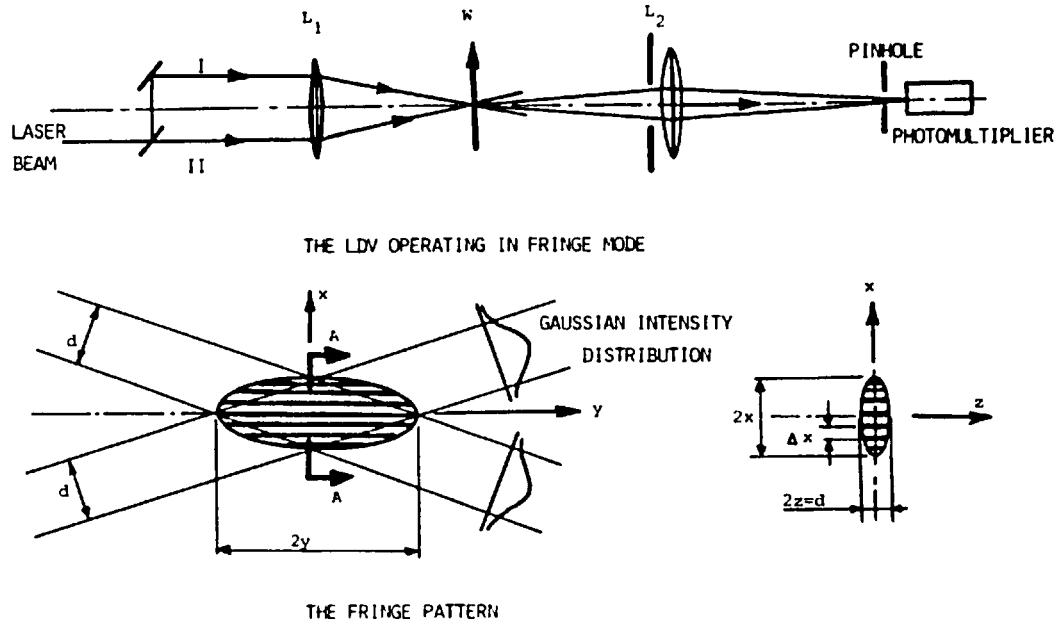


Fig.4.10 The LDV control volume.

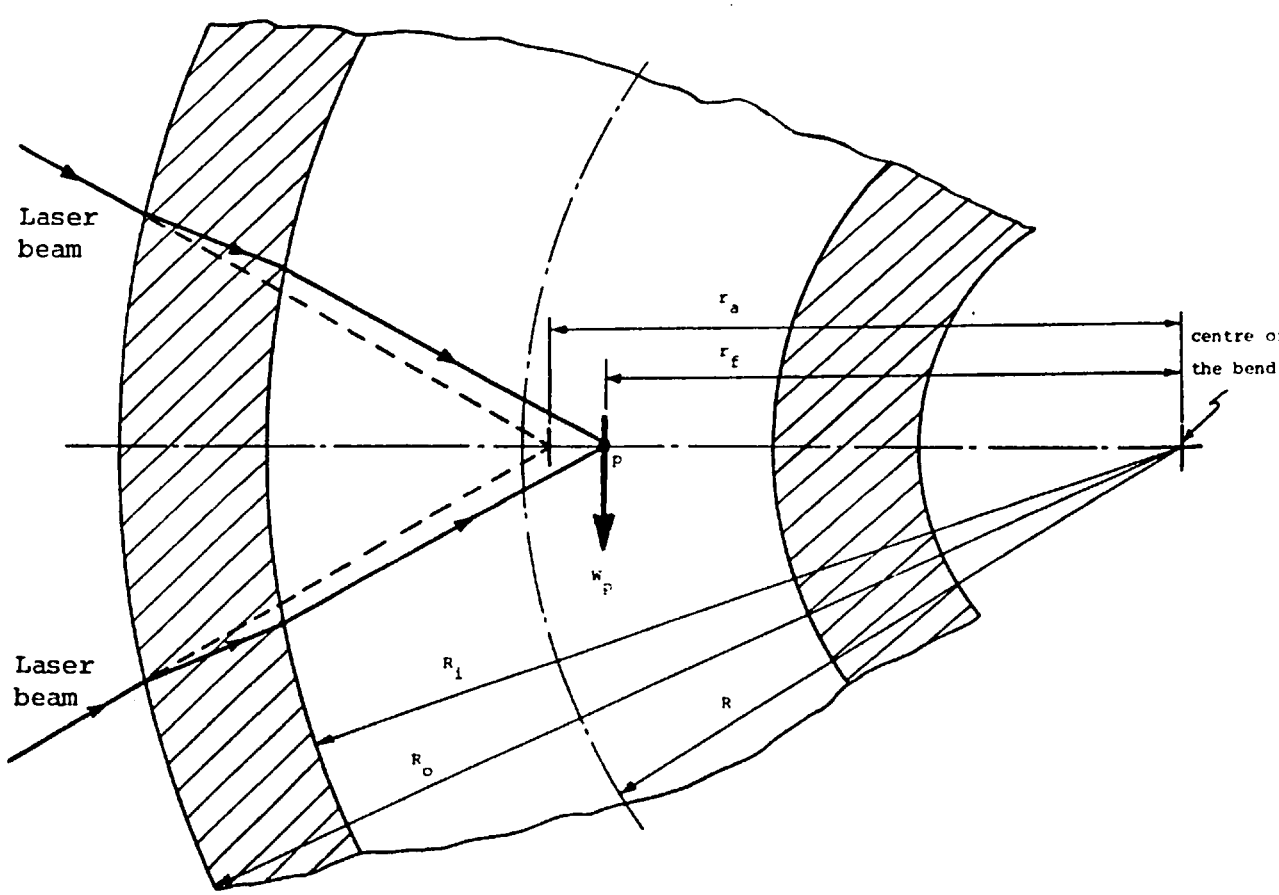


Fig.4.11 Refraction of laser beam during streamwise velocity measurements.

4.3.3 Control Volume Displacement Correction

Refraction of the laser beam at the water/perspex interface not only displaces the measurement volume by an amount which can be readily calculated but also, and more importantly, prevents the measurements of cross-section velocity components. The method employed successfully for the latter in the rectangular bend experiments as shown in Humphrey et al (1977 and 1981) fails for the round pipe, because, unless the refractive indices of the fluid and pipe wall are equal, the twin laser beams entering the pipe in a plane at 45^{o} to the axis cannot converge. Consideration was given to the use of fluids other than water which would allow the indices to be equalized. Unfortunately, it turns out that such fluids either possess highly unpleasant or toxic properties, or are so viscous that it is difficult to obtain Reynolds numbers high enough for turbulent flow. A case in point is the experiment described by Agrawal et al (1978) where the use of a glycerine-water mixture to match the indices limited the investigation to laminar flow.

The measurements were made at points along the optical axis which is refracted at the pipe wall at an angle to the plane of symmetry to which it was originally parallel. A straightforward calculation produced the beam trajectories shown in Appendix A5. The corrections described by Boadway and Karahan (1981) and Bicen and Whitelaw (1981), for the effects of refraction due to the bend curvatures, were applied to the streamwise velocity component data. The corrected velocity component was obtained by multipling the velocity W_p, calculated from equation (4.1), by a correction factor C_f given by the following relation:

$$1/C_f = n_f + (r_a/R_o)\{(R_o/R_i)(n_f/n_w - 1) + (n_w - 1).n_f/n_w\} \quad (4.10)$$

where:

n_f = refraction index of the fluid

n_w = refraction index of the wall

R_o = outer radius of the curved wall

R_i = inner radius of the cueved wall

r_a = radius position of the virtual intersection of beams with no refraction (as shown in Fig.4.11)

(note that r_a is positive for positions beyond the centre of curvature with respect to the laser source)

The true radius of beam intersection and corrected fluid velocity are given by the following equations:

$$r_f = C_f . r_a \quad (4.11)$$

$$W_p)_{corr} = W_p . C_f \quad (4.12)$$

It was found that signal quality was only slightly impaired by refraction effects and that measurements were feasible for points in the flow distant more than one tenth of the radius from the wall in the vertical plane.

4.3.4 Doppler Signal Processing

The scattered light was collected by the photomultiplier, from which the output was processed in a frequency tracking demodulator and associated equipment shown in the block diagram of Fig.4.12. Since the maximum velocity of the flows investigated here produced Doppler frequency much less than one MHz, with continuous signals of high signal-to-noise ratio, the tracker is well-suited for the present

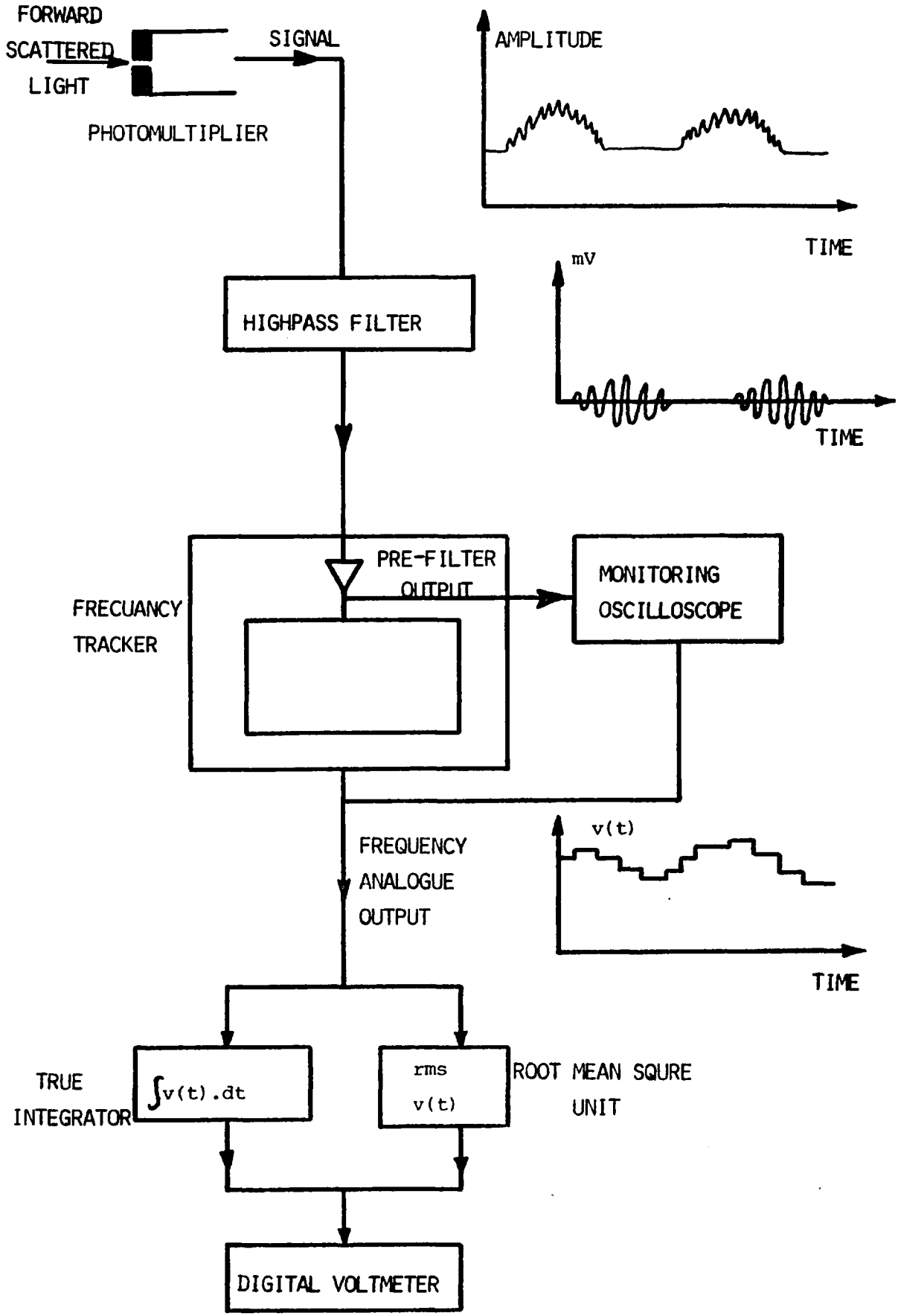


Fig.4.12 Block diagram of Doppler signal processing system.

measurements. Frequency trackers, their characterictics, performance, limitations and comparisons with alternative signal processing techniques, are reviewed and discussed by Durst et al (1976). For turbulent flow measurements, the flow is seeded (Durst et al 1976) with minute quantities of milk to increase the scattering particle concentration and thereby increase the particle arrival rate.

The output from the tracker was presented in parallel to the true time integrator and rms meter from which the mean velocities and turbulence intensities were found. The normal measuring procedure consisted in recording not less than three values of the average and rms voltages directly from the digital voltmeters. The rms meter was allowed sufficient time to stabilise after changes in the measuring volume position.

4.4 Scope And Accuracy Of The Measurements

For each cross-section in the bend the mean axial velocity was calculated from the measurements by dividing the flow domain into small areas, as shown in Fig.4.13, for circular cross-section, and Fig.4.14, for square cross-section, and assuming that the axial velocity is uniform along every cell. The percentage increases in mass flow rate with respect to the reading of the flowmeters are given in Table 4.3, for the circular cross-section, while for square cross-seection -1.67% increase, for $\phi=45^{\circ}$, and -0.6%, for $\phi=90^{\circ}$, are obtained. The changes in mass flow rate lie in an acceptable range.

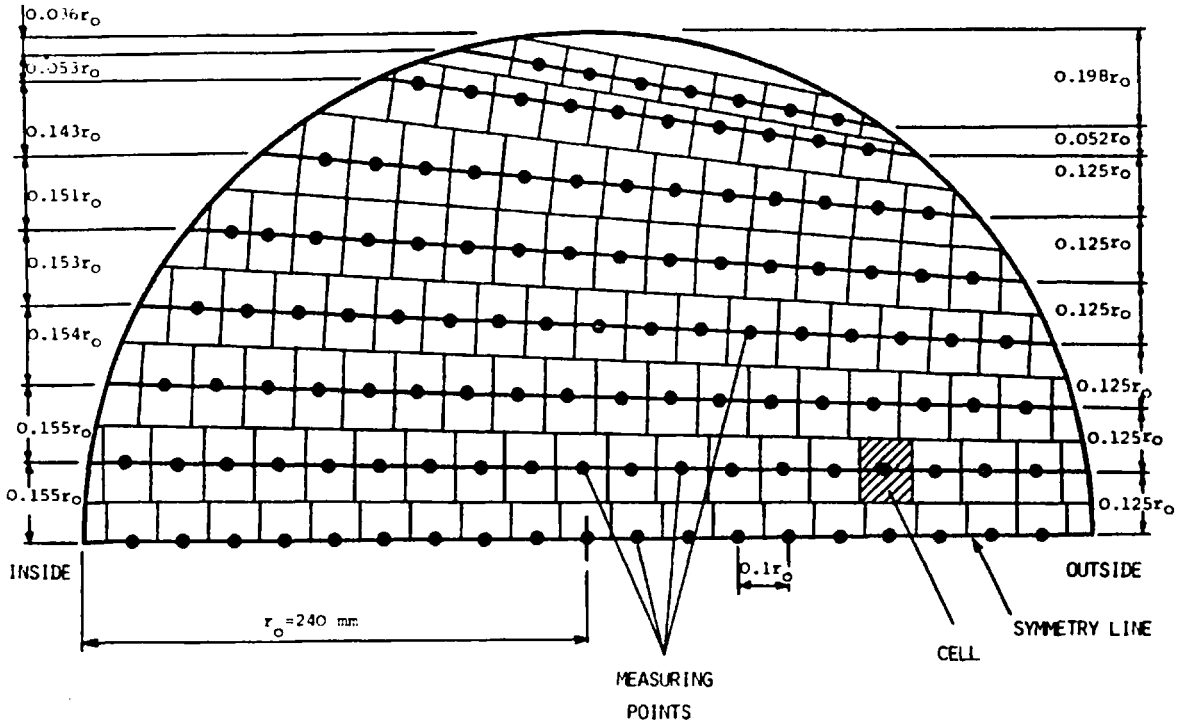


Fig.4.13 Flow measuring locations for the 90 degrees circular bend.

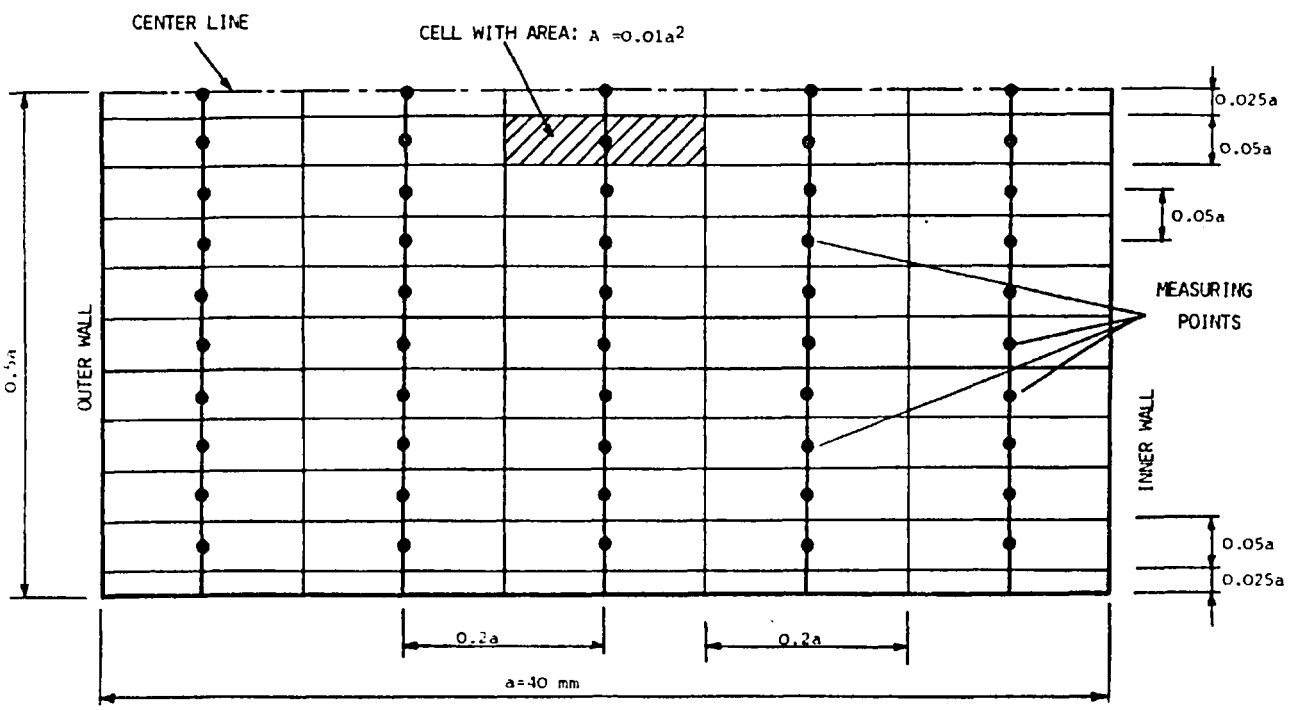


Fig.4.14 Flow measuring locations for the square bend.

4.5 Results And Discussion For Circular Cross Section Bend

4.5.1 Flow Visualization

Observation of hydrogen bubble paths in low speed flow revealed no unusual features such as the local separation reported by Humphrey et al (1977) for fully developed flow through the square section bend. The visual observations were entirely consistent with large scale secondary flow patterns detected by laser Doppler anemometry. Hydrogen bubbles were generated in the flow by a thin wire electrode inserted through the static pressure tappings and the trajectories were photographed with typical results shown in Fig.4.15. Figs.4.15a and 4.15b show bubble paths at the 15° and 30° stations where the inward movement of low velocity fluid in the upper part of the bend is clearly visible. The secondary flow appears to be directed inward at a greater angle at the 15° station than further downstream at 30°. The corresponding outward movement of the core flow is shown by the distinct trace from the electrode tip. Fig.4.15c shows the hydrogen bubble sheet generated near the wall at the 30° station; the flow here is upward and along the wall toward the inside of the bend.

4.5.2 Laminar Flow Measurements

The results of velocity measurements at Re=500 are presented in Figs.4.16 and 4.17. Fig.4.16 shows the inlet conditions: horizontal and vertical velocity profiles 0.58 diameters upstream of the bend. The boundary layer thickness is about 0.27 times the pipe diameter so that there is a significant potential core. The apparent slight asymmetry shown in the results is within the estimated error band. Contours of the streamwise velocity in four cross-stream planes are presented in Fig.4.17, and show the effects of strong secondary flow

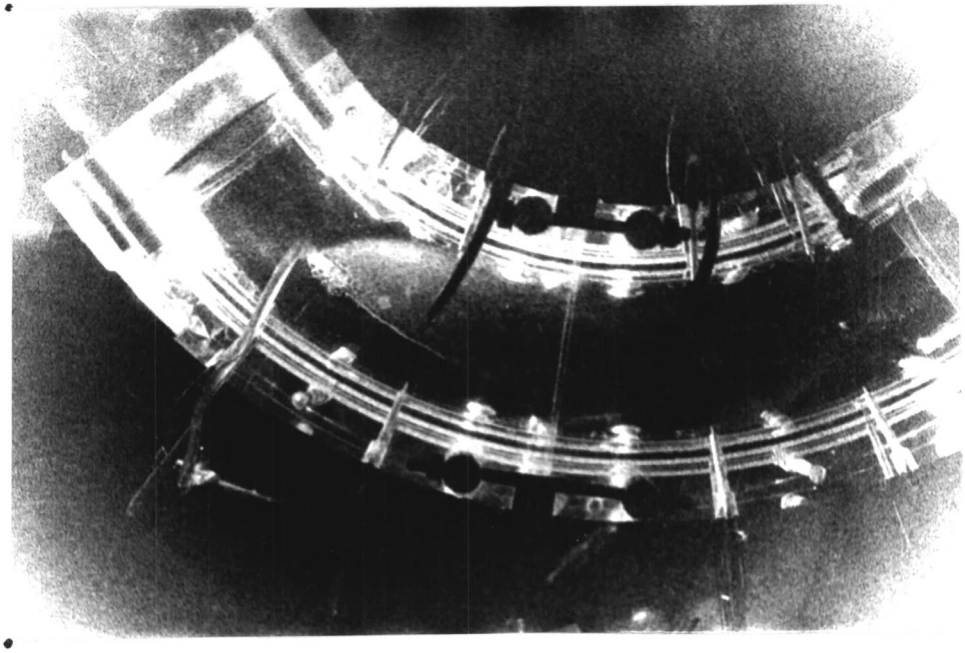


Fig.4.15a Flow visualization: Re=1093. Flow from top left to top right; wire inserted at $\phi=15^{o}$, y/r=0, z/r=1.

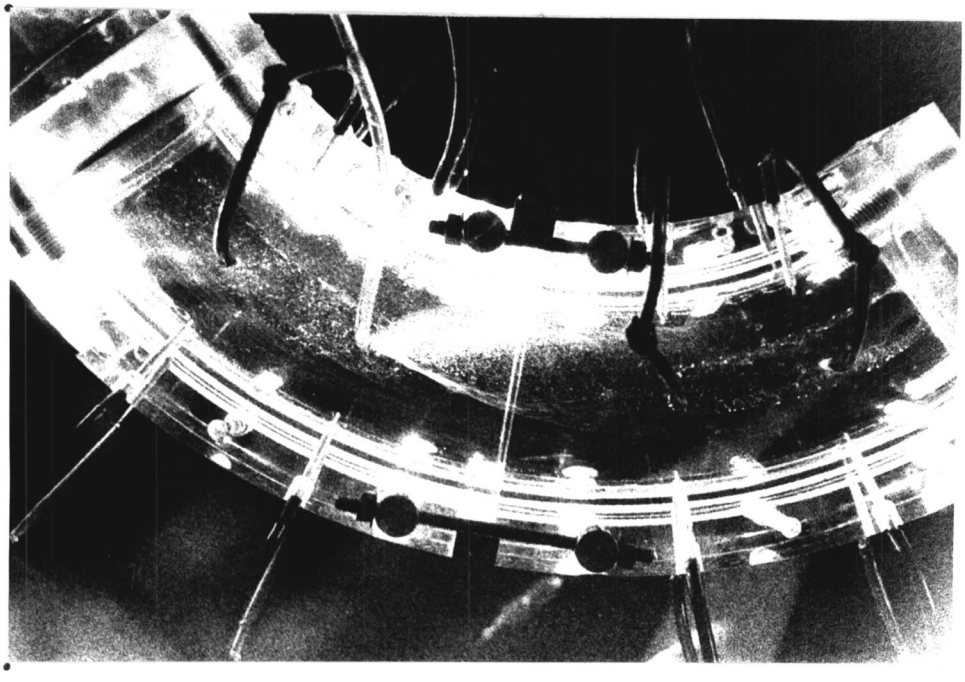


Fig.4.15b Flow visualization: Re=1093. Flow direction from top left to top right; wire inserted at $\phi=30^{o}$, y/r=0, z/r=1.

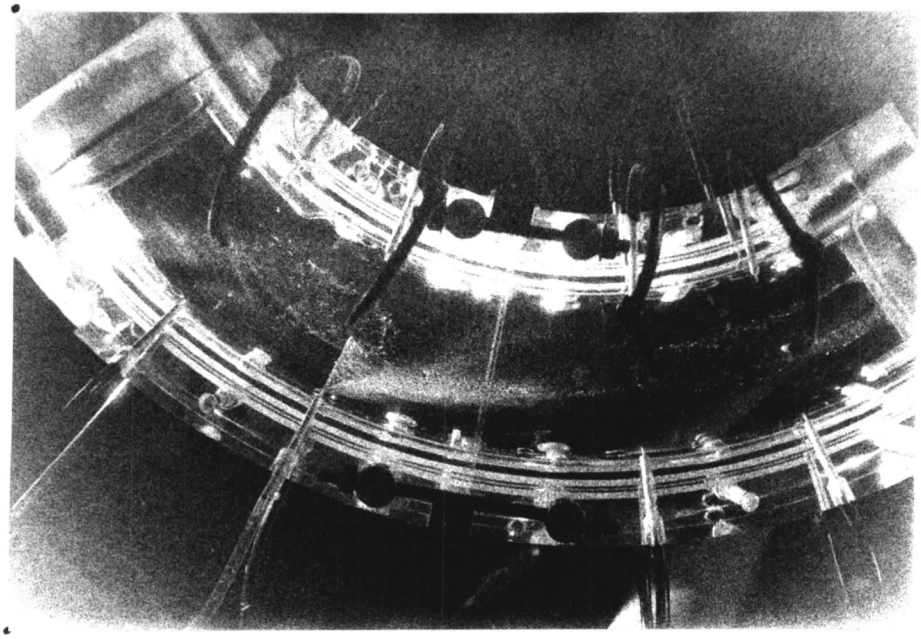


Fig.4.15c Flow visualization: Re=1093. Flow direction from top right to top left; wire inserted at $\phi=30^{\circ}$, y/r=1.0, z/r=0.

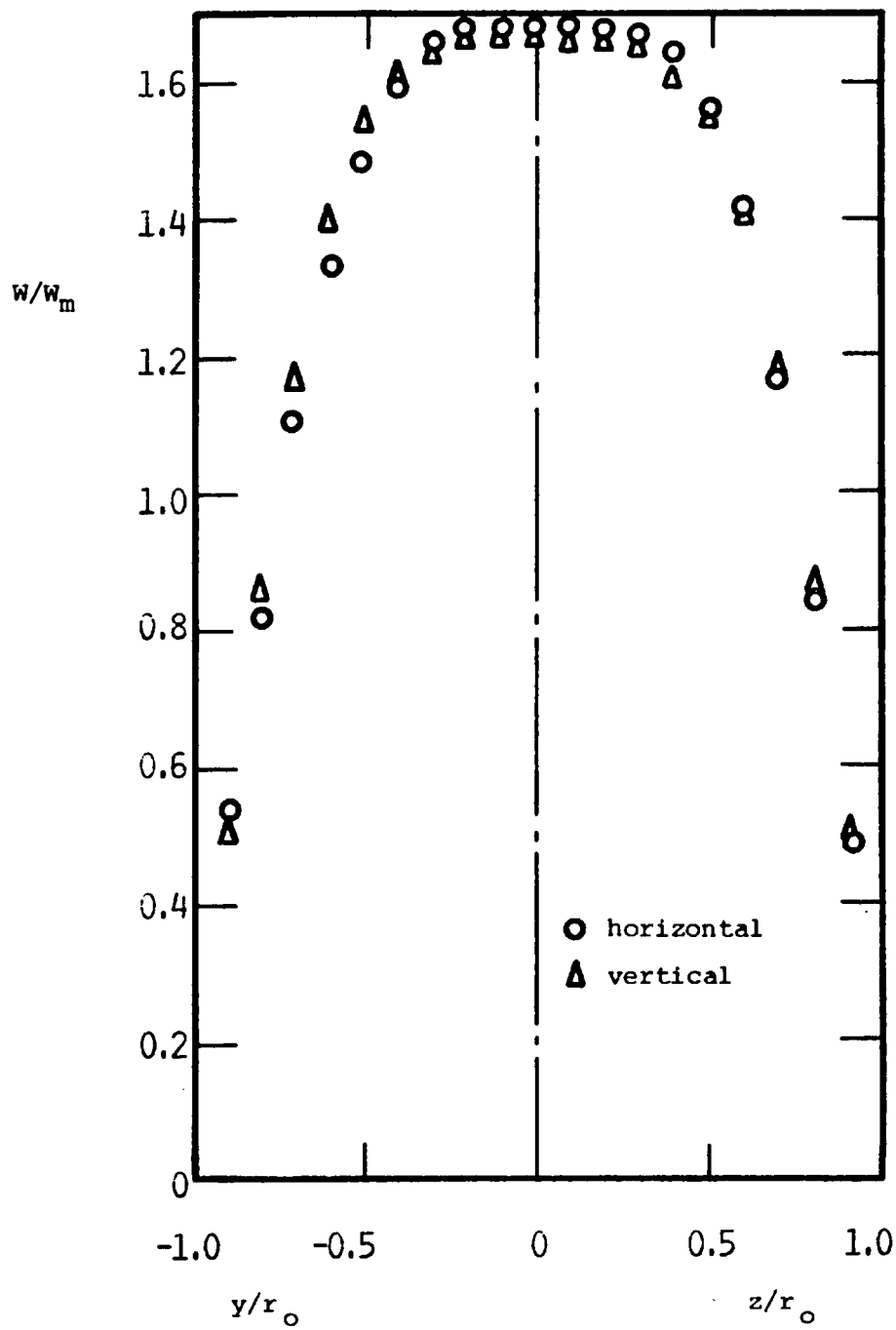


Fig.4.16 Profiles of mean axial velocity in the laminar approach flow 0.58 diameters upstream of the inlet plane. (Re=500)

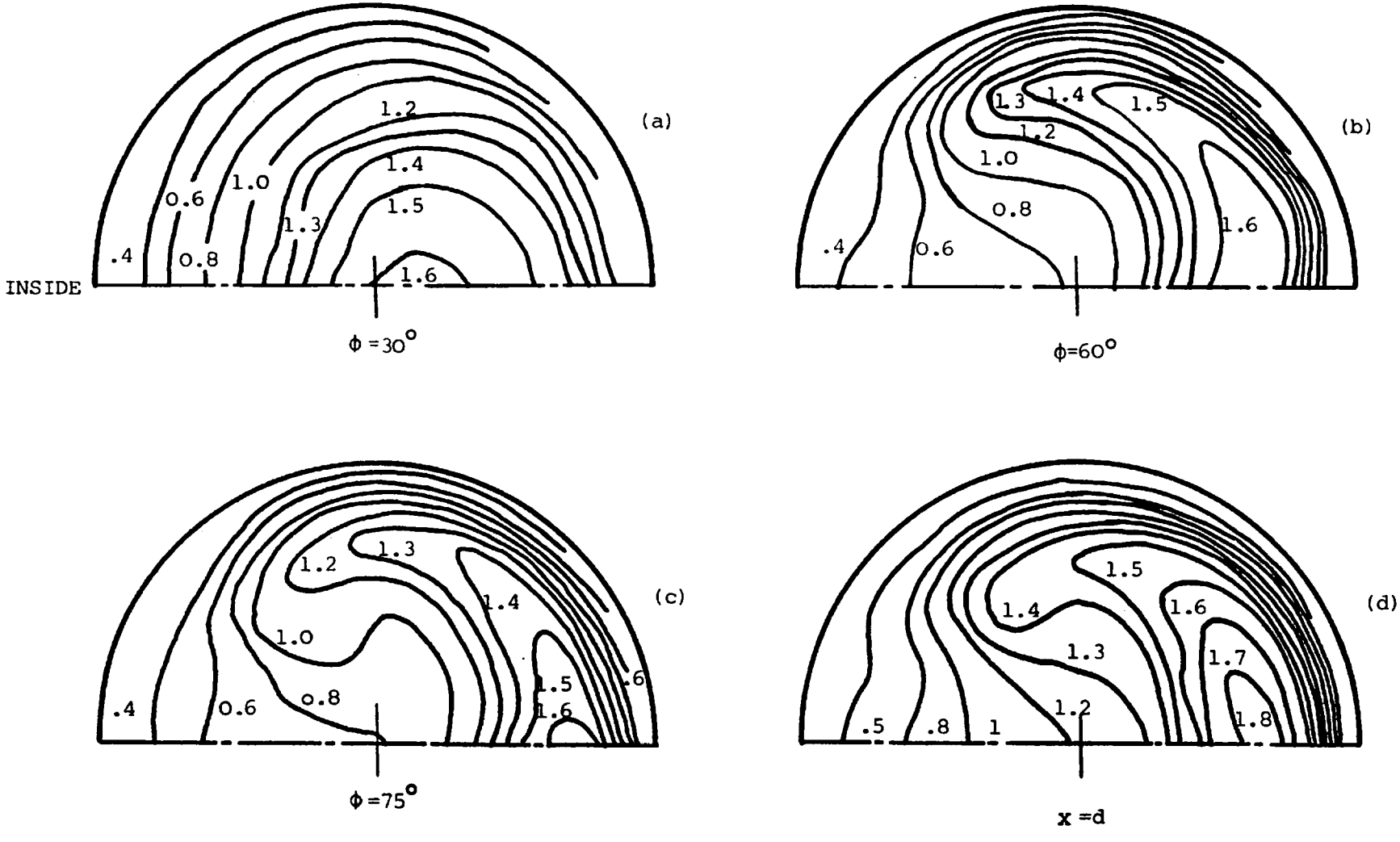


Fig. 4.17 Contours of mean velocity W/W_m in the bend laminar flow.(Re=500)

which displaces the region of maximum velocity to the outside of the bend. The secondary flow develops gradually: in the 30° plane the only visible effect is a thickening of the shear layer on the inside of the bend. By 60° the secondary flow becomes almost fully developed as is shown by the distortion of the contours. The fourth set of contours, in the plane one diameter downstream, shows that the secondary motion persists without significant decay to this distance.

The effect of doubling the Reynolds number to 1093 is shown in Figs.4.18 and 4.19. The inlet boundary layers are reduced in thickness by about 15% to 0.23 d, the transverse pressure gradient is increased and the secondary flow is intensified. The peak velocity in the 30° plane is displaced from the plane of symmetry but remains closer to the centreline. This displacement, which persists downstream, is also observed in the flow in a square bend (Taylor et al 1981). The shape of the contours near the outside of the bend reflect scatter in the data attributable mainly to difficulties in locating accurately the measurement volume near the wall and partly, perhaps, to slight asymmetry in the flow.

In neither case do the measurements show any unexpected feature: the secondary flow is superimposed on the main motion; it develops gradually and persists downstream after the removal of the transverse pressure gradient responsible for its generation in the bend. The strength and location of the pressure-driven secondary flow depend on the inlet conditions and Re which cannot be varied independently in the present experiments. The stronger secondary flow observed at Re=1093 must be attributable mainly to the increased centrifugal forces and transverse pressure gradient rather than to the relative small changes noted in the initial conditions. The present

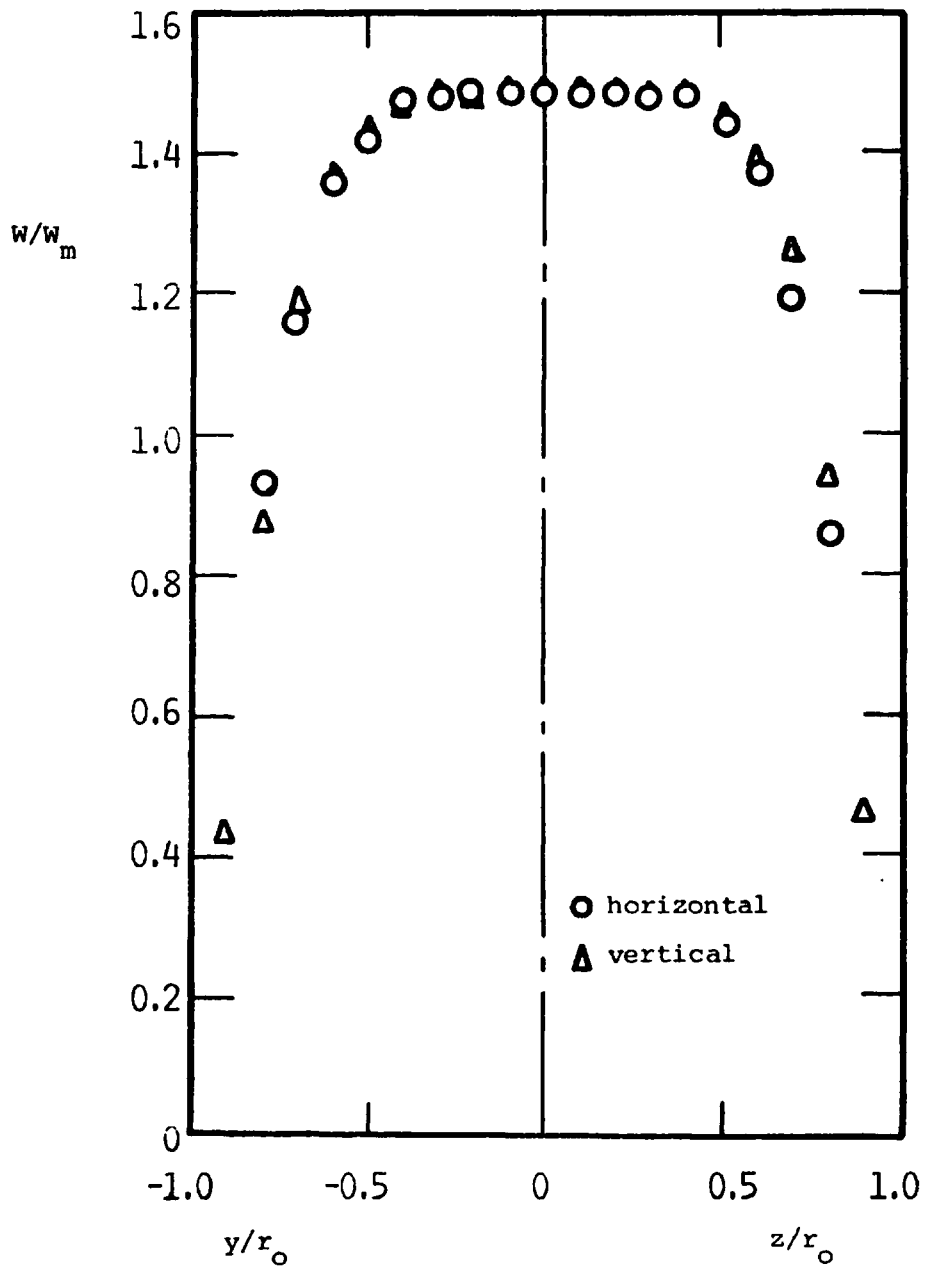


Fig.4.18 Profiles of mean axial velocity in the laminar approach flow 0.58 diameters upstream of the inlet plane.
(Re=1093)

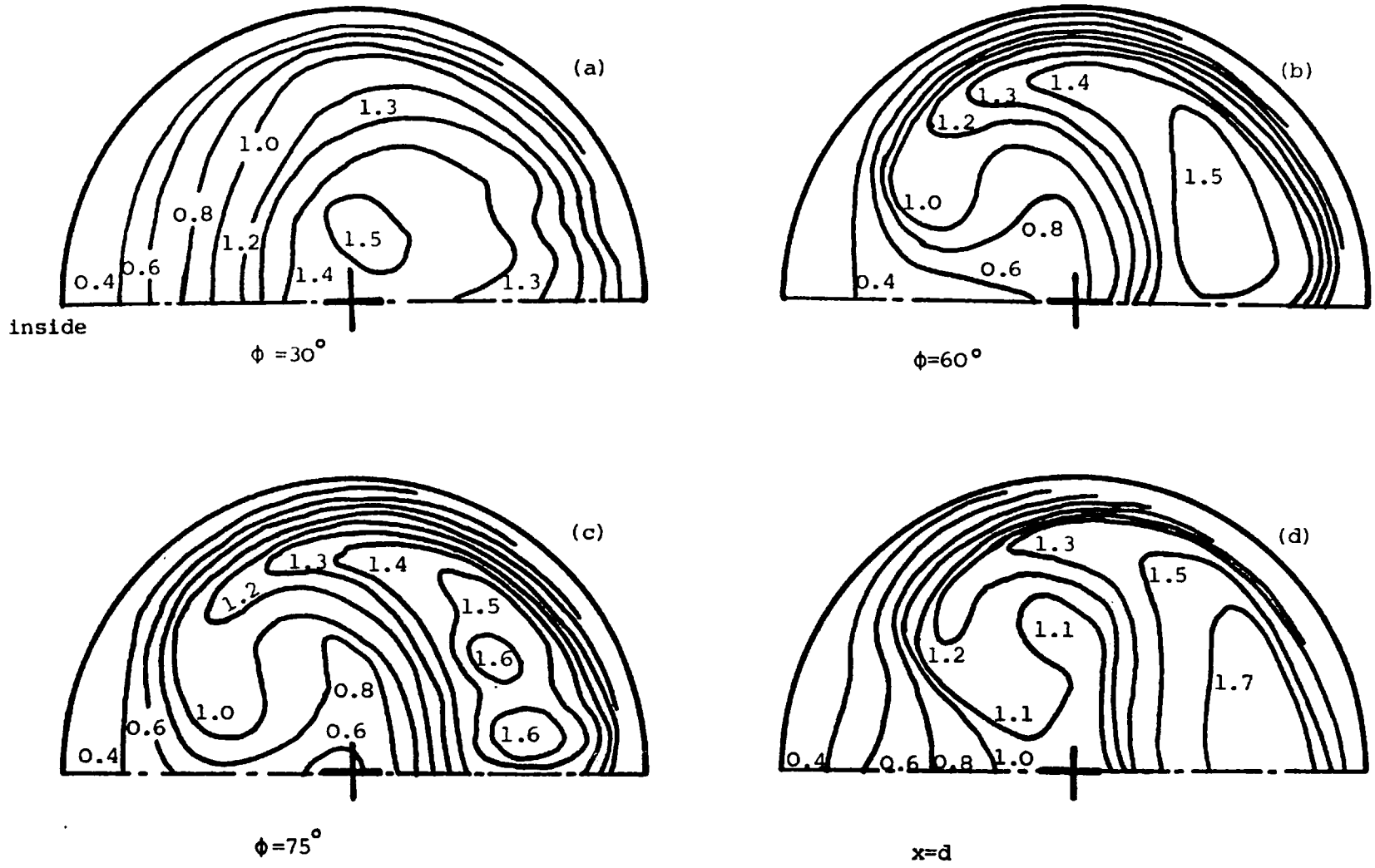


Fig.4.19 Contours of mean velocity W/W_m in the bend laminar flow.(Re=1093)

contribution is of quantitative velocity data in the bend: these are considered to be accurate enough to be useful in checking the numerical accuracy of flow prediction methods.

4.5.3 Turbulent Flow Measurements

At the maximum flow velocity of 0.92 m/s, Reynolds number 43000, the inlet boundary layers are turbulent. The static pressure variation on the bend wall is large enough to be measured accurately with the results shown in Fig.4.20. At the bend inlet the negative pressure gradient on the inner wall is roughly twice the positive gradient on the outside. These initial gradients resulting from the change from straight to curved flow disappear at about 25°, so that in the mid-section of the bend ($25^{\circ} < \phi < 75^{\circ}$) a quasi equilibrium condition is reached with an almost uniform pressure on the inner and outer walls. The transition to straight flow downstream is signalled by the appearance of strong gradients for $\phi > 75^{\circ}$. The overall pressure drop is about $0.3\rho W_m^2$.

Laser Doppler measurements of the mean and rms fluctuation of the streamwise velocity at inlet are shown in Fig.4.21, and contours of these quantities at downstream stations are shown in Figs.4.22 and 4.23. The inlet boundary layers of Fig.4.21 are much thinner, 0.09d, than in the two laminar flows investigated and the presence of a large central region of uniform velocity flow influences significantly the development of secondary flow downstream. The mean velocity contours presented in Fig.4.22 show that by the 30° plane the potential core has adjusted to the cross-stream pressure gradient imposed by the bend and the region of maximum velocity is displaced toward the inside. The results also differ from the corresponding laminar flow

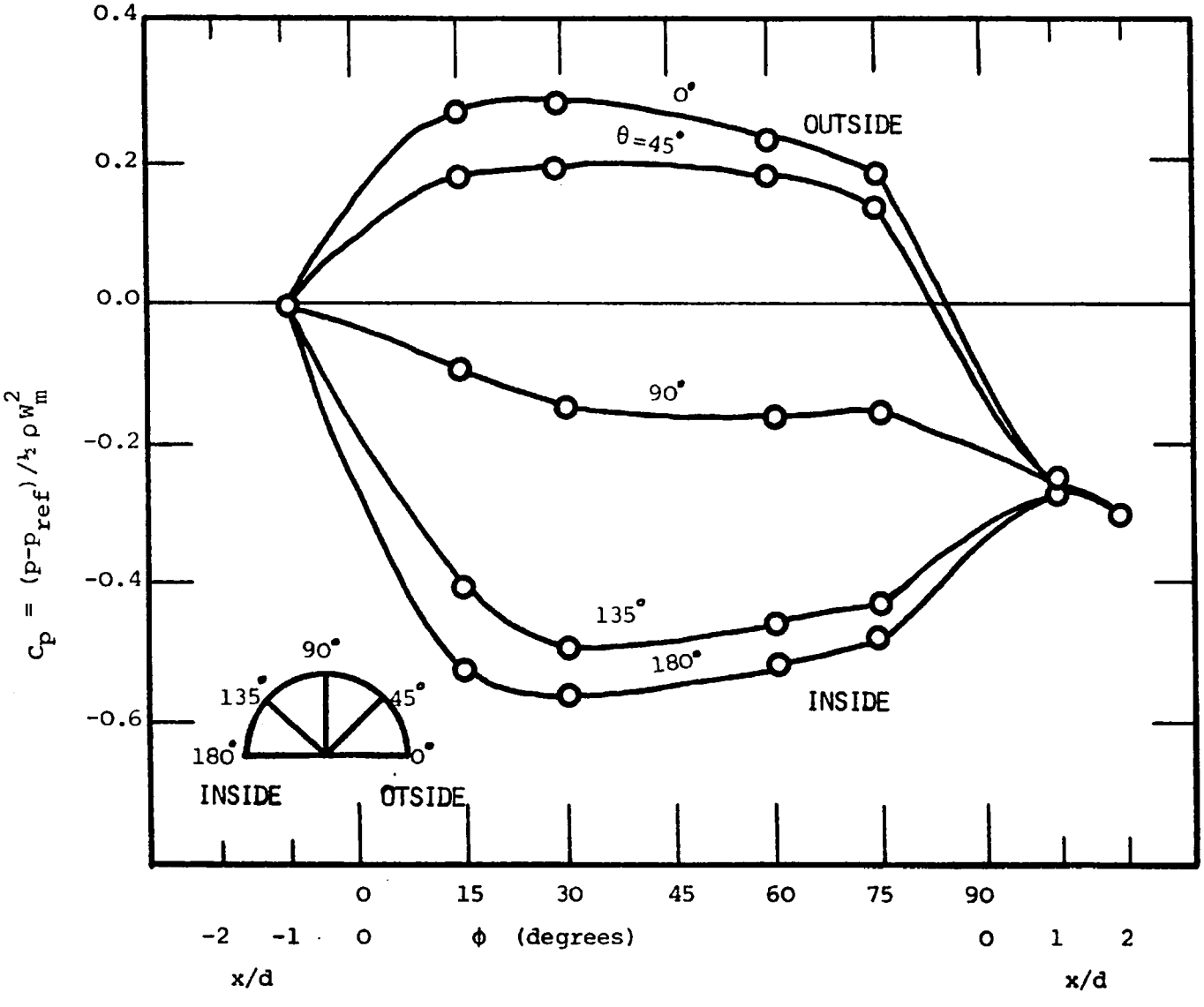


Fig.4.20 Wall static pressure variation for turbulent flow. (Re=43 000)

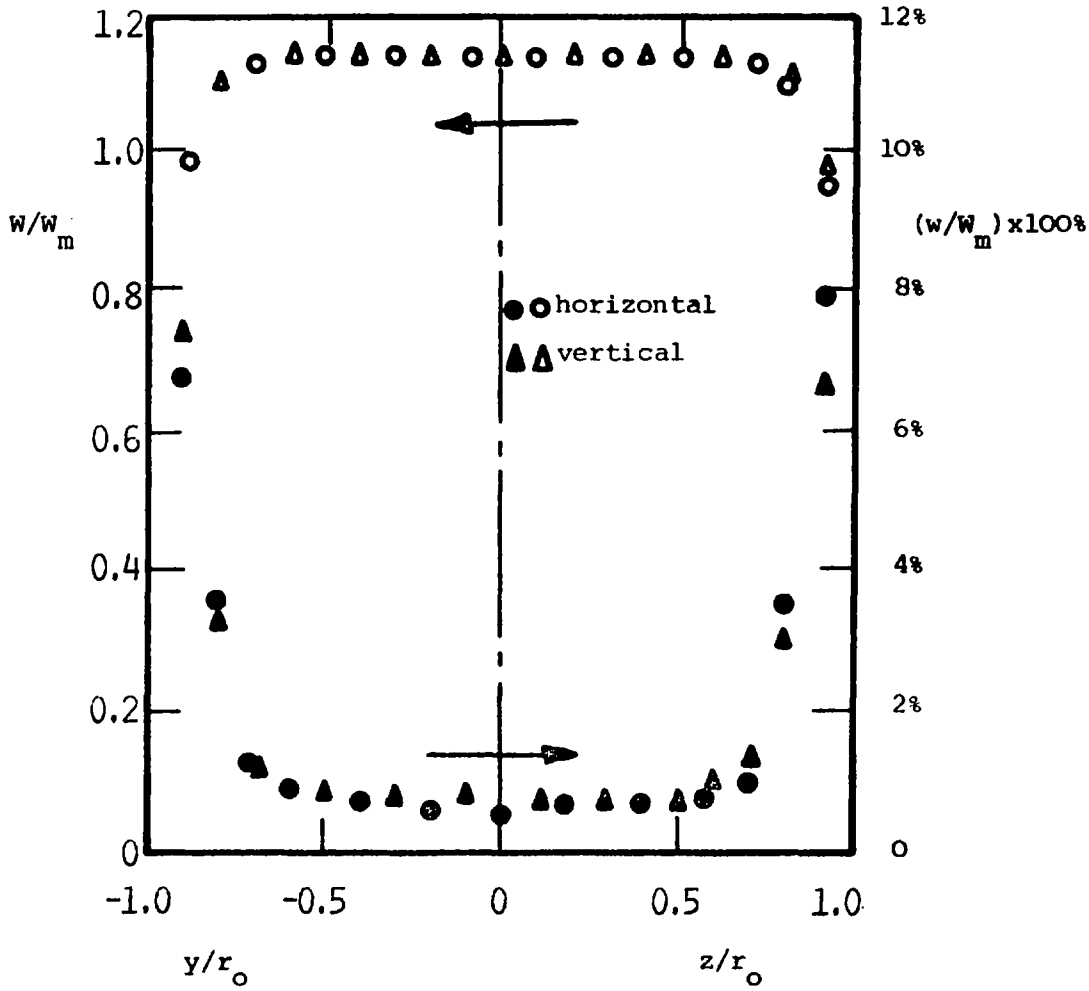


Fig.4.21 Profiles of mean axial velocity W/W_m and turbulence intensity w/W_m in the turbulent approach flow 0.58 diameters upstream of the bend.
(Re=43 000)

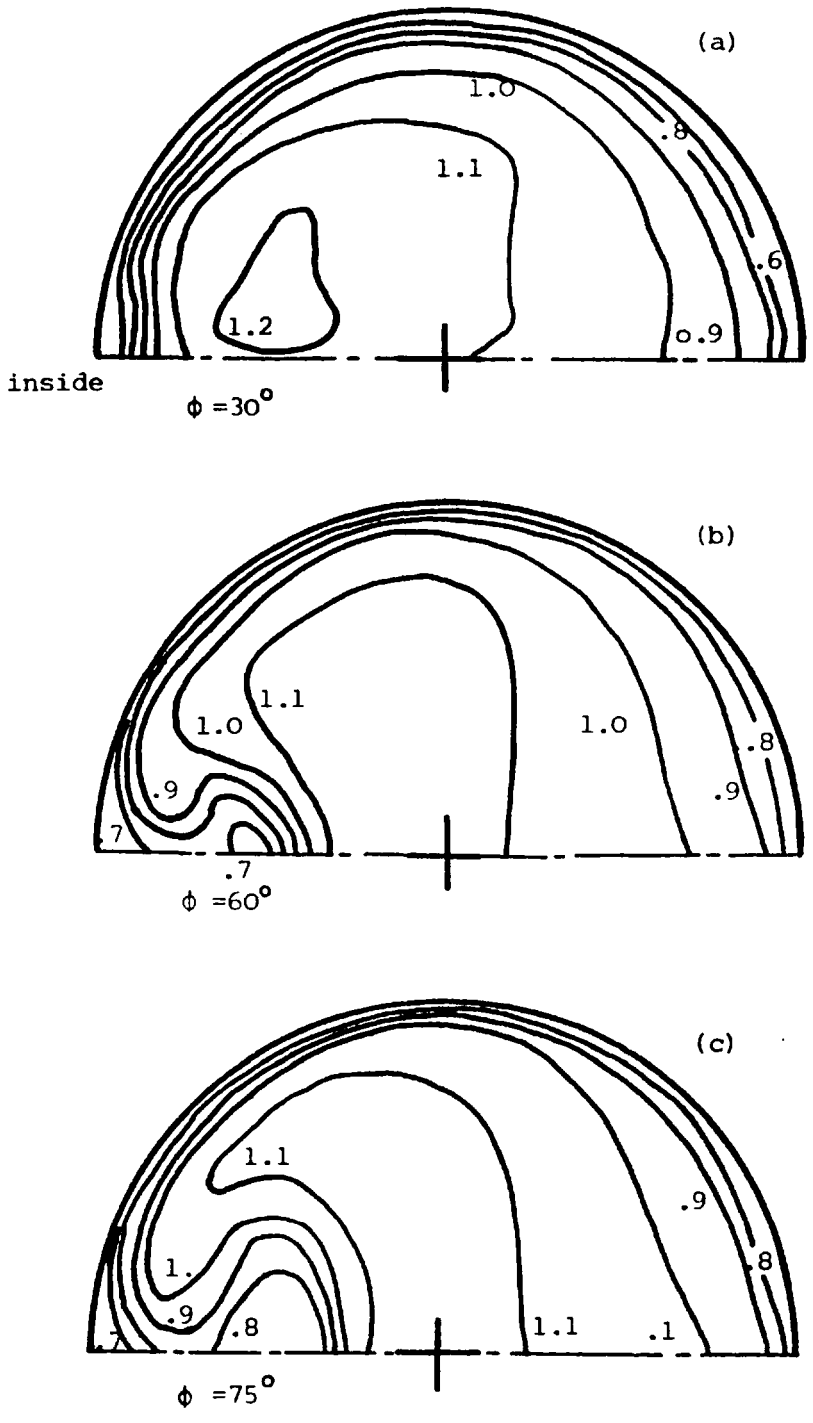
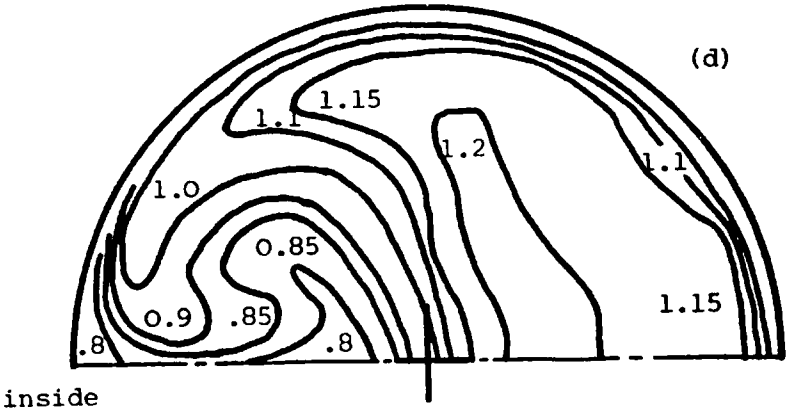


Fig.4.22 (a)-(c) Contours of mean axial velocity W/W_m in the bend for turbulent flow.
(Re=43 000)



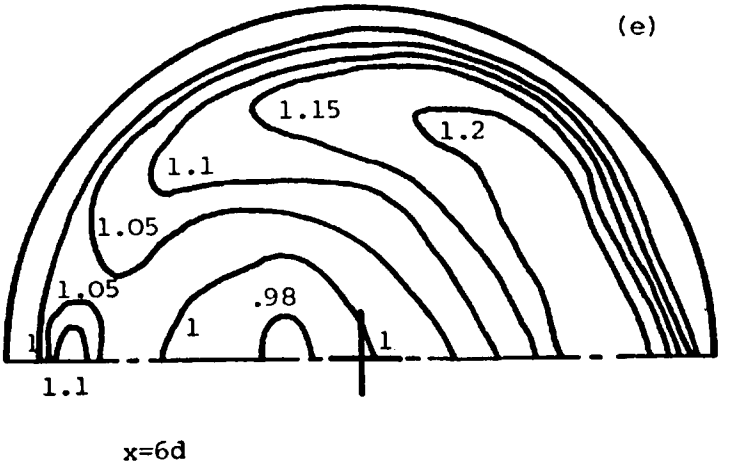


Fig.4.22 (d)-(e) Contours of mean axial velocity W/W_m downstream of the bend for turbulent flow.
(Re=43 000)

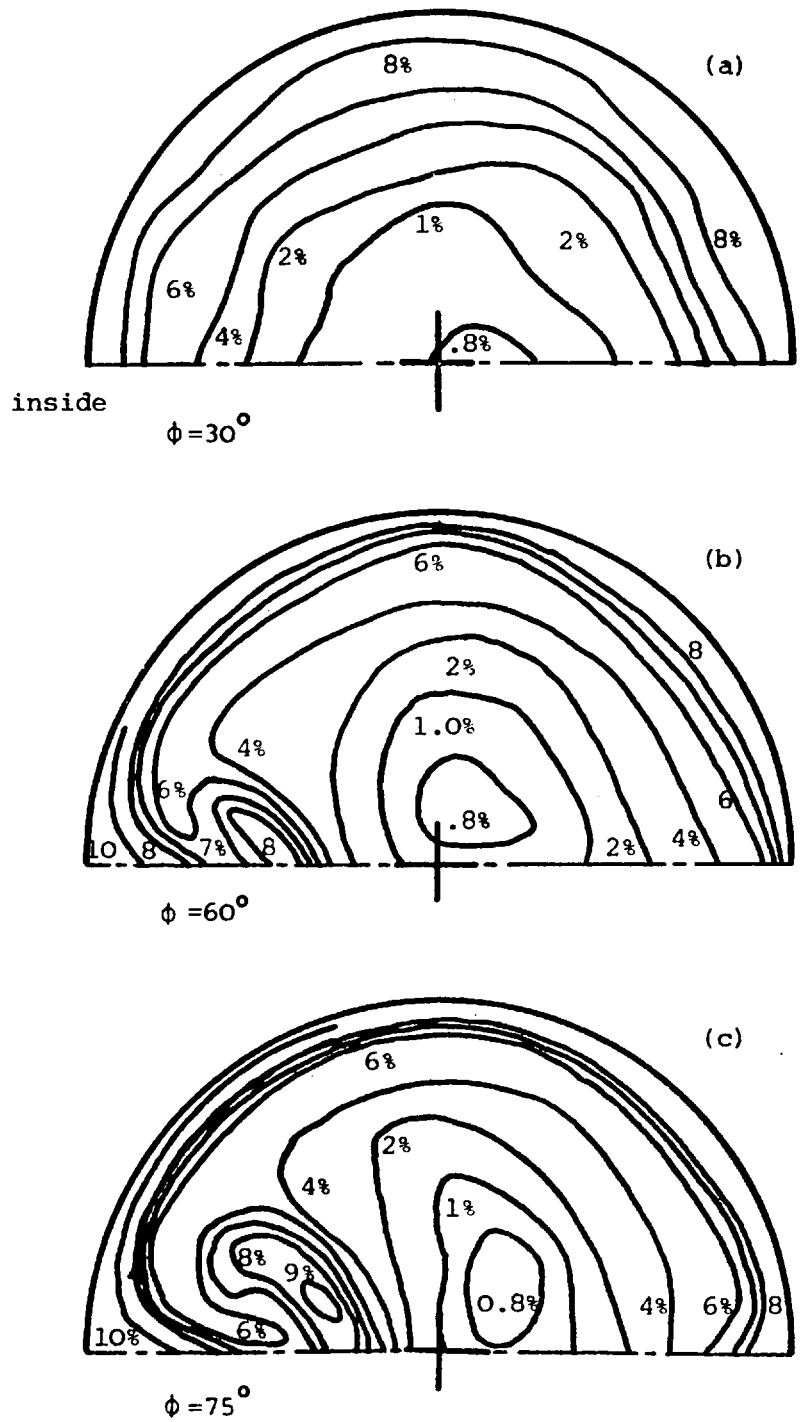


Fig.4.23 (a)-(c) Contours of turbulence intensity $(w/W_m)x100\%$ in the bend for turbulent flow.
(Re=43 000)

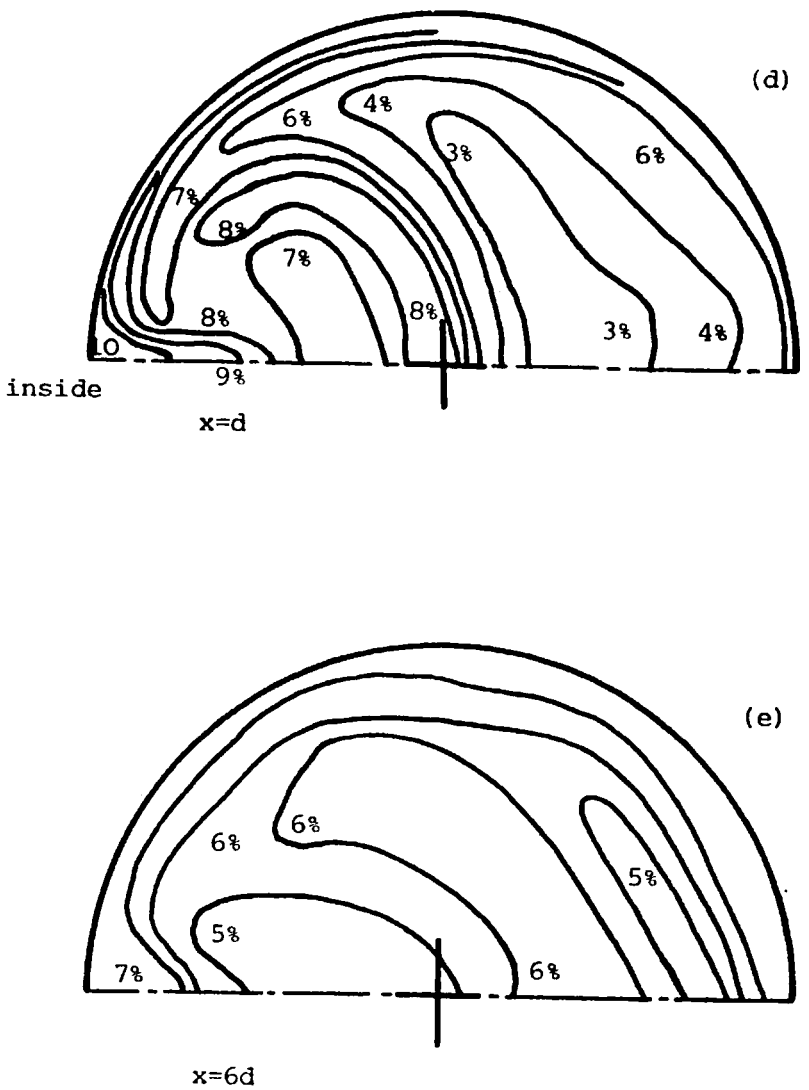


Fig.4.23 (d)-(e) Contours of axial turbulence intensity $(w/W_M)x100\%$ downstream of the bend for turbulent flow. (Re=43 000)

measurements in that the thickness of the outer wall boundary layer is increased relative to that on the inside of the bend due mainly to the effects of the potential flow adjustment and the wall pressure gradient of opposite sign but also, quite possibly, to the effects of longitudinal curvature on the turbulence structure. In the 60° plane distortion of the contours suggests the presence of strong secondary flow largely confined to the region of steep velocity gradients near the inner wall. This secondary flow grows with distance through the bend and by the 75° plane extends over and beyond the inner half of the section. The removal of the transverse pressure gradient in the straight flow downstream results in a shift of the velocity maximum toward the outside. A large secondary flow, comparable with those observed in the laminar flow experiments, now extends over the entire flow area and persists in the plane 6 diameters downstream of the bend where, however, the transverse velocity gradients decay to about one half of their values one diameter downstream.

The contours of turbulence intensity presented in Fig.4.23 are consistent with those of mean velocity. As is to be expected high values of the velocity fluctuation are associated with steep mean velocity gradients and with the distortion of the symmetrical inlet flow.

These results may be compared with the measurements made by Humphrey et al (1981) in a tight bend of square cross-section. The inlet boundary layers of that flow are substantially thicker than in the present flow and contain stress-driven secondary flows towards the corners. As a result the pressure-driven secondary flow in the bend extend over the entire flow area as in the two laminar flows of the present study.

4.5.4 Closure

The measurements show , as expected, the presence in bend flow of strong cross-stream flows produced by the inward motion of slow moving fluid in a radial pressure gradient. The strength of the secondary flow is influenced by the initial inlet flow conditions: when the inlet boundary layers are thin, as in the turbulent flow case reported here, the initial flow adjustment is an inward shift of the velocity peak in the potential core. The secondary flow then develops initially in the inside of the bend. For all cases the secondary flow takes some time to develop and its effects are still increasing by the exit and persist downstream.

The effects of refraction at the doubly curved fluid-wall interface prevent the measurement of cross-stream velocity components. The investigation of flows in the round bend to the same level of detail as is achieved previously in square bends will require refractive index matching. For the streamwise velocity measurements reported here simple geometrical corrections allowed for the displacement of the measurement volume by refraction as shown in Appendix A5.

4.6 Results And Discussion For Square Cross Section Bend

Because the flow is symmetrical, only the lower half of the duct need be considered; the measurements locations are shown in Fig.4.13.

The bulk velocity was 0.88m/s giving Re=35200 (based on the bulk velocity and duct width). The boundary layers in the bend inlet plane were turbulent and about 0.14 duct widths thick. Measurements were made in 45° and exit (90°) planes, the optical axis being vertical.

The results consist of the streamwise and radial mean velocity components W and V, the corresponding turbulence intensities w and v and the Reynolds shear stress $\overline{wv}$. Measurements in the inlet plane for Re=40000 were made by Taylor et al (1981) when an S bend was fitted to the water rig. It was supposed that the inlet conditions did not differ significantly in the present bend flow and the data from Taylor et al (1981) are reproduced in Fig.4.24. These show fairly uniform inlet boundary layers with an appreciable potential core. The radial component of the mean velocity, which is not presented, nowhere exceeded 0.07 W_m and the shear stress levels, also not presented, appear to be consistent with the intensities, but the boundary layers are too thin for more detailed measurements of the cross-correlation in the high shear regions adjacent to the walls. The measurementss in the 45° and exit planes, presented in Fig.4.23 to Fig.4.27, may usefully be compared with the equivalant data from the more stongly curved bend reported by Humphrey et al (1981) and Taylor et al (1981). As in the previous experiments, the flow responds in two ways to the imposition by the bend of a radial pressure gradient. Initially, the peak velocity in the core moves towards the inside of the bend as required for radial equilibrium in the centre, but further downstream the development of secondary flows results in a shift of this peak to the outside region. Both these effects are very evident in the tight bend flow, see Humphrey et al (1981) and Taylor et al (1981), but the former is not apparent in the present measurements where the transverse pressure gradients are considerably smaller and less influential. The secondary flows, whose presence is evident in the mean velocity contours at 45°, effectively displace the velocity maximum to the outside of the bend and result in an accumulation of slow moving fluid on the inner wall. The inward flow at the side

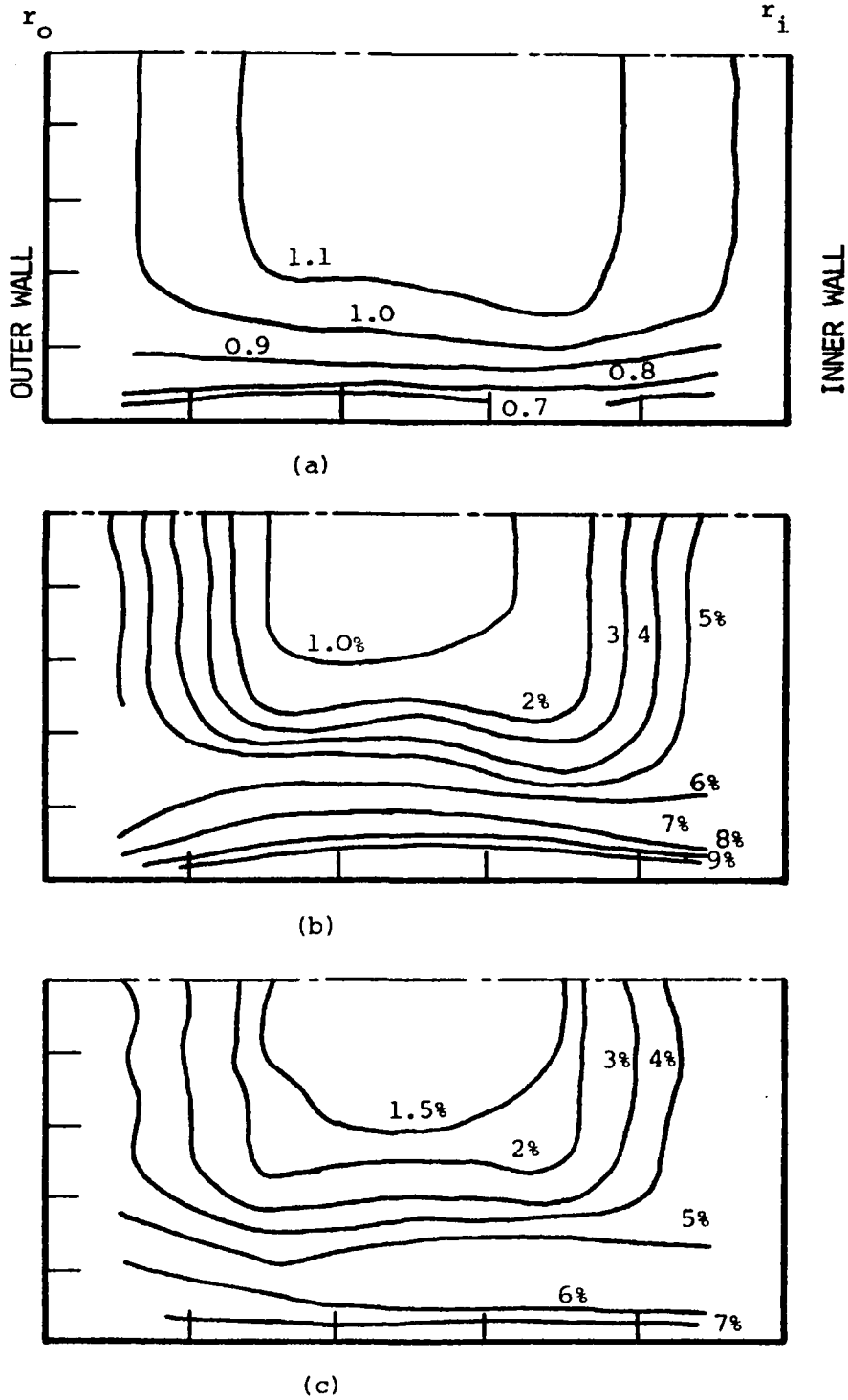


Fig.4.24 Contours of mean axial velocity and rms turbulence intensity in the inlet plane of the square duct.

(a) axial velocity W/W_m

(b) axial turbulence intensity $(w/W_m)\times 100\%$

(c) radial turbulence intensity $(v/W_m)\times 100\%$

(Data from Taylor, Whitelaw and Yianneskis, 1981 for Re=40 000)

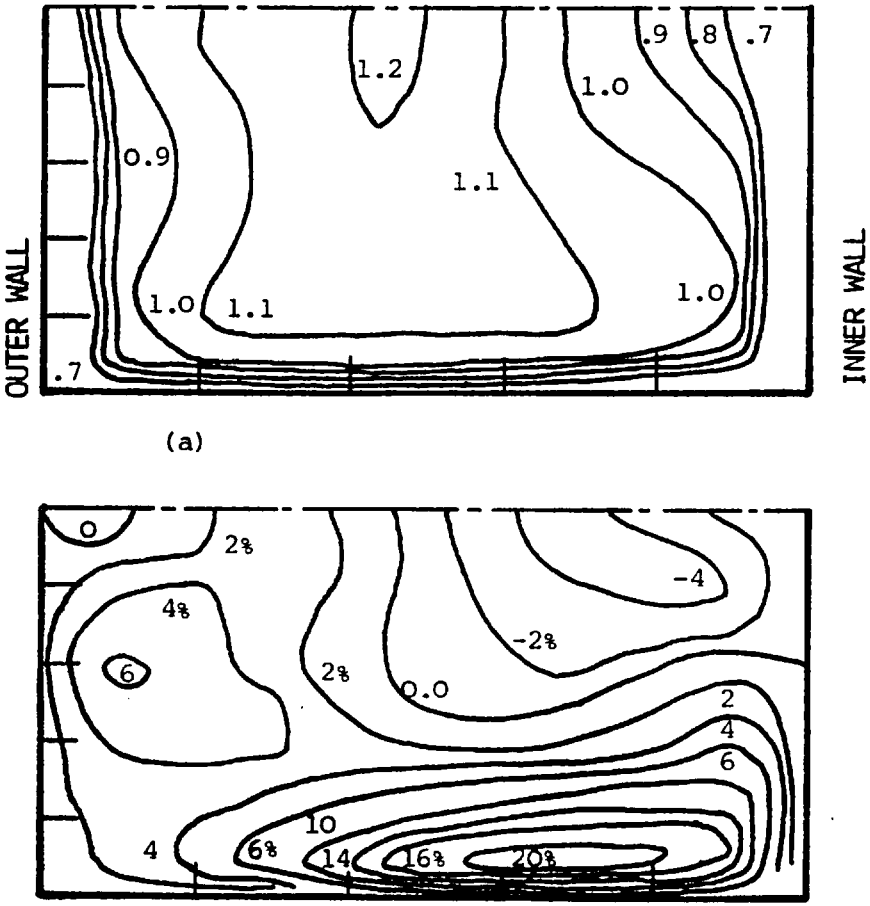


Fig.4.25 Contours of mean velocity in the 45 degree plane:
(a) axial velocity component W/W_m
(b) radial velocity component $(V/W_m)x100\%$
(Re=43 000)

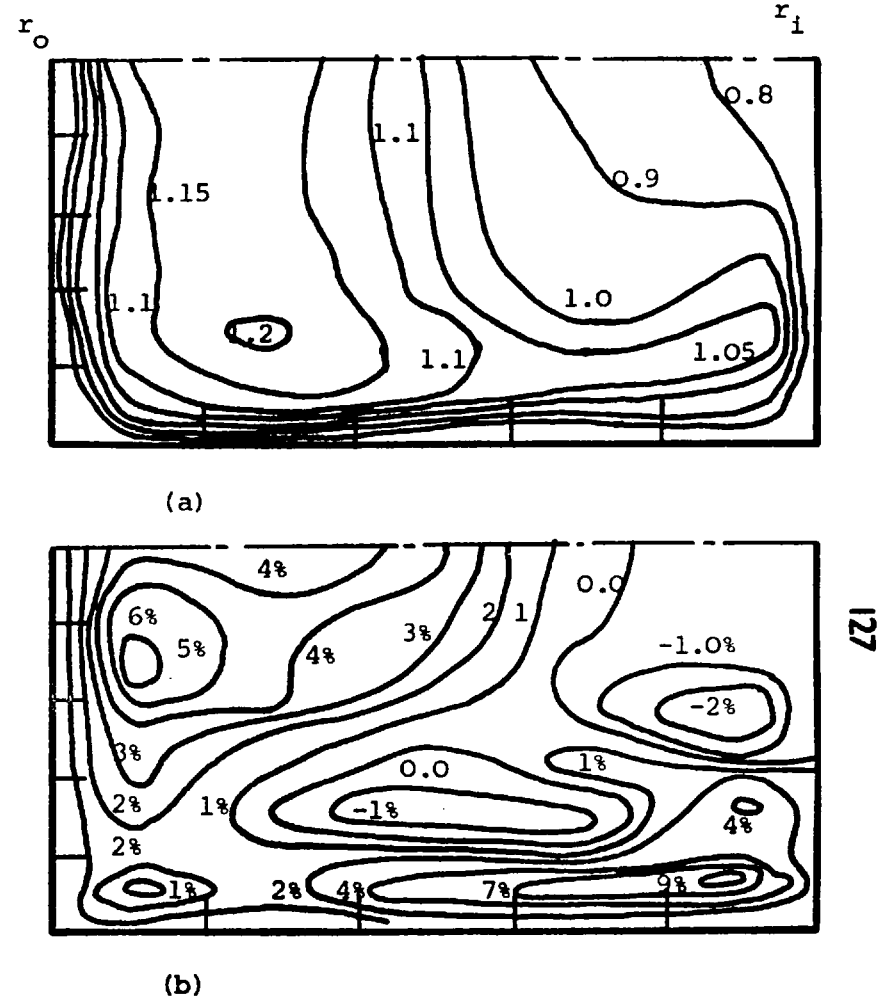


Fig.4.26 Contours of mean velocity in the exit plane; 90 degree plane:
(a) W/W_m (b) $(V/W_m)x100\%$
(Re=43 000)

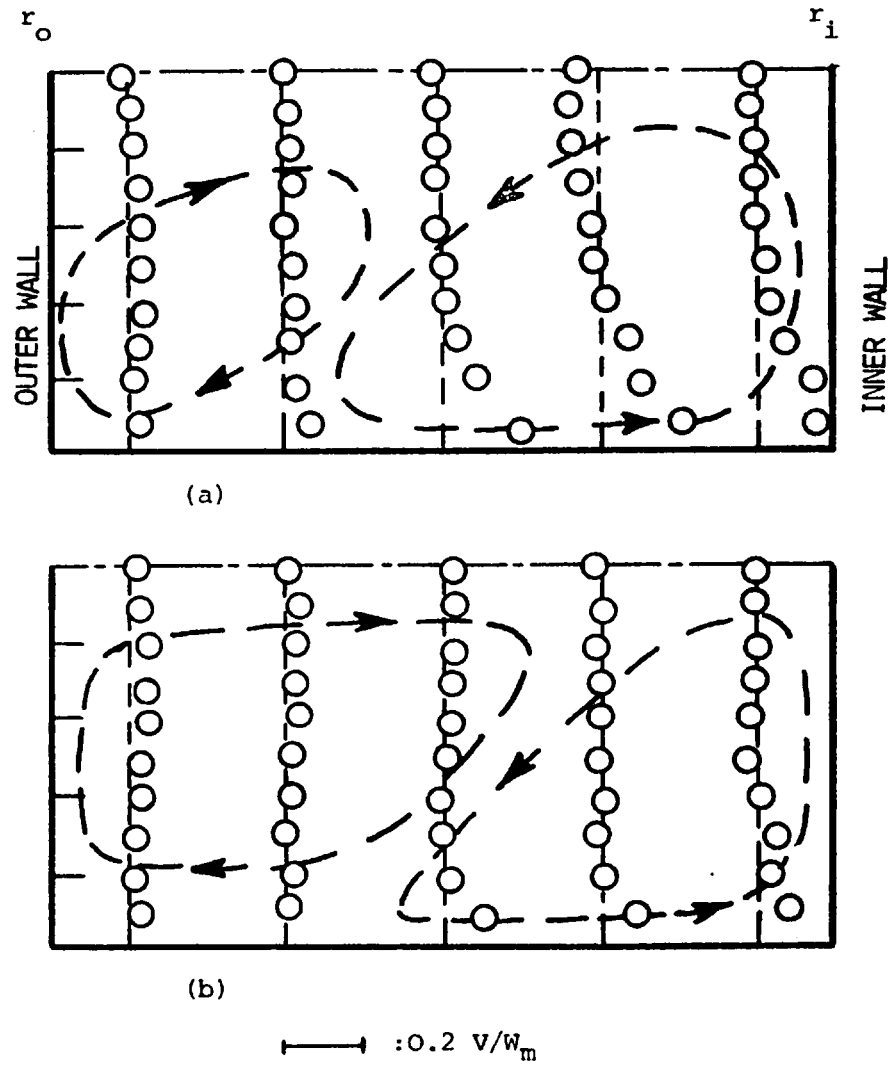


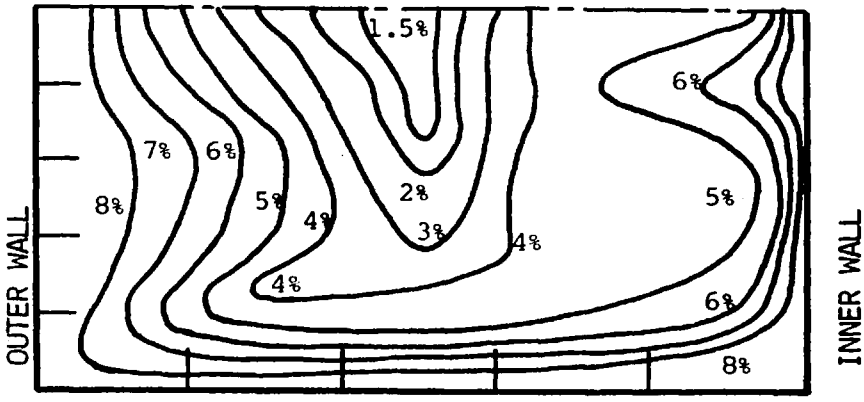
Fig.4.27 Profiles of radial velocity V/W_m for turbulent flow (Re=43 000):

(a) 45 degree plane

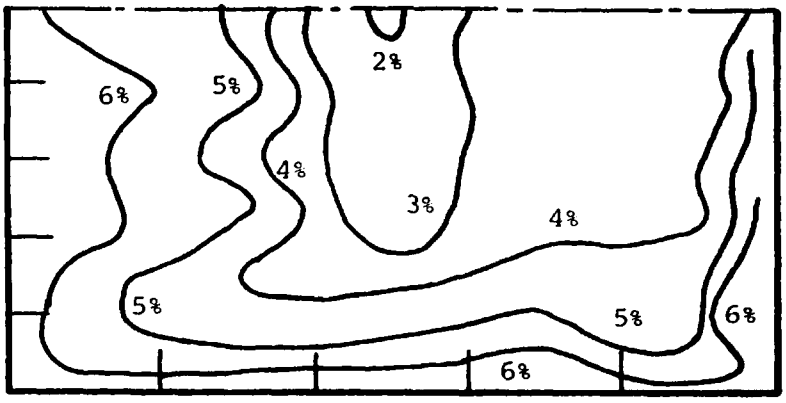
(b) 90 degree plane

walls ensure that the boundary layers there remain thin. As the flow approaches the bend exit, it is accelerated on the outer wall and retarded on the inner one. The adjustment to rectilinear flow is rapid: the measurements of Fig.4.26 show that in the exit plane the transverse mean velocities fall to roughly half their values at 45°, while the much-distorted contours of W simply record the history of the flow. Profiles of the transverse component V, plotted in Fig.4.25, show strong inward flow in the inner part of the duct, and also suggest the presence of a weak secondary circulation of the opposite sense in the outer part of the duct. These circulations, presumably, arise from the destabilising action of concave curvature on the outer wall boundary layer, and persist because the curvature is sufficiently mild for it not to be swept into the main pressure-driven secondary motion of the opposite sense. Weak secondary circulations of this nature are also reported in Rowe (1970) and Cheng, Nakayama and Akiyama (1979).

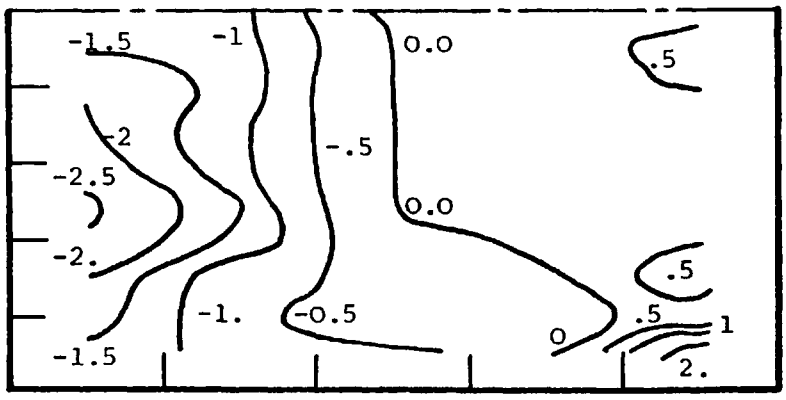
Contours of the rms turbulence intensities w and v and the Reynolds shear stress $\overline{wv}$ are plotted in Figs.4.28 and 4.29. The distortion of the nearly symmetrical inlet contours, Fig.4.24, is very evident and generally consistent with the development of local high shear zones in the mean flow. The high level of v measured near the inner corner in the exit plane are rather surprising, and is in contrast with the strong curvature results of Humphrey et al (1981), where peak values of v, of the same order as w are distributed in the outer part of the exit plane. The shear stress plots contain less detail but show higher levels on the whole near the inside of the bend consistent with high shear and turbulence activity there. There appears to be no evidence of significant damping or amplification of



(a)



(b)



(c)

Fig.4.28 Turbulence measurements in the 45 degree plane:
(a) axial turbulence intensity $(w/W_m)x100\%$
(b) radial turbulence intensity $(v/W_m)x100\%$
(c) shear stress $(\overline{vw}/W_m^2)x10^3$
(Re=43 000).

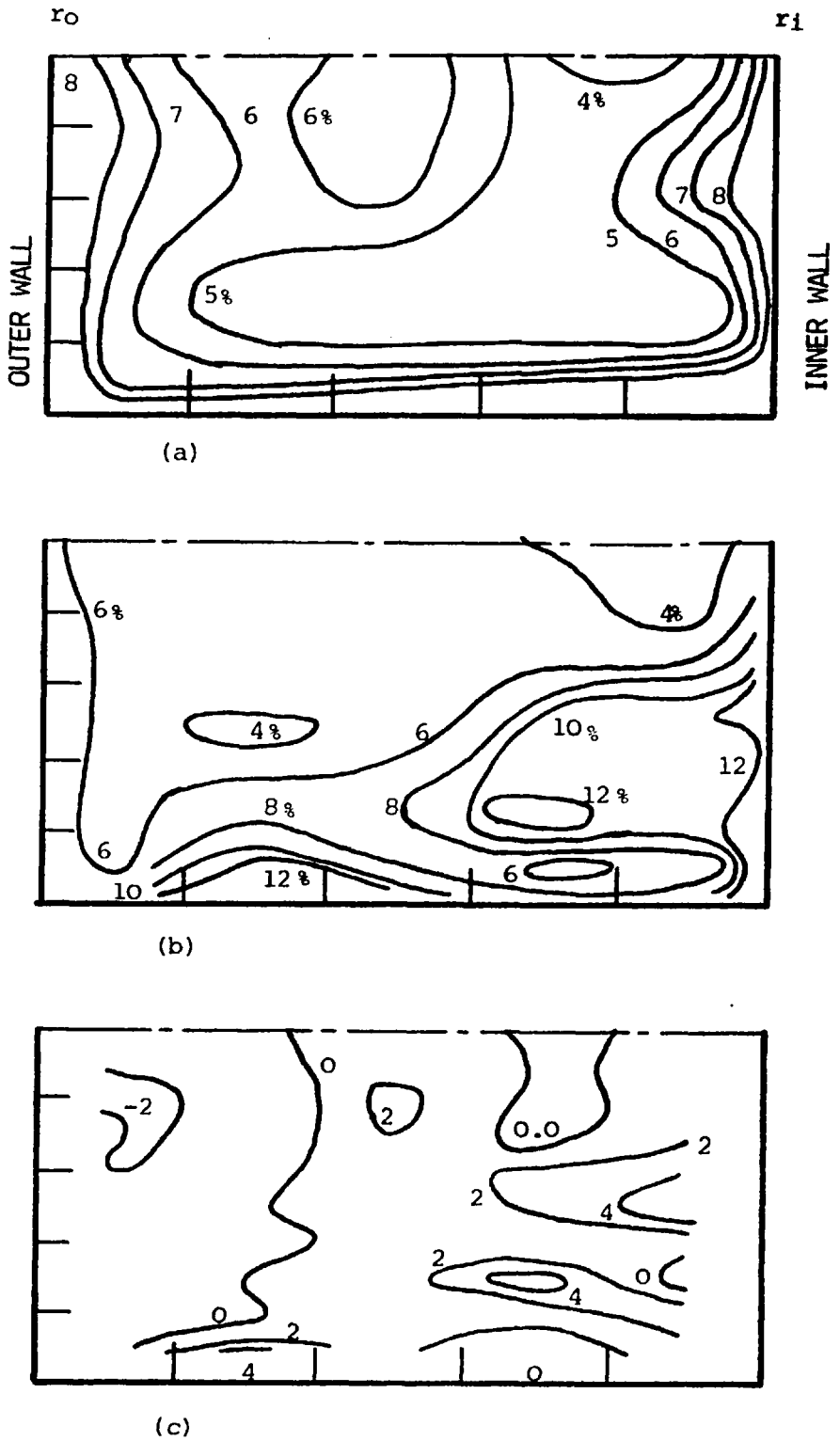


Fig.4.29 Turbulence measurements in the exit plane; 90 degrees:

(a) axial turbulence intensity $(w/W_m)x100\%$

(b) radial turbulence intensity $(v/W_m)x100\%$

(c) shear stress $(\overline{vw}/W_m^2)x10^3$

(Re=43 000)

turbulence due to longitudinal curvature as observed in the strongly-curved bend by Humphrey et al (1981) and the position of zero shear stress coincides approximately with that of the maximum mean velocity.

CHAPTER 5

PREDICTION OF FLOW THROUGH ROTATING DUCTS

5.1 Laminar Flow

5.1.1 Laminar Isothermal Flow

We consider laminar flow of a uniform-property fluid. U, V and W are velocity components in the tangential, radial and axial directions respectively as shown in Fig.1.1. The equations of motion given by Morris (1965) are reproduced in Appendix A1. The effects of rotation appear in radial and tangential momentum equations as Coriolis and centripetal acceleration terms. Elimination of the pressure-gradient terms between radial and tangential momentum equations shows that the Coriolis terms can sustain a secondary flow in the (r,θ) plane if $\partial W/\partial z$ is non-zero; that is if the flow field is still developing (Morris and Woods 1977). For fully-developed flow, $\partial W/\partial z=0$, secondary flow is not induced and the Coriolis terms are identically zero (Morris 1965a). The centripetal terms can be combined with the pressure gradient by defining

$$P' = p - .\Omega^2(r^2/2 + H.r.\cos\theta) \qquad (5.1)$$

$$\partial P'/\partial r = \partial p/\partial r - \rho.\Omega^2(r + H.\cos\theta) \qquad (5.2)$$

$$\partial P'/\partial \theta = \partial p/\partial \theta - \rho.\Omega^2.r.H.\cos\theta \qquad (5.3)$$

Calculations have been performed for fully-developed flow in a rotating tube. Fig.5.1 shows the effect of grid size and geometry of the calculated pressure distribution in the (r,θ) plane compared to the exact result, equation (5.1), where the dimensionless groups used are:

$$\omega = \Omega.d/W_m \qquad (5.4)$$

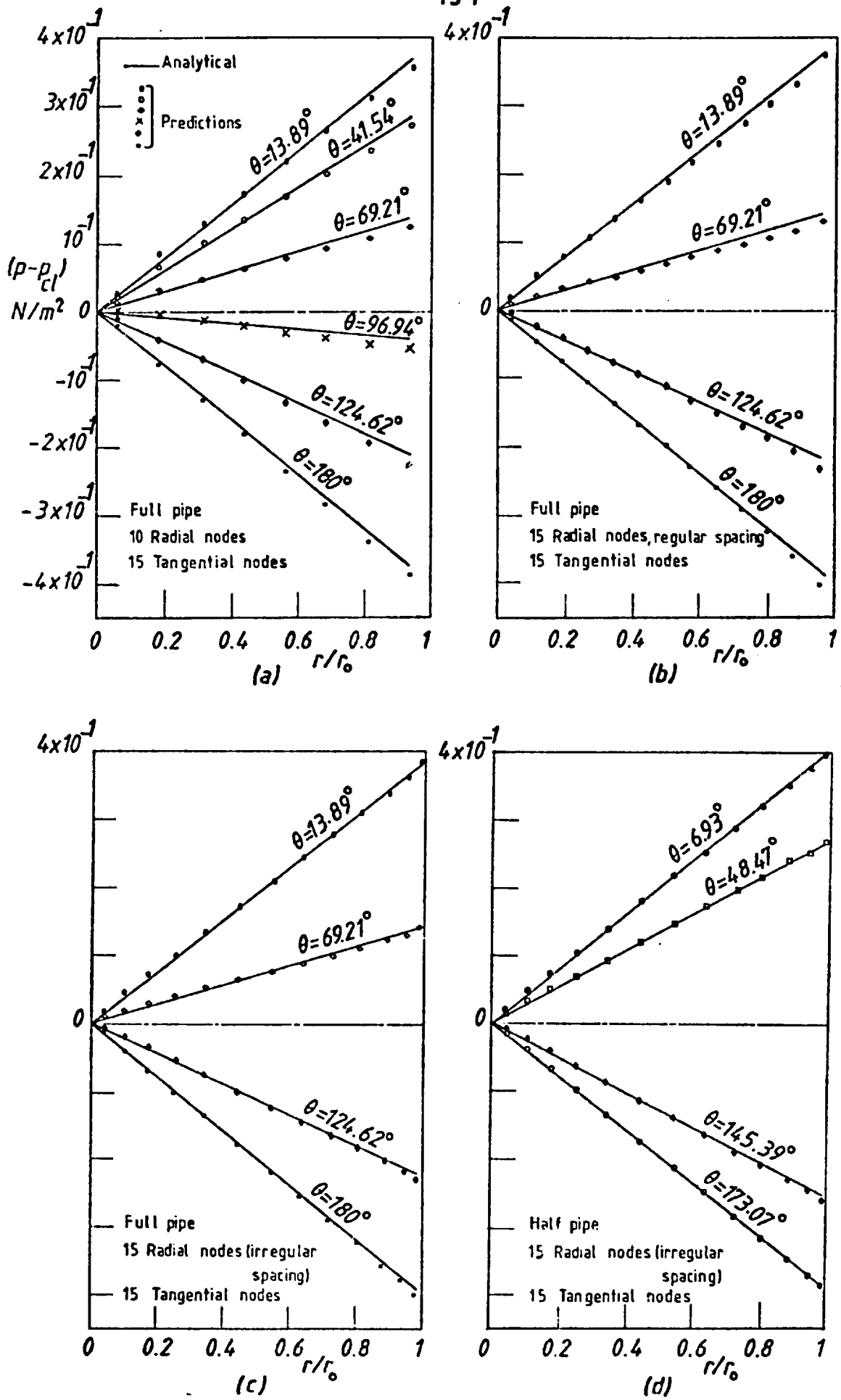


Fig.5.1 Effect of grid size and distribution on pressure in fully-developed laminar flow without heat transfer. (Re=1000, $\omega=\Omega d/W_m=0.111$, $J=\Omega r_o^2/2\nu=13.875$).

$$J = \Omega . r_o^2/(2\nu) \qquad (5.5)$$

and the points represent the values calculated at the grid nodes and it is shown that irregular spacings, with nodes concentrated near the wall and centre line, gives the best results.

5.1.2 Laminar Flow With Heat Transfer

For flow with heat transfer, we make the usual Boussinesq approximation that the effects of temperature on density are significant only in the body-force terms in the momentum equations, as shown in Appendix A1. The results of calculations for the case of uniform surface heat flux in fully-developed flow have been illustrated in Fig.5.2. The conditions were chosen to correspond approximately to those reported by Morris and Woods (1977) and Skiaderessis and Spalding (1976) with which the present results are compared. Fig.5.2 shows the dependence of the average Nusselt number on the product of Reynolds and rotational Rayleigh numbers ($Re.Ra_r$) where:

$$Ra_r = Gr_r . Pr \qquad (5.6)$$

and the rotational Grashof number Gr_r is defined as:

$$Gr_r = \Omega^2 . \beta . H . r_o^4 . (\partial T/\partial z)/\nu^2 \qquad (5.7)$$

and Nu_o represents the mean Nusselt number for stationary tube for the same Reynolds number and heat flux. Good agreement with the Skiadaressis and Spalding results is obtained. It is shown that rotation increases the heat transfer. For the present prediction, as shown in Fig.5.2, the correlation between the fully-developed mean Nusselt number and the product of the Reynolds and Rayleigh numbers can be obtained, for $3x10^4 \leq (Re.Ra) \leq 2x10^6$, as following:

$$Nu/Nu_o = 0.335x(Re.Ra_r)^{0.154} \qquad (5.8)$$

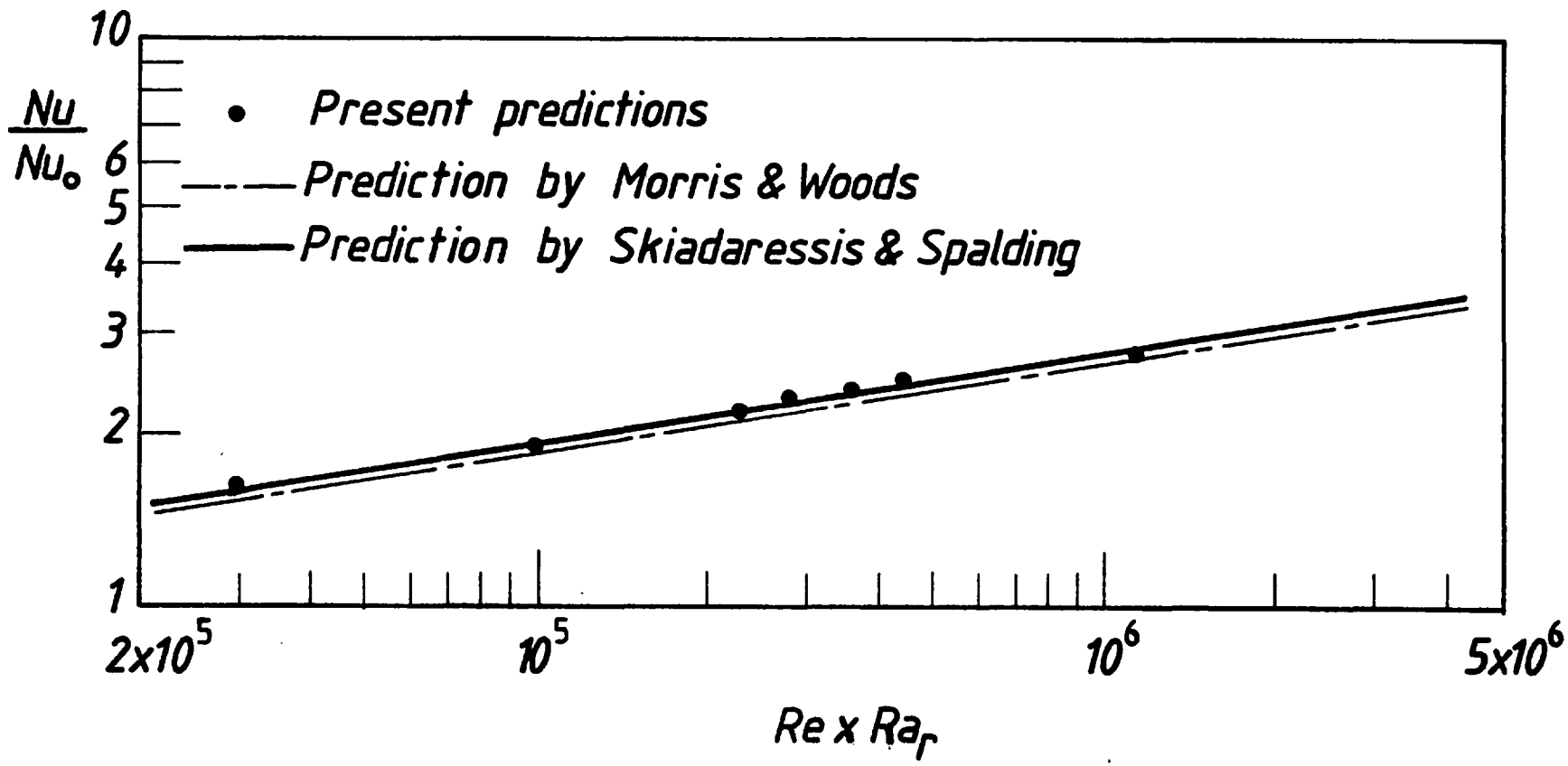


Fig.5.2 Dependence of Nusselt number for air on rotation and heat transfer in fully-developed laminar flow.

Contour plots of axial velocity component are shown in Fig.5.3 and the equivalent temperature contours are shown in Fig.5.4. The secondary flow effects are very evident. It can be seen that the maximum axial-velocity and maximum dimensionless temperature $(T_w-T)/(T_w-T_m)$ are shifted from the centre-line to the outside of the pipe.

Tangential and radial velocity contour plots are shown in Fig.5.5 It can be seen that the direction of the tangential velocity component in the outer region of the pipe is opposing that in the inner region and the maximum value of tangential velocity is 6% of the mean axial velocity W_m. The direction of the radial velocity in the outside half of the pipe with respect to the centre of rotation is opposing that in the inside half and the maximum value of radial velocity is 2.5% of W_m. Taking into consideration the directions of the velocity components it is concluded that the secondary flow in the cross section plane form two vorticies going from inside to outside of the centre of rotation as shown in Fig.5.6. All the previous results are shown for fully-developed pipe flow.

5.2 **Turbulent Flow**

5.2.1 Isothermal Turbulent Flow With The k-ε Model

It has been noted in section (5.1) that the characteristic feature of the isothermal, fully-developed laminar flow in a rotating tube is that there are no secondary flows in the cross-stream plane. This situation does not obtain for isothermal fully-developed turbulent flow where additional Reynolds-stress gradients appear in the equations of the mean motion. The appearance of secondary flows in the turbulent case is shown in the calculated velocity profiles of

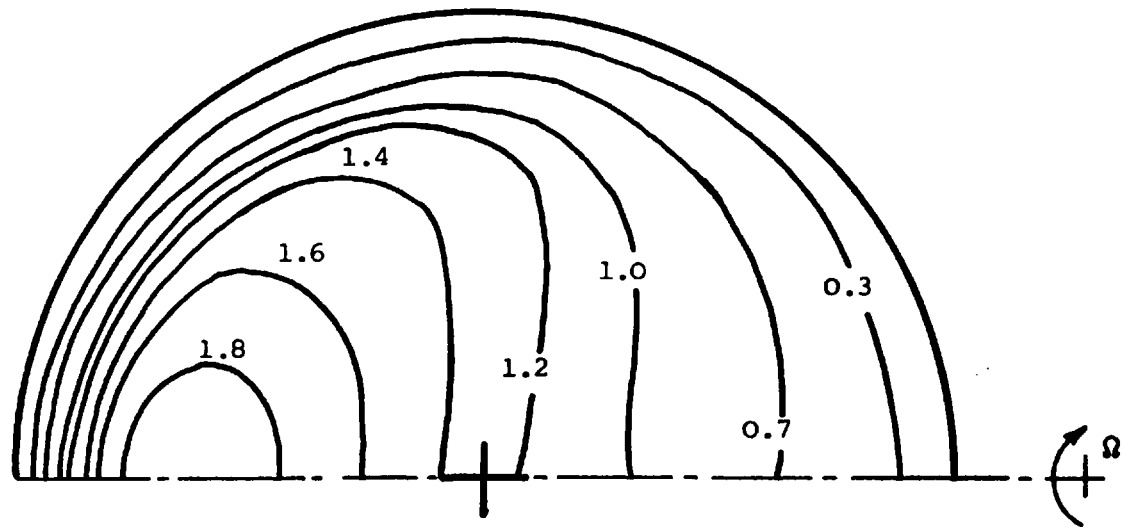


Fig.5.3 Velocity contours (W/W_m)
(Re=2200, Pr=0.7, H/d=24, Gr=230.3, J=3.125 and ω=0.05)
(where:
$\omega = \Omega d/W_m$, $J = \Omega r_o^2/2\nu \equiv \omega.Re/8$)

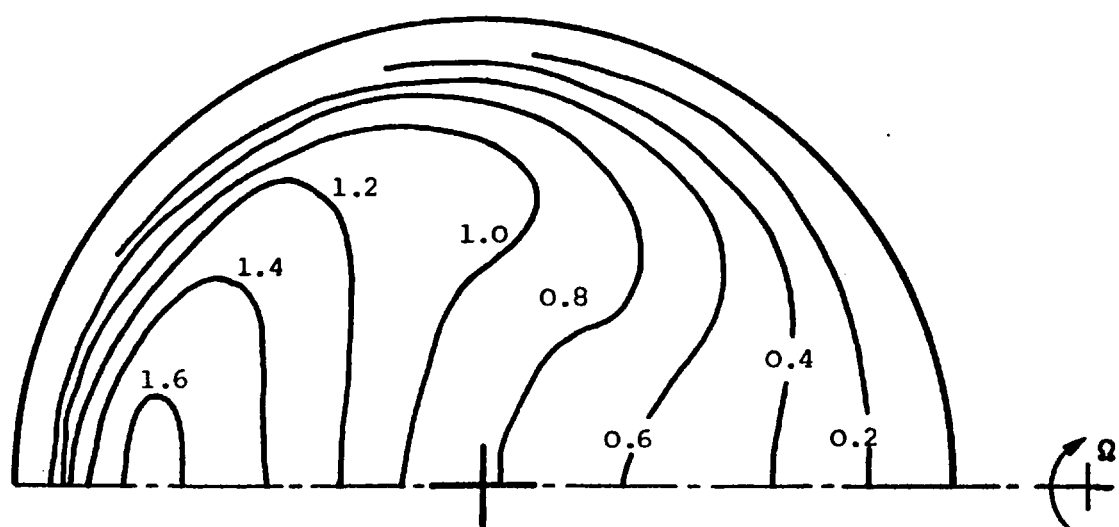
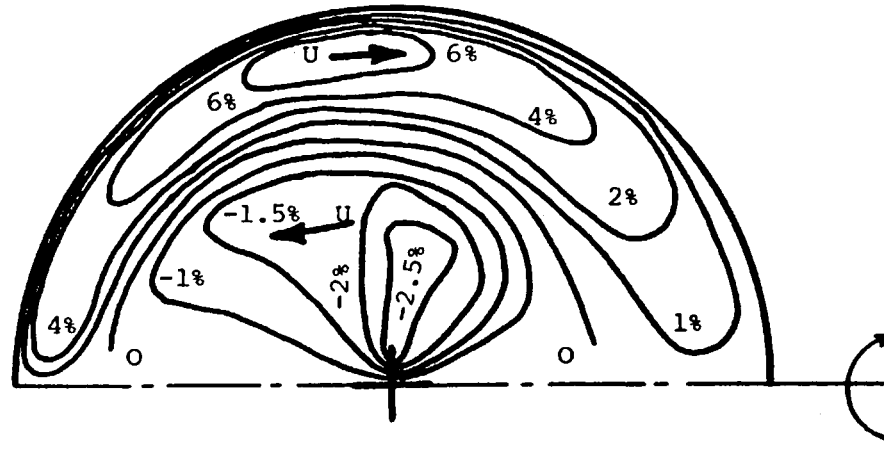
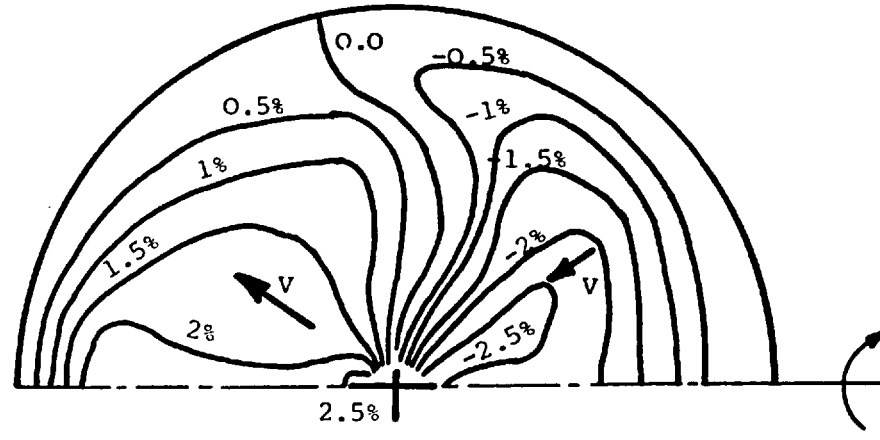


Fig.5.4 Temperature contours $(T_w-T)/(T_w-T_m)$
(Re=2200, Pr=0.7, H/d=24, Gr=230.3, J=3.125 and ω=0.05)



TANGENTIAL VELOCITY CONTOURS (U/W_m)



RADIAL VELOCITY CONTOURS (V/W_m)

Fig.5.5 Lateral velocity components for fully-developed flow (Re=2200, Pr=0.7, H/d=24, Gr=2303, J=3.125 and ω=0.05).

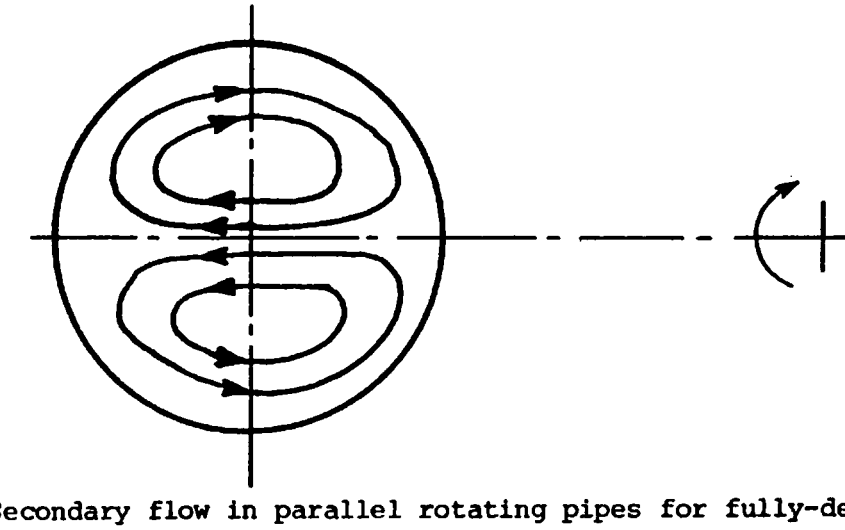


Fig.5.6 Secondary flow in parallel rotating pipes for fully-developed flow.

Fig.5.7. The contour plots of Fig.5.8 clearly show that the assumption of symmetry is valid, since flow through the full pipe section has been calculated (with 15 tangential and 11 radial grid nodes) with identical results for half pipe calculations (with 10 tangential and 10 radial grid nodes). The average coefficient of friction $\overline{C}_f$ increases with increasing rotational speed as shown in Fig.5.9, where:

$$\overline{C}_f = \tau_m/(\rho.W_m^2/2) \qquad (5.8)$$

Rotation also produces a circumferential variation in $\overline{C}_f$ in developing flow and the maximum value is moved to the outside of the pipe, as shown in Figs.5.10 and 5.11. The pipe length required for fully-developed flow increases with rotational speed. This length is around 40 diameters for small rotation and around 55 diameters when the rotational speed is doubled.

Tangential and radial velocity contours are plotted in Fig.5.12, showing that the same type of secondary flow, similar to that of the laminar case with heat transfer reported in Fig.5.6, is induced. The secondary flow is not stronge and the maximum value of the tangential velocity component is about 2.5% of W_m and that of the radial component is about 1.5% of W_m for the larger value of rotation with dimensionless number J is equal to 277.8. The corresponding dimensionless static pressure contours $(P-P_{CL})/\frac{1}{2}W_m^2\rho$ are shown in Fig.5.13. High pressure regions move outside and low pressure regions move inside with respect to the centre of rotation. Fully-developed dimensionless turbulence energy contours $(k/u_{\tau_m}^2)$ are shown in Fig.5.14. The corresponding minimum values have been moved outside of the pipe as that of the maximum axial velocity as shown in Fig.5.8.

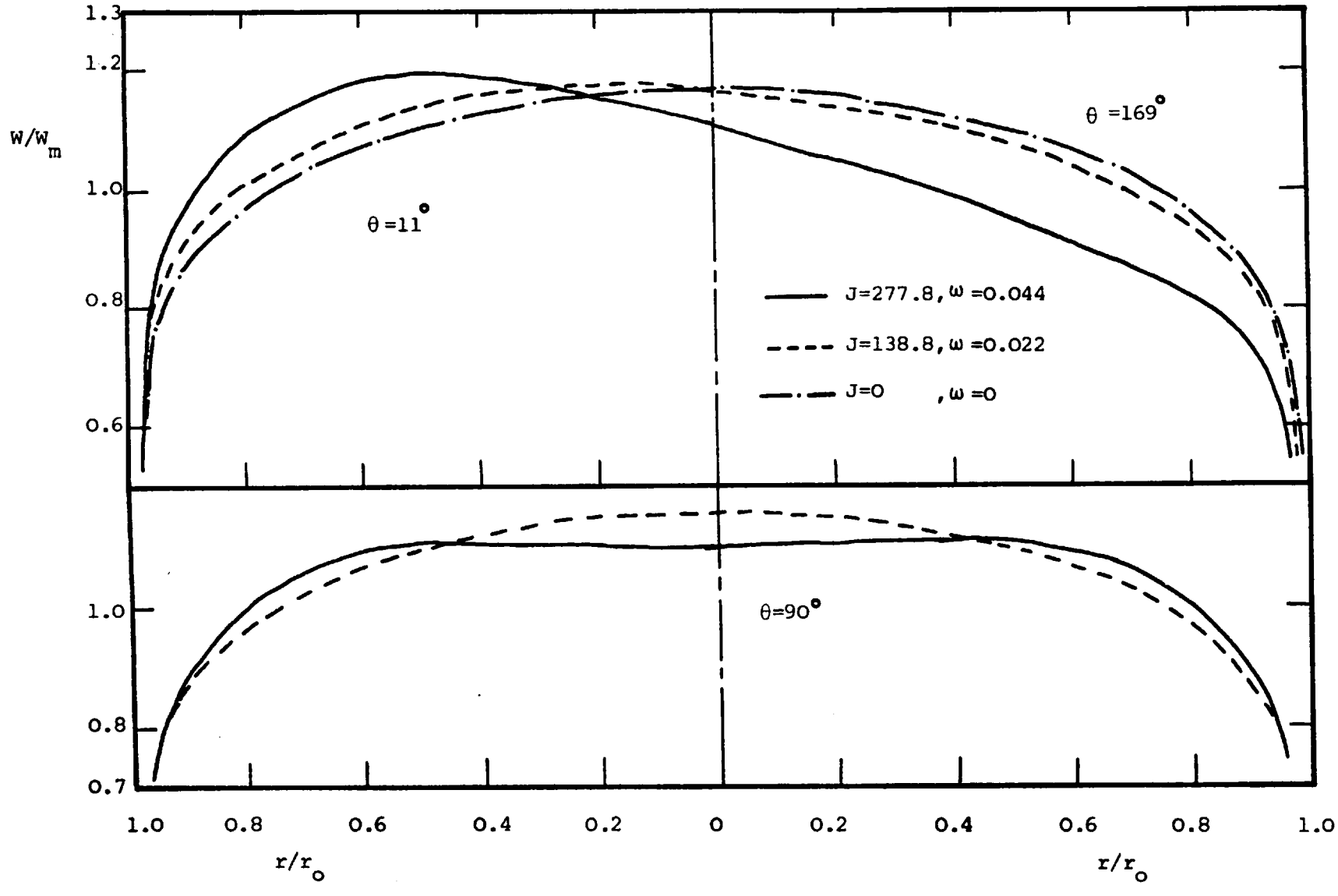


Fig.5.7 Fully-developed axial velocity profiles at various rotational speeds for isothermal flow. (Re=50 000, H/d=25, k-ε model used).

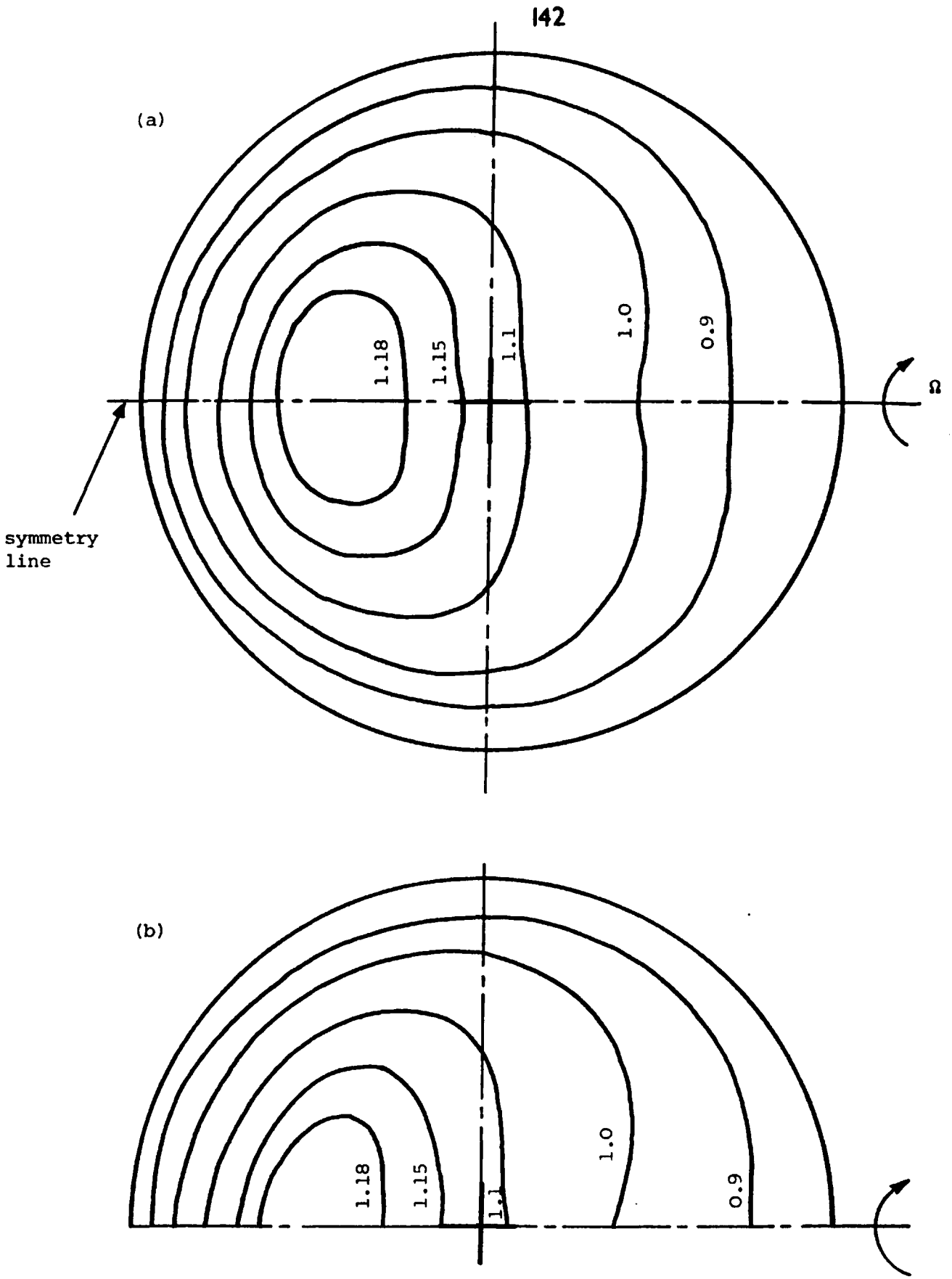


Fig.5.8 Isothermal fully-developed axial velocity contours (W/W_m)
(a) results obtained by solving the full pipe; 360°
(b) results assuming symmetry and solving half pipe; 180°
(k-ε model used, Re=50 000, J=277.8 and ω =0.044).

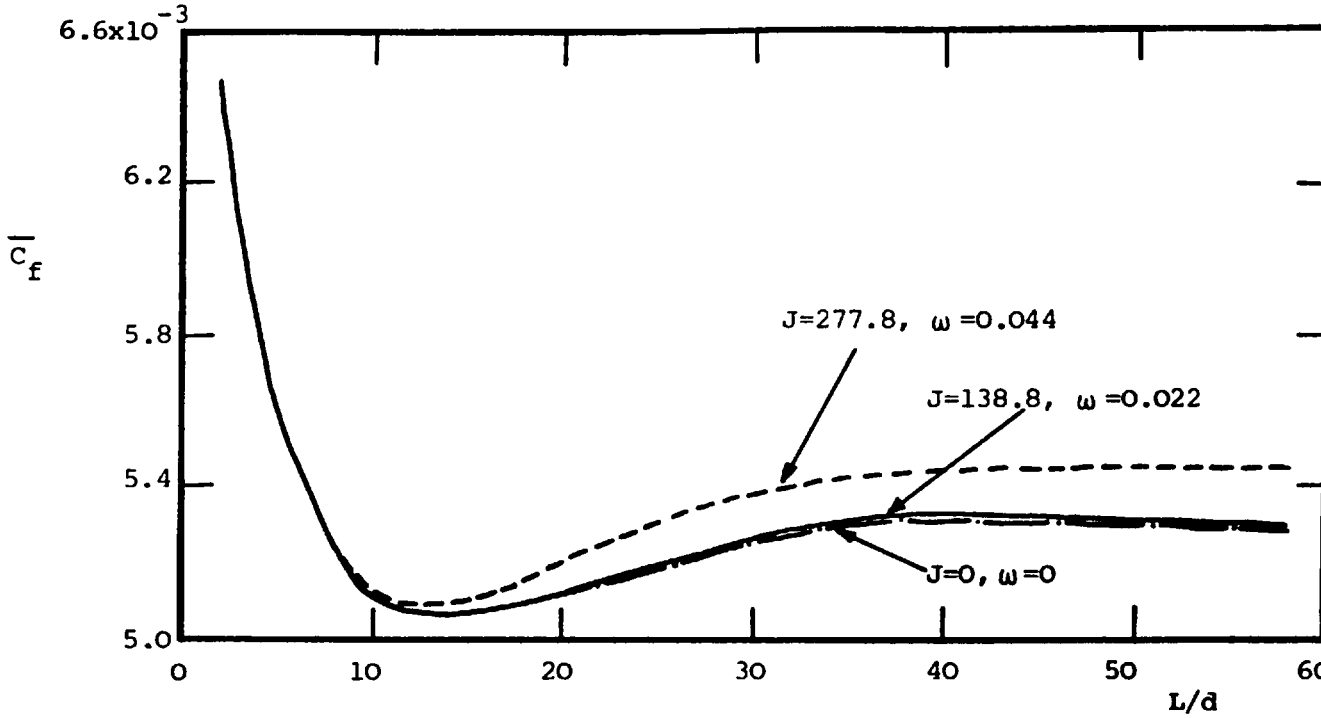


Fig.5.9 Developing of the average coefficient of friction at various rotational speeds for isothermal flow for Re=50 000 and H/d=25.
($\overline{C_f} = \tau_w / \frac{1}{2} \rho W_m^2$)

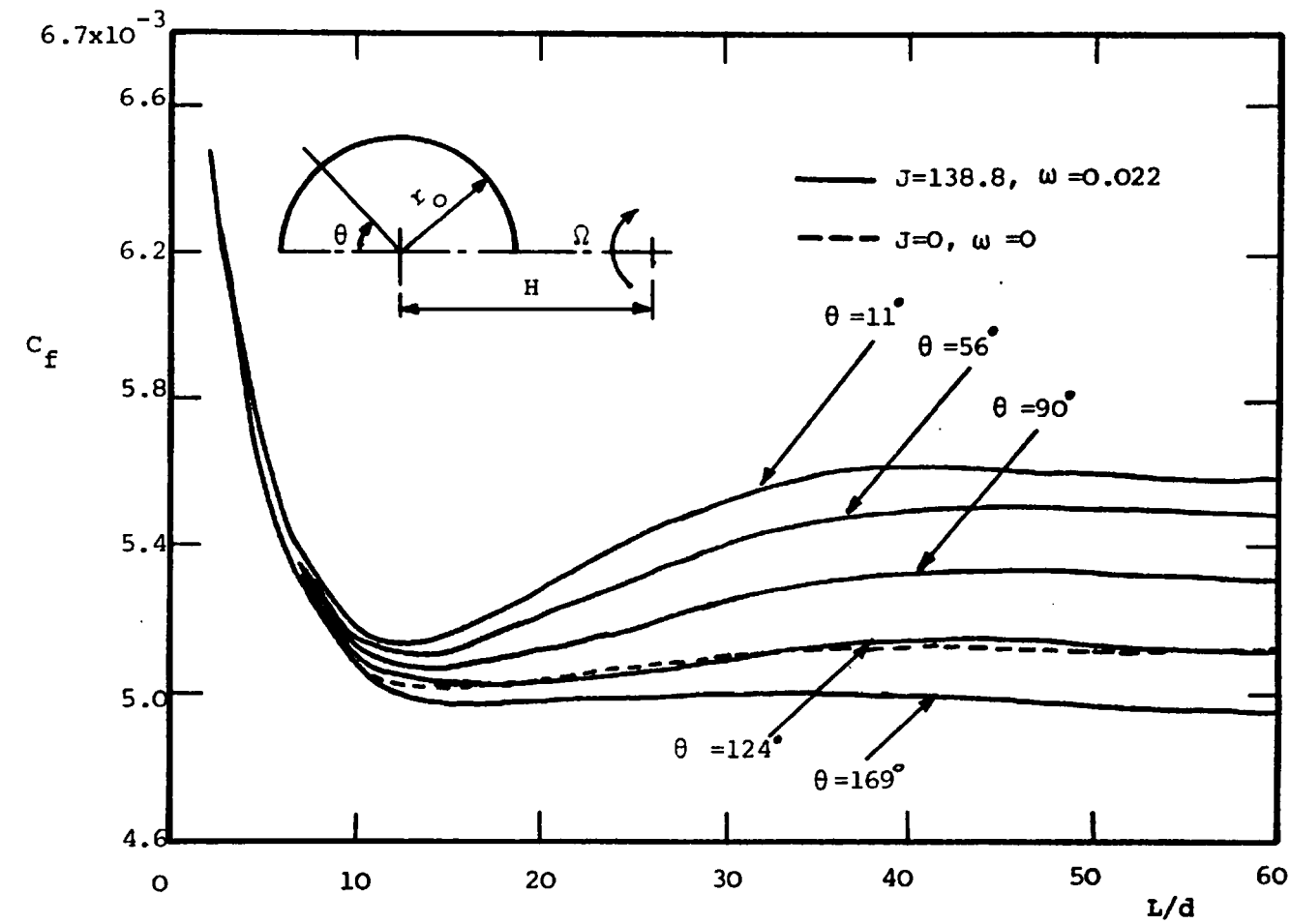


Fig.5.10 Developing of the coefficient of friction at different angles for isothermal flow for Re=50 000 and H/d=25.

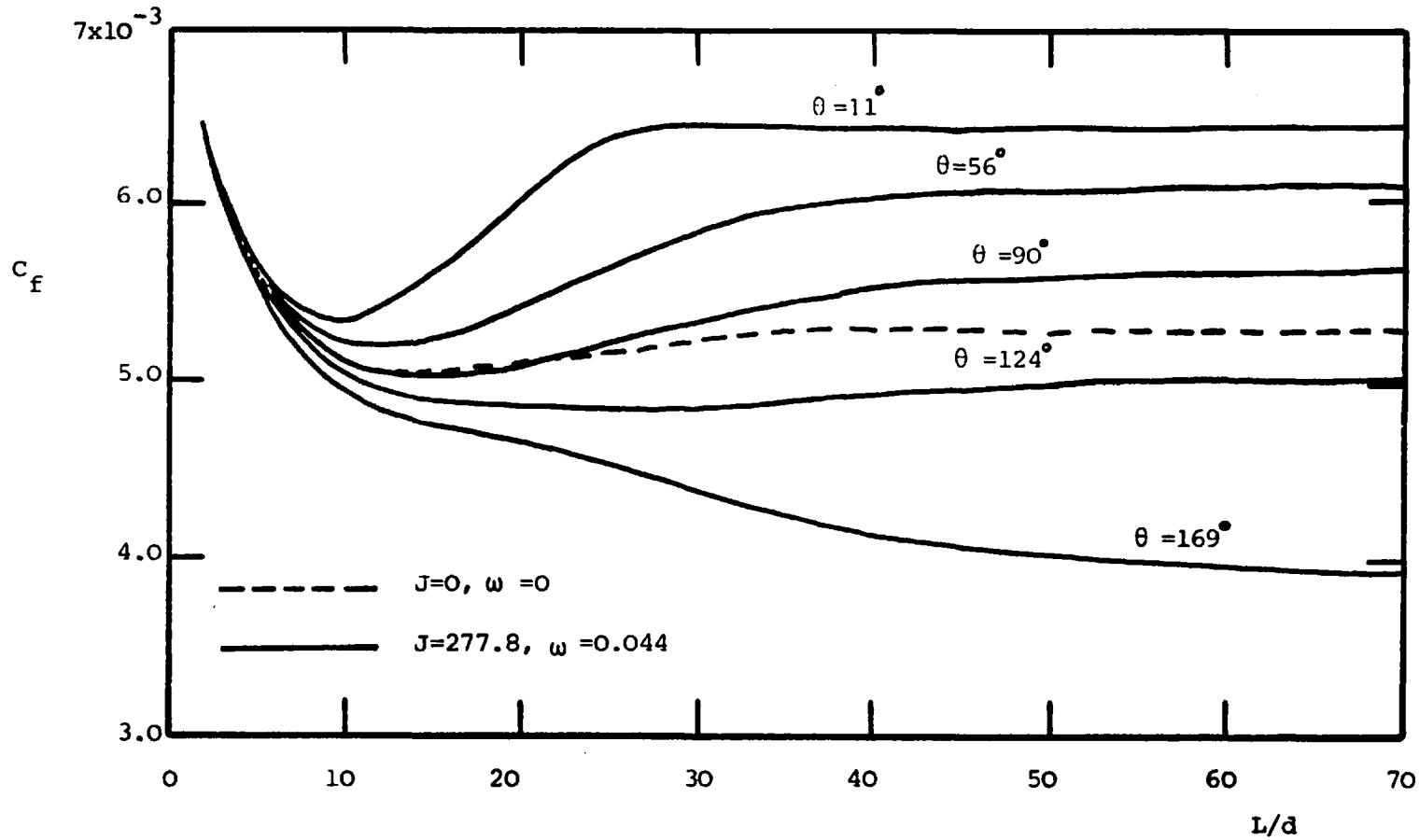
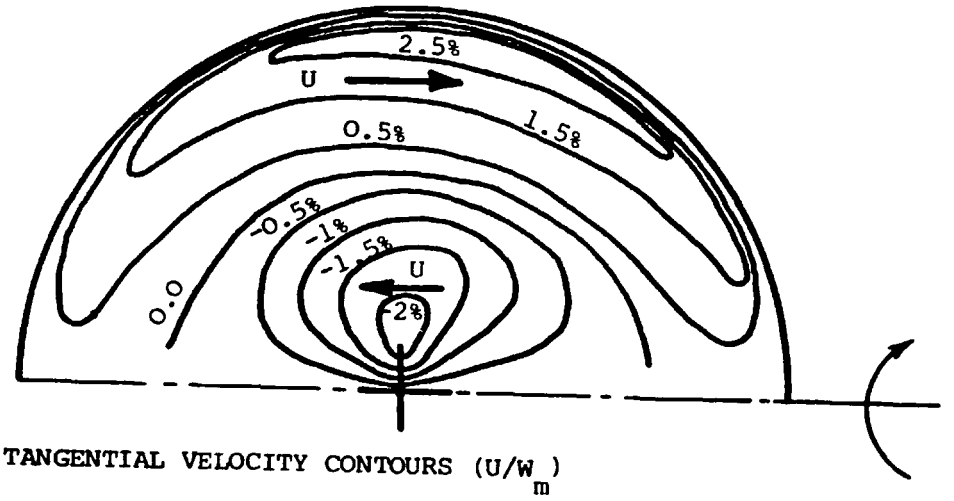
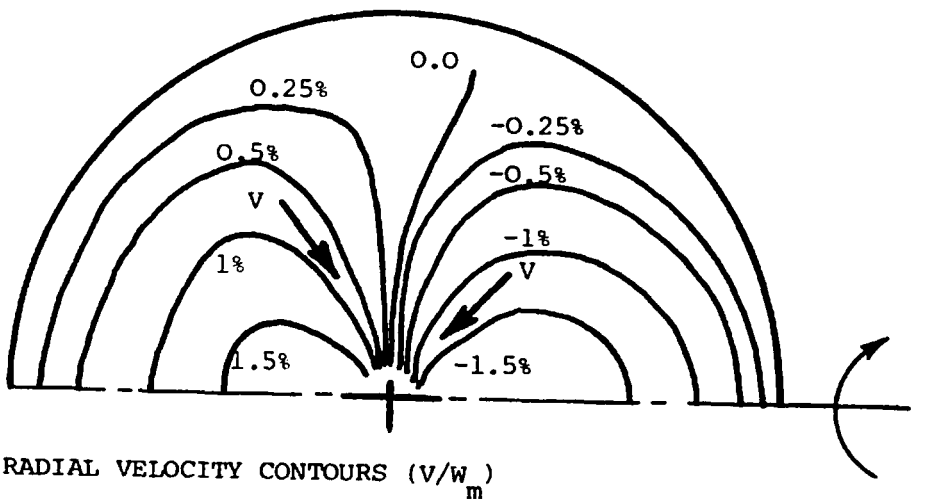


Fig.5.11 Developing of the coefficient of friction at different angles for isothermal flow.
(Re=50 000, H/d=25)



TANGENTIAL VELOCITY CONTOURS (U/W_m)



RADIAL VELOCITY CONTOURS (V/W_m)

Fig.5.12 Lateral velocities for fully-developed isothermal flow. (Re=50 000, H/d=25, J=277.8, ω=0.044, k&ε model used)

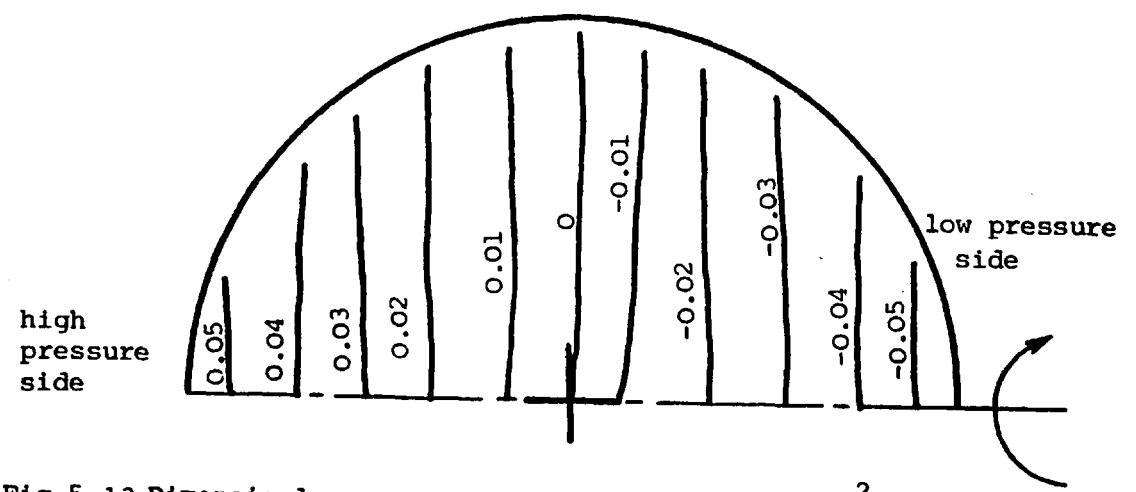


Fig.5.13 Dimensionless pressure contours $(p-p_{cl})/\frac{1}{2}\rho W_m^2$ for fully-developed isothermal flow (Re=50 000, H/d=25, J=277.8, ω=0.044 and k&ε model used).

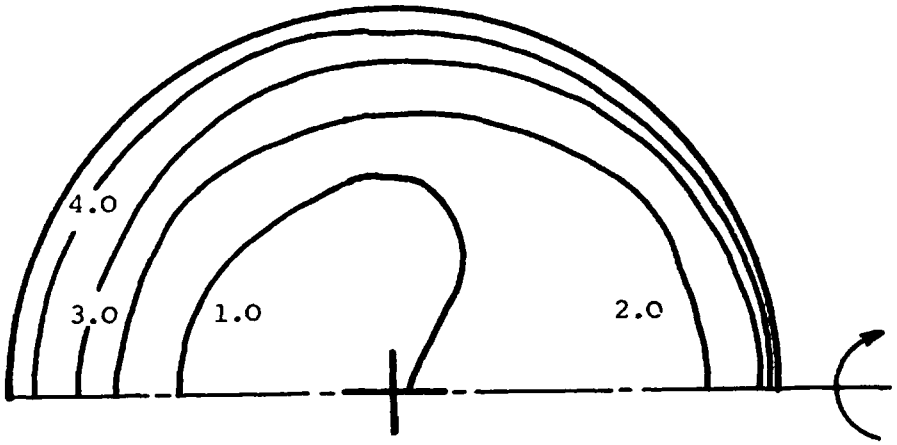


Fig.5.14 DIMENSIONLESS TURBULENCE ENERGY CONTOURS ($k/u^2_{\tau_{mean}}$) for fully-developed isothermal flow. (Re=50 000, H/d=25, J=277.8, ω=0.044, k-ε model used).

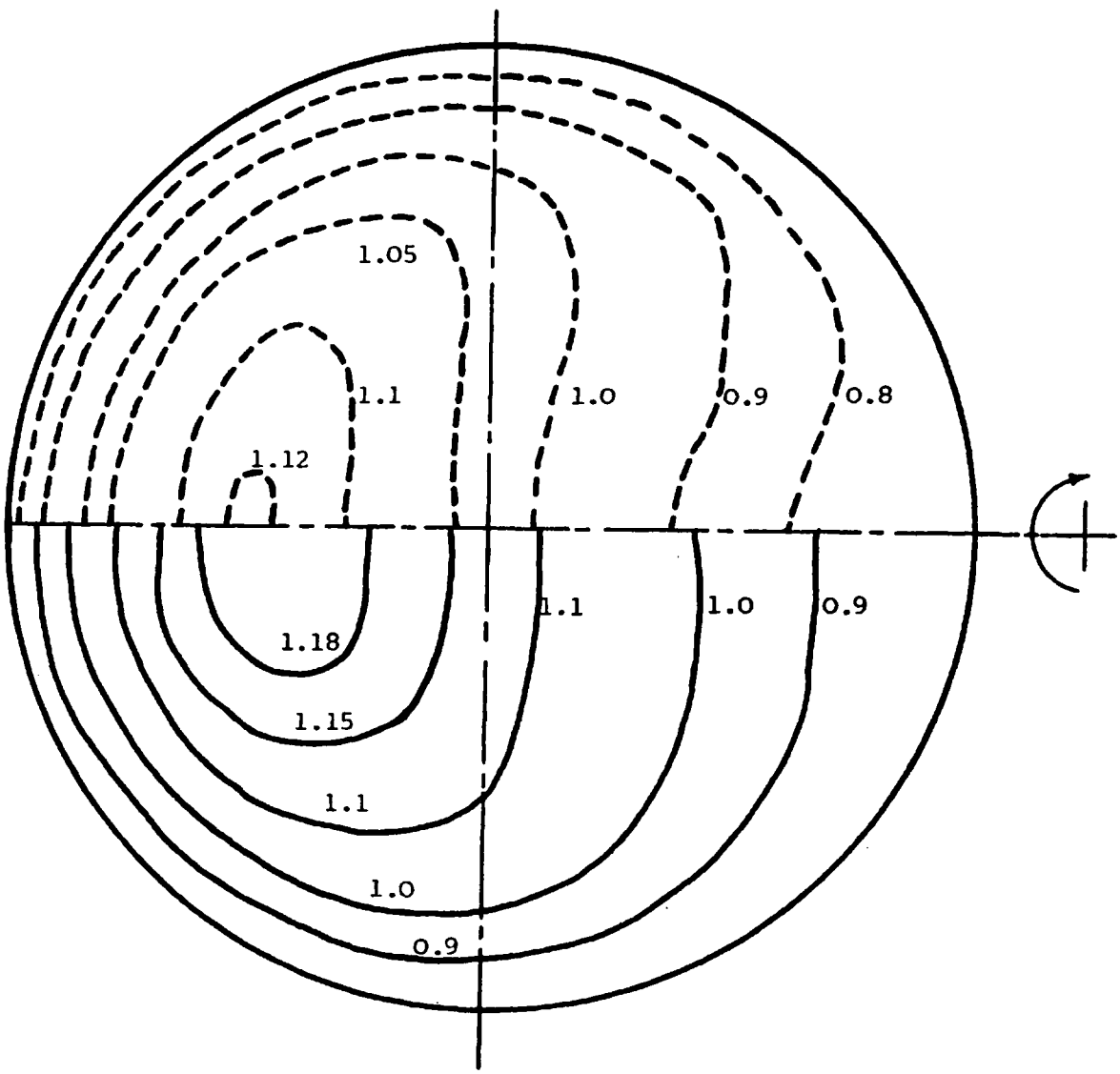


Fig.5.15 Isothermal fully-developed axial velocity contours (W/W_m)
(Re=50 000, ω=0.044, H/d=25, J=277.8)
—— k-ε model ----- algebraic model with P/ε=1.

5.2.2 Isothermal Turbulent Flow With The Algebraic Model

Applying the procedure mentioned before in Chapter 2, for turbulent flow in rotating ducts, a set of algebraic equations for different Reynolds stresses were obtained, which are shown in detail in Appendix A2. The algebraic Reynolds stress model and computation method were first tested for stationary pipe flow. Typical results are shown in Appendix A4. The results agree reasonably well with the experimental data but are not expected to be noticeably superior to the k-ε predictions for this simple flow. Fig.5.15 shows contours of mean axial velocity W/W_m in a rotating tube, using the algebraic Reynolds stress model, with the assumption $P/\varepsilon=1$, compared with the results obtained from k-ε model calculations. This is a situation in which the Reynolds stress method would be expected to give results superior to those of the simpler k-ε method used before snd indeed the figure shows quite significant differences. The main point of difference in the algebraic stress model calculations is that the velocity profile is appreciably more distorted and less peaked. The corresponding lateral velocity components are shown in Fig.5.16. When they are compared with the k-ε model results the same trend is obtained but higher values of tangential and radial velocities are observed. This means that the algebraic model is able to predict more distorted flow than the k-ε model. The pressure distribution, shown in Fig.5.17, seems to be almost the same as that reported in Fig.5.13 for the k-ε prediction. The corresponding dimensionless turbulence energy contours are shown in Fig.5.18. The contours show less distortion than k-ε model results of Fig.5.14. In addition to those results the effect of rotation on different turbulence intensities and Reynolds stresses are obtained as shown in Figs.5.19 and 5.20. All

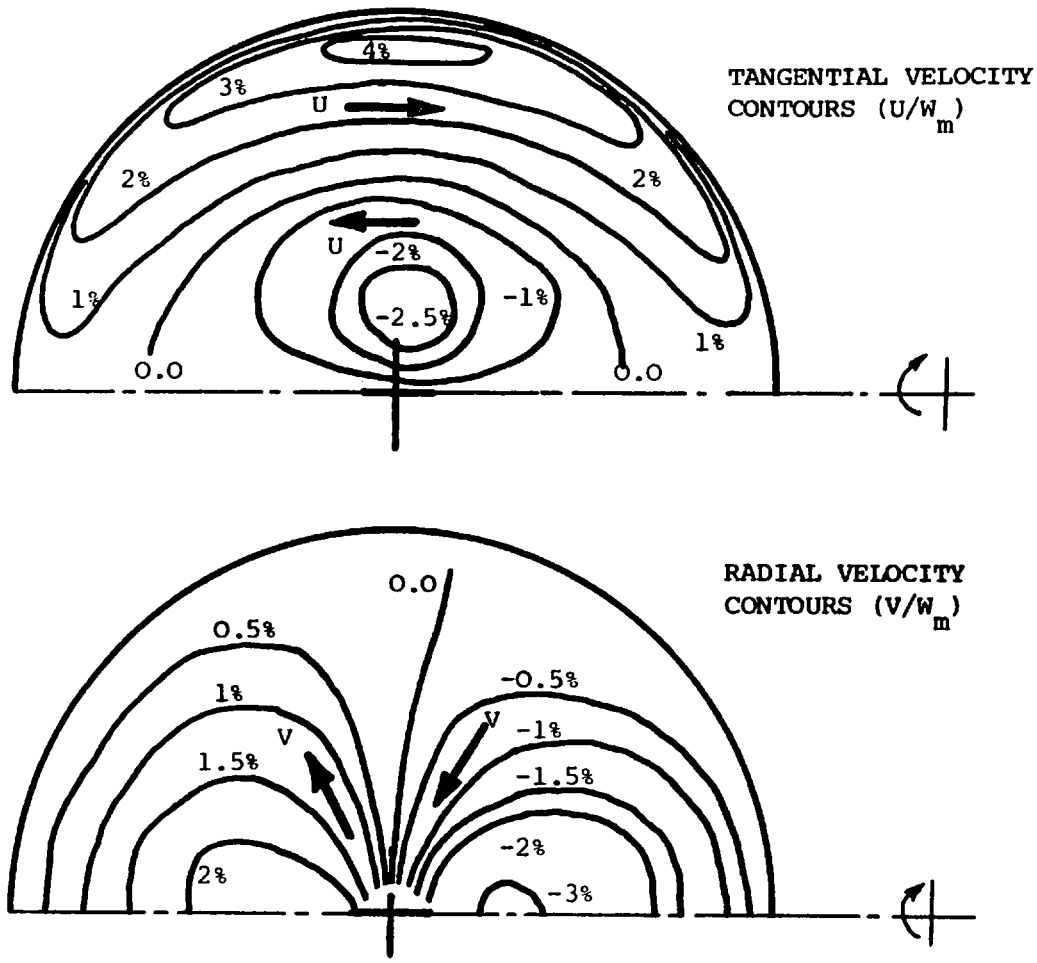


Fig.5.16 Lateral velocities for fully-developed isothermal flow.
Re=50 000, H/d=25, J=277.8, ω=0.044 ,algebraic model used.

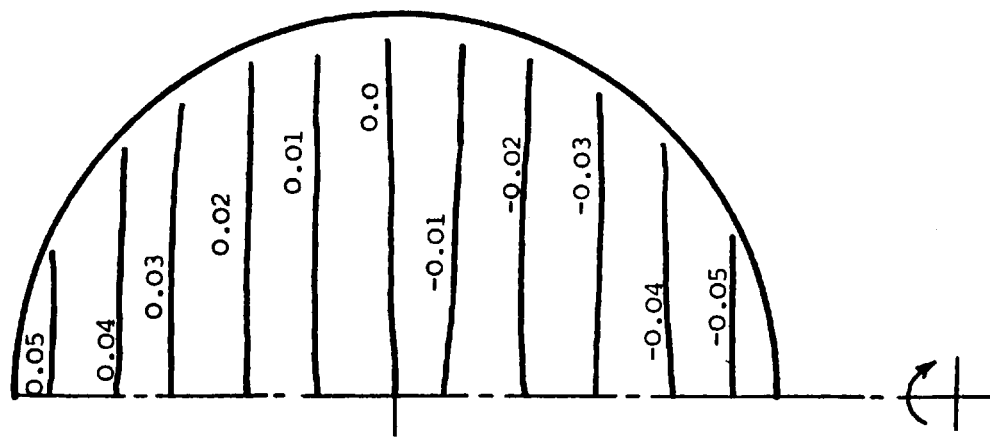


Fig.5.17 Dimensionless pressure contours $(p-p_{cl})/\frac{1}{2}\rho W_m^2$ for fully-developed isothermal flow.
Re=50 000, H/d=25, J=277.8, ω=0.044 , algebraic model used.

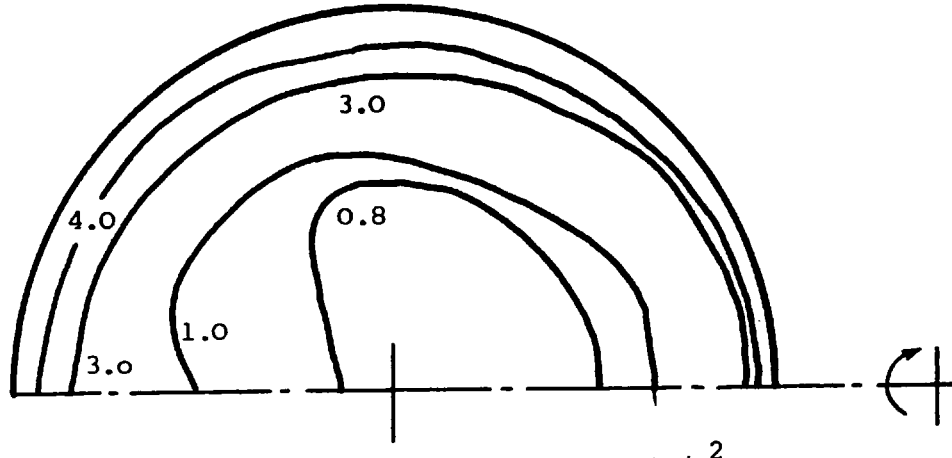
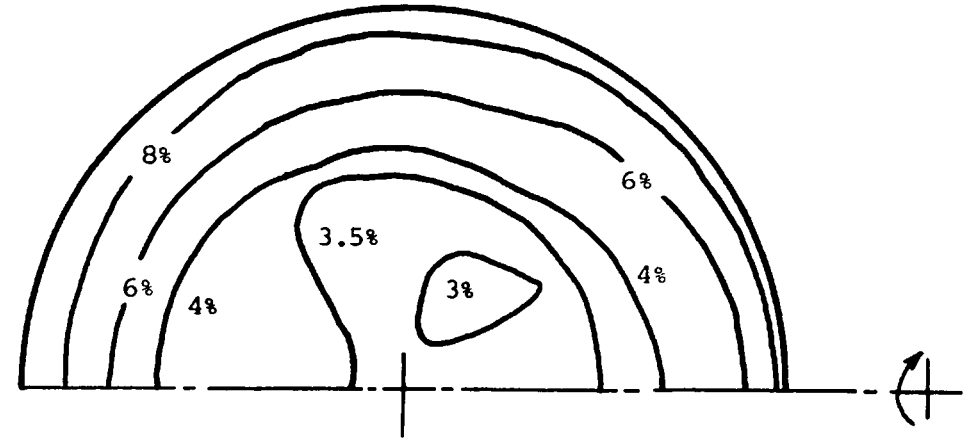
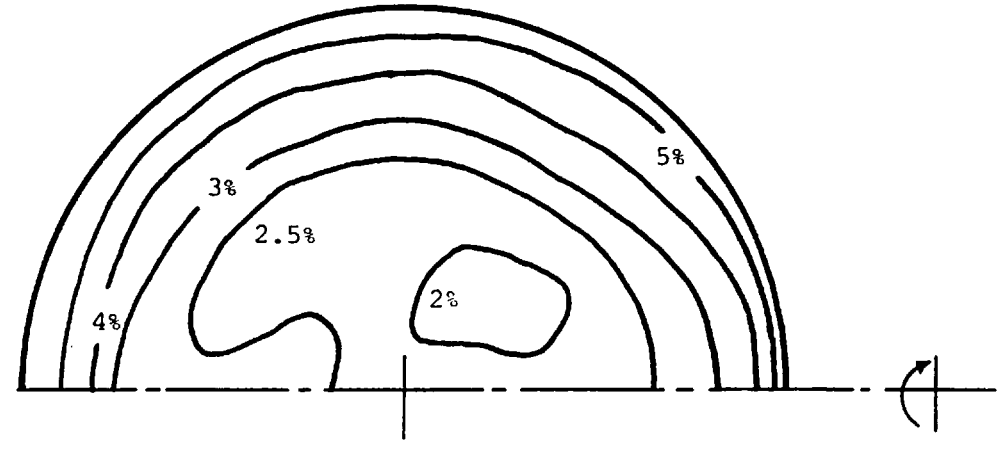


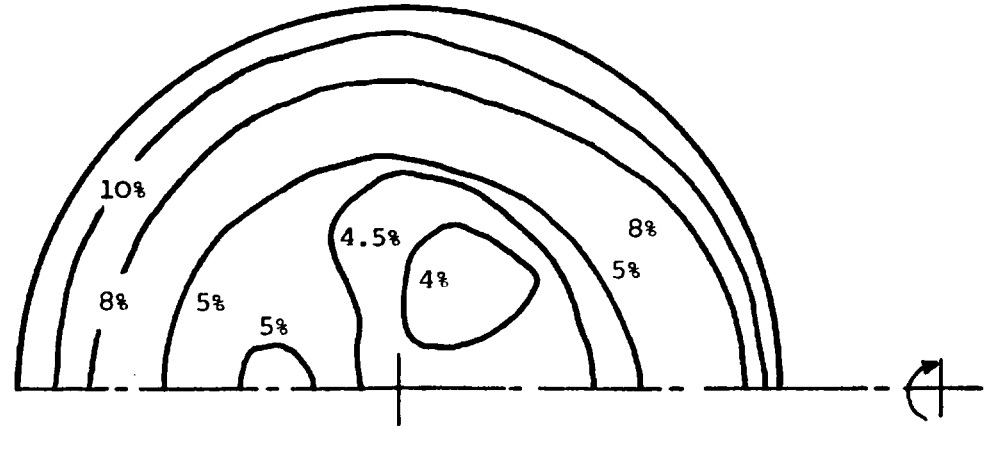
Fig.5.18 DIMENSIONLESS TURBULENCE ENERGY CONTOURS ($k/u^2_{\tau\ mean}$) for fully-developed isothermal flow. (Re=50 000, H/d=25, J=277.8, ω=0.044, algebraic model used).



TANGENTIAL COMPONENT $(u/W_m) \times 100\%$

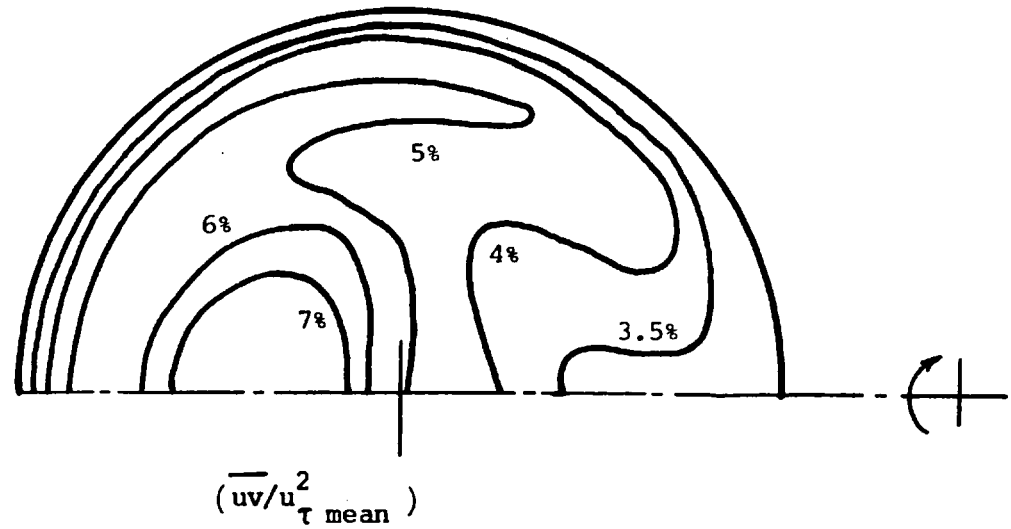


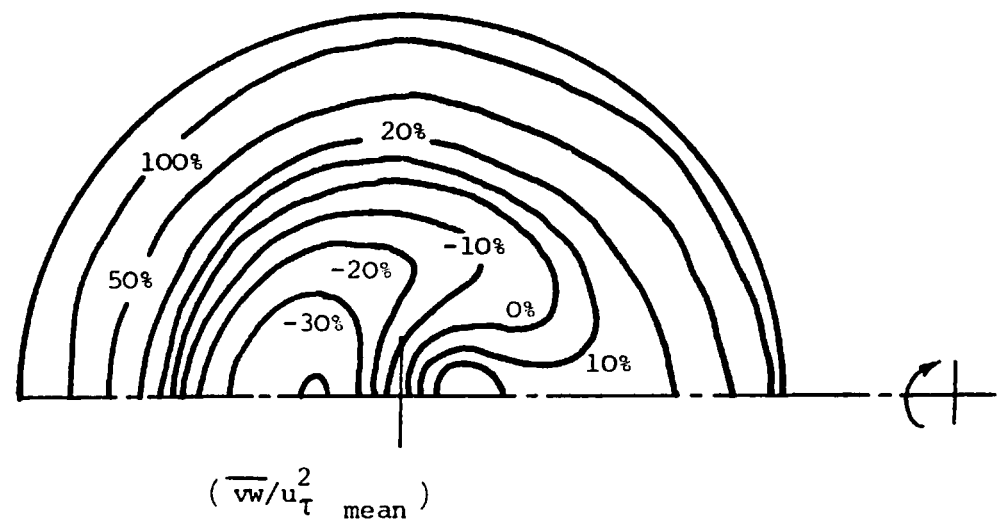
RADIAL COMPONENT $(v/W_m) \times 100\%$



AXIAL COMPONENT $(w/W_m) \times 100\%$

Fig.5.19 Contours of rms turbulence intensities for fully-developed isothermal flow.





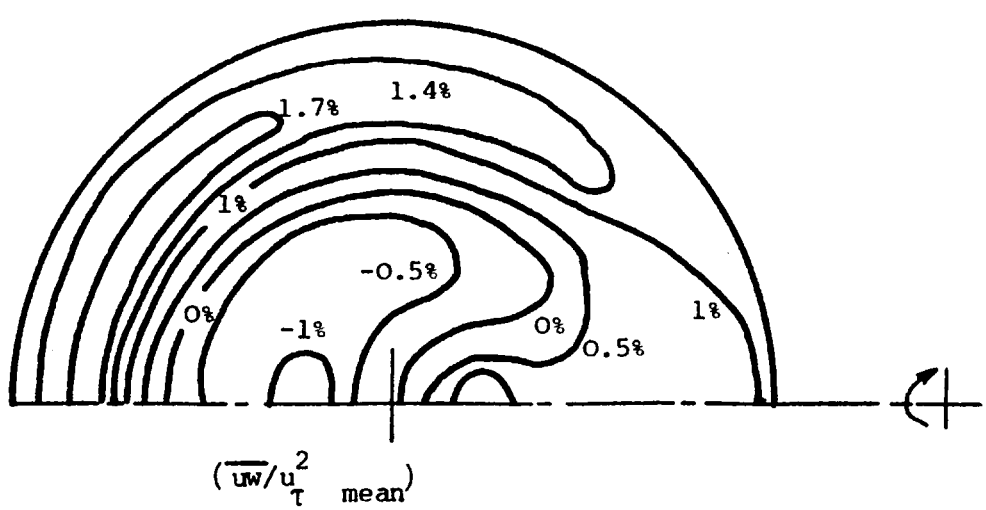


Fig.5. 20 Contours of the Reynolds shear stresses for fully-developed isothermal flow.
(Re=50 000, H/d=25, J=277.8,ω =0.044, algebraic model used)

the results are obtained for fully-developed flow.

5.2.3 Turbulent Flow With Heat Transfer Using the k-ε Model

Turbulent flow in parallel rotating ducts with heat transfer was studied, at first using the k-ε model of turbulence. The results of calculations are compared with four experimental data sets supplied by Stephenson (1982). The values of the dimensionless groups used in both the experimental data and the present prediction are shown in Table 5.1. The axial wall temperature distribution was used as a thermal boundary condition for the present prediction, and it was obtained as a continuous curve passing through the experimental measurements for each case. The inlet fluid temperature was taken from measurements, and was assumed with other variables and properties to be uniform in the inlet plane. This assumption is probably not very accurate, but unfortunately there are no mesurements of velocity, pressure or temperature fields for this type of flow in rotating ducts. The assumption of uniform inlet conditions affects the calculated flow in the entrance region of the duct. The grid used for the numerical calculation consisted of 10x10 uniformly spaced nodes in the radial and tangential directions respectively. The number of axial steps was chosen according to the rotational speed. For zero rotation and for case II of small rotation, the axial step was chosen to be 0.02 of the duct diameter at the inlet and was increased gradually up to 0.1 of the diameter. But for higher rotations, very small axial steps were necessary; these were chosen as 0.02 of the diameter along the duct length for case III, and 0.015625 of the diameter for case IV. A small step length is usually required for this type of flow with high body forces to overcome numerical instabilities associated with the use of upstream quantities in the parabolic solution procedure.

case number		Re	$\omega=\Omega.d/W_m$	$Sw=\Omega.H/W_m$	H/d
I	experiment	34 930	0	0	25.2
	prediction	33 333	0	0	25.2
II	experiment	33 200	0.060	1.523	25.2
	prediction	33 333	0.069	1.745	25.2
III	experiment	32 790	0.094	2.366	25.2
	prediction	33 333	0.112	2.834	25.2
IV	experiment	32 160	0.125	3.145	25.2
	prediction	33 333	0.153	3.860	25.2

Table 5.1 Values of the dimensionless groups used for the experimental data of STEPHENSON (1982), and the present prediction of turbulent flow in parallel rotating ducts.

CORRECTIONS

page no.	line no.	wrong	correct
154	21	decreased.	decreased, and is displaced away from the symmetry line for the cases III and IV due to strong body forces effect.
154	29	is increased.	is increased. The maximum dimensionless temperature is displaced away from the symmetry line for case IV.

Fig.5.21 displays the calculated axial temperature distribution compared with the experimental data. These results are depicted for cases I and IV; for the other two cases only the inlet and outlet temperatures were available. Good agreement is shown in the figure, even for very high rotation case IV. The corresponding Nusselt number variation with axial distance is shown in Fig.5.22. The comparison of the predicted Nu with the experimental data shows good agreement in the regions far enough from the two ends of the test section. The larger discrepancies are found in the inlet region of the duct, where the inlet boundary conditions were assumed to be uniform. These uniform distributions affect the calculation of the heat flux and Nusselt number. The fully-developed cases are considered at L/d=60 for cases I and II, and at L/d=55 for cases III and IV. For fully-developed flow, the maximum difference between the predicted Nu and the experimental value is around 12% for case IV as shown in Fig.5.22. The corresponding predicted fully-developed axial velocity contours for the four cases considered are shown in Fig.5.23. The maximum axial velocity is displaced to the outside of the centre of rotation. When the rotational speed is increeased, the axial velocity distortion is increeased, while the maximum axial velocity is slightly decreased. The corresponding tangential and radial velocity components are shown in Fig.5.24 and 5.25 respectively. The lateral velocity components are increased when the rotational speed is increeased. The maximum tangential velocity component is U/W_m=17%, and the maximum radial velocity componenet is V/W_m=19%, as shown in figures for case IV. The dimensionless temperature contours are shown in Fig.5.26. The minimum temperature is displaced to the outside of the centre of rotation as shown in the figure, and its value is slightly increased when the rotational speed is increased. The

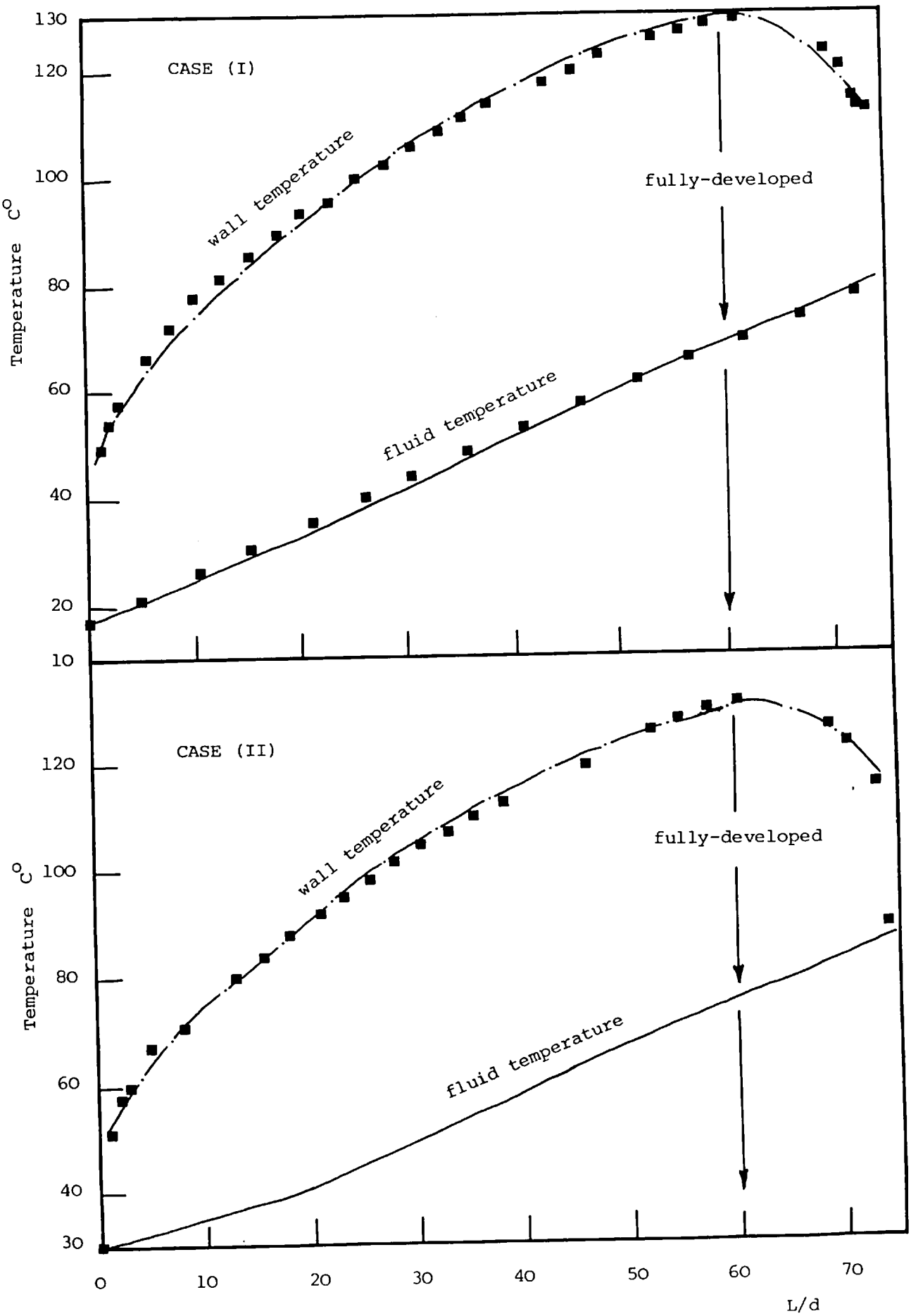


Fig.5.21 For legend see following page.

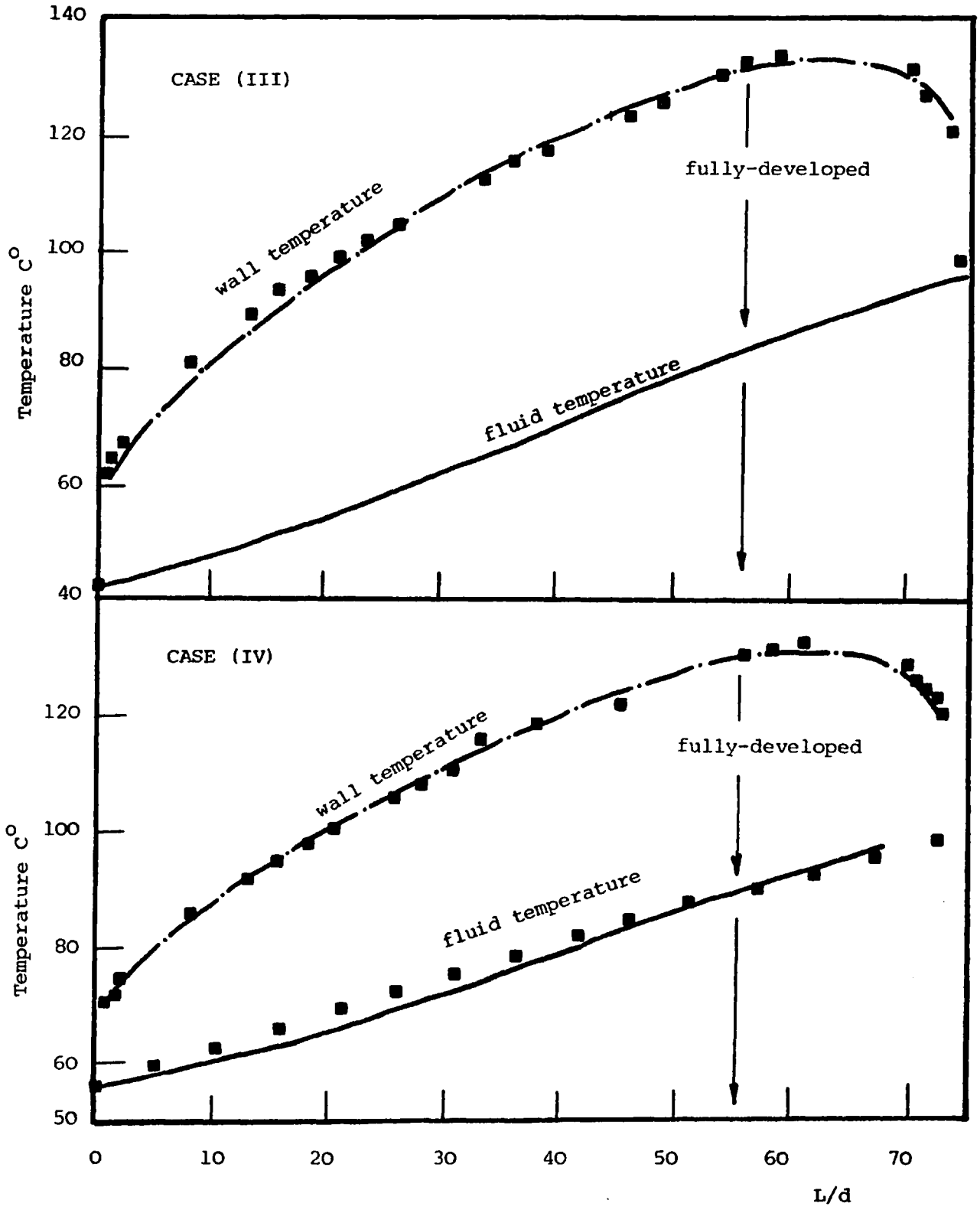


Fig.5.21 Variation of temperature with axial distance for turbulent flow in parallel rotating ducts for different rotational speeds.

——— present prediction using k-ε model

■ ■ data of STEPHENSON (1982)

—·— boundary condition used for the present prediction.

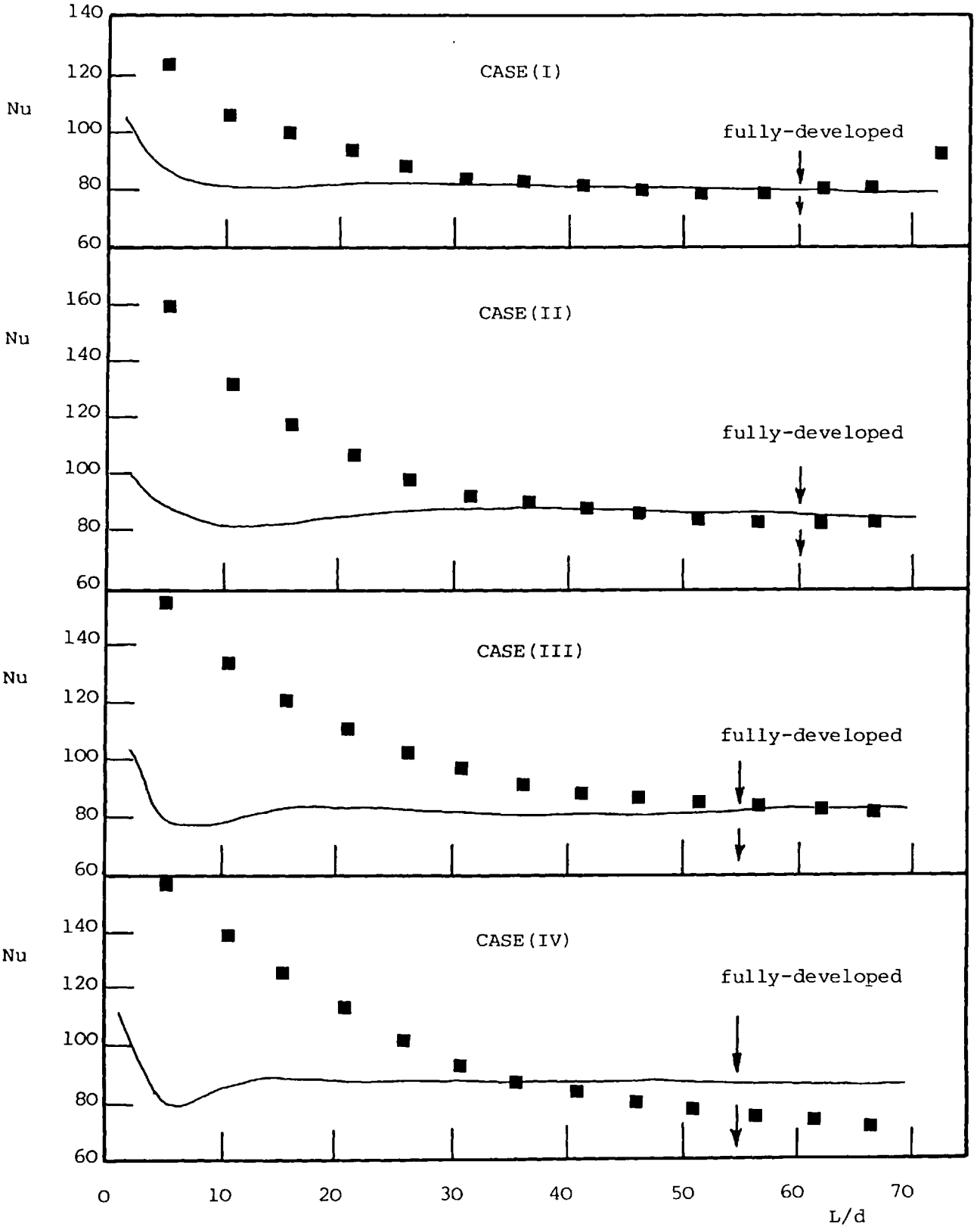


Fig.5.22 Variation of the mean Nusselt number with axial distance for turbulent flow in parallel rotating ducts for different rotational speeds.

——— present prediction using k-ε model

■ ■ data of STEPHENSON (1982).

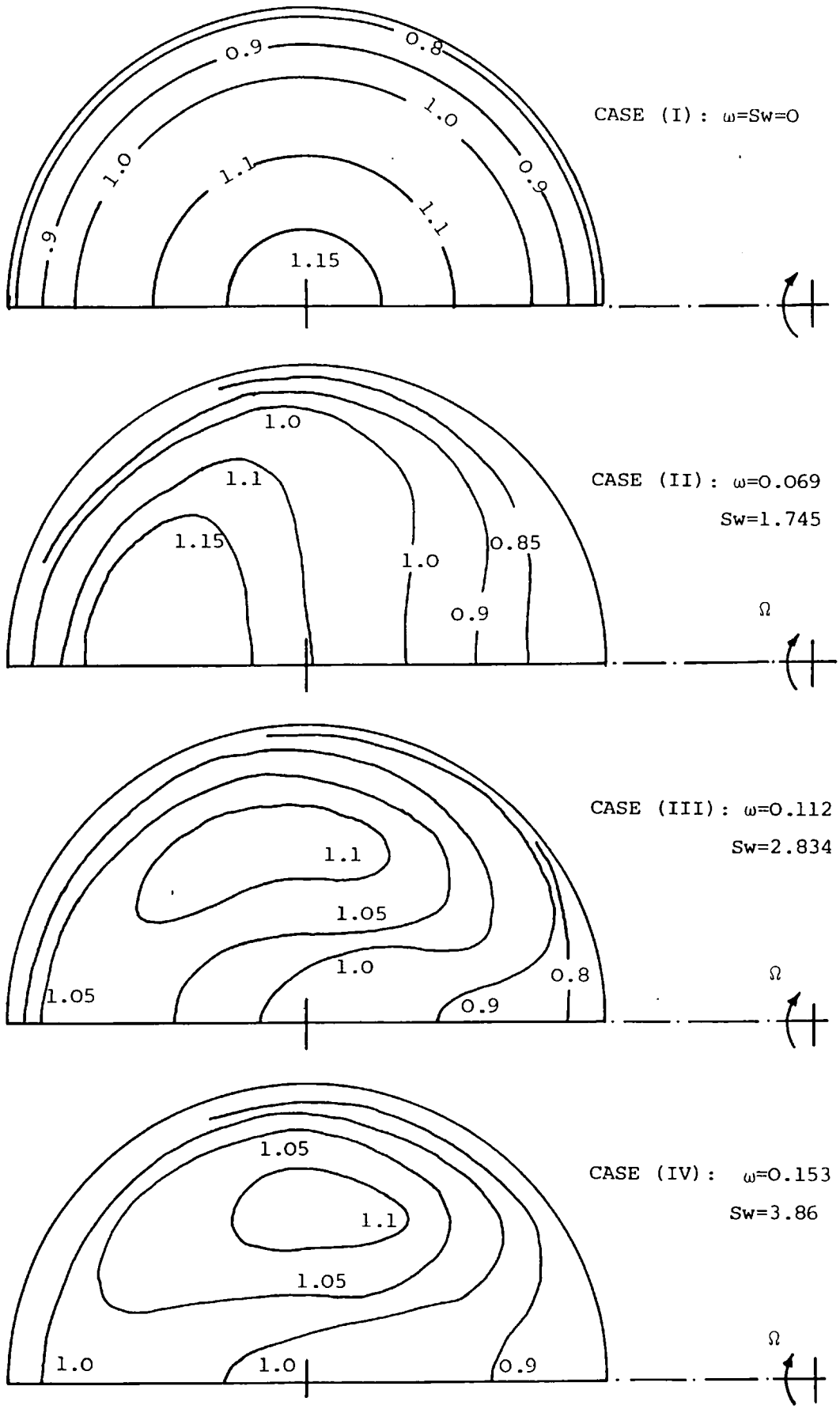


Fig.5.23 Fully-developed axial velocity contours (W/W_m) for turbulent flow with heat transfer using k-ε model.
(Re=33 333, H/d=25.2, $\omega=\Omega.d/W_m$, $Sw=\Omega.H/W_m$)

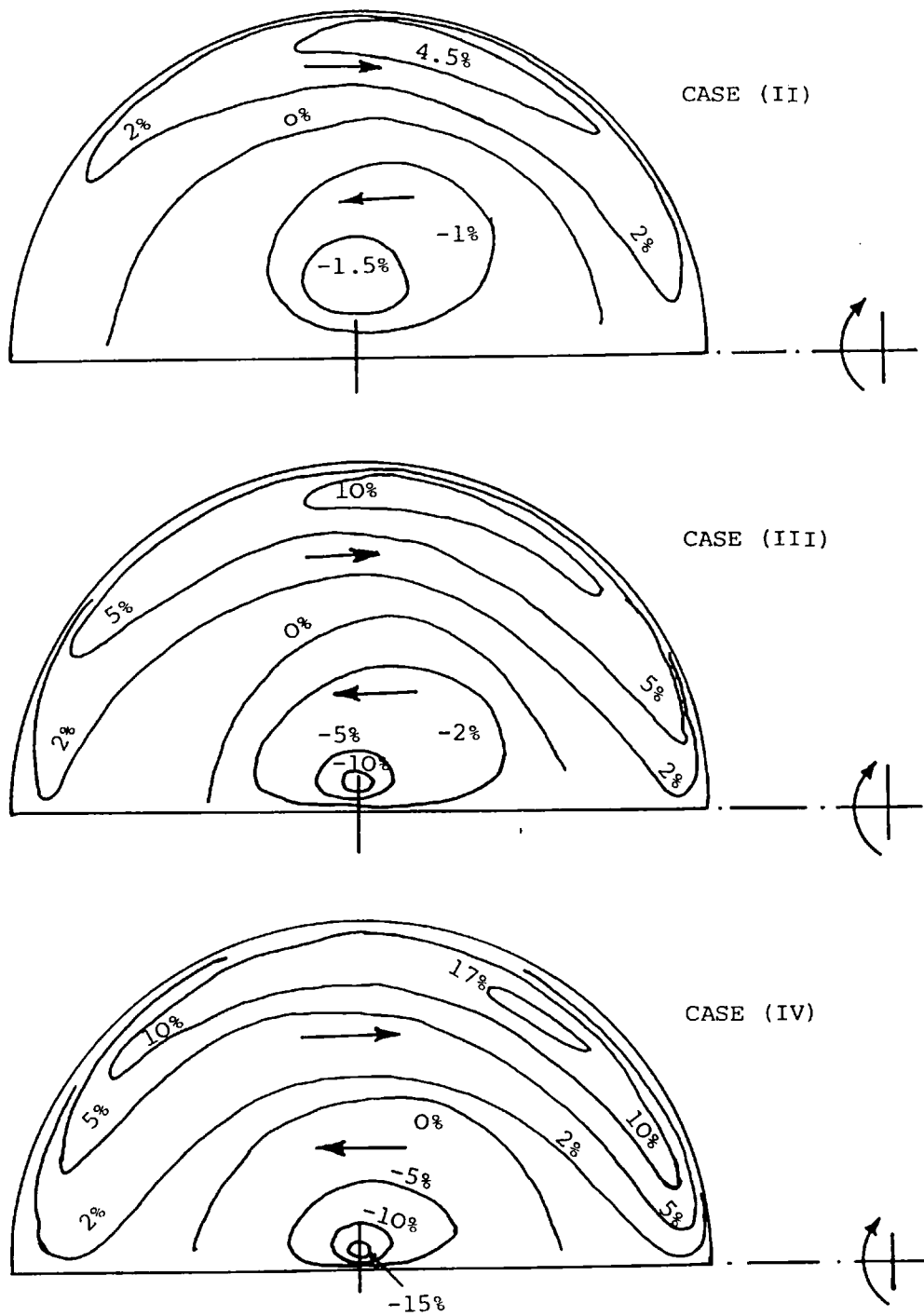


Fig.5.24 Fully-developed tangential velocity contours (U/W_m) for turbulent flow with heat transfer using k-ε model.

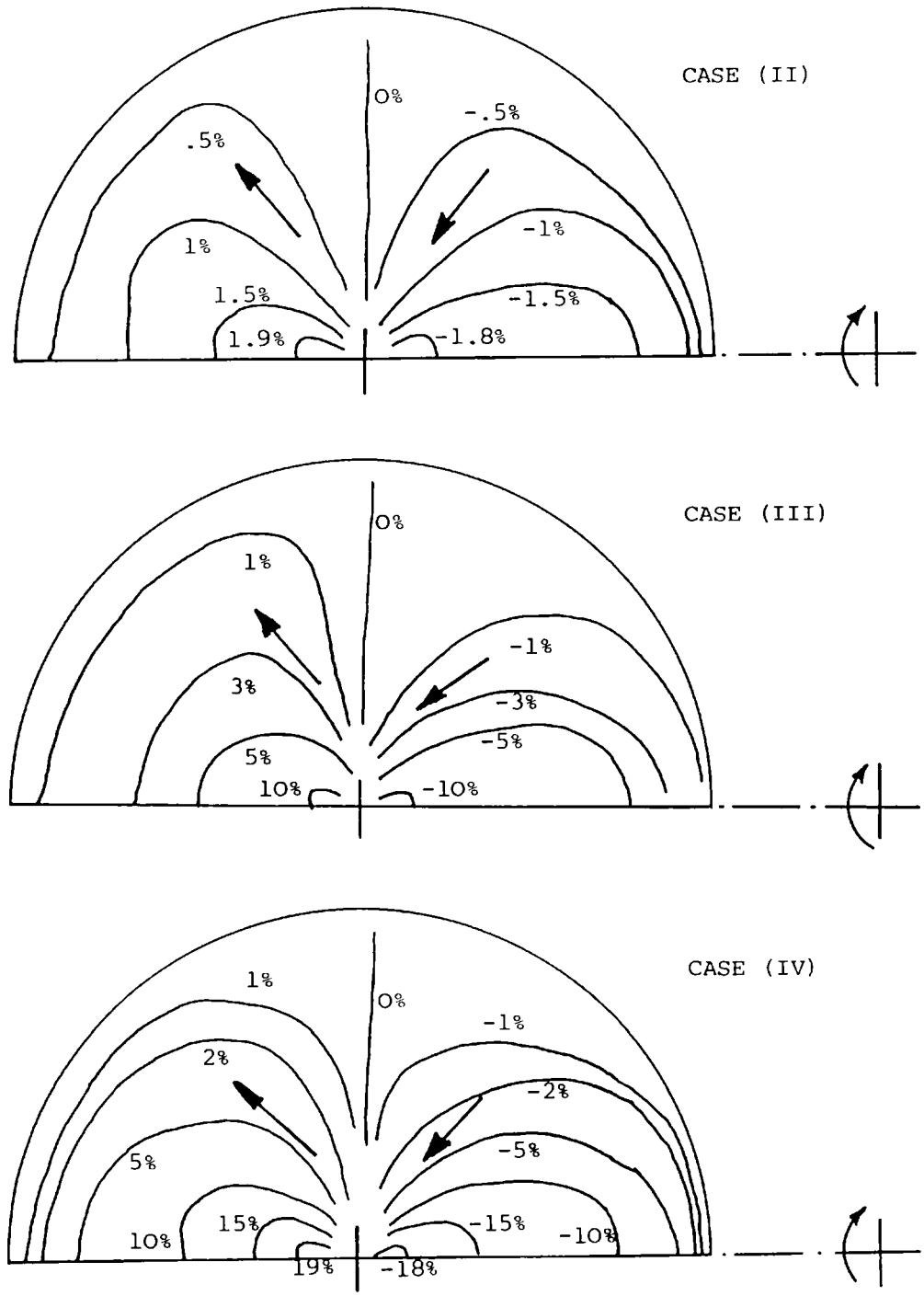


Fig.5.25 Fully-developed radial velocity contours (V/W_m) for turbulent flow with heat transfer using k-ε model.

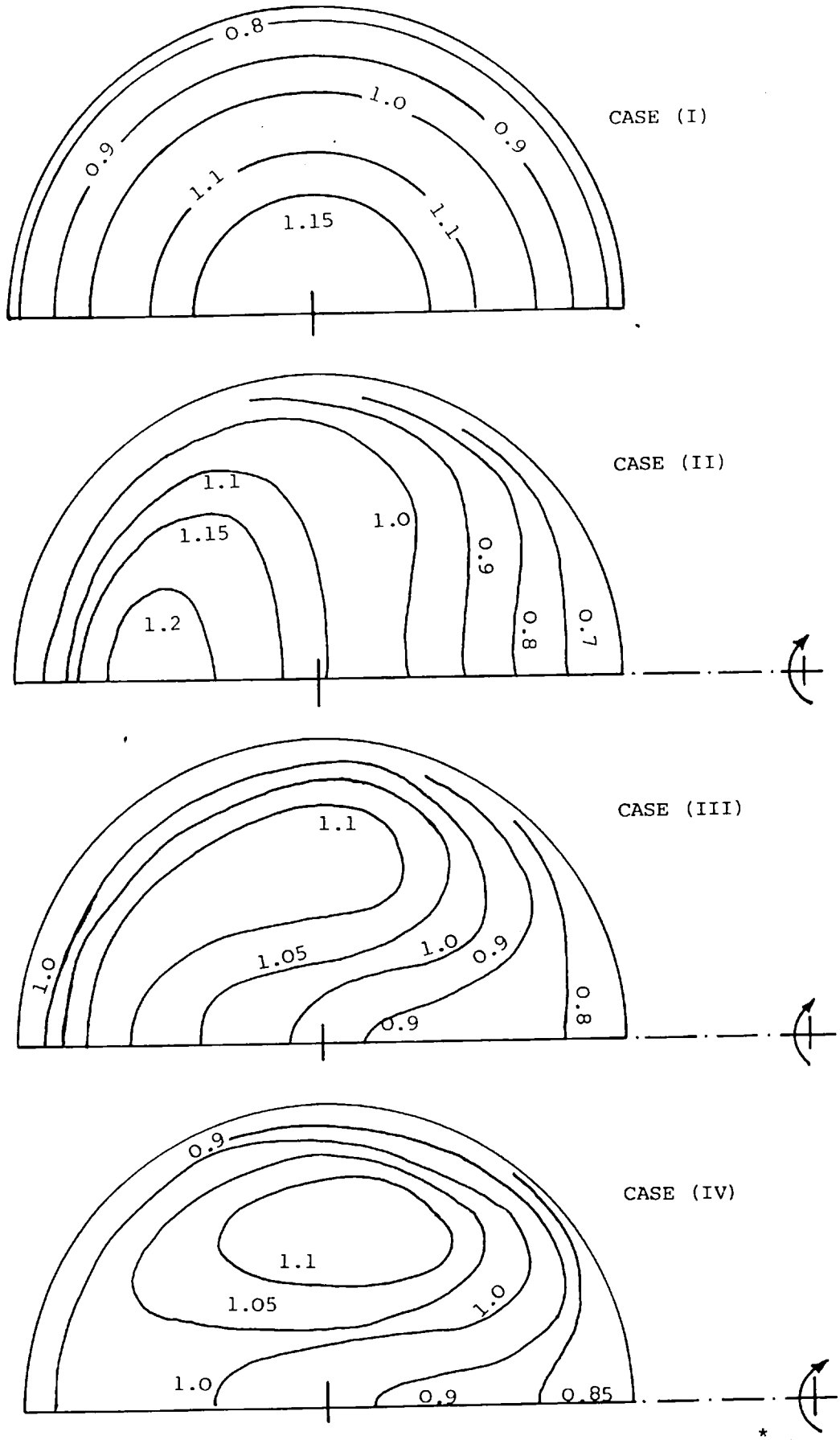


Fig.5.26 Fully-developed dimensionless temperature contours $T^{*}=(T_{w}-T)/(T_{w}-T_{m})$ for turbulent flow with heat transfer using k-ε model.

dimensionless preessure contours are shown in fig.5.27. There is a little disturbance in the region near the centre of the duct for case III, and this is may be due to the coarse grid chosen for the numerical solution. The predicted pressure, in general, behaves as expected; the lateral pressure difference is increased with the rotational speed, with the higher pressures outside the centre of rotation. Fig.5.28 shows the dimensionless kinetic energy of turbulence contours.

5.2.4 Turbulent Flow With Heat Transfer Using The Algebraic Heat Flux Model

The same four cases were recalculated using the algebraic Reynolds stress and heat flux models. The theoretical details are given in Appendix A2. Initially the algebraic models were tested for stationary pipe flow. Typical results are shown in Figs.A4.5 and A4.6 in Appendix A4. The grid used in prediction consisted of 10 uniform spaced nodes in both tangential and radial directions. The smaller number of nodes used permitted extra storage for the extra variables (e.g. different Reynolds stresses and heat fluxes). Due to the absence of full information of the different Reynolds stresses and heat fluxes at the inlet of the parallel rotating ducts, the fully-developed case was solved using an iterative procedure. The repeated converged solution was obtained approximately after 400 iterations, as shown in Fig.5.29. The under-relaxation factor for the different velocity componenets (U, V and W) was taken as 0.5, while the under-relaxation factor used for the scalar variables such as presure, temperature, kinetic energy of turbulence and dissipation rate of turbulence kinetic energy was 0.8, and no under-relaxation was used for the turbulent viscosity. Fig.5.29 shows the comparison of

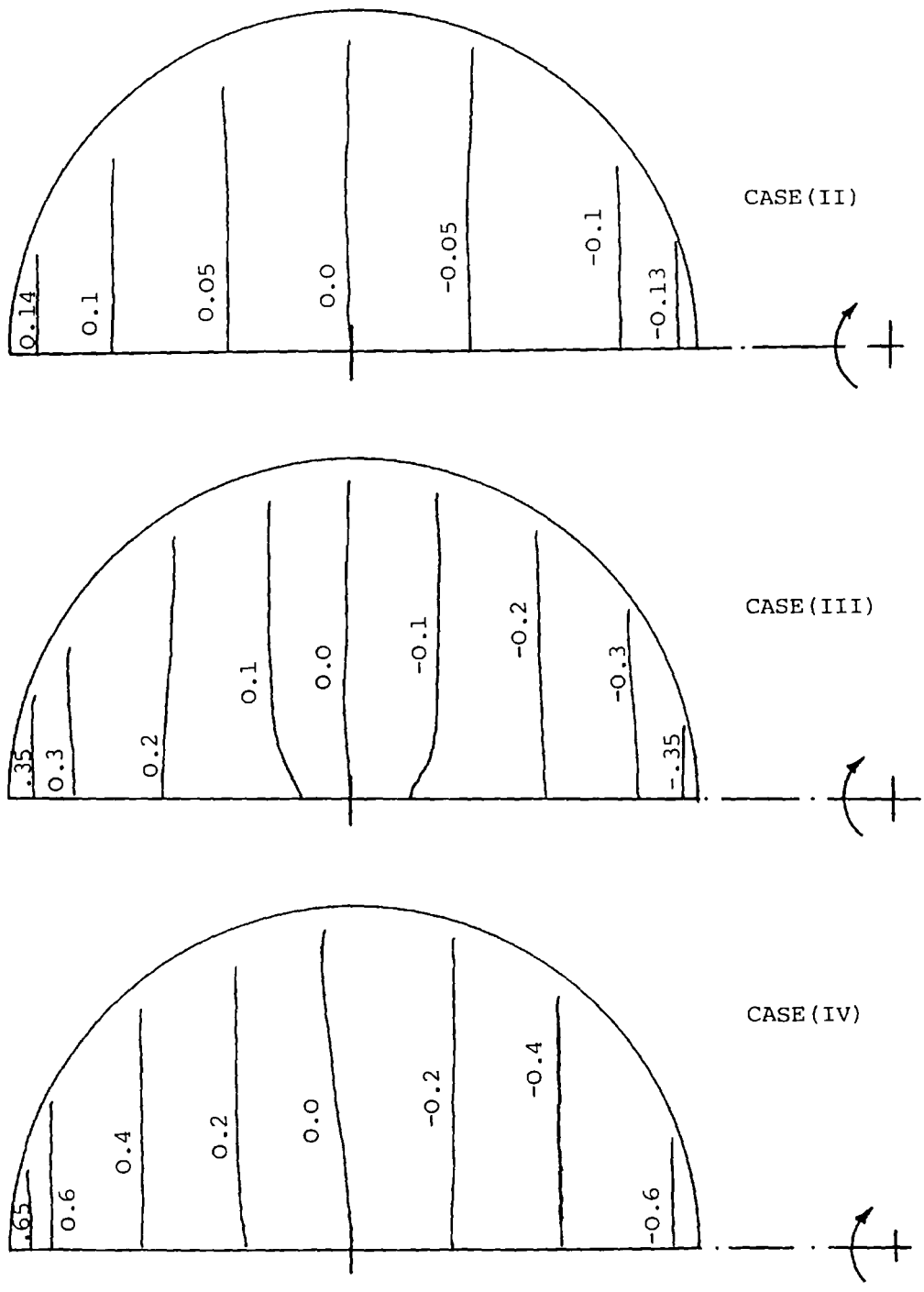


Fig.5.27 Fully-developed dimensionless pressure contours $(P-P_{CL})/\frac{1}{2}\rho W_m^2$ for turbulent flow with heat transfer using k-ϵ model.

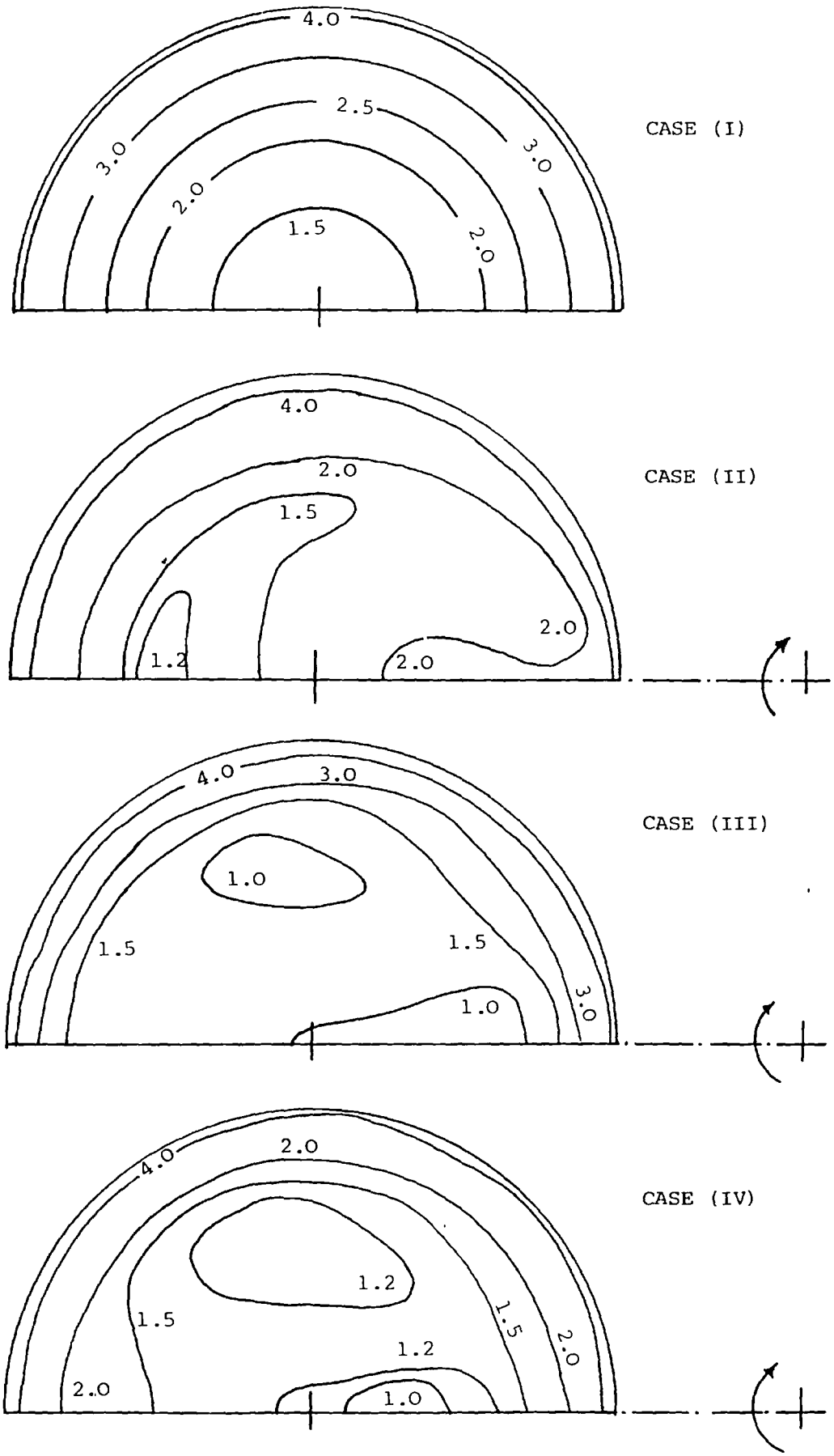


Fig.5.28 Fully-developed dimensionless turbulence energy contours $(k/u_{\tau_m}^2)$ for turbulent flow with heat transfer using k-ε model.

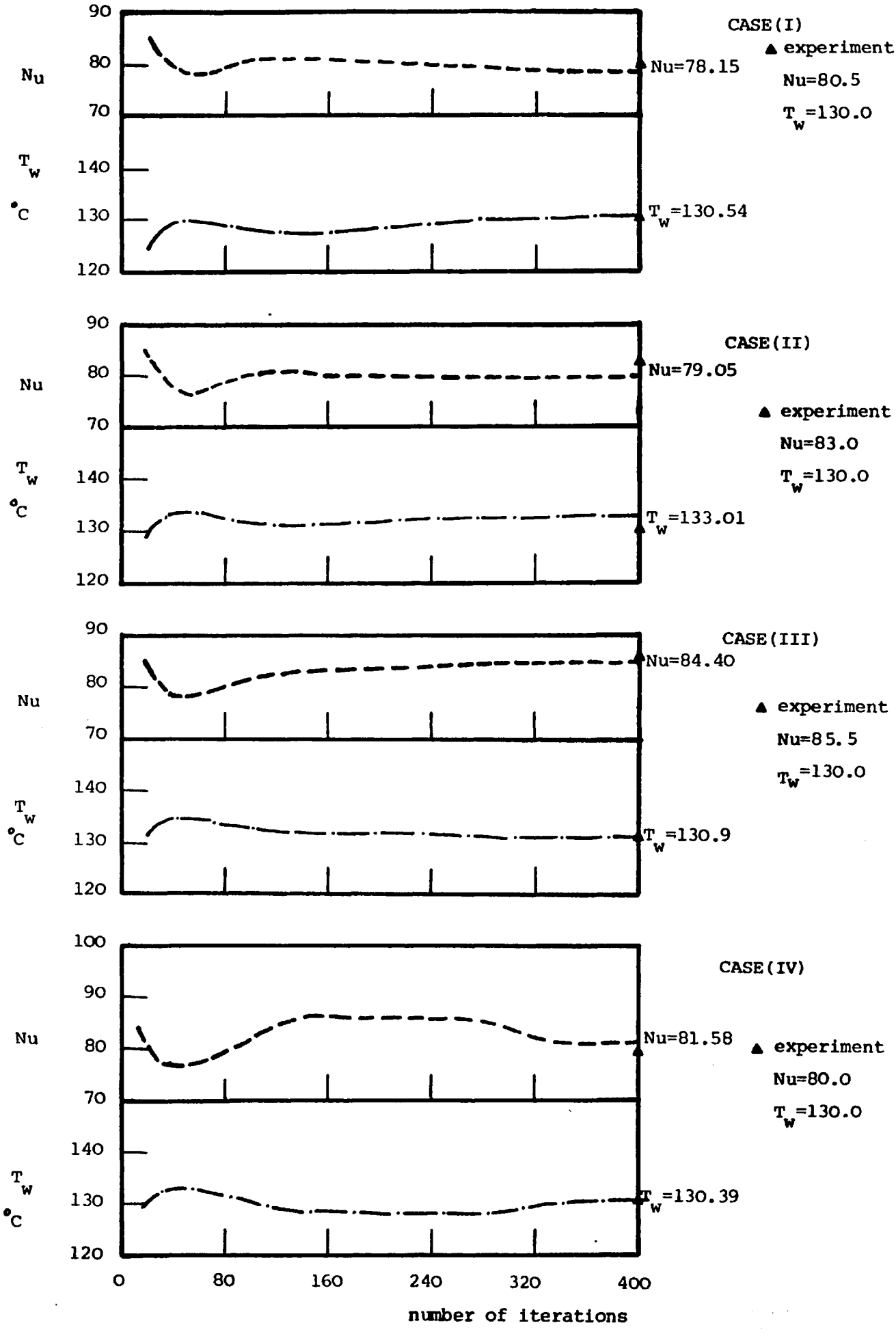


Fig.5.29 Variation of Nusselt number and wall temperature with number of iterations (heat flux model used) and comparison with data of STEPHENSON, 1982 is shown.

the predicted wall temperature and Nusselt number with the experimental data for different cases. Good agreement is obtained for the wall temperature; the maximum difference is 2.3% for case II. For the Nusselt number the maximum difference is 4.8% for case II. The algebraic Reynolds stress and heat flux models appear to give better results than the k-ε model for this complex flow. The corresponding predicted fully-developed axial velocity contours are shown in Fig.5.30. When comparing the axial velocity contours with the results using the k-ε model which are shown in Fig.5.23, it was noticed that the algebraic and heat flux models give more distorted contours, especially for high rotation, which means that the more complex turbulence models are able to predict high steep gradients of the flow due to high body forces effects as is expected because these models take into consideration the anisotropy behaviour of the turbulent diffusivities in the different directions in the flow. A similar result is clearly shown for the dimensionless temperature contours in Fig.5.31 compared with that of Fig.5.26 for the k-ε model. The maximum value of the axial velocity and the dimensionless temperature are displaced from away the symmetry line for case IV with very high rotation, due to the effect of strong body forces. This displacement is also observed in the k-ε model results. The corresponding lateral velocities are shown in Figs.5.32 and 5.33 for tangential and radial componenets respectively. For case IV, the maximum tangential velocity near the centre of the duct is 20% of the mean velocity, which is about 18% higher than the k-ε model result, and the maximum radial velocity is 24% of the mean velocity, which is 26% higher than the k-ε model value. For the other cases, no considerable changes are shown. Different variables (such as pressure, turbulence energy, different Reynolds stresses and different heat fluxes) are shown, as

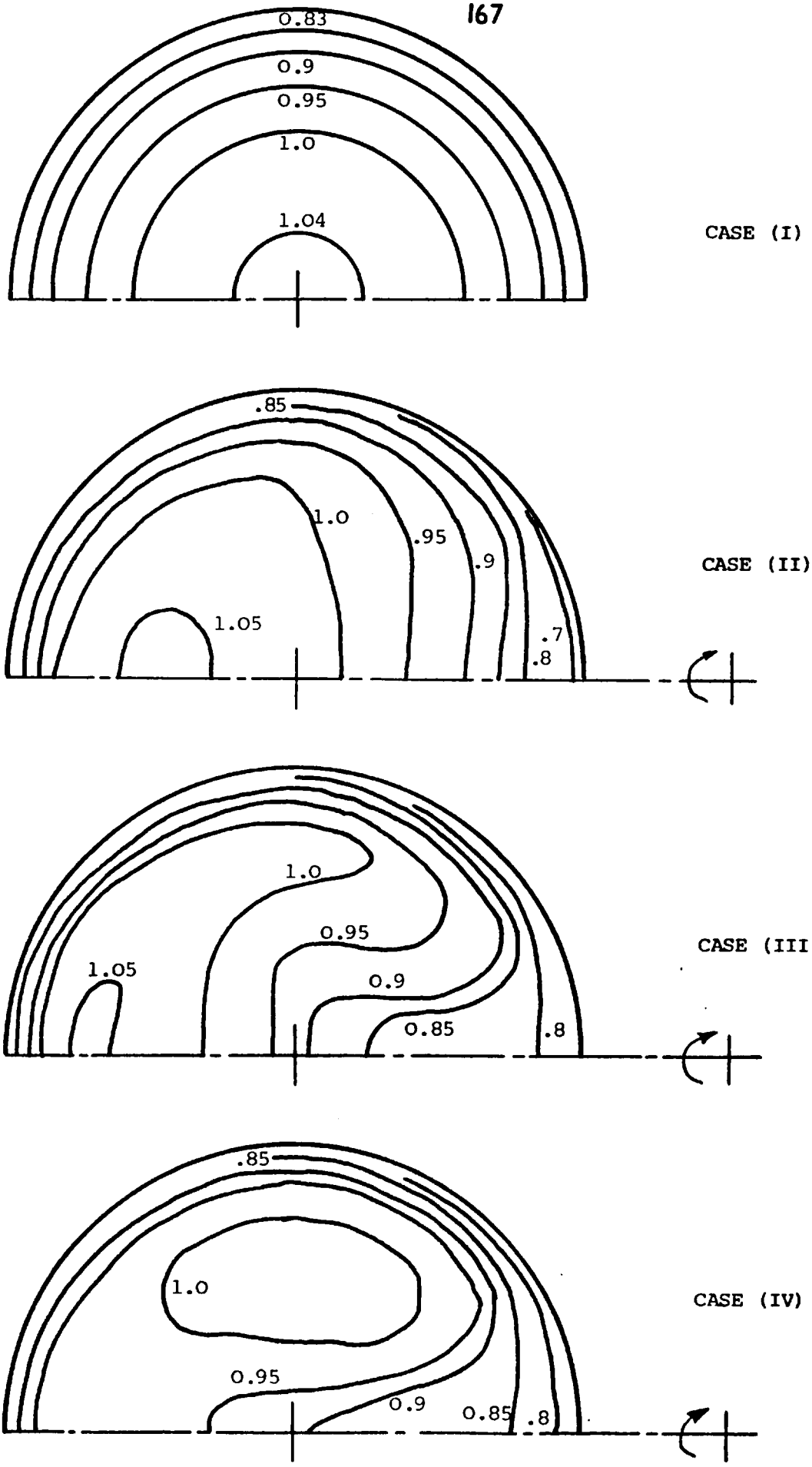


Fig.5.30 Fully-developed axial velocity contours (W/W_m) for turbulent flow with heat transfer. (heat flux model used)

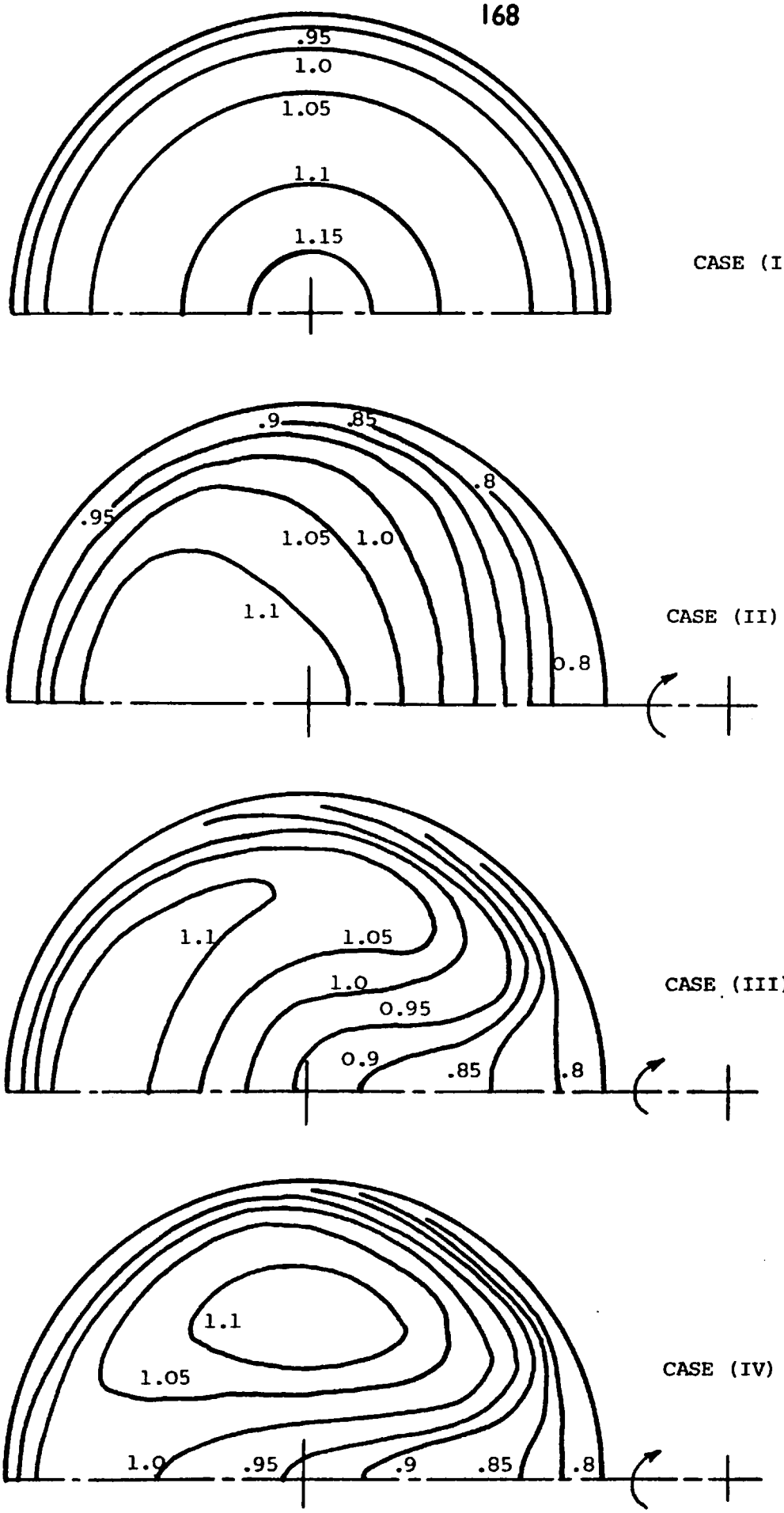


Fig.5.31 Fully-developed dimensionless temperature contours $T^* = (T_w - T)/(T_w - T_m)$ for turbulent flow with heat transfer. (heat flux model used)

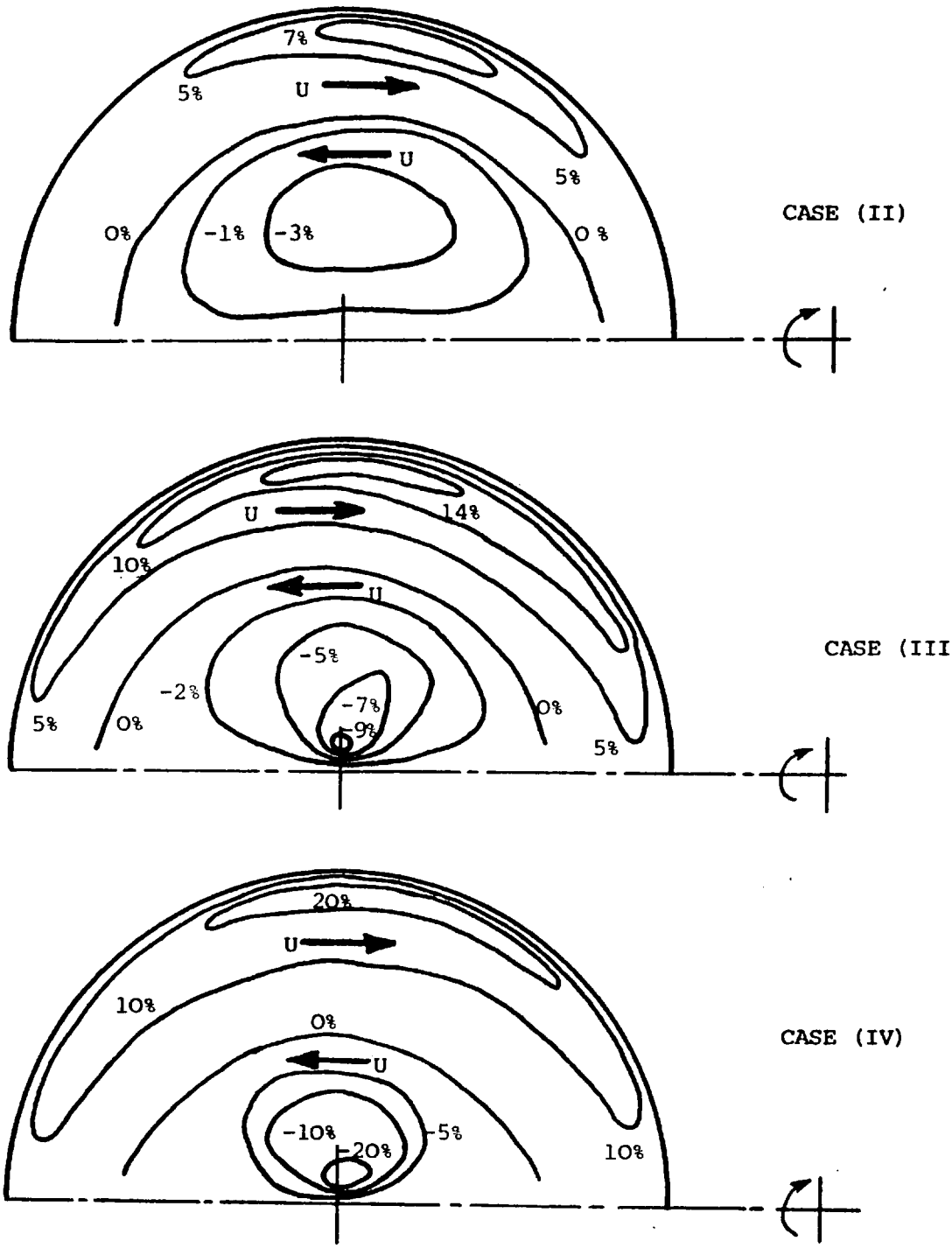


Fig.5.32 Fully-developed tangential velocity countours $(U/W_m)_{x100\%}$ for turbulent flow with heat transfer.

heat flux model used.

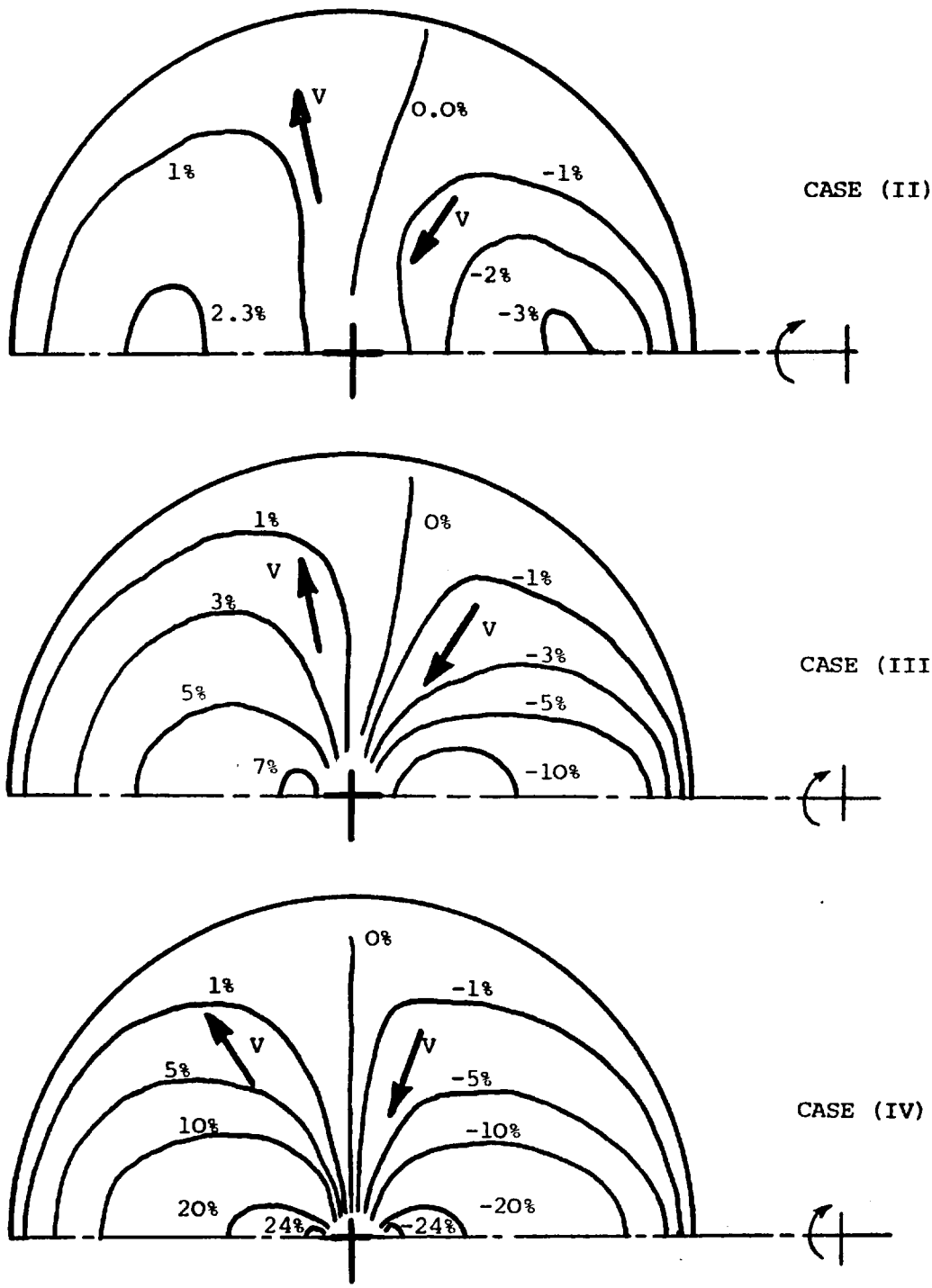


Fig.5.33 Fully-developed radial velocity countours (V/W_m)x100% for turbulent flow with heat transfer. heat flux model used.

dimensionless contours, in the remaining figures from 5.34 to 5.44. The final plot, Fig.5.45, shows the tangential/radial ratio of turbulent heat diffusivities for the rotating ducts. This ratio, which is assumed to be unity in the k-ε, uniform turbulent Prandtl number model, reaches higher values, in the outside region of the duct, which account, no doubt, for many of the differences in model predictions shown in previous figures. This ratio is not a well-behaved two-dimensional function, but a complex three-dimensional function strongly dependent on the boundary conditions.

5.3 Concluding Remarks

It is seen that there is large discrepancy between predicted results and measurements in the entrance region of the duct. This discrepancy is due to the assumption of the inlet boundary conditions which are far from reality, but unfortunately there is no detailed measurements for this type of flow. At the same time the inlet conditions are dependent on the geometry of the plenum chamber and the entrance to the test section, which vary for different experimental arangements, and it is difficult to generalize the inlet profile. Thus it is better to solve the fully-developed case with initial guesses for velocity, pressure, temperature etc.

The algebraic Reynolds stress and heat flux models are probably superior than k-ε model with uniform turbulent Prandtl number for this type of complex flow, because they take into consideration the variations of shear stresses and heat fluxes in different directions. But in the same time, these models require more storage space in the computer, and to obtain better results fine grids are required, hence extra storage space is required.

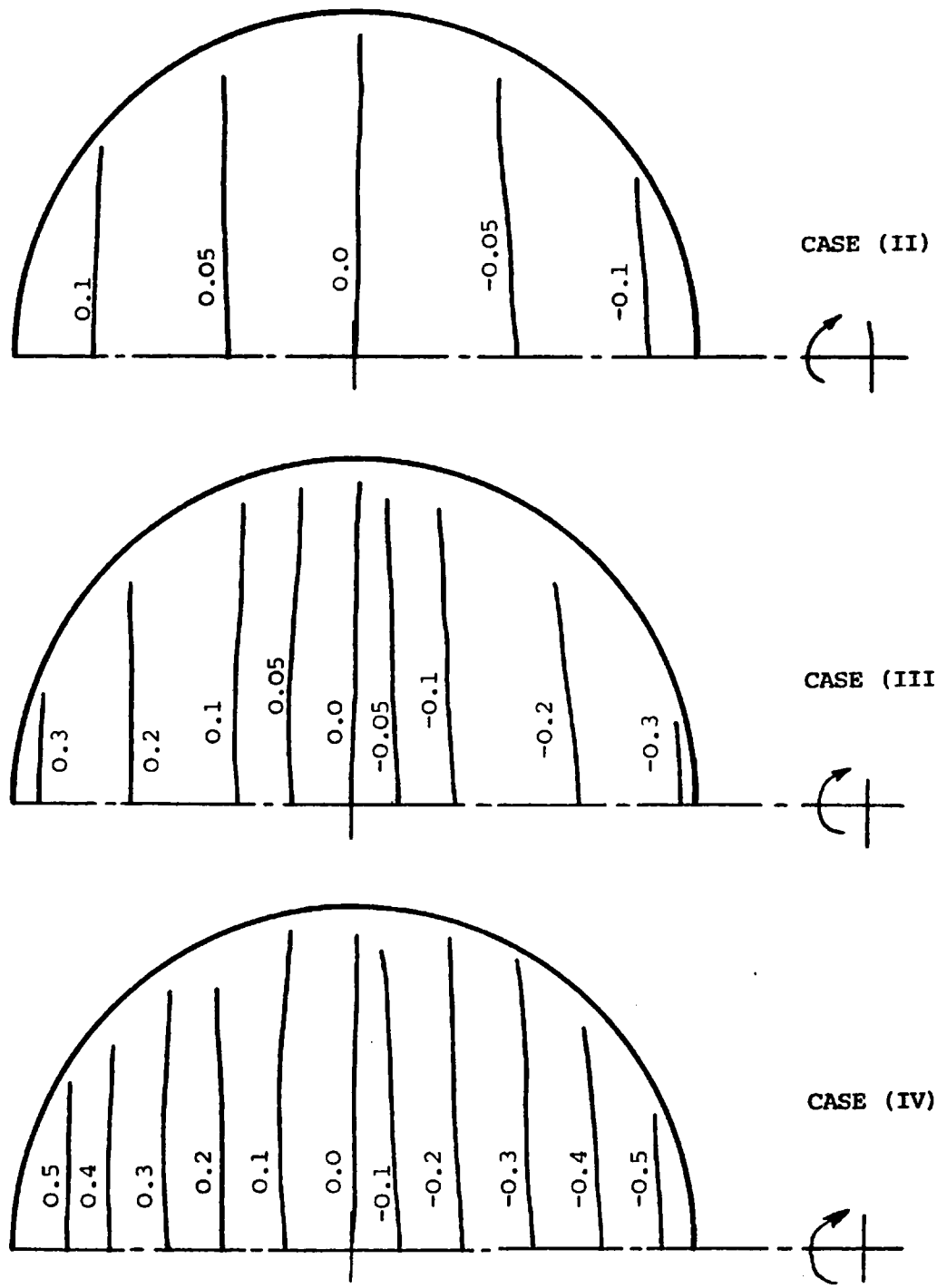


Fig.5.34 Fully-developed dimensionless pressure contours $(P-P_{cl})/(\frac{1}{2}\rho W_m^2)$ for turbulent flow with heat transfer. (heat flux model used)

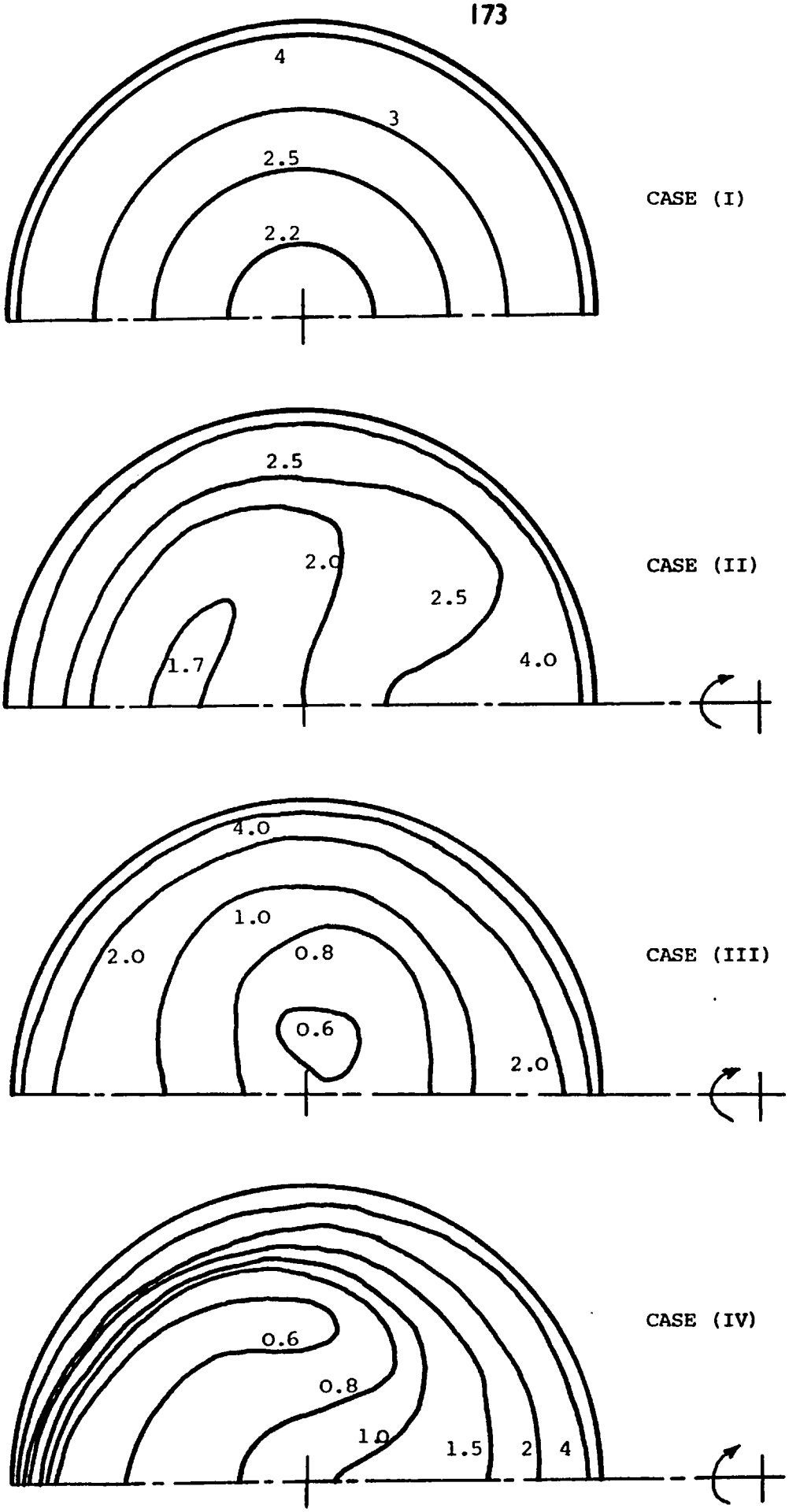


Fig.5.35 Fully-developed dimensionless turbulence energy contours (k/u_τ^2) for turbulent flow with heat transfer.

(heat flux model used)

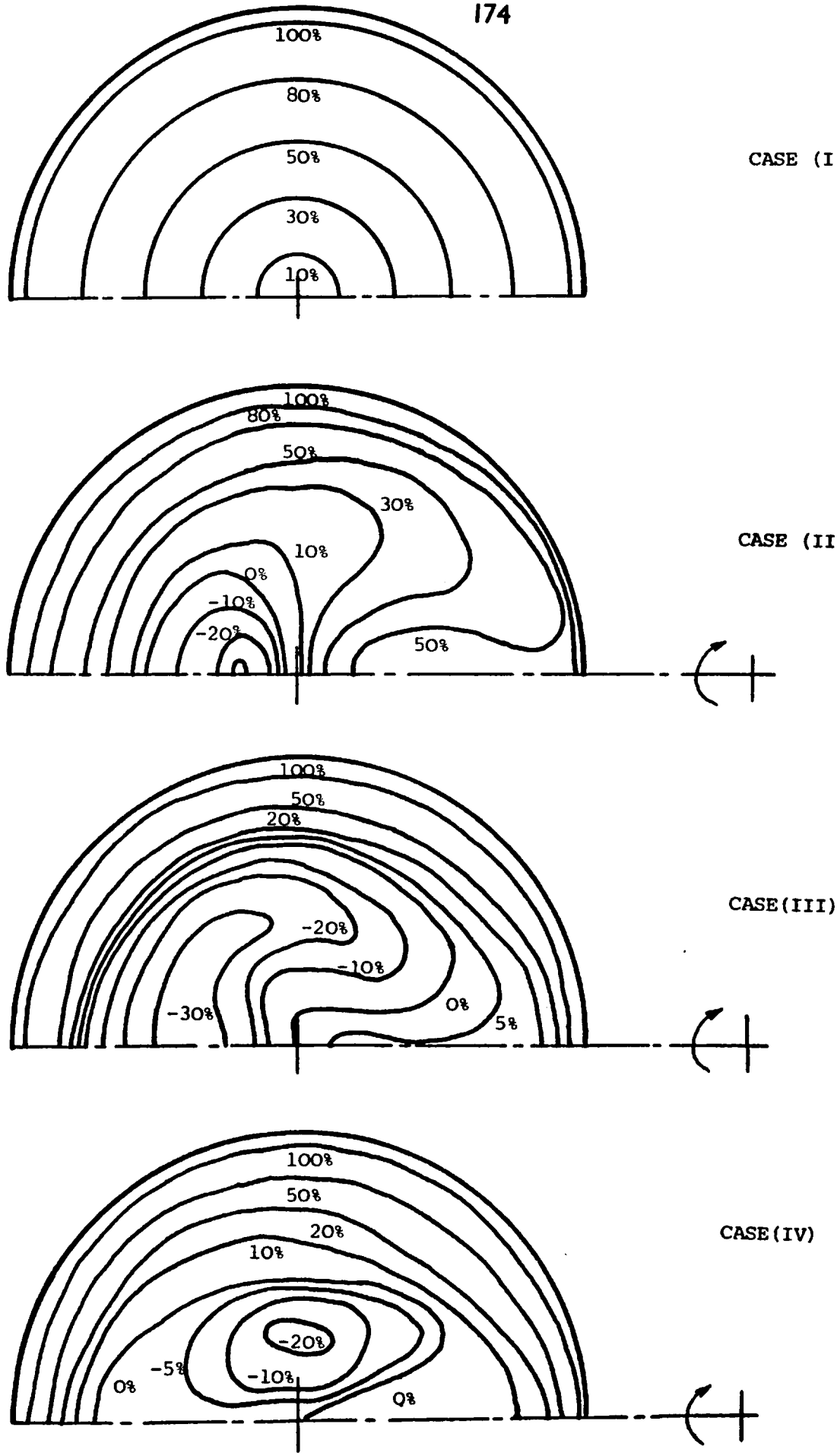


Fig.5.36 Fully-developed Reynolds stress contours ($\overline{vw}/u_{\tau_m}^2$) for turbulent flow with heat transfer.

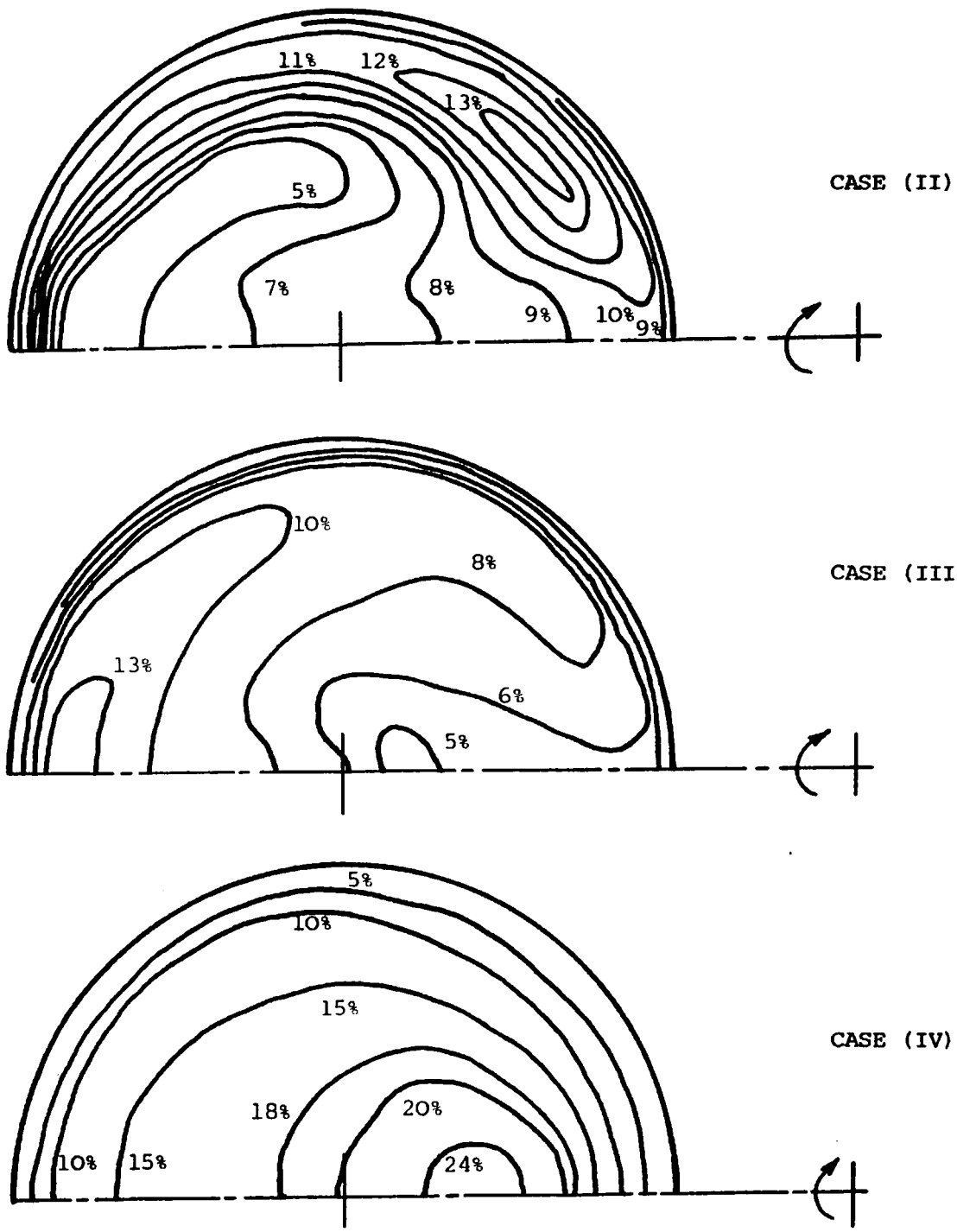


Fig.5.37 Fully-developed Reynolds stress contours $(\overline{uv}/u_{\tau_m}^2)$ for turbulent flow with heat transfer.
(heat flux model used)

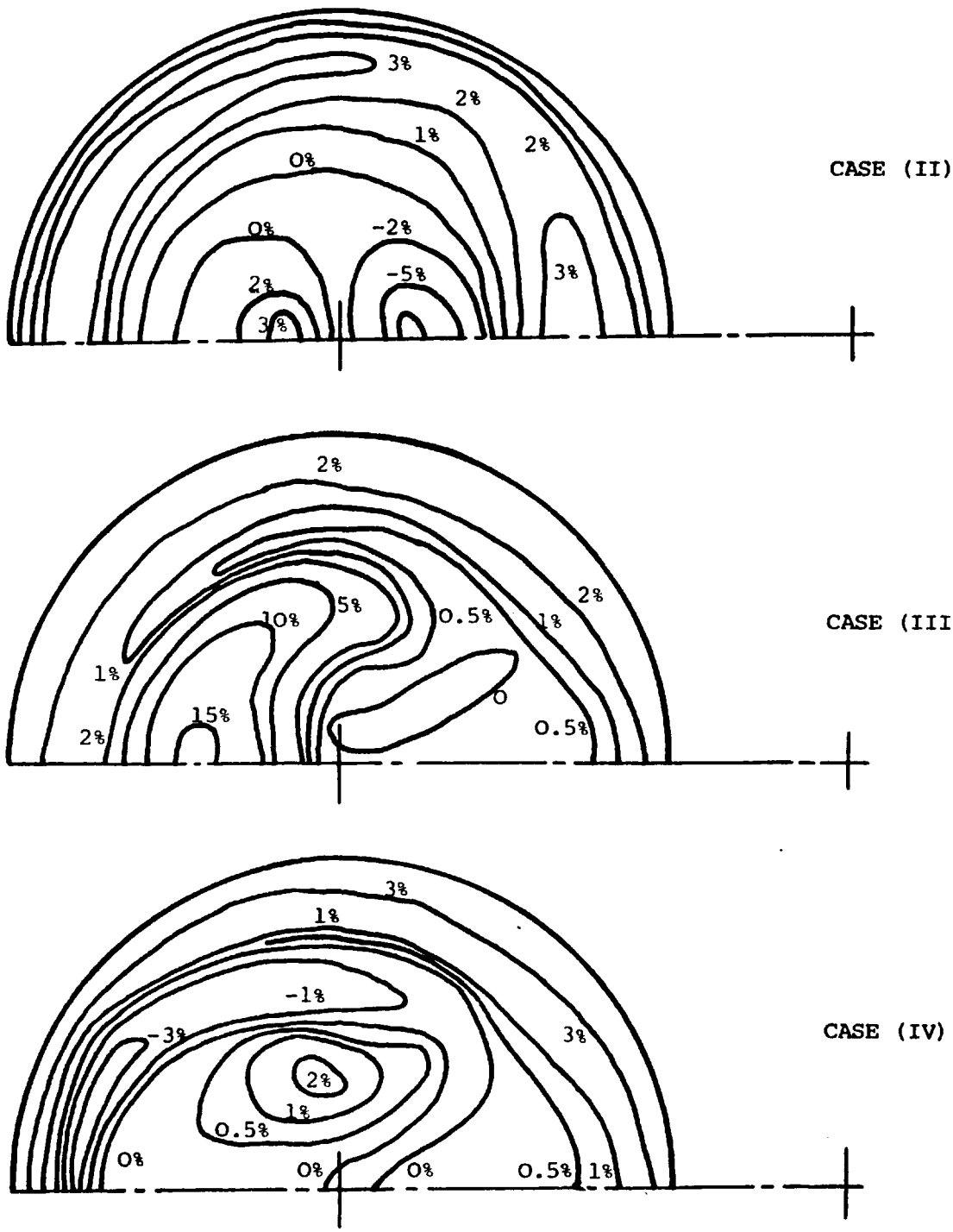


Fig.5.38 Fully-developed Reynolds stress contours ($\overline{uw}/u_{\tau_m}^2$) for turbulent flow with heat transfer. (heat flux model used).

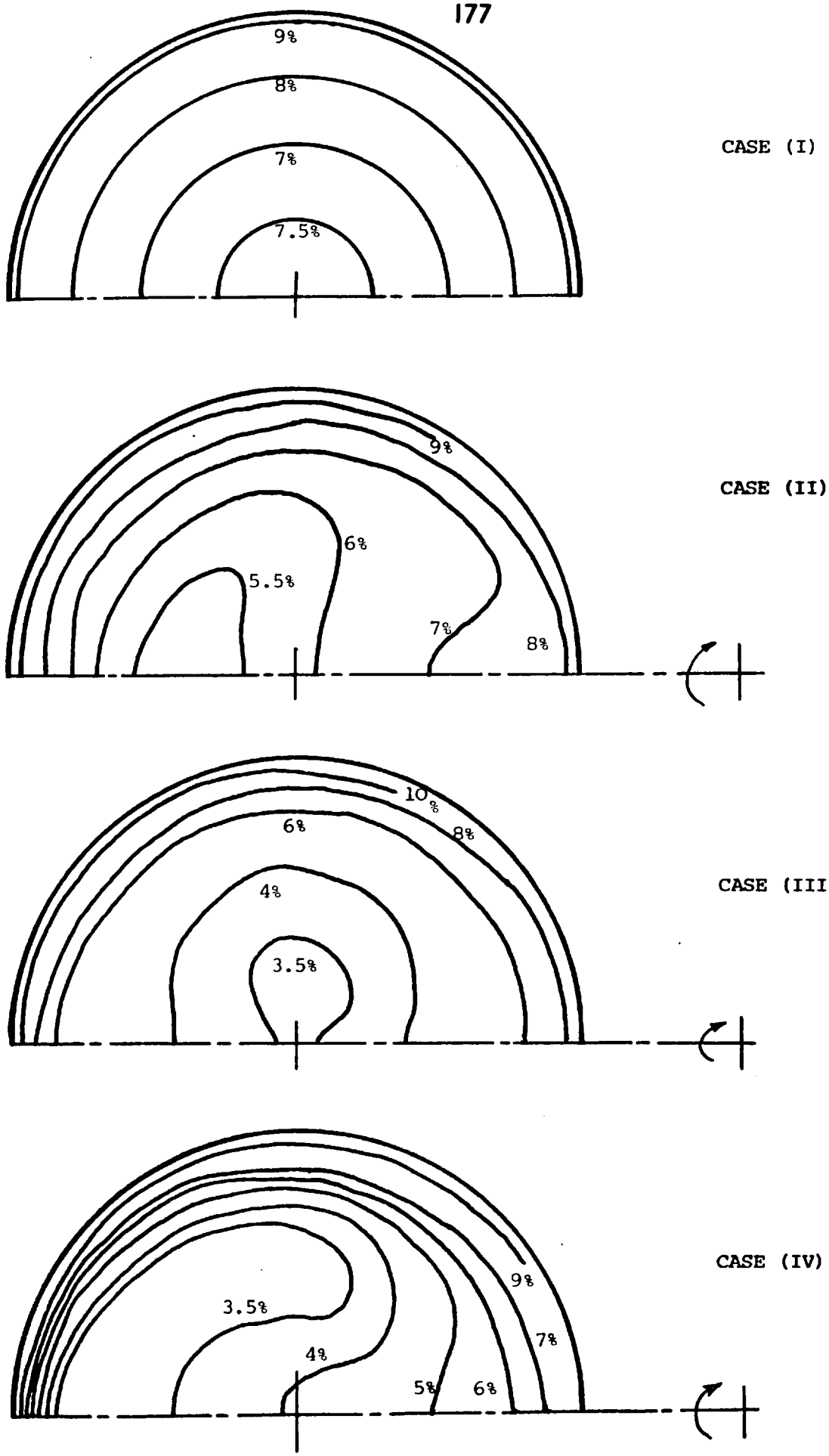


Fig.5.39 Fully-developed tangential turbulence intensity contours $(u/W_m)\times 100\%$ for turbulent flow with heat transfer.

(heat flux model used)

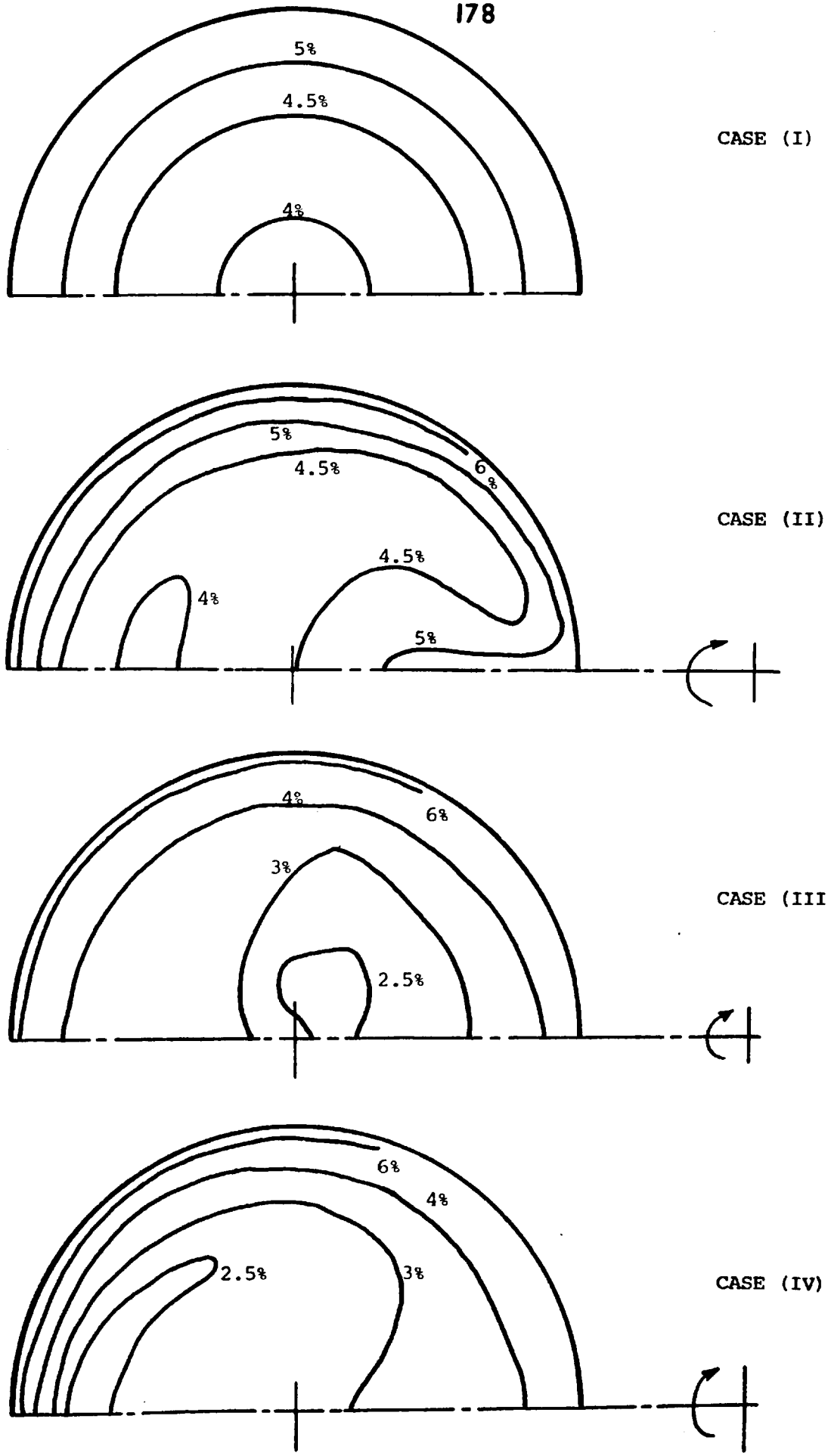


Fig.5.40 Fully-developed radial turbulence intensity contours $(v/W_m)\times 100\%$ for turbulent flow with heat transfer.

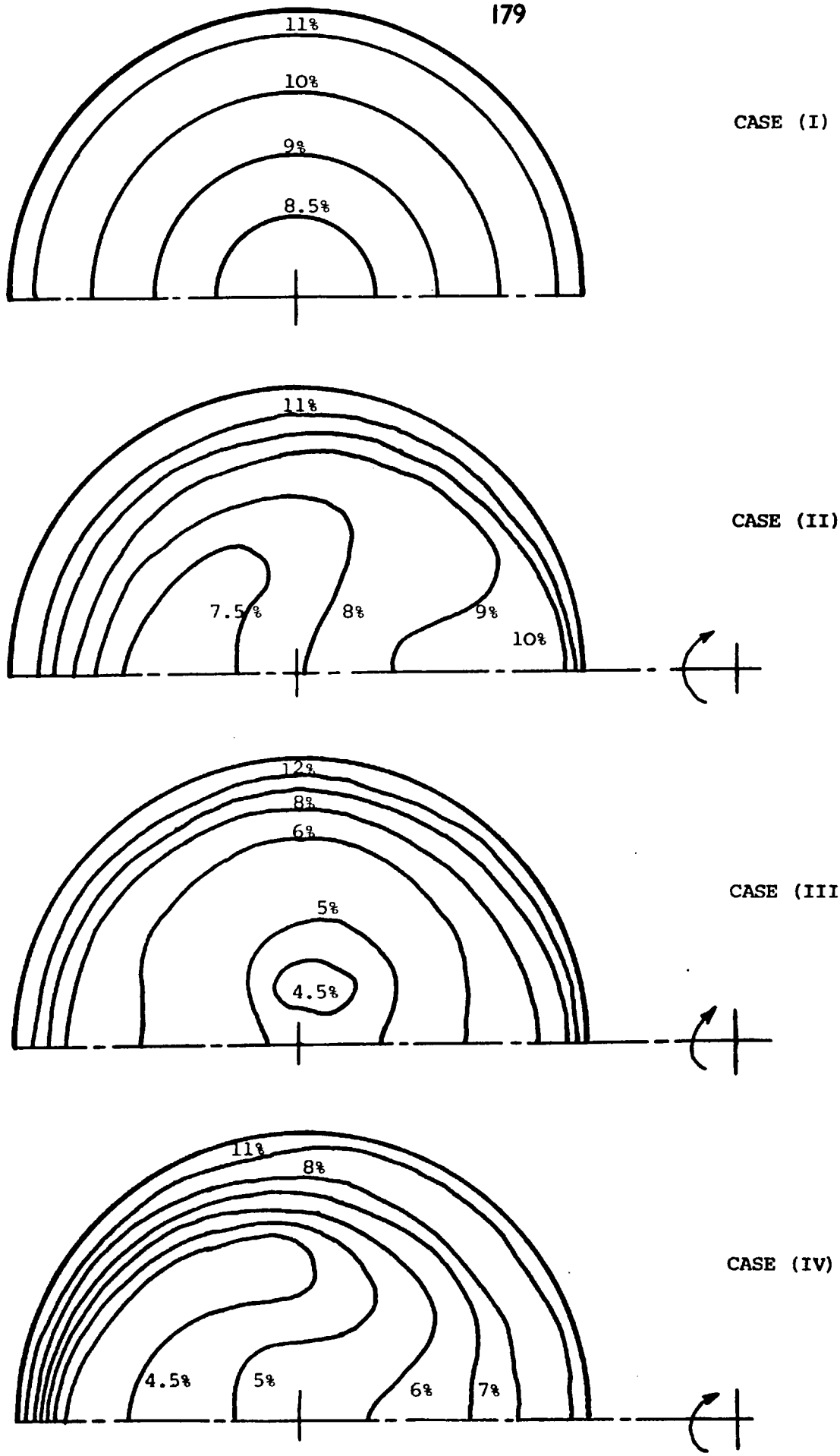


Fig.5.41 Fully-developed axial turbulence intensity contours $(W/W_m)\times 100\%$ for turbulent flow with heat transfer.

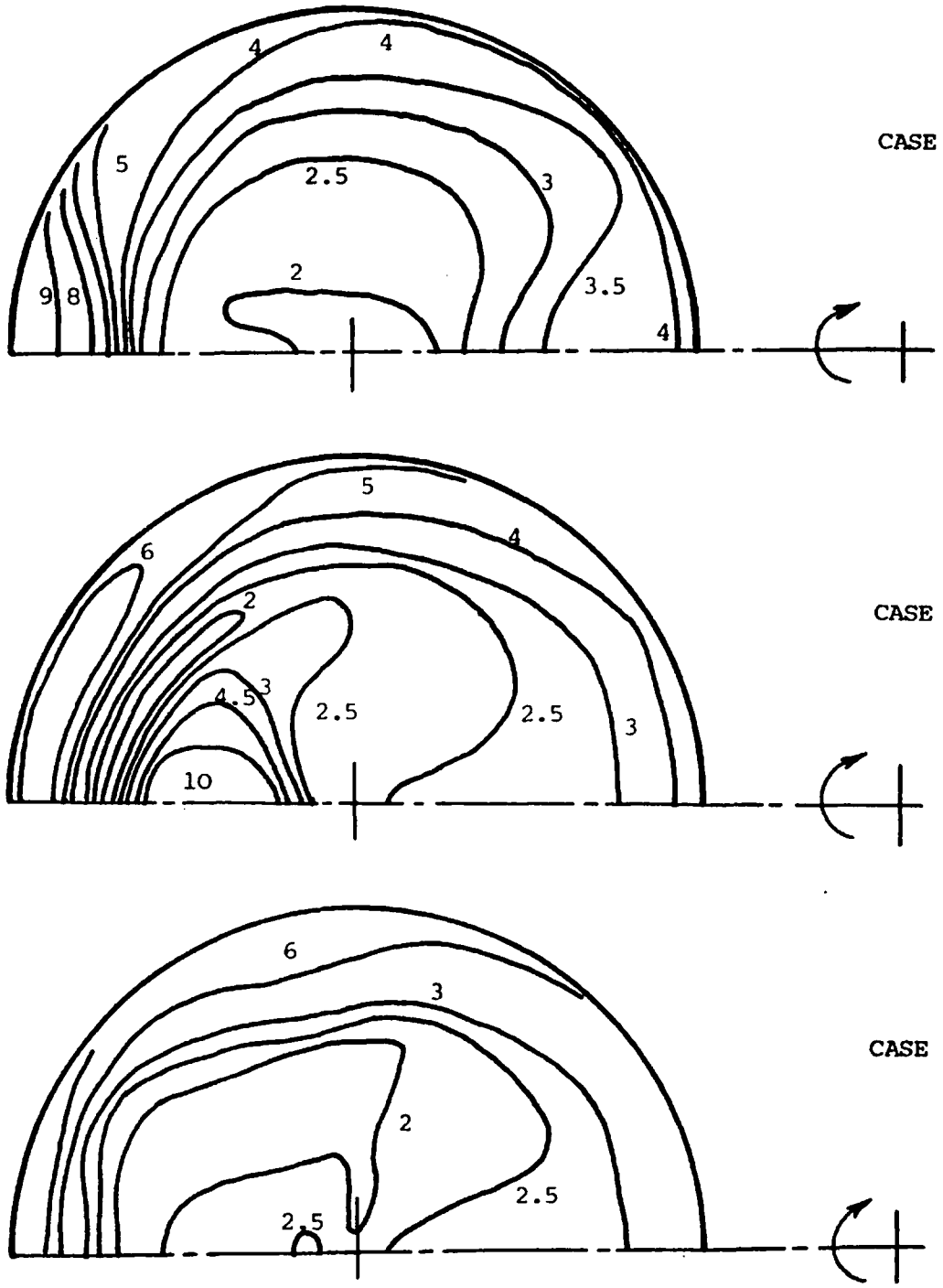
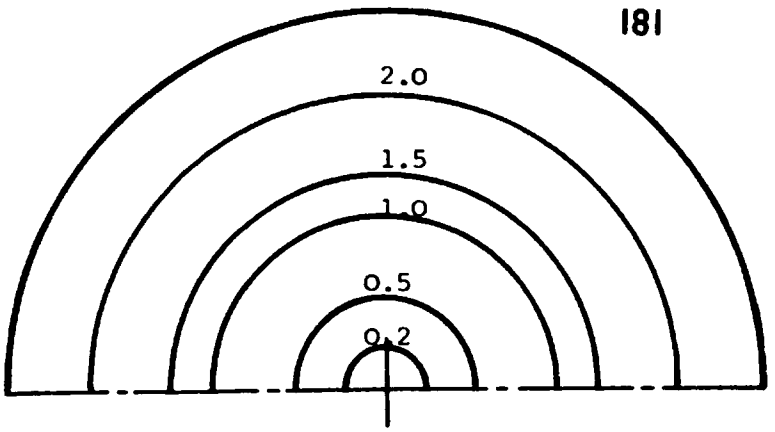
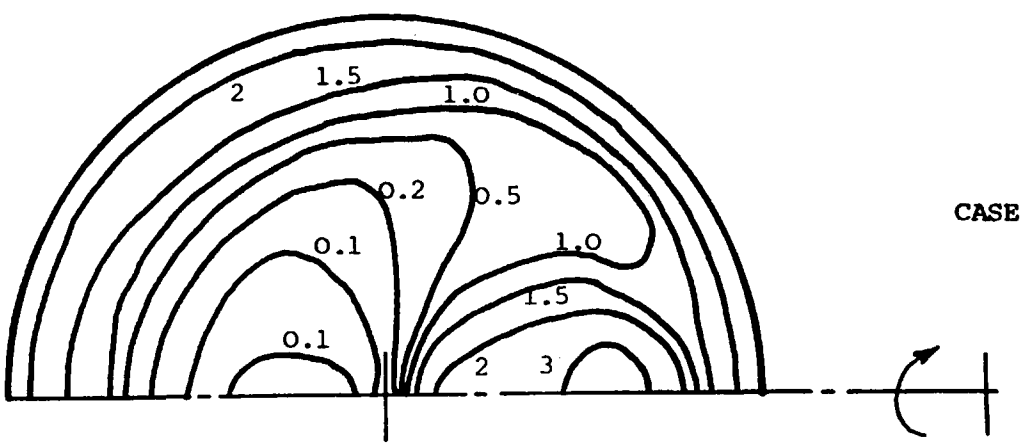


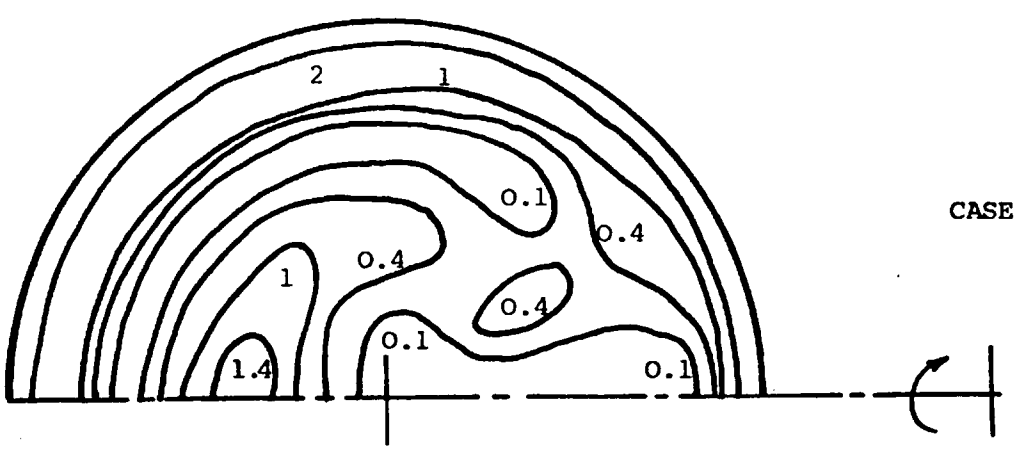
Fig.5.42 Fully-developed ratio of diffusivity of heat in tangential to radial direction contours (Γ_θ / Γ_r) for turbulent flow with heat transfer.
(heat flux model used)



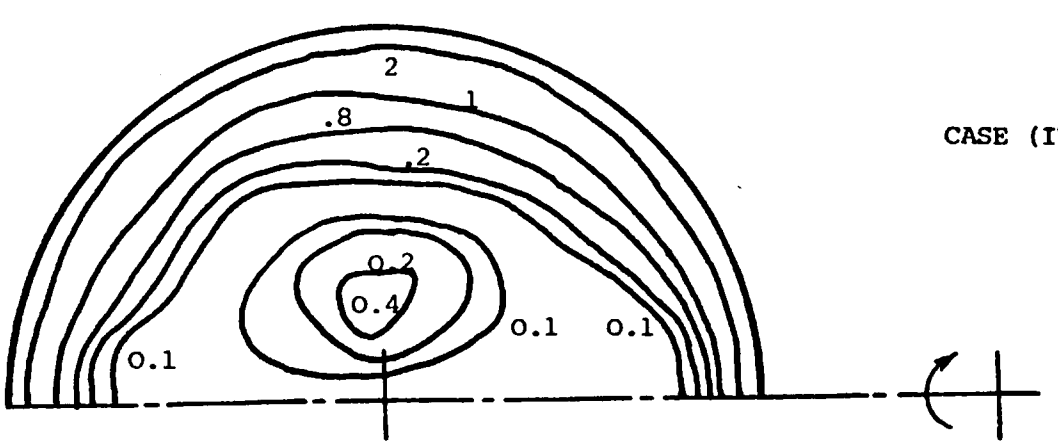
CASE (I)



CASE (II)

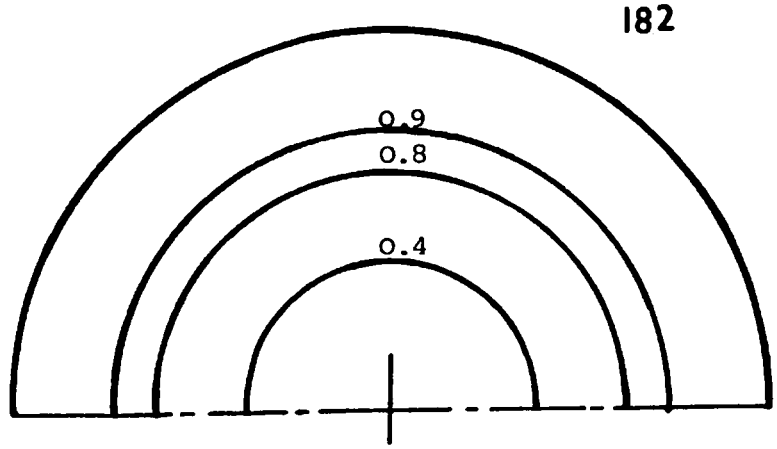


CASE (III)

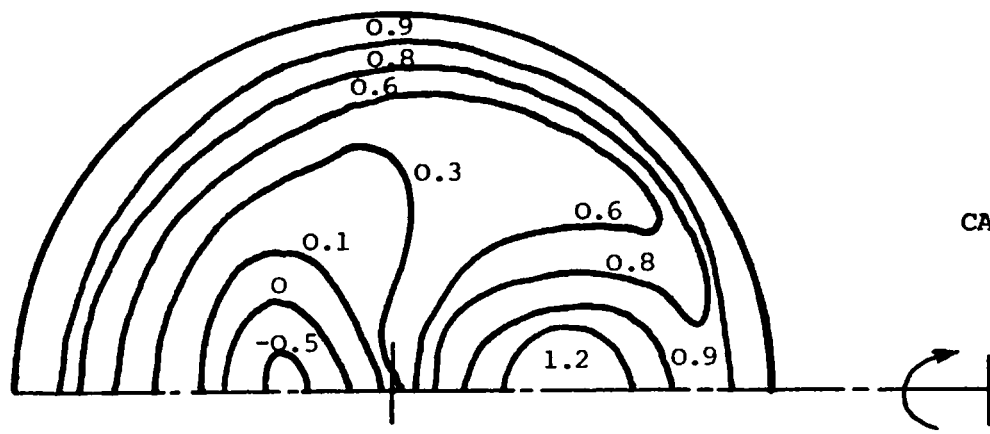


CASE (IV)

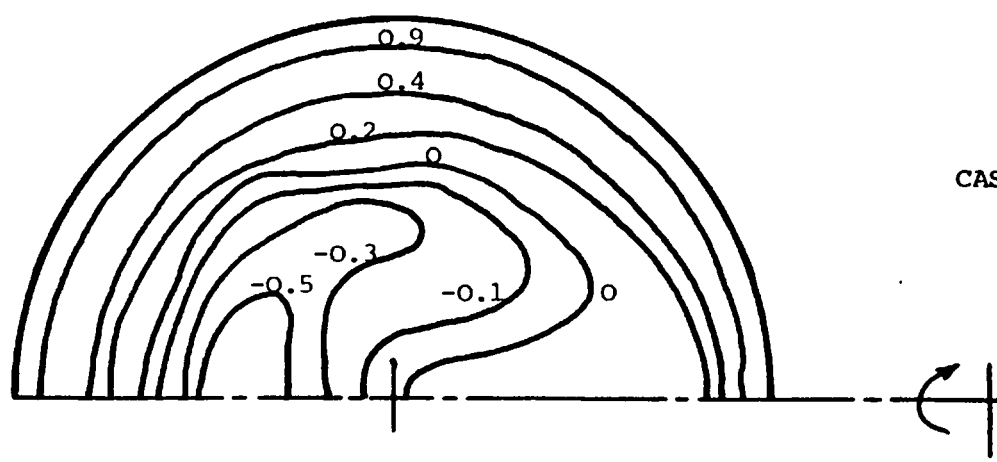
Fig.5.43 Fully-developed dimensionless axial heat flux contours ($\overline{wt}/u_\tau . C_\tau$) for turbulent flow with heat transfer. (heat flux model)



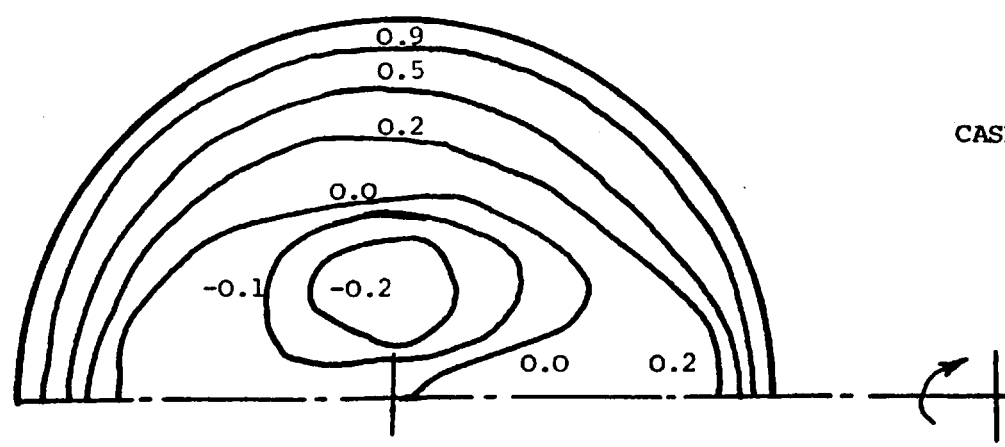
CASE (I)



CASE (II)



CASE (III)



CASE (IV)

Fig.5.44 Fully-developed dimensionless radial heat flux contours ($\overline{vt}/u_\tau.c_\tau$) for turbulent flow with heat transfer.

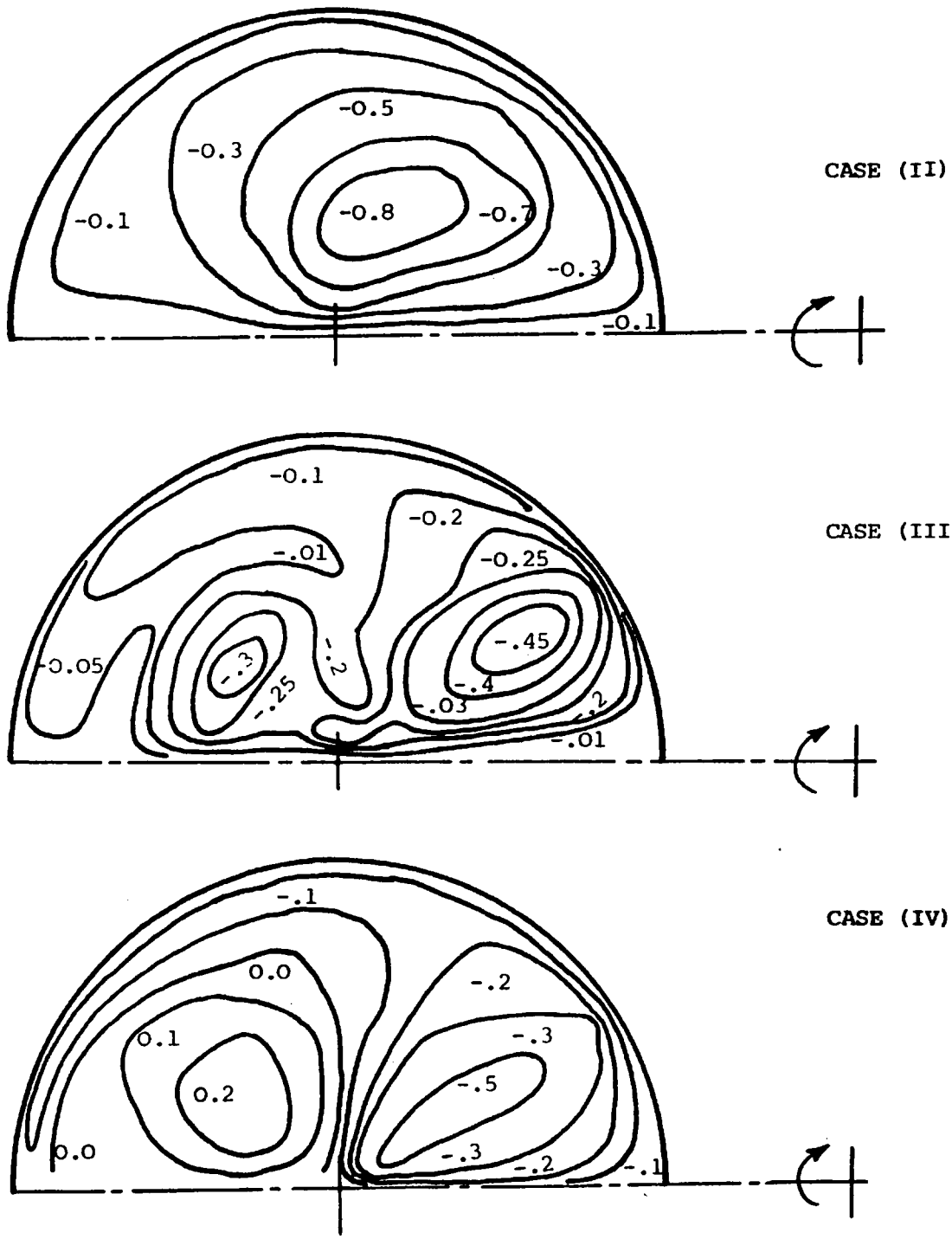


Fig.5.4 5 Fully-developed dimensionless tangential heat flux contours ($\overline{ut}/u_\tau.C_\tau$) for turbulent flow with heat transfer. (heat flux model used).

The detailed solution for the flow in parallel rotating ducts is useful to illustrate the similarity with the flow in bends which are shown in the next chapter. The analogies with similar flows, particularly asymmetrically heated pipe flows (with secondary flows due to buoyancy) are noticed. The main feature is the relative magnitude of the tangential thermal diffusivity with respect to the radial one. Ad-hoc assumptions were made in previous works in order to treat the ratio of the tangential to radial thermal diffusivities for this type of flow; Reynolds (1963) assumed that the tangential and radial diffusivities were equal throughout the flow, while Quarmby and Quirk (1972) found experimentally that the tangential to radial thermal diffusivities ratio was much greater than unity near the wall and appeared to be at least ten there, and fall steeply to become unity over the greater part of the flow. Chieng and Launder (1979) assumed, in their calculation, that the ratio of tangential/radial thermal diffusivities was equal to the ratio of the mean square velocity fluctuations in these directions. Samaraweera (1978) solved the transport equations for the turbulent fluxes and the thermal diffusivities were an outcome of the calculation rather than an input, and he found that the ratio of the diffusivities was a strongly three-dimensional function under conditions of strong three-dimensionality. These researches support the present result of non-isotropic eddy diffusivities in the rotating pipe flows.

CHAPTER 6

PREDICTION OF FLOW THROUGH BENDS OF CIRCULAR CROSS-SECTION

6.1 Introduction

The object of this part of the investigation is to check out the numerical solution method and the turbulence models against data from flow in stationary bends. A computer code was set up and tested first for laminar flow in mildly-curved ducts, using the marching solution procedure. Modifications were made to the marching procedure in order to take into consideration the axial pressure effects from downstream to upstream, and a so-called "partially-parabolic" solution procedure was obtained. This procedure was checked for laminar flow in strongly-curved ducts. The computer code was modified again to solve the turbulent flow in strongly-curved ducts using the k-ε model of turbulence.

The correct choice of method to be used for calculating the flow in bends is strongly dependent on the bend geometry. When the bend radius is large compared to the pipe diameter the thin shear layer approximation may be applied to the equations of motion and the equations solved by a "once-through" marching method (the parabolic procedure). For strongly curved bends the discarded terms must be retained, the flow conditions are dependent on downstream events, and consequently more elaborate iterative solution methods must be used. A useful time saving approximation to the full numerical treatment is provided by the so-called "partially-parabolic" method described earlier. The present calculations, and those of Pratap (1975),

suggest that a marching or parabolic procedure suffies only for bend flows with a radius ratio $R/r_o > 15$ and that for smaller values the partially-parabolic method at least is necessary.

The bend geometry used is illustrated in Fig.1.13. The governing equations are represented in the (r,θ,ϕ) coordinate system, as shown in Appendix A1.

6.2 **Laminar Flow**

6.2.1 Laminar Flow In A Mildly-Curved Duct

In this case, some data from Austin (1971), with $R/r_o=29.1$, were available for comparison with the results of computaion. With this mild curvature the marching method was appropriate. The fluid viscosity and density were assumed to be uniform throughout the flow domain. The computations were started at the 0^o plane of the bend with the inlet conditions prescribed to be those of a fully-developed pipe flow. Because the flow is symmetrical about the diameter in the plane of curvature, the finite-difference grid covered only a semi-circular sector of the cross-section, as shown in Fig.3.1. The finite-difference grid in the cross-sectional plane possessed 15 non-uniform intervals in the r-direction, and 11 uniform intervals in the θ-direction. The forward-step was chosen to be 0.05 degrees at the inlet of the bend, and was increased gradually up to a maximum value of 0.2 degrees. This grid gave sufficient accuracy by comparison with the results obtained using finer and coarser grids as shown in Fig.6.1.

Fig.6.2 displays the development of the axial-velocity field along the ϕ-direction for two Reynolds numbers compared with the

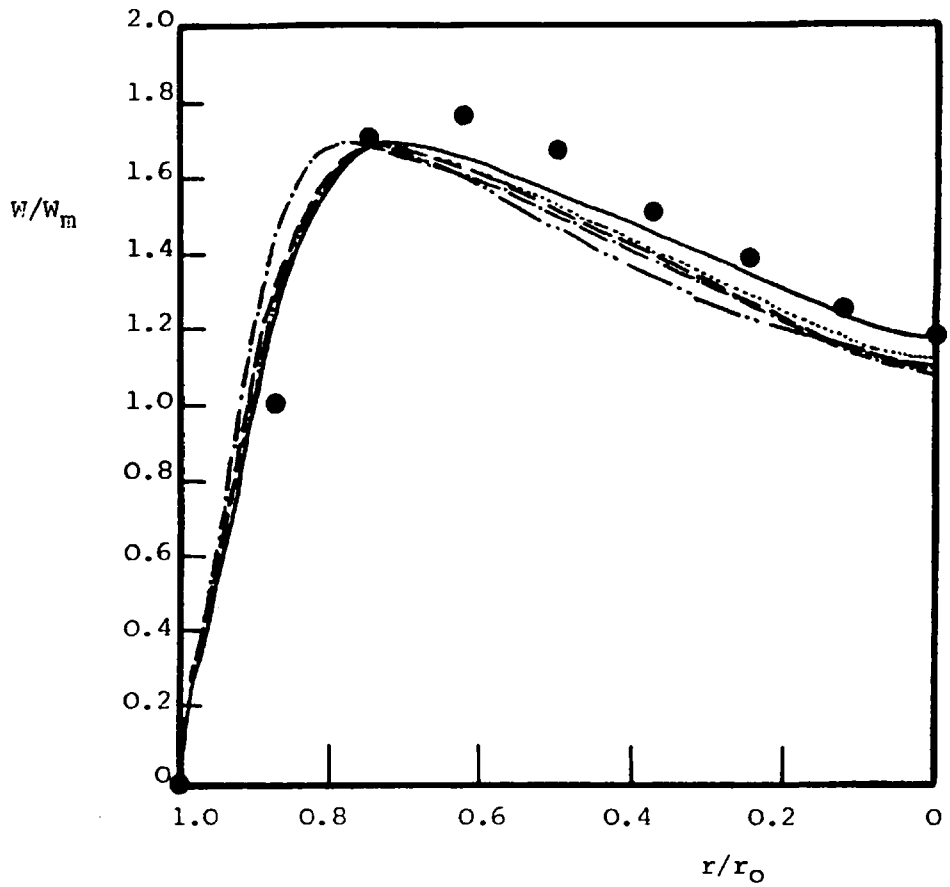


Fig.6.1 Effect of the finite-difference grid size on the axial velocity for laminar flow in curved ducts.
(Re=1068, R/r_o=29.1, θ=0 and φ=90°)

NI x NJ

—·—·— 15 x 15

——— 11 x 15 (non-uniform spacing in the radial direction)

— — — 11 x 15 (uniform spacing)

····· 11 x 20 (uniform spacing)

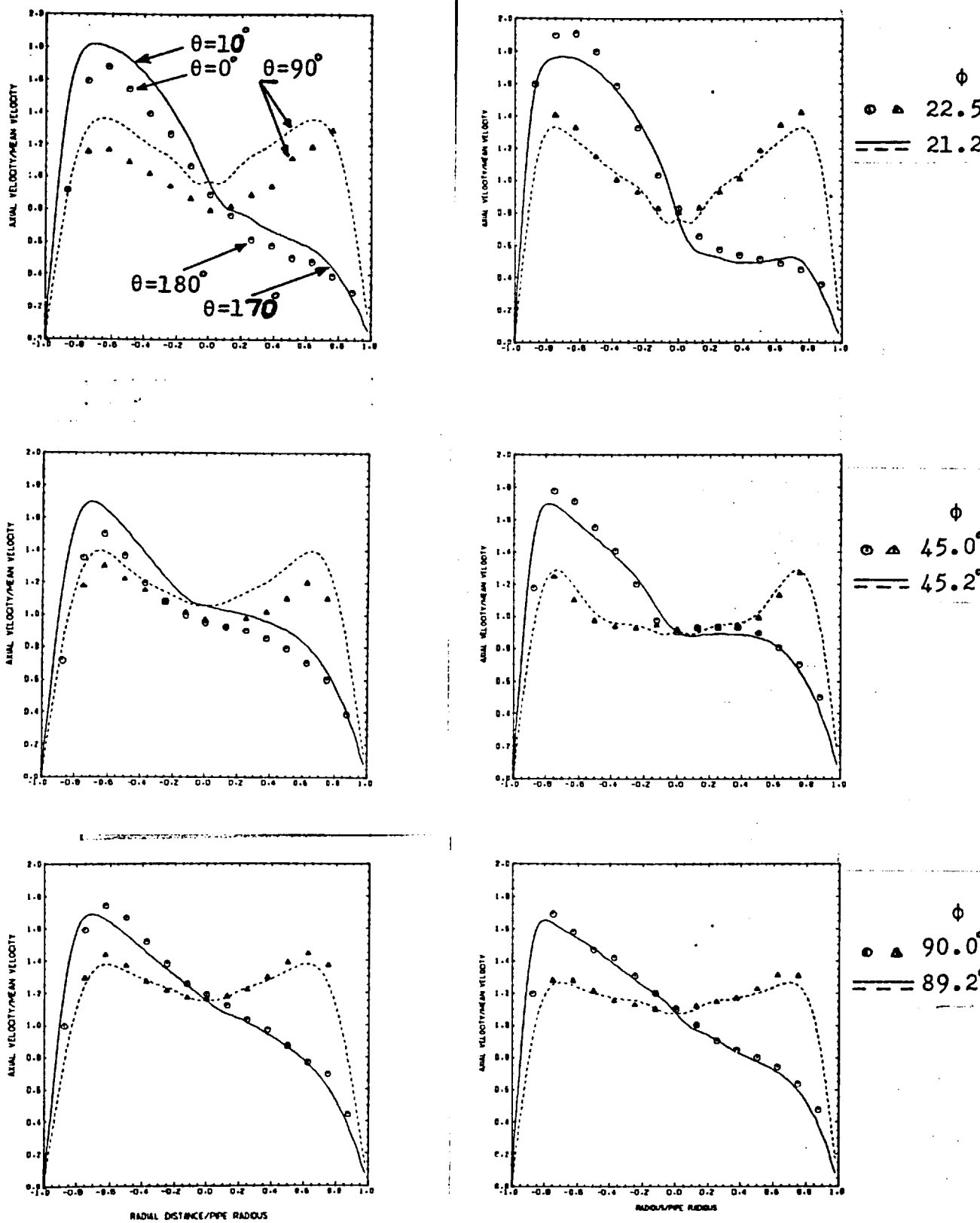
—·—·— 10 x 10 (uniform spacing)

● ● Austin data, 1971 (experimental data)

where:

NI is the number of nodes in the tangential direction

NJ is the number of nodes in the radial direction.



(a) Re=1068.1
K =198

(b) Re=2006.7
K =372

Fig.6.2 Development of axial velocity in mildly curved ducts (R/r_o=29.1, $K=Re.\sqrt{r_o/R}$)

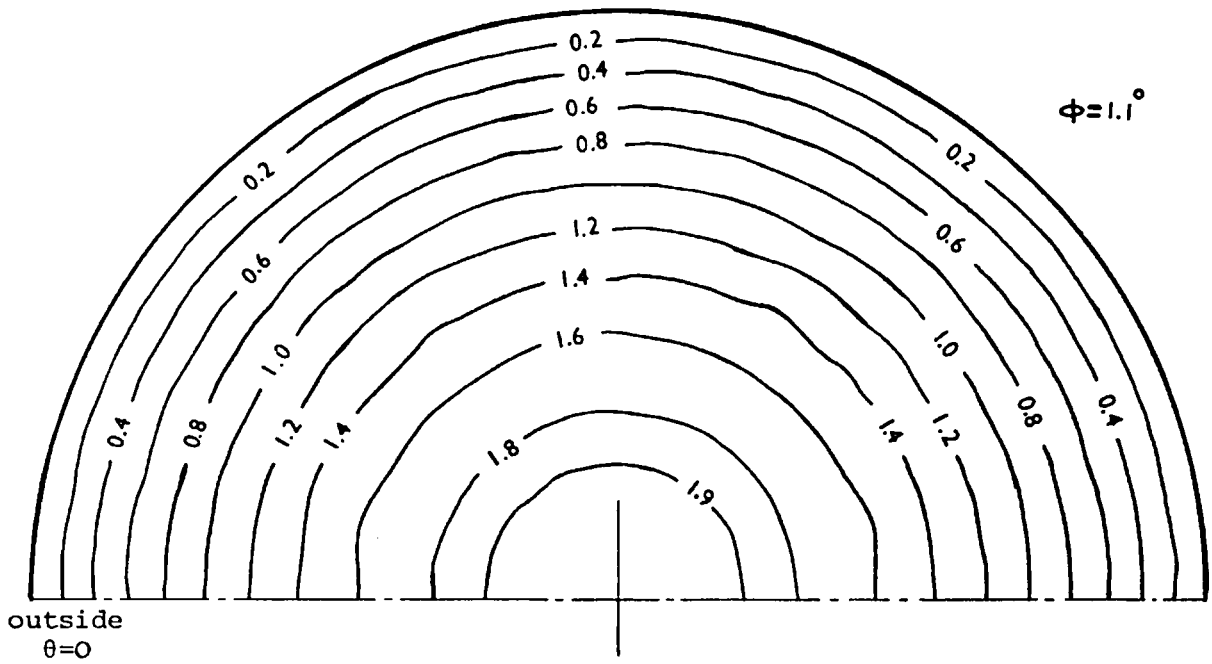
● ▲ data of AUSTIN, 1971

present prediction.

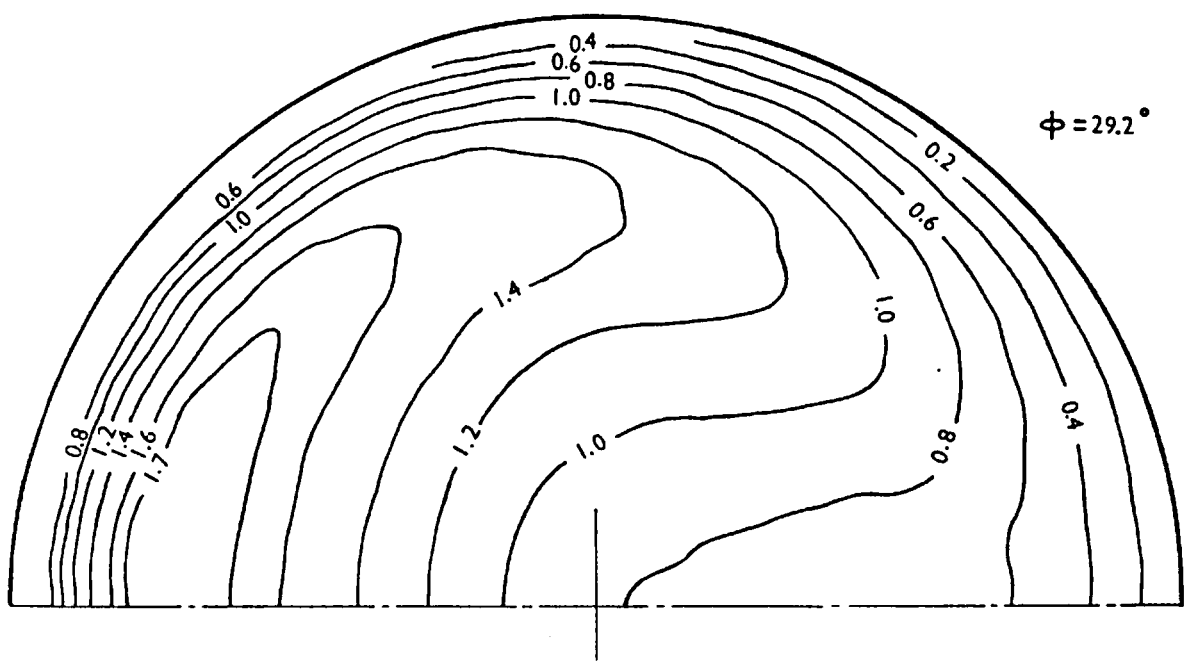
experimental data of Austin (1971). The agreement is quite good considering the fact that the inlet velocity-profiles in the experiments were not exactly parabolic. Fig.6.3 shows the predicted velocity contours at different six planes in the bend for Re=1068.1 corresponding to a Dean number, K, of 198. The effect of curvature on the flow is shown as a distortion of the axial-velocity contours from the symmetrical position along the centre of the duct. As shown in the figure, the maximum velocity is displaced forwards the outside of the bend along the symmetry line. The distortion is continued from the inlet plane of the bend, increases to a maximum level at about 30° ($W_{max} \simeq 1.7W_m$), and then decreases slightly up to about 60° ($W_{max} \simeq 1.6W_m$) where profiles of fully-developed flow are shown. The same trend is shown in Fig.6.4 for Re=2006.7 (corresponding to K=372), with larger distortion of the velocity contours. Figs.6.5 and 6.6 show the tangential and radial velocities respectively for both Re=1068.1 and 2006.7 at $\phi=45.2^{\circ}$ and 89.2°. The secondary velocities increase slightly with the axial direction, and the maximum absolute value of the tangential and radial velocities are about 10% and 5% of the mean axial velocity respectively for Re=2006.7 at $\phi=89.2^{\circ}$. Fig.6.7 displays the dimensionless pressure contours $(P-P_{CL})/(\rho.W_m^2/2)$ for the two Reynolds numbers at $\phi=45.2^{\circ}$ and 89.2°. The pressure is nearly the same for the two planes, with higher pressure outside and lower pressure inside. The satisfactory measure of agreement with the data justifies the use of the marching method.

6.2.2 Laminar Flow In A Strongly-Curved Duct

For the flow in a strongly-curved duct, the partially-parabolic solution procedure was applied. The geometry of the bend used was that of the experimental test-section described in Chapter 4. The

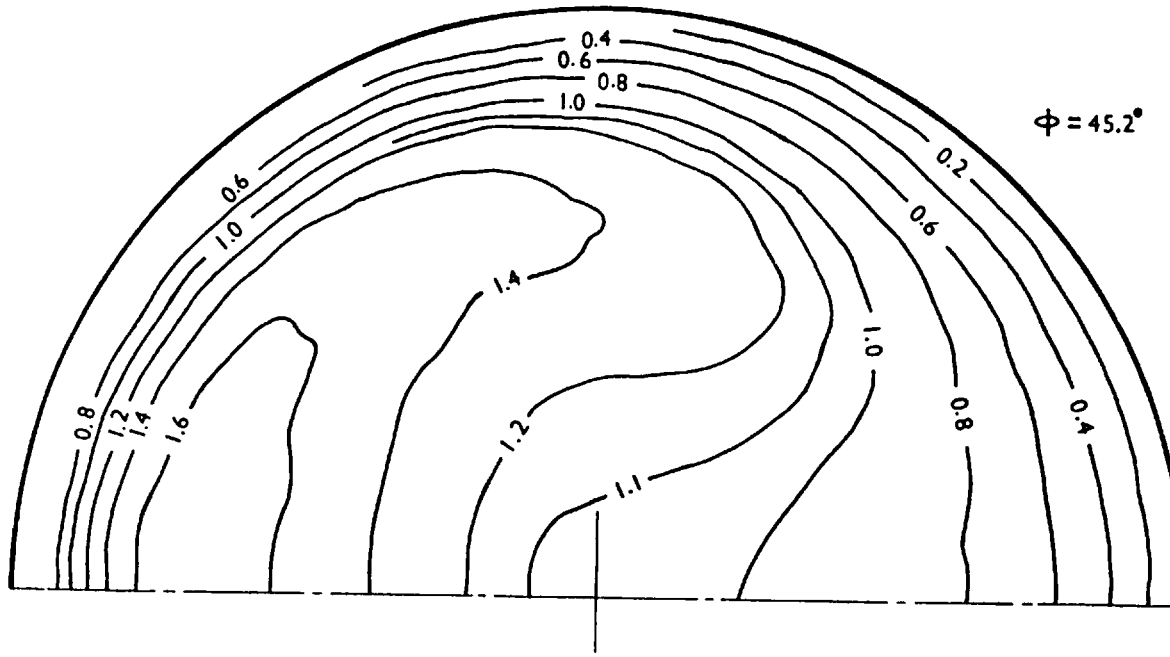


(a)

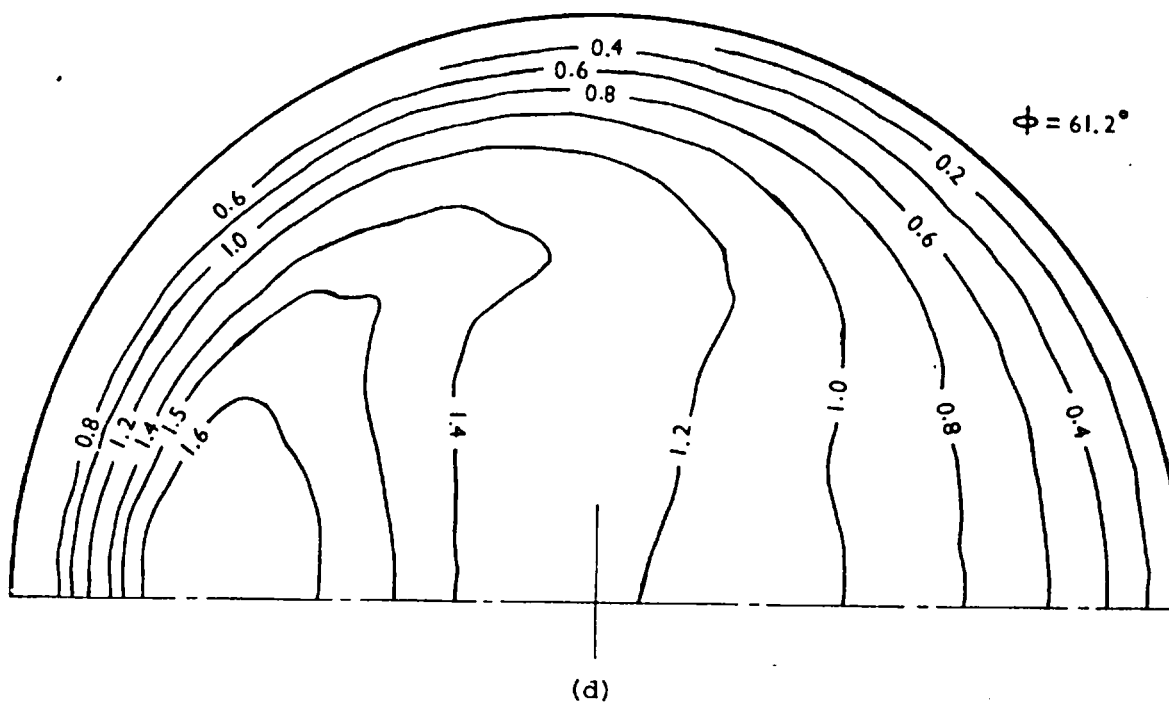


(b)

Fig.6.3-(a),(b) Development of axial velocity contours W/W_m for laminar flow in mildly curved ducts.
(Re=1068.1, R/r_o=29.1, K=198).

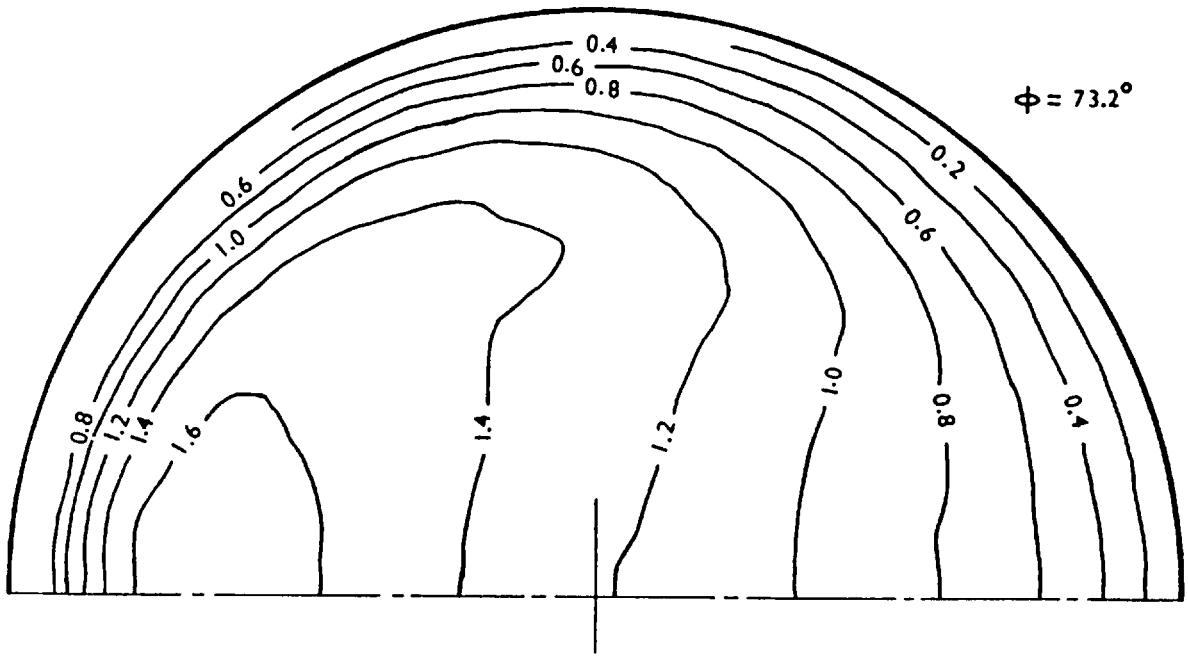


(c)

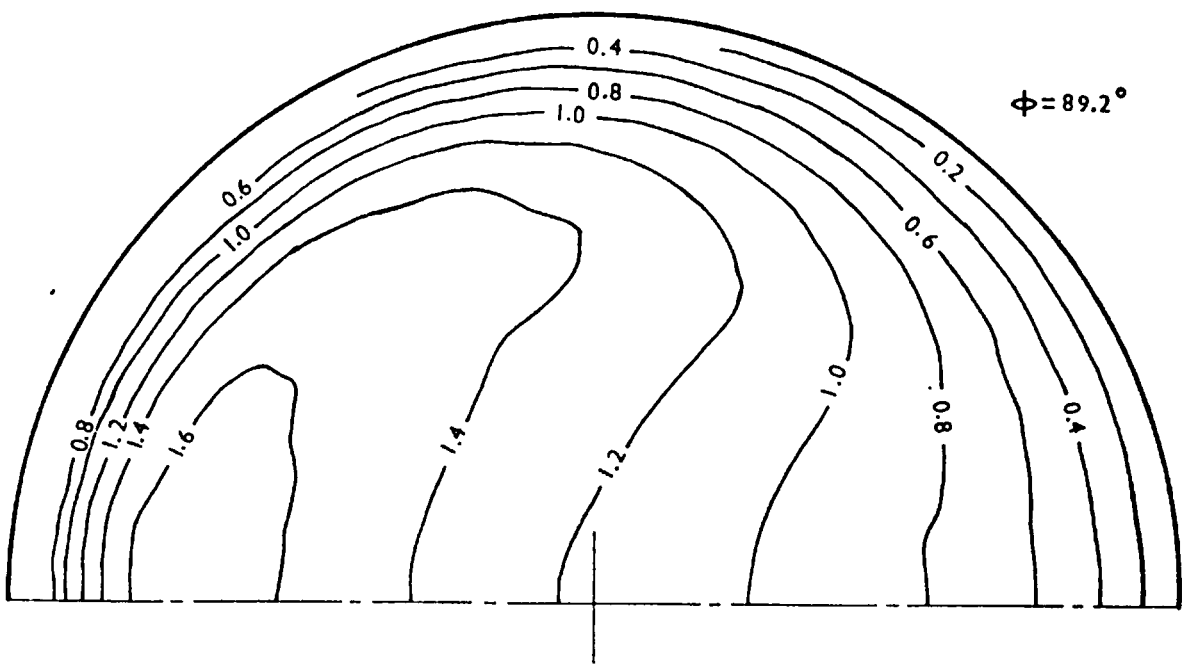


(d)

Fig.6.3-(c),(d) Development of axial velocity contours W/W_m for laminar flow in mildly curved ducts.
(Re=1068.1, R/r_o=29.1, K=198).



(e)



(f)

Fig.6.3-(e),(f) Development of axial velocity contours W/W_m for laminar flow in mildly curved ducts.
(Re=1068.1, R/r_o=29.1, K=198).

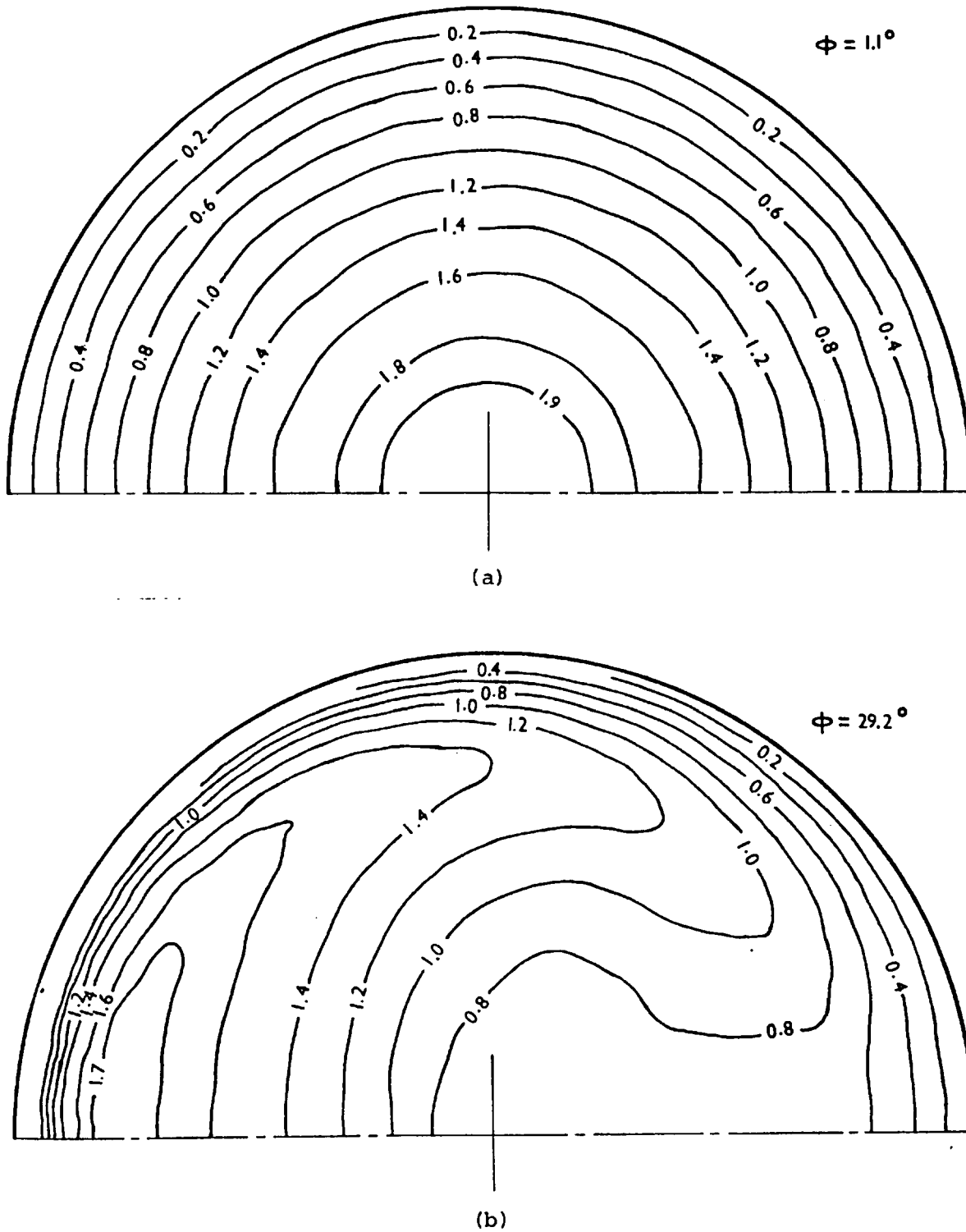
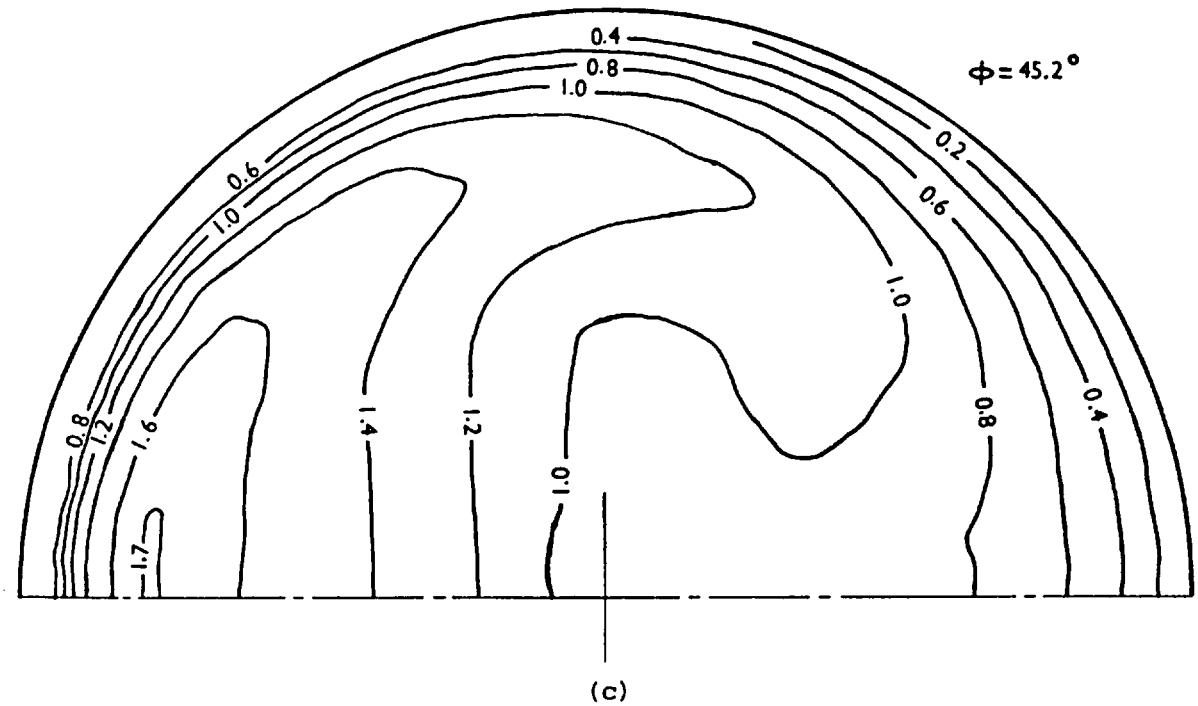
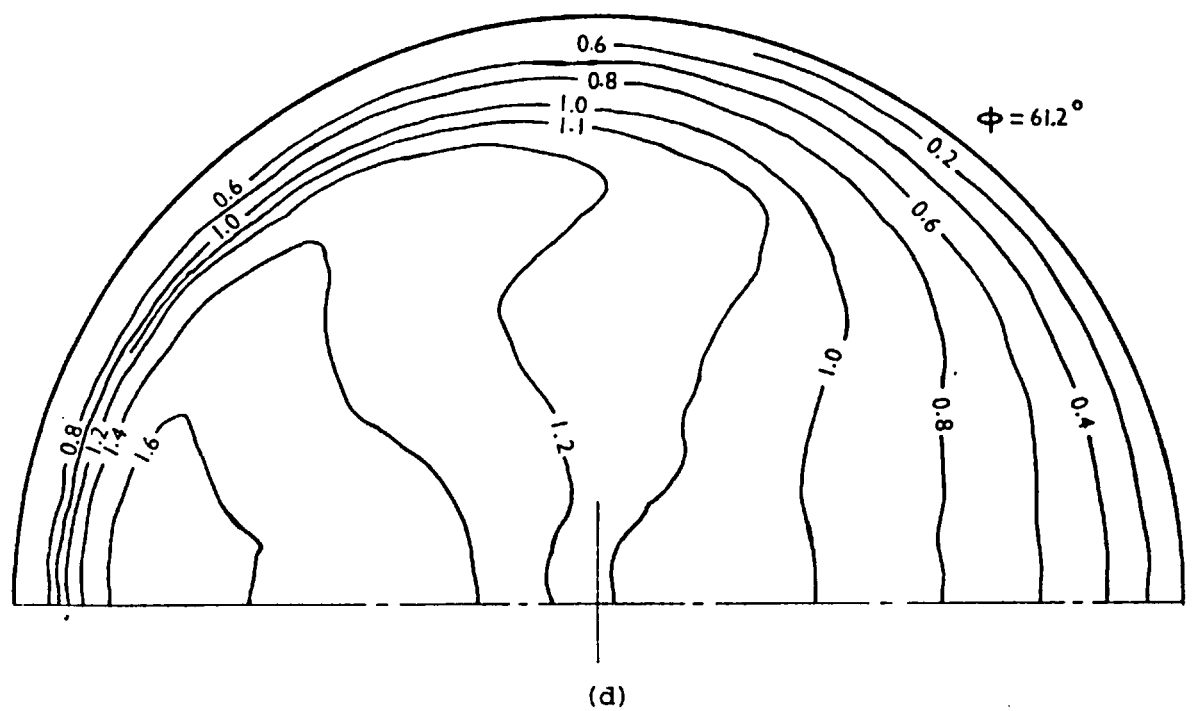


Fig.6.4-(a),(b) Development of axial velocity contours W/W_m for laminar flow in mildly curved ducts.

(Re=2006.7, R/r_o=29.1, K=372).

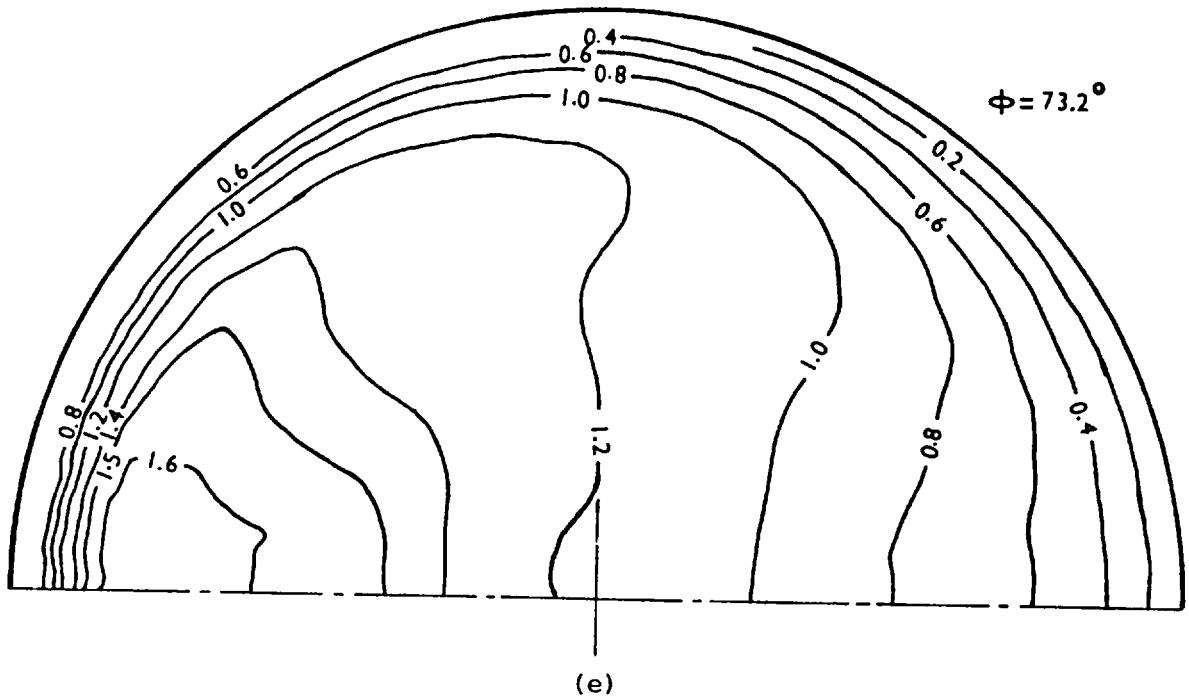


(c)

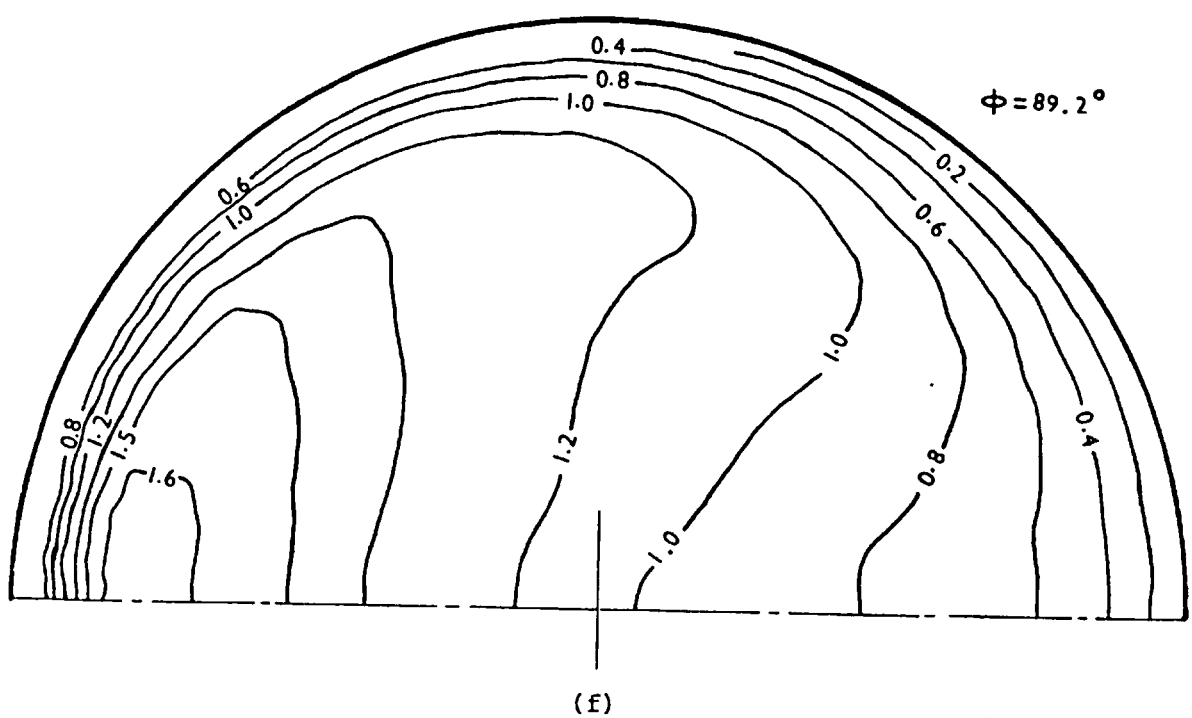


(d)

Fig.6.4-(c),(d) Development of axial velocity contours W/W_m for laminar flow in mildly curved ducts.
(Re=2006.7, R/r_o=29.1, K=372).



(e)



(f)

Fig.6.4-(e),(f) Development of axial velocity contours W/W_m for laminar flow in mildly curved ducts.

(Re=2006.7, R/r_o=29.1, K=372).

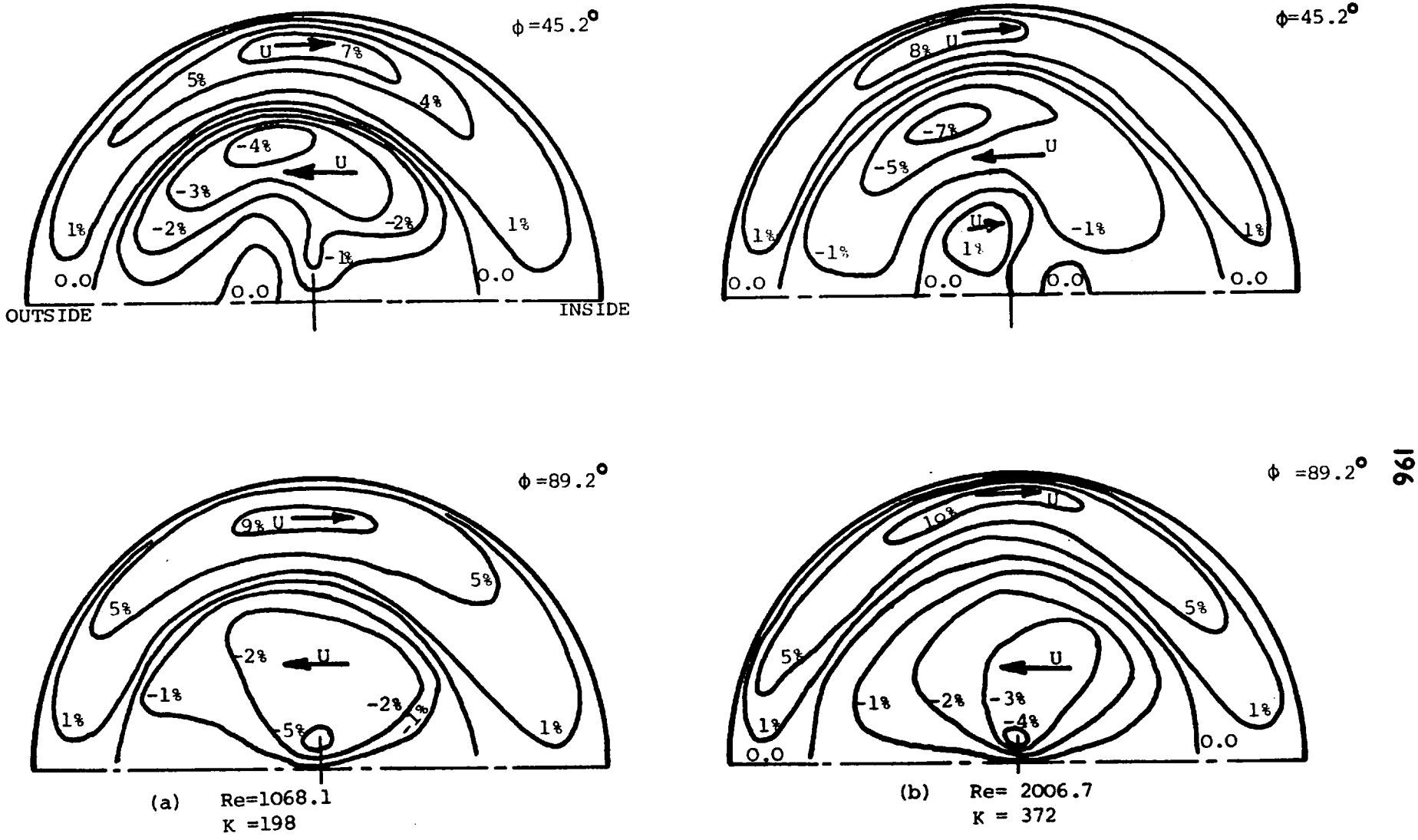
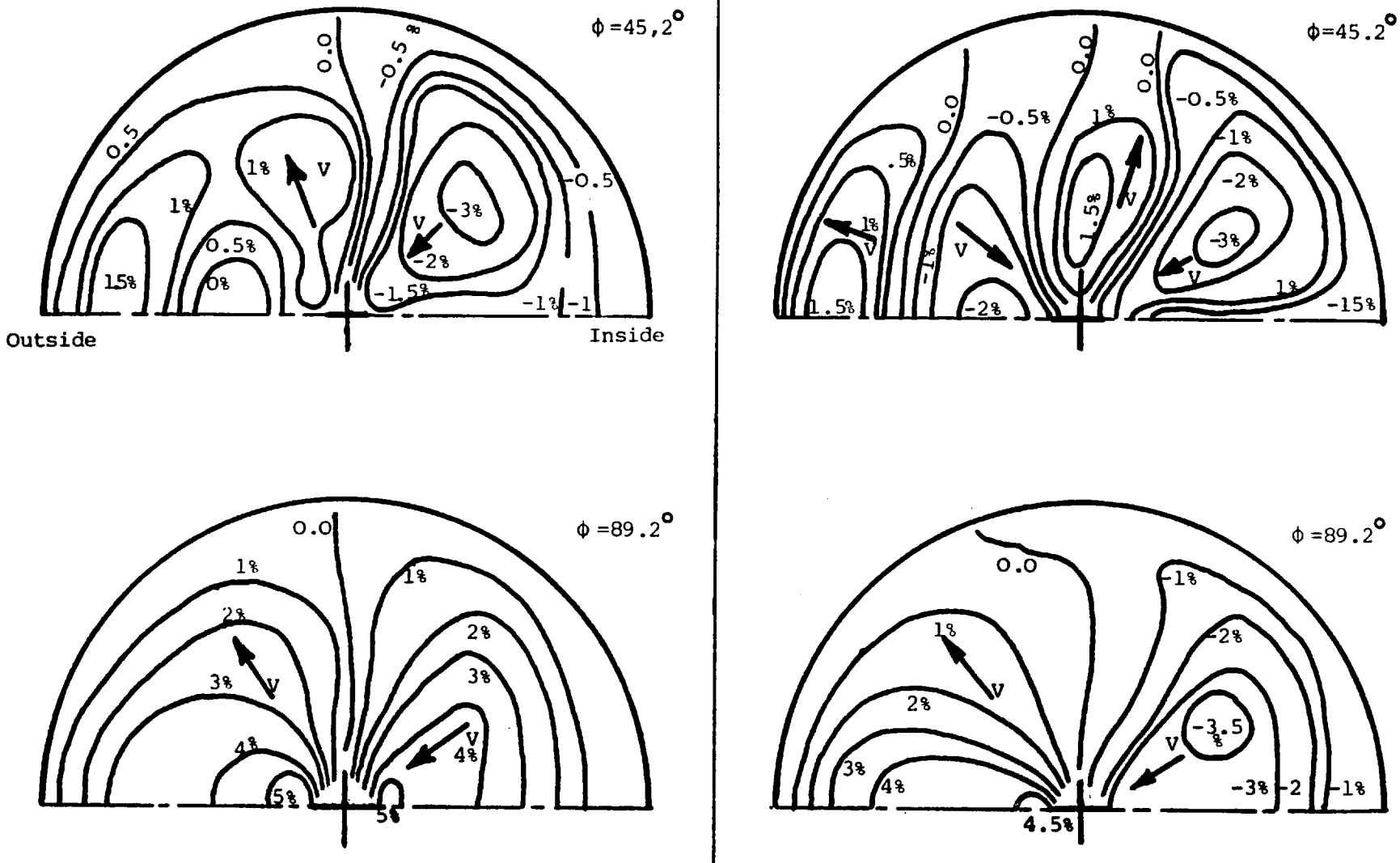


Fig.6. 5 Tangential velocity contours $U/W_m \times 100\%$ for mildly curved ducts.
$R/r_o = 29.1$.



(a) Re=1068.1
K =198

(b) Re=2006.7
K =372

Fig.6.6 Radial velocity contours $(V/W_m)\times 100\%$ for mildly curved ducts $(R/r_o=29.1)$

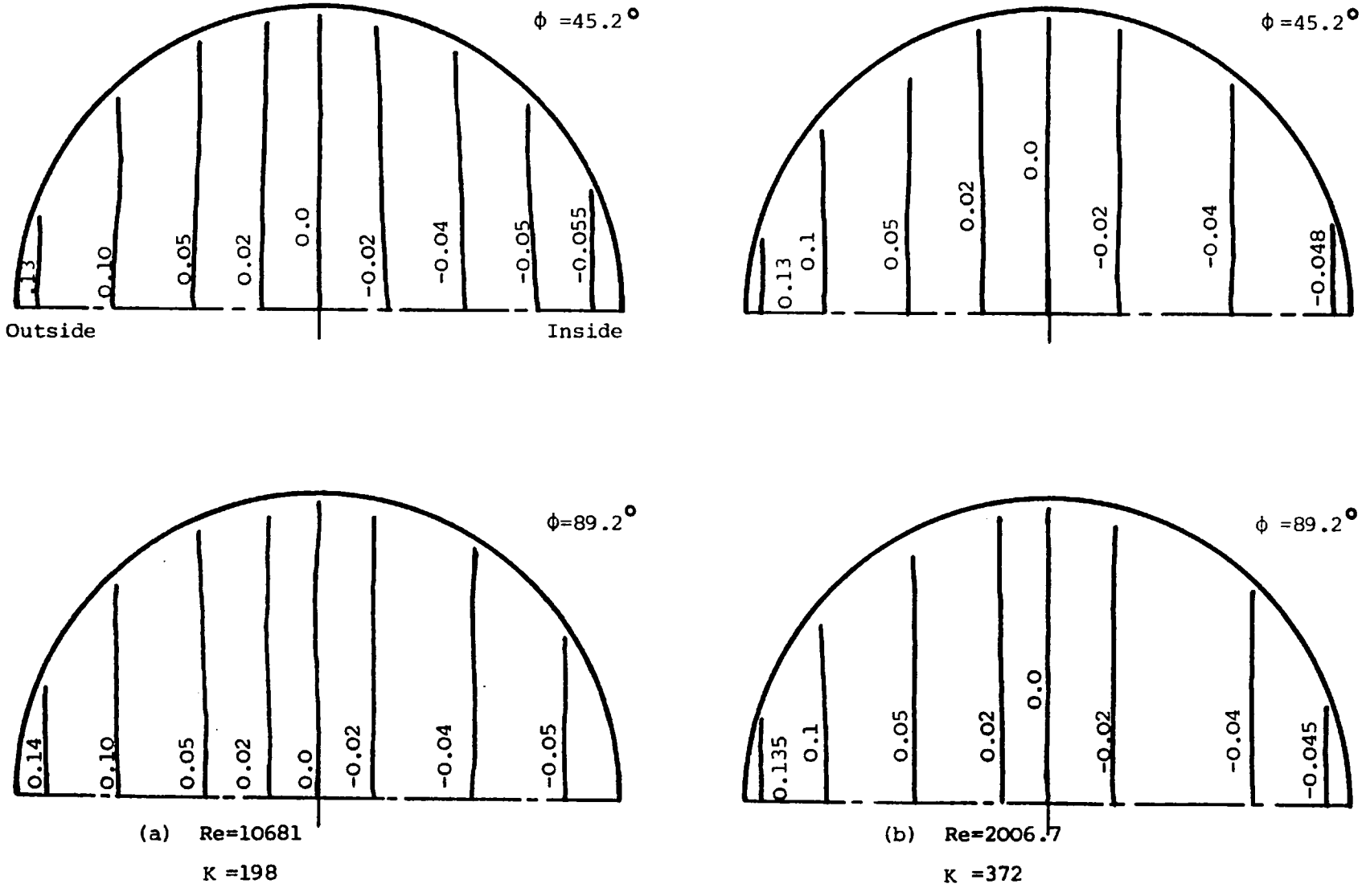


Fig.6.7 Dimensionless pressure contours $(P-P_{c1})/\frac{1}{2}\rho W_m^2$ for mildly curved ducts. $(R/r_o=29.1)$.

finite-difference grid used in the present prediction possessed 15 non-uniform intervals in the radial direction, and 11 uniform intervals in the tangential direction (similar to that grid used for mildly curved ducts). The forward-step was uniform along each part of the test section. For the upstream straight duct, 10 uniform axial intervals was chosen, and the forward step was equal to the pipe radius. For the 90^{o} bend, 30 uniform intervals in the axial direction was used, and the forward step was 3^{o}. For the downstream straight part, 24 uniform intervals was used, and the forward step was equal to $0.5r_{o}$. For the partially-parabolic procedure, the pressure field was under relaxed, and it was found that an under-relaxation factor equal to 0.4 was required to give stable solution. No under-relaxation was used for the velocity components, k and ε fields. The final solution was obtained after twenty iterations, where the axial velocity and the pressure of a specified point in the flow domain was unchanged.

Fig.6.8 displays the development of the predicted axial-velocity contours (the solid lines), and the comparison with the present experimental data (the dotted lines) is also shown for Re=500 (corresponds to K=211.3). Although the agreement of the prediction with the experimental data, in general, is fairly good, and the behaviour of the flow is the same, the experimental data show more distorted contours, and the maximum velocity is greater than the predicted one. The maximum difference between the two values is about 7%. The figure shows that the maximum velocity is displaced outside the bend at the same distances for both the experimental and predicted contours. Figs.6.9 and 6.10 show the corresponding tangential and radial velocity contours respectively. The maximum absolute values of the tangential and radial velocities are approximately 38% and 25% of

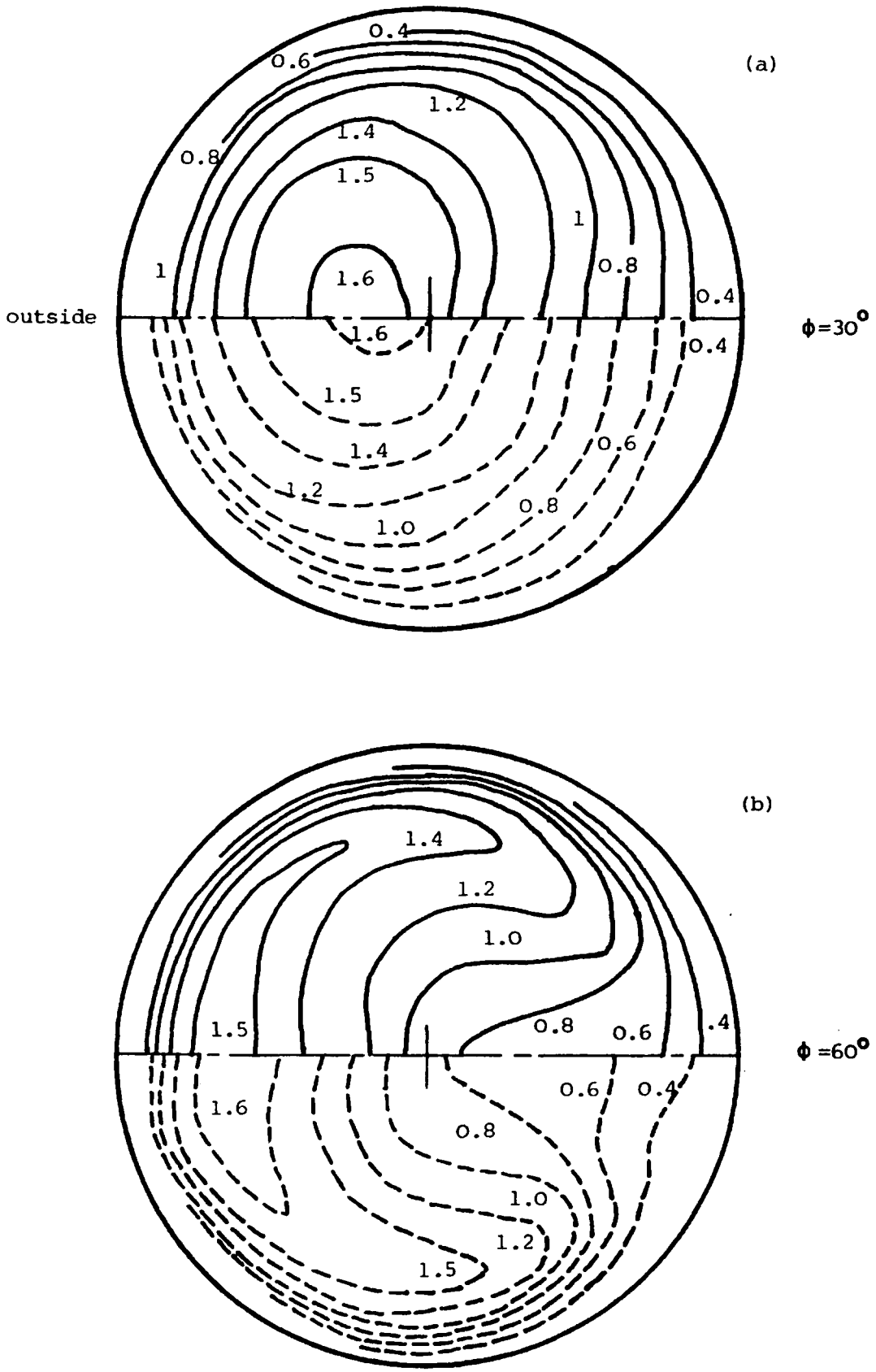


Fig.6.8-(a),(b) Contours of axial velocity W/W_m for laminar flow in strongly curved ducts.

(Re=500, R/r_o=5.6, K=211.3)

(——— prediction, ------ experimental results)

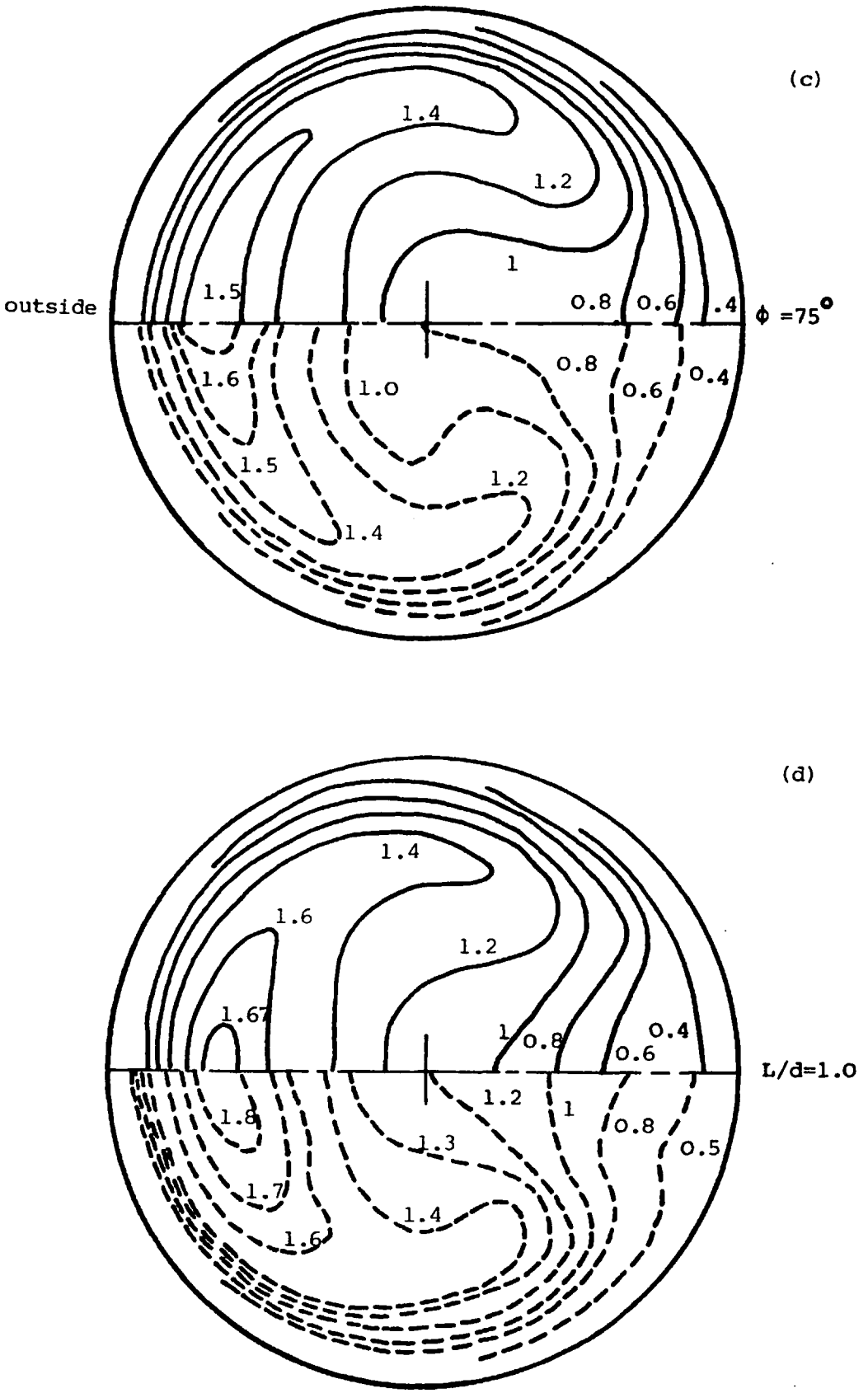


Fig.6.8-(c),(d) Contours of axial velocity W/W_m for laminar flow in strongly curved ducts.
(Re=500, R/r_o=5.6, K=211.3)
(——— prediction, ------ experimental results)

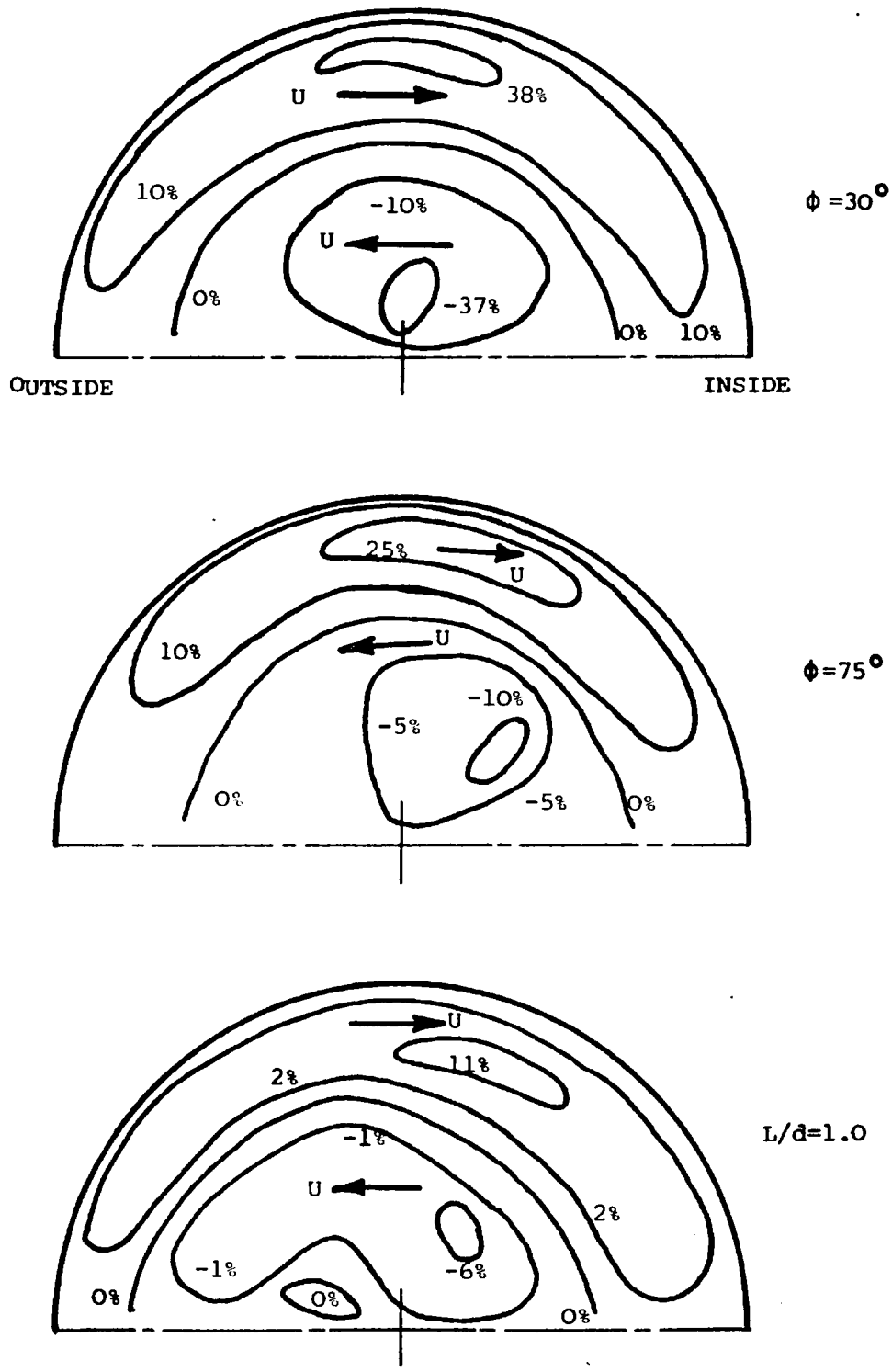


Fig.6.9 Tangential velocity contours $(U/W_m)x100\%$ for laminar flow in strongly curved ducts (Re=500, R/r_o=5.6, K=211.3)

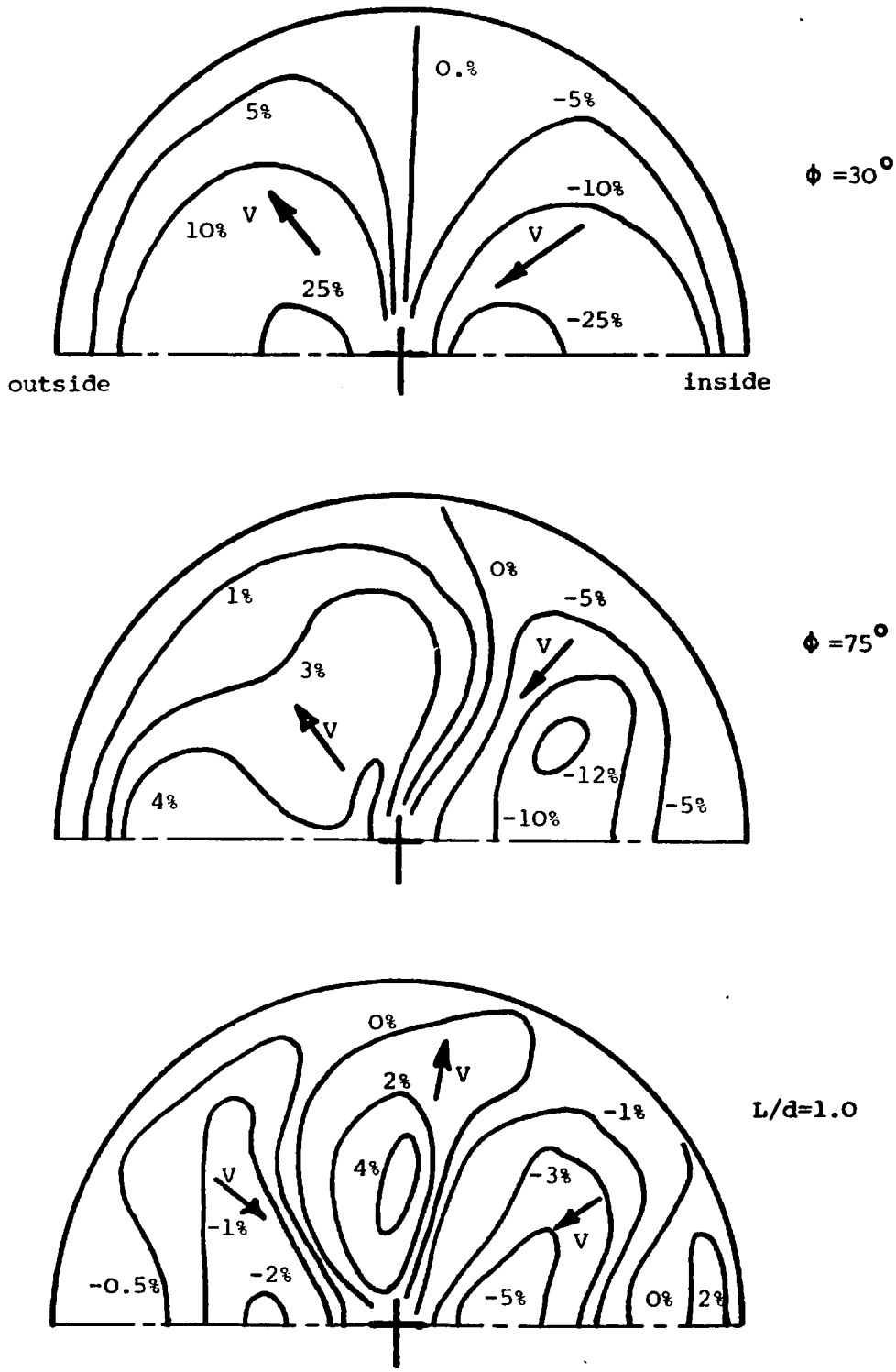


Fig.6.10 Radial velocity contours $V/W_m \times 100\%$ for laminar flow in strongly curved ducts. (Re=500, R/r_o=5.6, K=211.3)

W_m respectively at $\phi=30^\circ$. The lateral velocities are decreased again inside the bend and in the downstream section as the flow slowly reverts to Poiseuille flow in a straight pipe. The maximum tangential and radial velocities at L/d=1 are approximately 11% and 5% of W_m respectively. Fig.6.11 shows the corresponding dimensionless pressure contours with maximum pressure differences between outside and inside occur at $\phi=30^\circ$.

Fig.6.12 shows the measured and predicted axial-velocity contours for the second laminar test-case (Re=1093, K=461.9). The agreement between the prediction and the experimental data is not as good as that obtained for the results of the first test-case (Re=500). The maximum difference, of the maximum axial-velocity, between experimental data and prediction is about 13% at $\phi=75^\circ$. The maximum velocity is displaced outside the bend for both the experimental data and the prediction, but the maximum velocity of the experimental data is positioned off the symmetry line in the bend, and these trend are not observed in the predicted contours. The discrepancy may arise because the grid used in the prediction is not fine enough, especially in the tangential direction, to let the solution follow the very steep changes in the velocity which occur in the inside region of the test-section, but finer grids require more nodes which means more computing time and storage space. The agreement between the experimental data and the prediction is fairly good for the flow in the downstream section at L/d=1. Fig.6.13 displays the tangential velocity contours. The maximum value observed is higher than the first test-case result, and is equal to 40% at $\phi=30^\circ$. The radial velocity contours are shown in Fig.6.14. The maximum radial velocity is less than that of the first test-case and is equal to 20% of W_m at

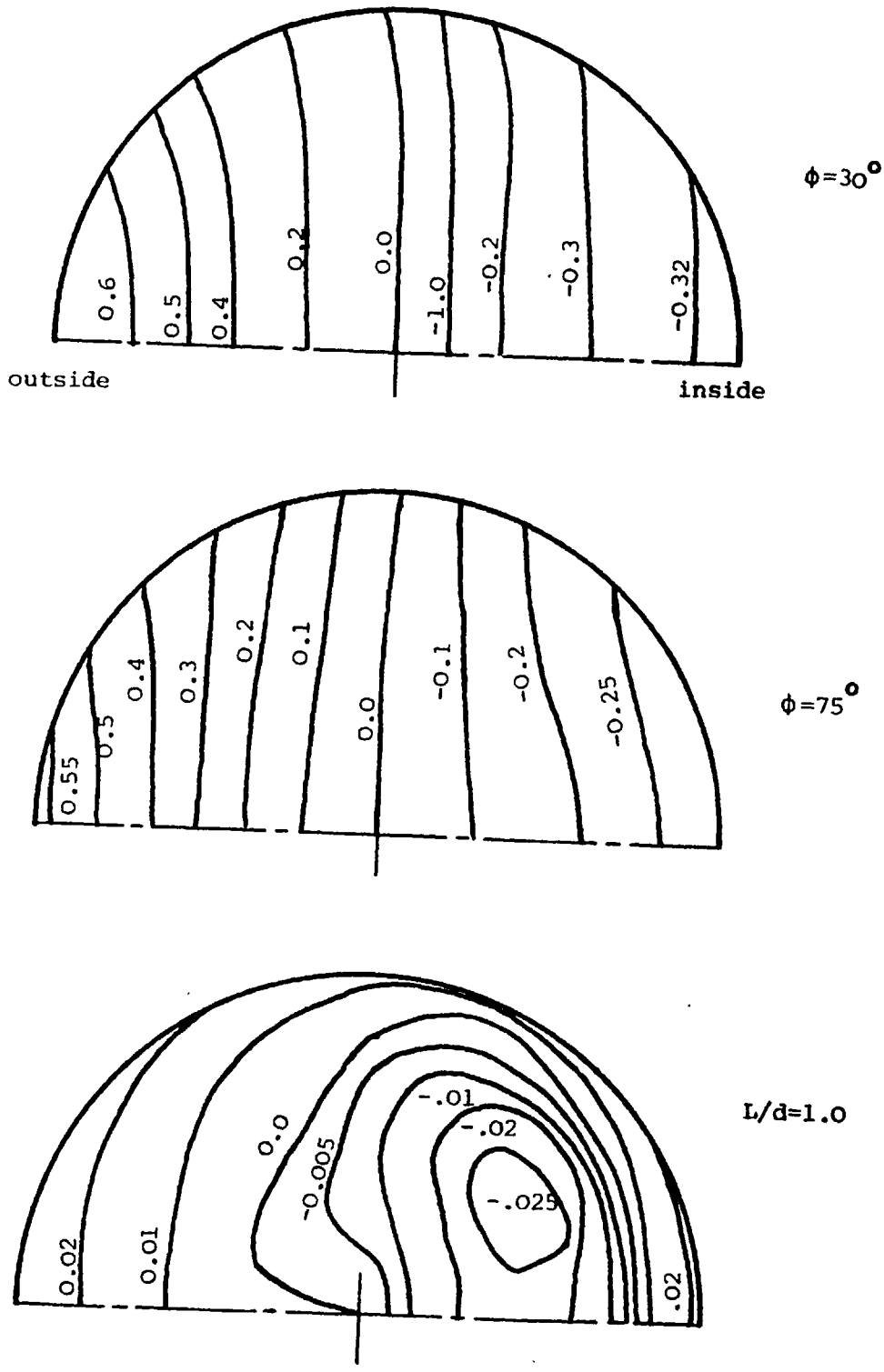


Fig.6.11 Dimensionless pressure contours $(P-P_{cL})/\frac{1}{2}\rho W_m^2$ for laminar flow in strongly curved ducts. (Re=500, R/r_o=5.6, K=211.3)

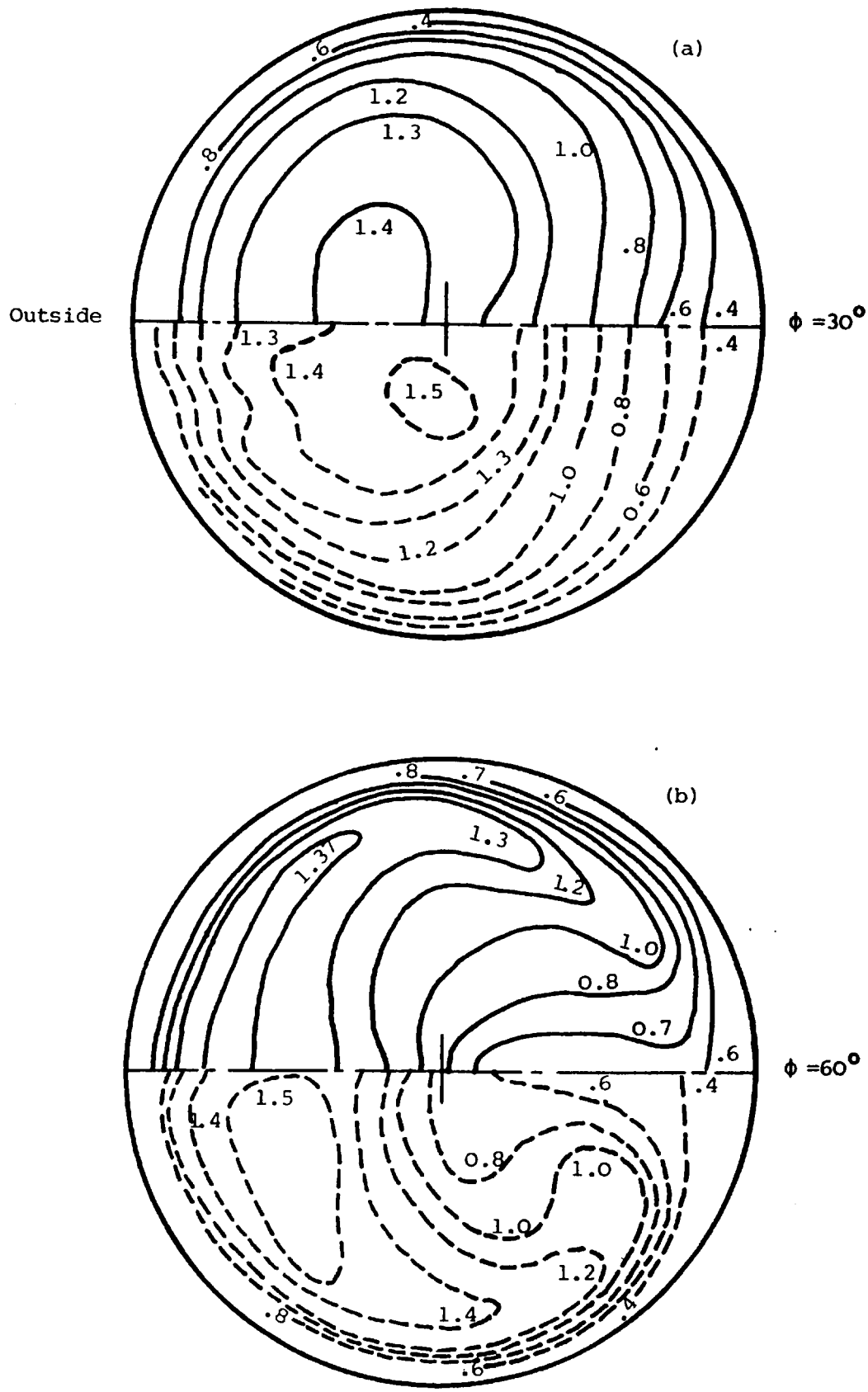


Fig.6.12-(a),(b) Contours of axial velocity W/W_m for laminar flow in strongly curved ducts.
(Re=1093, R/r_o=5.6, K=461.9)
(——— prediction, ------- experimental results)

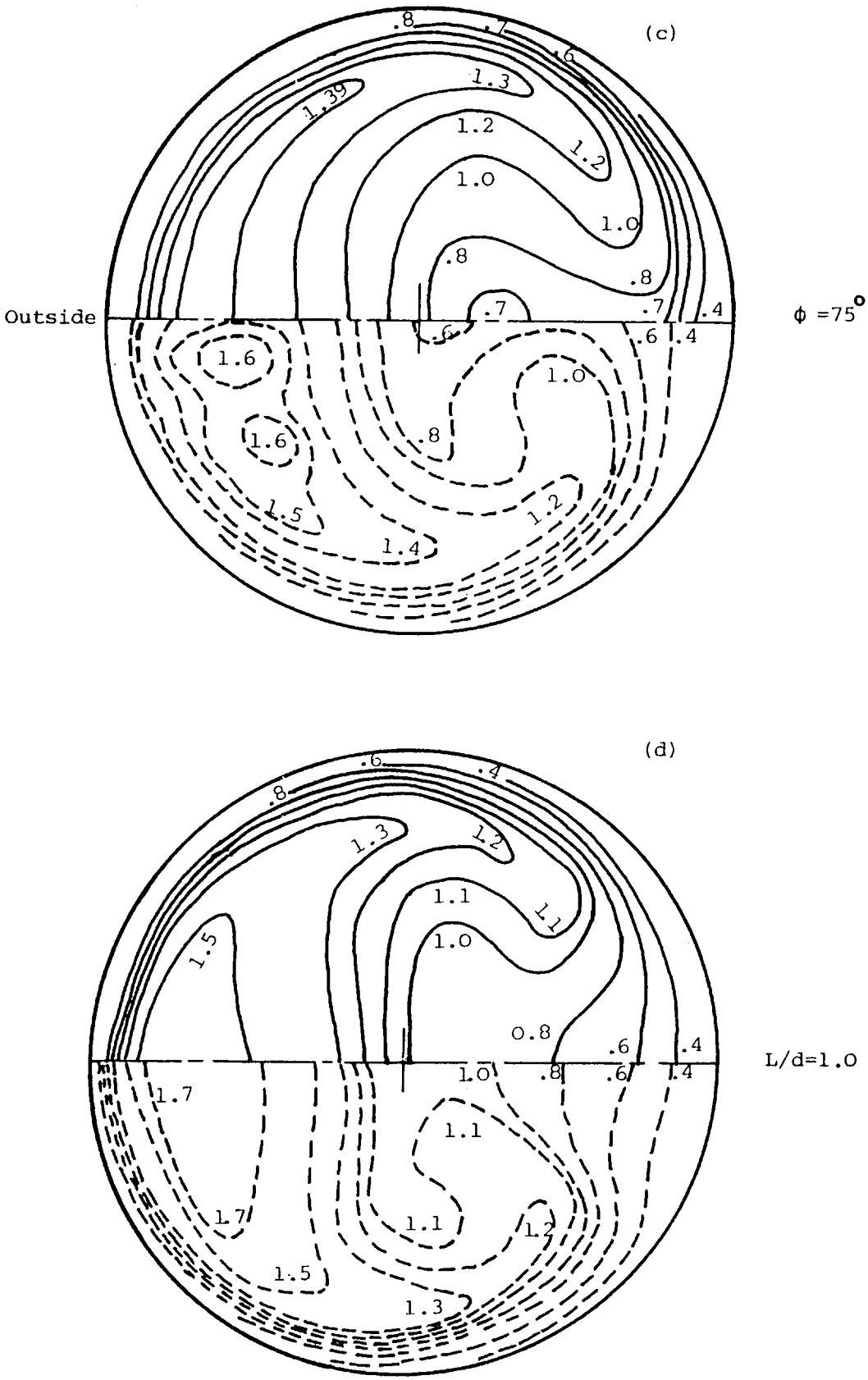


Fig.6.12-(c),(d) Contours of axial velocity W/W_m for laminar flow in strongly curved ducts.
(Re=1093, R/r_o=5.6, K=461.9)
(———— Prediction, ------ experimental results)

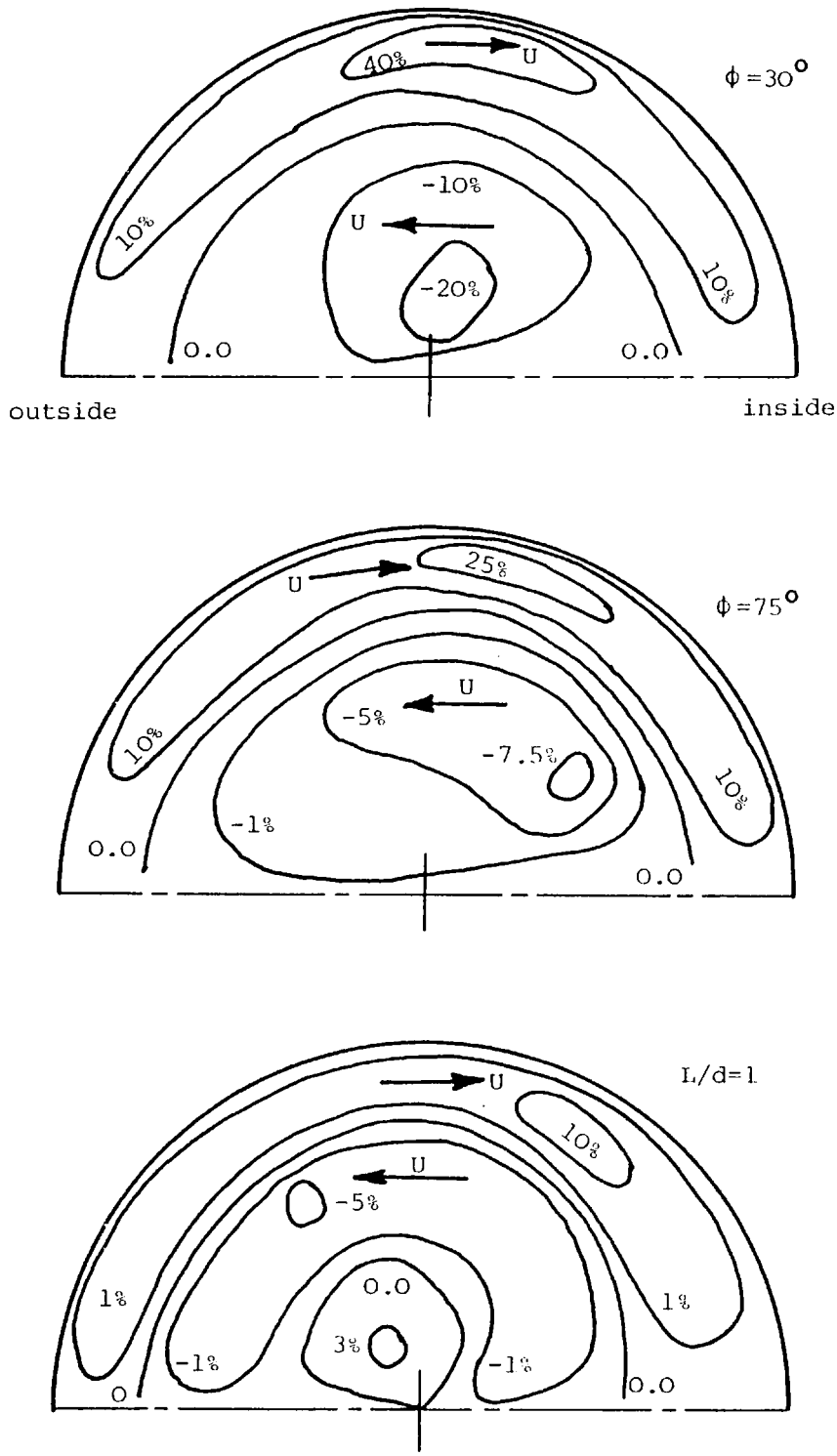


Fig.6.13 Tangential velocity contours $U/W_m \times 100\%$ for laminar flow in strongly curved ducts.
(Re=1093, R/r_o=5.6, K=461.9)

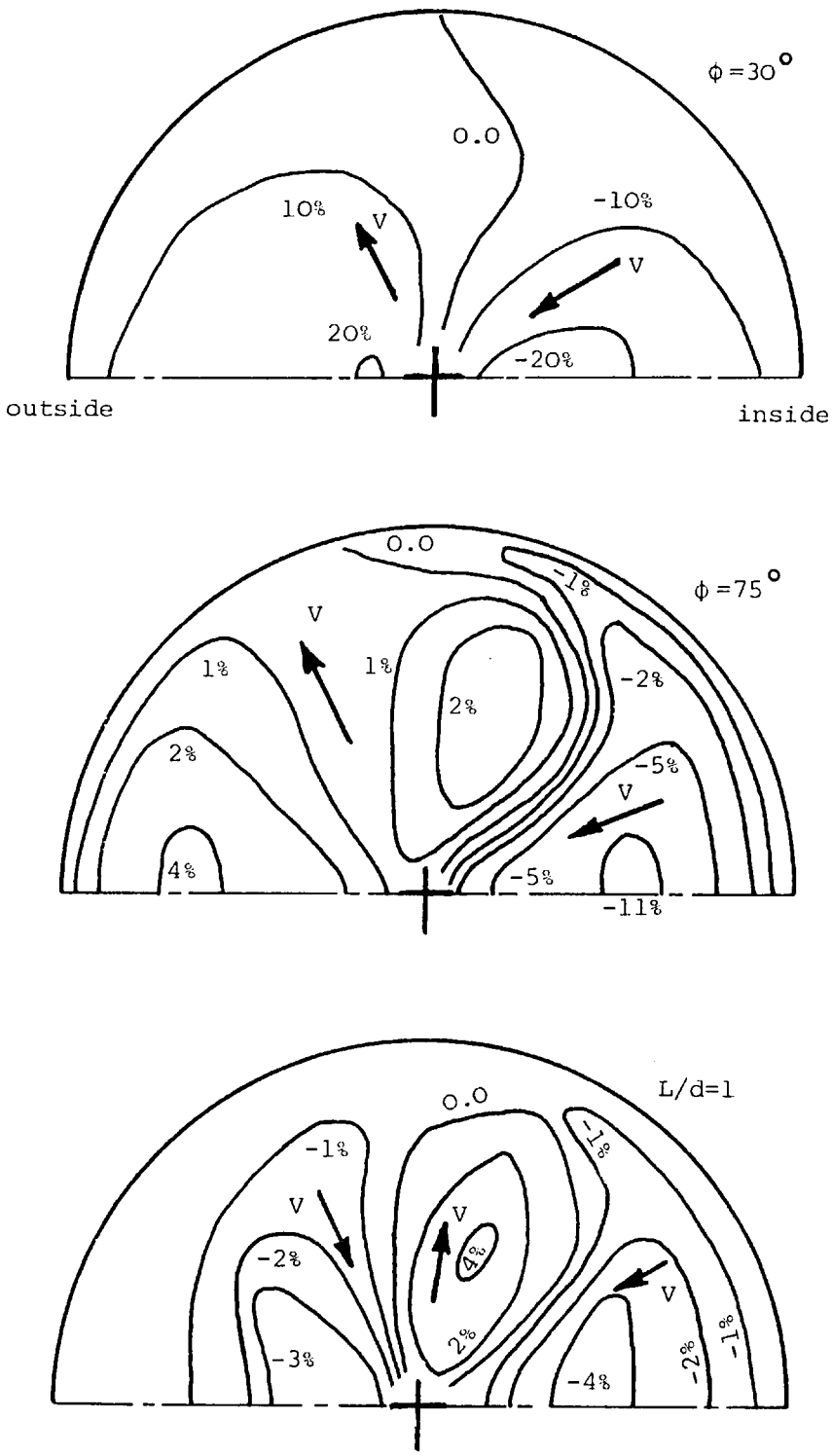


Fig.6.14 Radial velocity contours $V/W_m \times 100\%$ for laminar flow in strongly curved ducts.

(Re=1093, R/r_o=5.6, K=461.9)

ϕ=30°, but the radial velocity contours are more distorted for the second test-case. Fig.6.15 displays the dimensionless pressure contours. The maximum value is slightly less than that of Re=500.

6.3 k-ϵ Model Predictions Of Turbulent Flow In Strongly-Curved Ducts

The turbulent flow in a strongly-curved duct was calculated using the k-ϵ model of turbulence, described in Chapter 2, with the partially-parabolic solution procedure. The same number of grid nodes and iterations was used as in the laminar flow calculations after comparing with the results obtained using finer and coarser grids as shown in Fig.6.16. One test-case was studied and the predicted axial-velocity is compared with the present experimental data for Re=43 000, K=18 171, as shown in Fig.6.17. The maximum axial-velocity difference, between the experimental data and the prediction, is about 8% in the downstream straight part at L/d=1. The general trend of the flow is similar in both experimental and prediction results; and the maximum axial-velocity is moved inside towards the centre of the curvature in the 90° bend, as shown for ϕ=30°, 60° and 75°, and after that it is moved outside in the opposite direction, as shown for L/d=1 and 6. The predicted axial-velocity contours are less distorted than the experimental data. Considering that very steep changes in the velocity contours are well predicted for the chosen grid size, the discrepancy between experimental and predicted results for turbulent flow may be mainly due to turbulence model used. The results draw attention to the defect in simple eddy-viscosity modelling used in the present prediction, and the more advanced algebraic Reynolds stress model, mentioned in Appendix A3, is suggested to obtain better results for turbulent flow in bends. The tangential velocity contours are shown in Fig.6.18. The value of U reaches a maximum of $0.3W_m$ at ϕ=75°

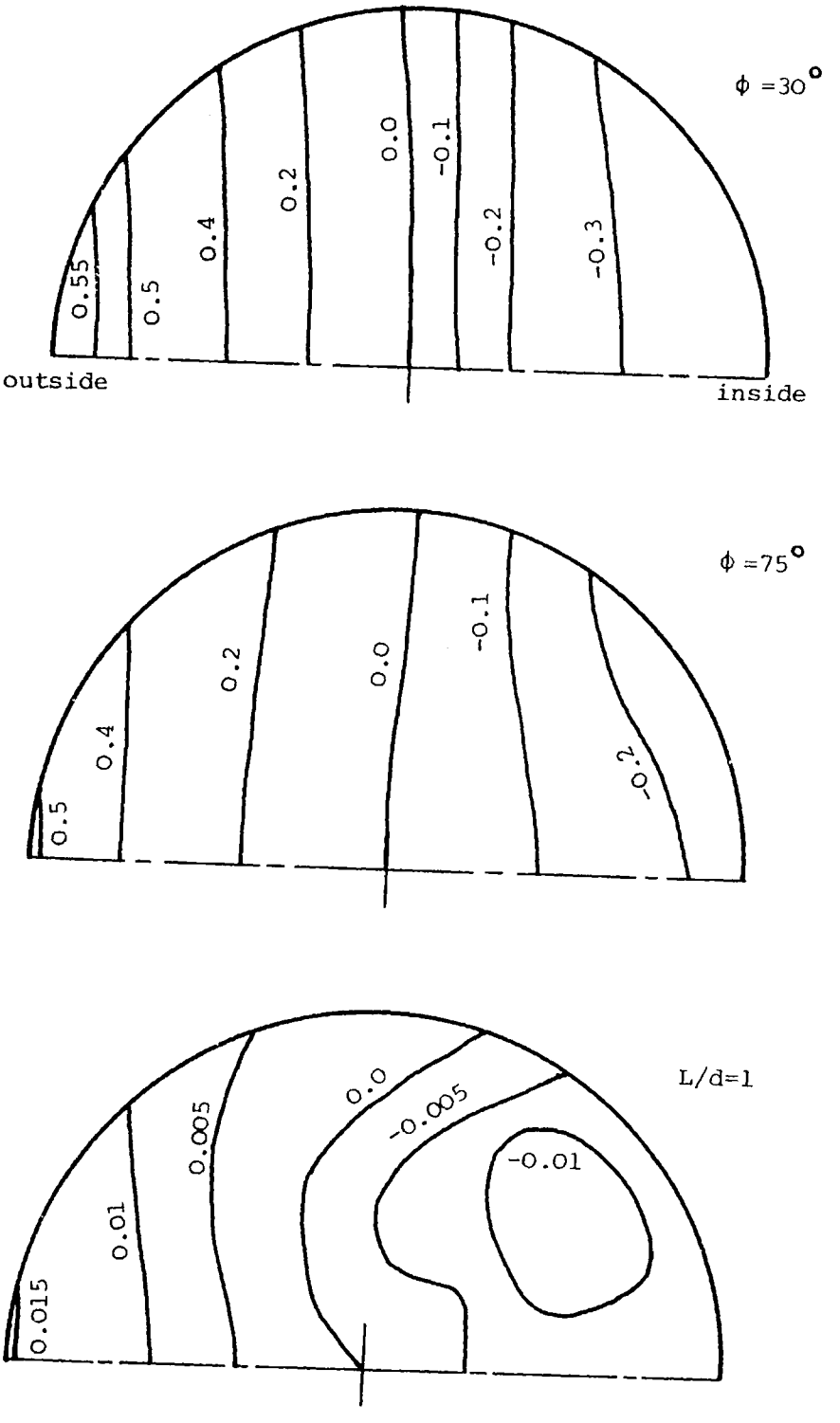


Fig.6.15 Dimensionless pressure contours $(P-P_{CL})/\frac{1}{2}\rho W_m^2$ for laminar flow in strongly curved ducts.
(Re=1093, R/r_o=5.6, K=461.9)

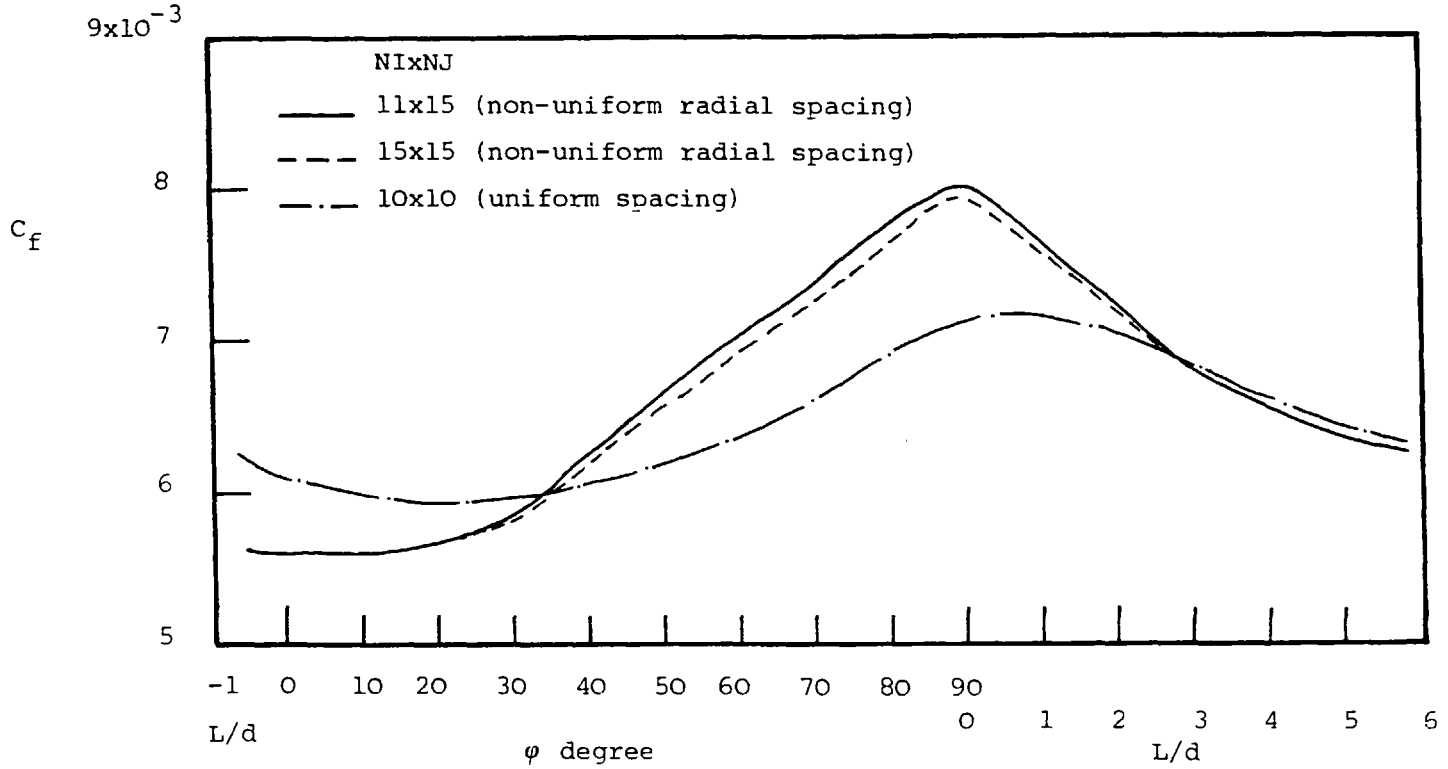


Fig.6.16 Effect of the finite-difference grid size on the average coefficeint of friction C_f for turbulent flow in bends. (Re=43 000, R/r_o=5.6, K=18 171, $C_f=\tau_w/\frac{1}{2}\rho W_m^2$, NI and NJ are the number of nodes in the tangential and radial directions respectively).

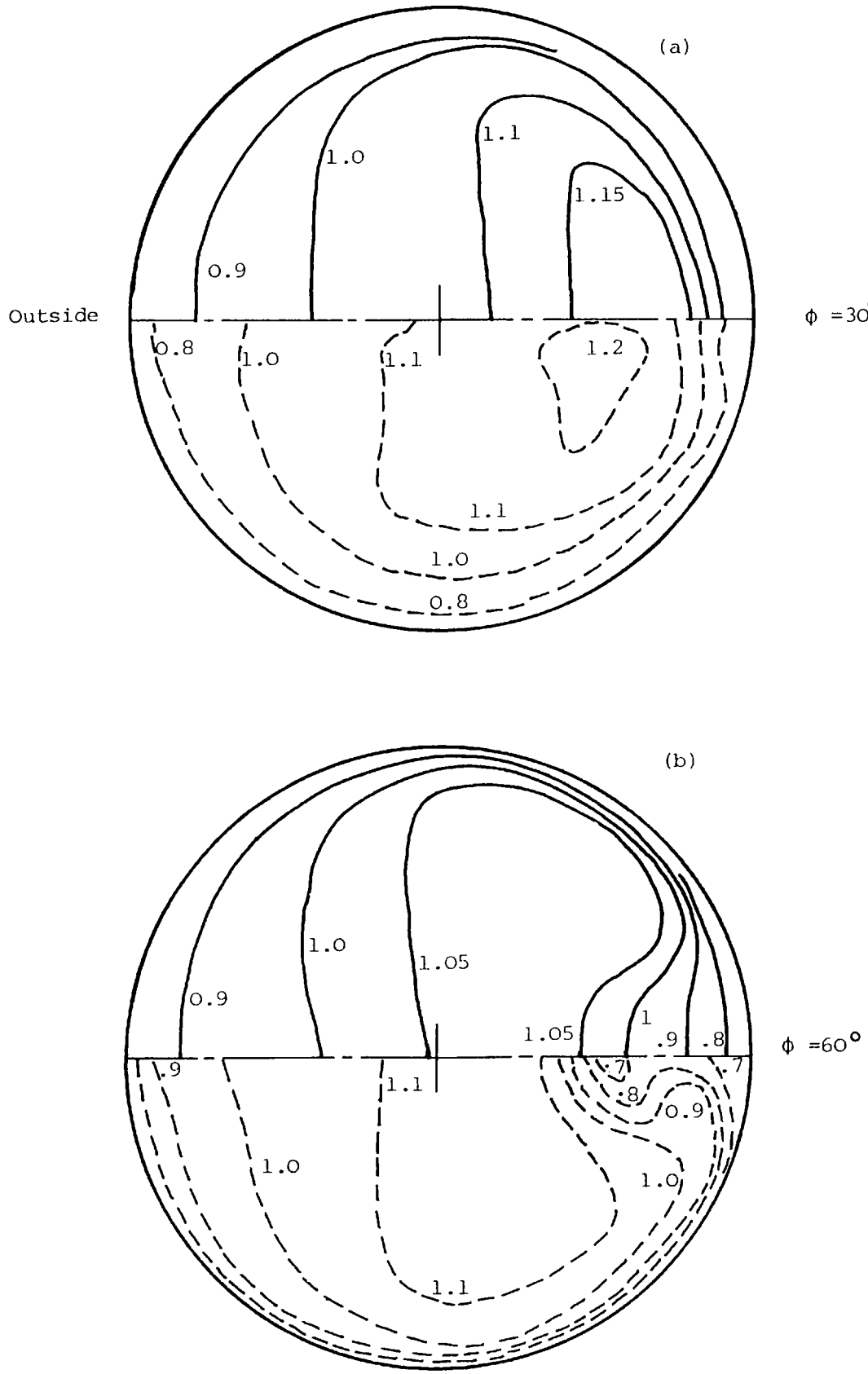


Fig.6.17-(a),(b) Contours of axial velocity W/W_m for turbulent flow in strongly curved ducts.
(Re=43 000, R/r_o=5.6, K=18171)
(———— Prediction, ------- experimental results)

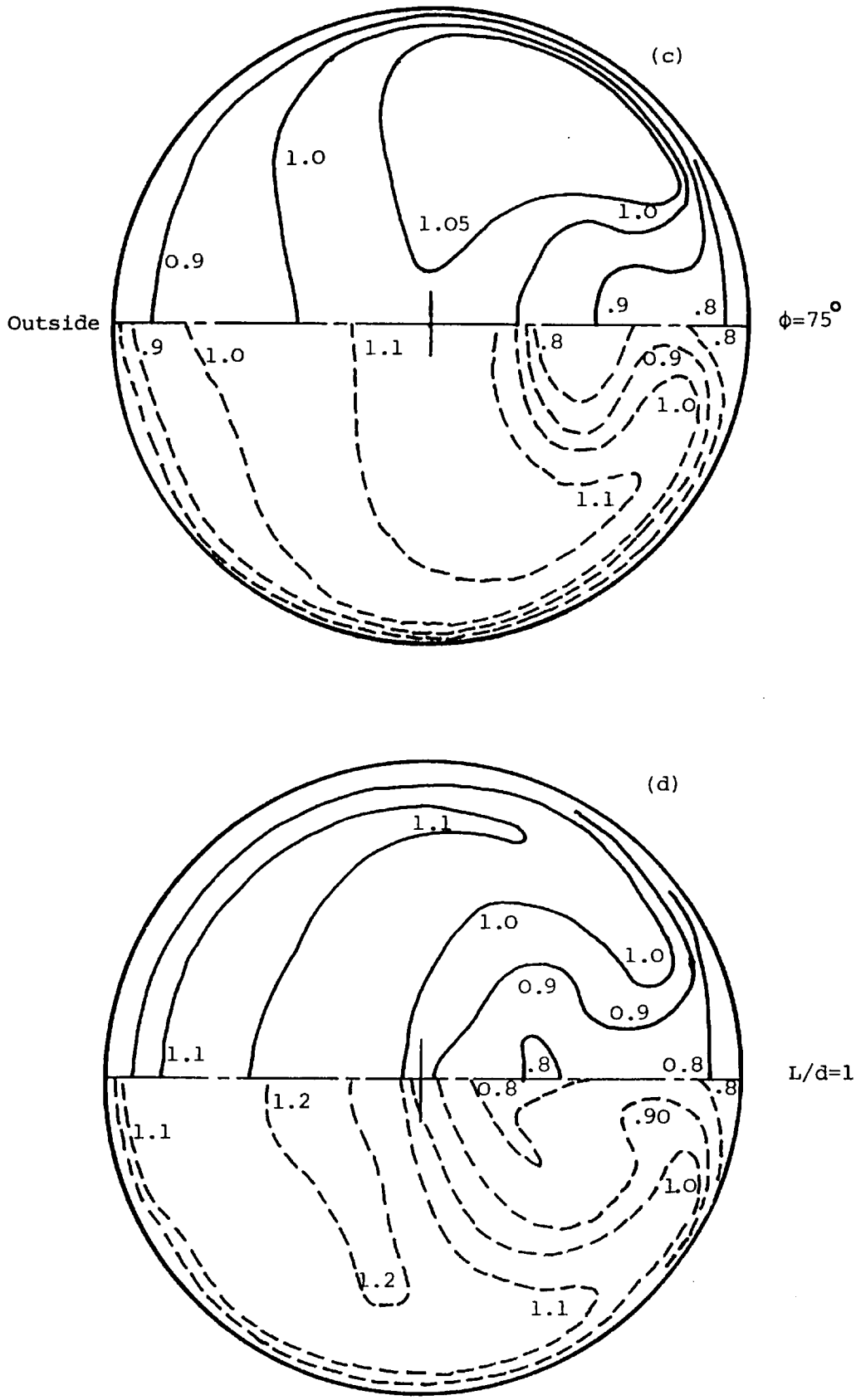


Fig.6.17-(c),(d) Contours of axial velocity W/W_m for turbulent flow in strongly curved ducts.
(Re=43 000, R/r_o=5.6, K=18171)
(——— prediction, -------- experimental results)

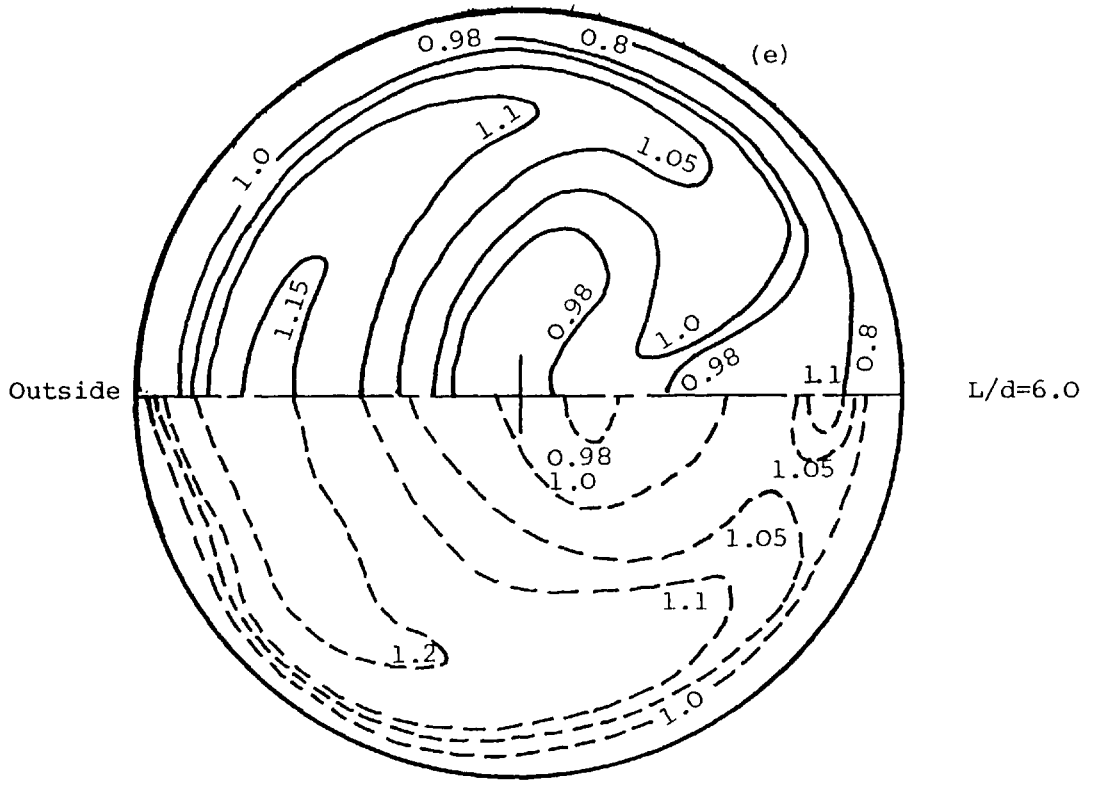


Fig.6.17-(e) Contours of axial velocity W/W_m for turbulent flow in strongly curved ducts.
(Re=43 000, R/r_o=5.6, K=18171)
(———— prediction, -------- experimental results)

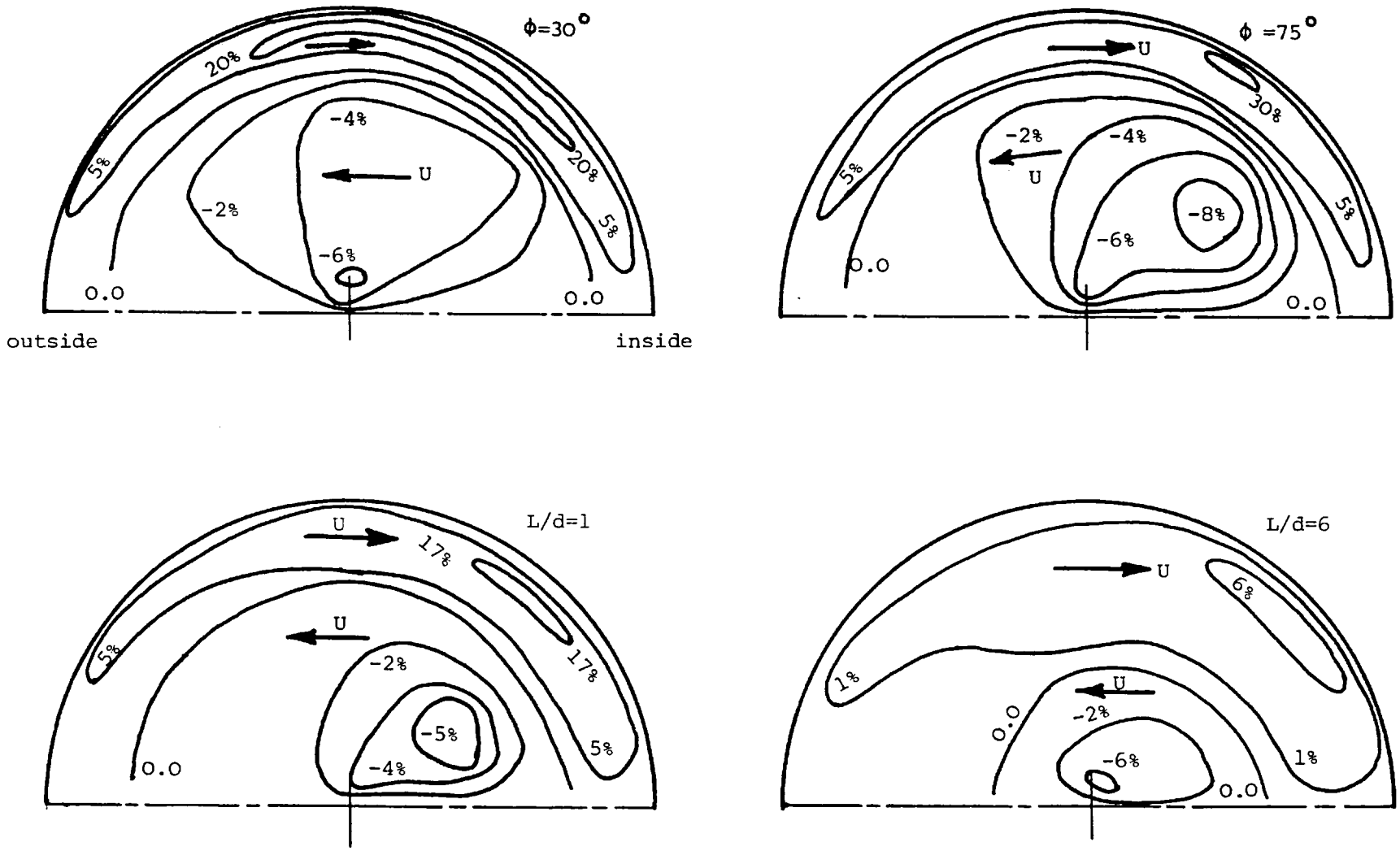


Fig.6.18 Tangential velocity contours U/W_m x100% for turbulent flow in strongly curved ducts.
(Re=43 000, R/r_o=5.6, K=18171)

and decreases downstream. The maximum values of the tangential velocity contours are shifted from the line passing through the centre of the duct and perpendicular to the symmetry line to the inner region of the duct. This shift is also shown for the radial velocity contours in Fig.6.19. The maximum radial-velocity value of $0.11W_m$ occurs at $\phi=75^o$. The corresponding dimensionless pressure contours are shown in Fig.6.20. The cross-stream pressure field is uniform throughout the bend, but decreases quickly in the recovery straight section to nearly zero at L/d=1. The corresponding dimensionless turbulence energy contours are shown in Fig.6.21. Fig.6.22 displays the comparision between the predicted wall static pressure variation with the axial length and the present experimental data. It is shown that the pressure is uniform along the upstream section up to L/d=-1, then the difference between the outside and the inside values increases rapidly in the end of the upstream straight section and in the inlet part of the 90^o bend up to around $\phi=20^o$, then it becomes approximately uniform up to around $\phi=75^o$, then it decreases again rapidly in the end part of the 90^o bend as well as the inlet region of the downstream section up to L/d=1, then the pressure field becomes uniform again. There is good agreement between the predicted wall static pressure variation and the experimental data.

6.4 Concluding Remarks

The laminar flow calculations constitute a test of the numerical method used in the present study. From the results shown above, it is observed that at some locations, for the strongly-curved ducts, the predicted contours do not follow exactly the steep measured velocity gradients. It is probable that a finer grid is required in this case, with consequential uneconomical computer times and storage. It may be

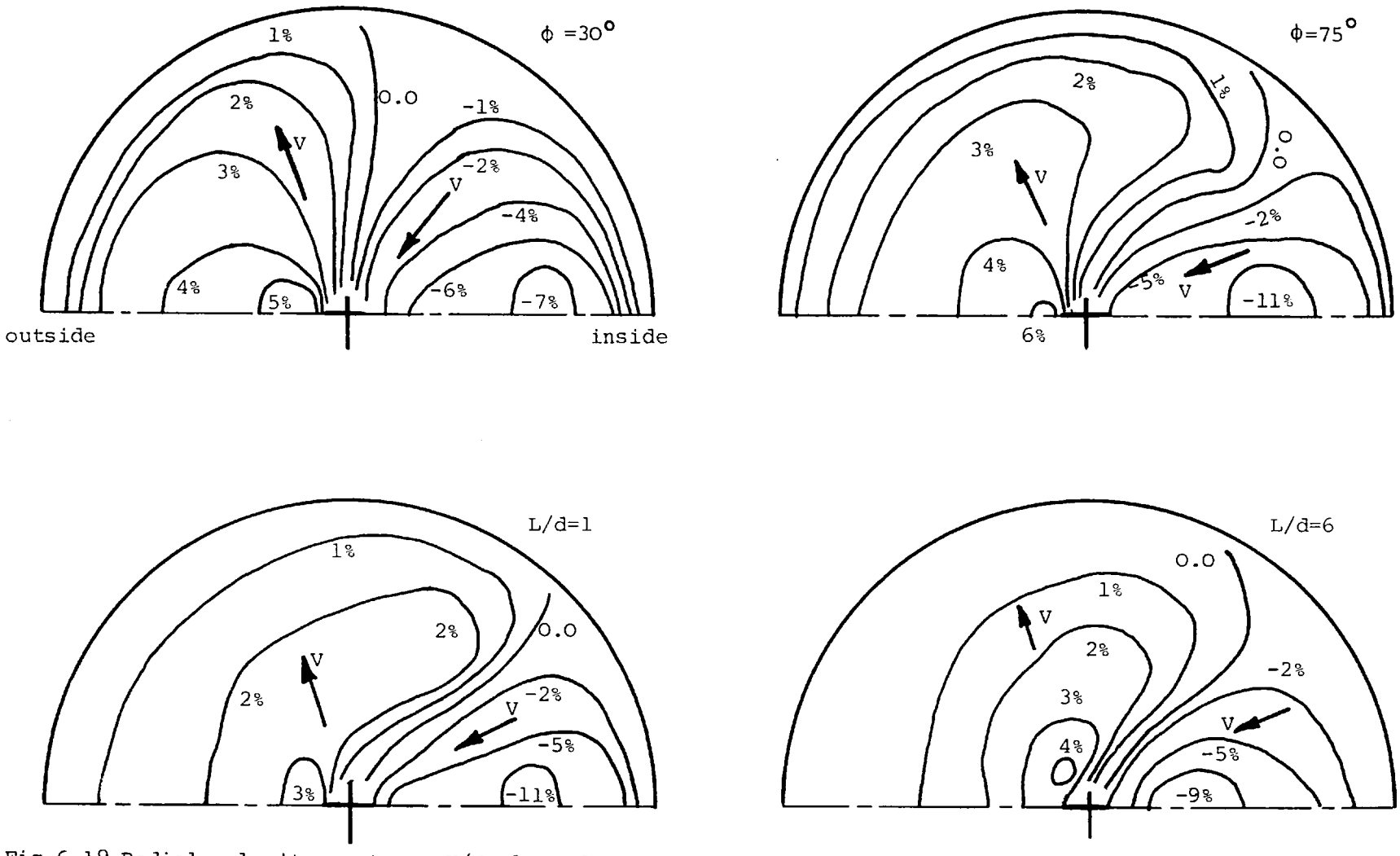


Fig.6.19 Radial velocity contours V/W_m x100% for turbulent flow in strongly curved ducts.
(Re=43 000, R/r_o=5.6, K=18171)

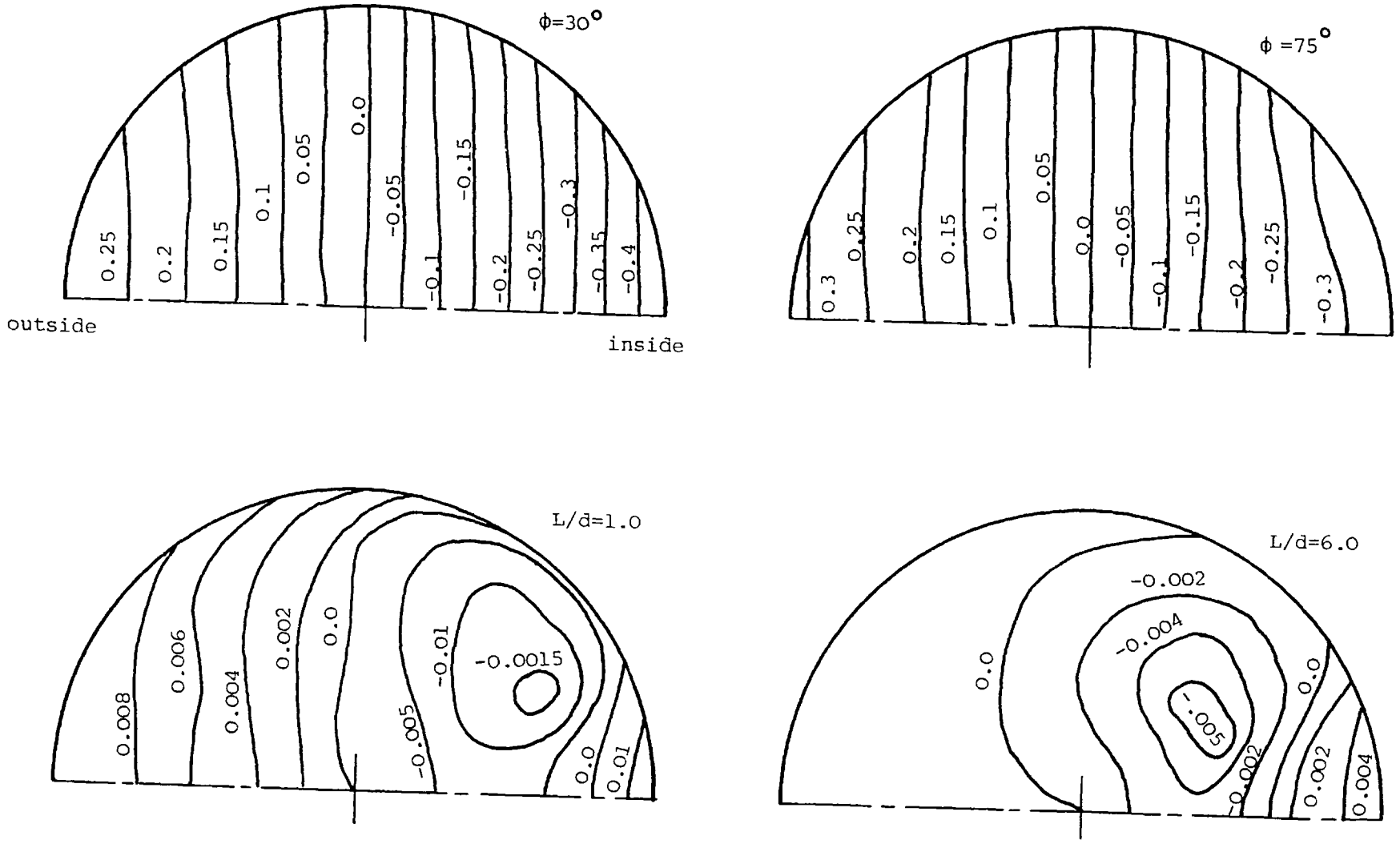


Fig.6. 20 Dimensionless pressure contours $(P-P_{CL})/\frac{1}{2}\rho W_m^2$ for turbulent flow in strongly curved ducts.
(Re=43 000, R/r_o=5.6, K=18171)

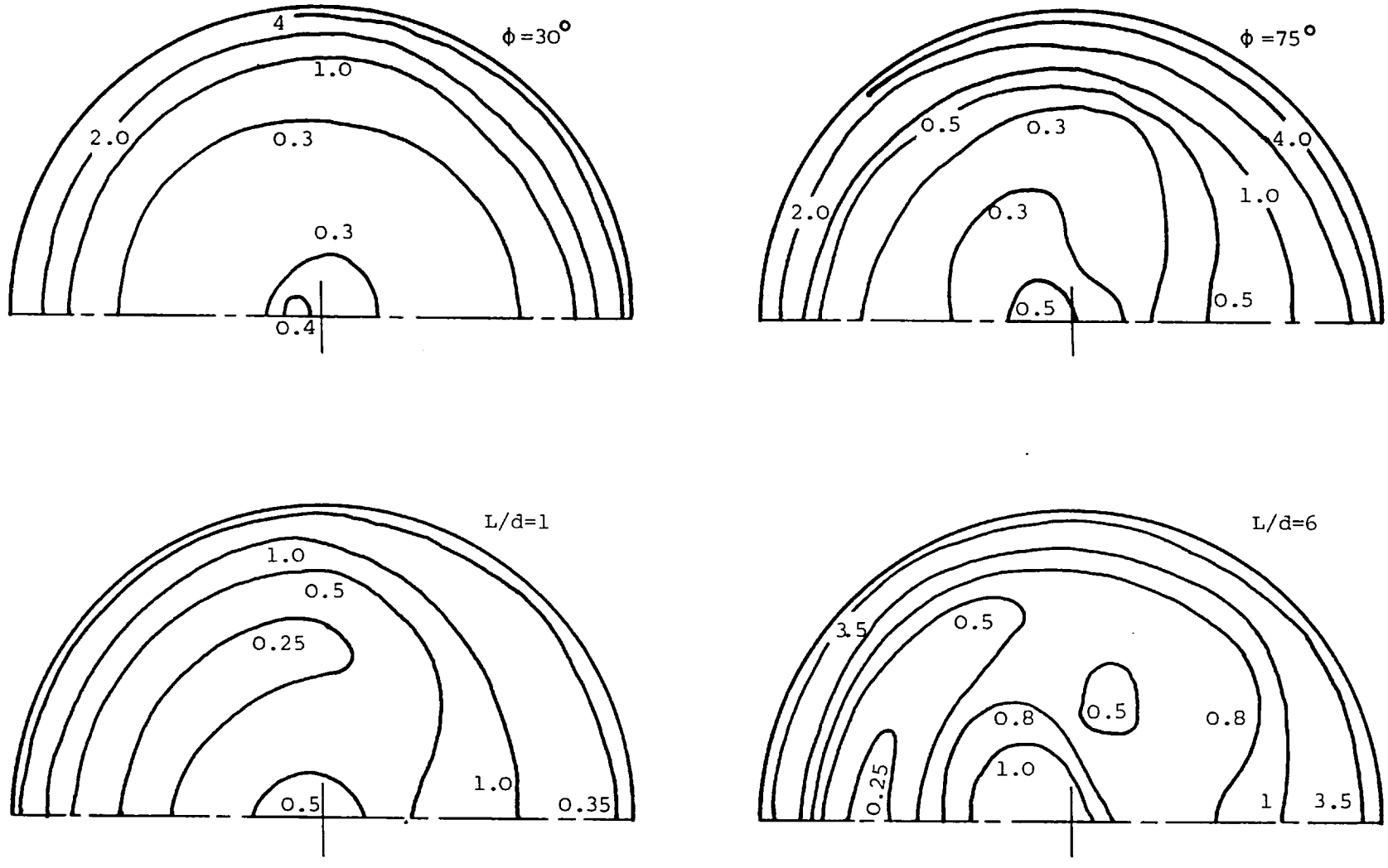


Fig.6.21 Dimensionless turbulence energy contours ($k/u_{\tau\ mean}^2$) for turbulent flow in strongly curved ducts.
(Re=43 000, R/r_o=5.6, K=18171)

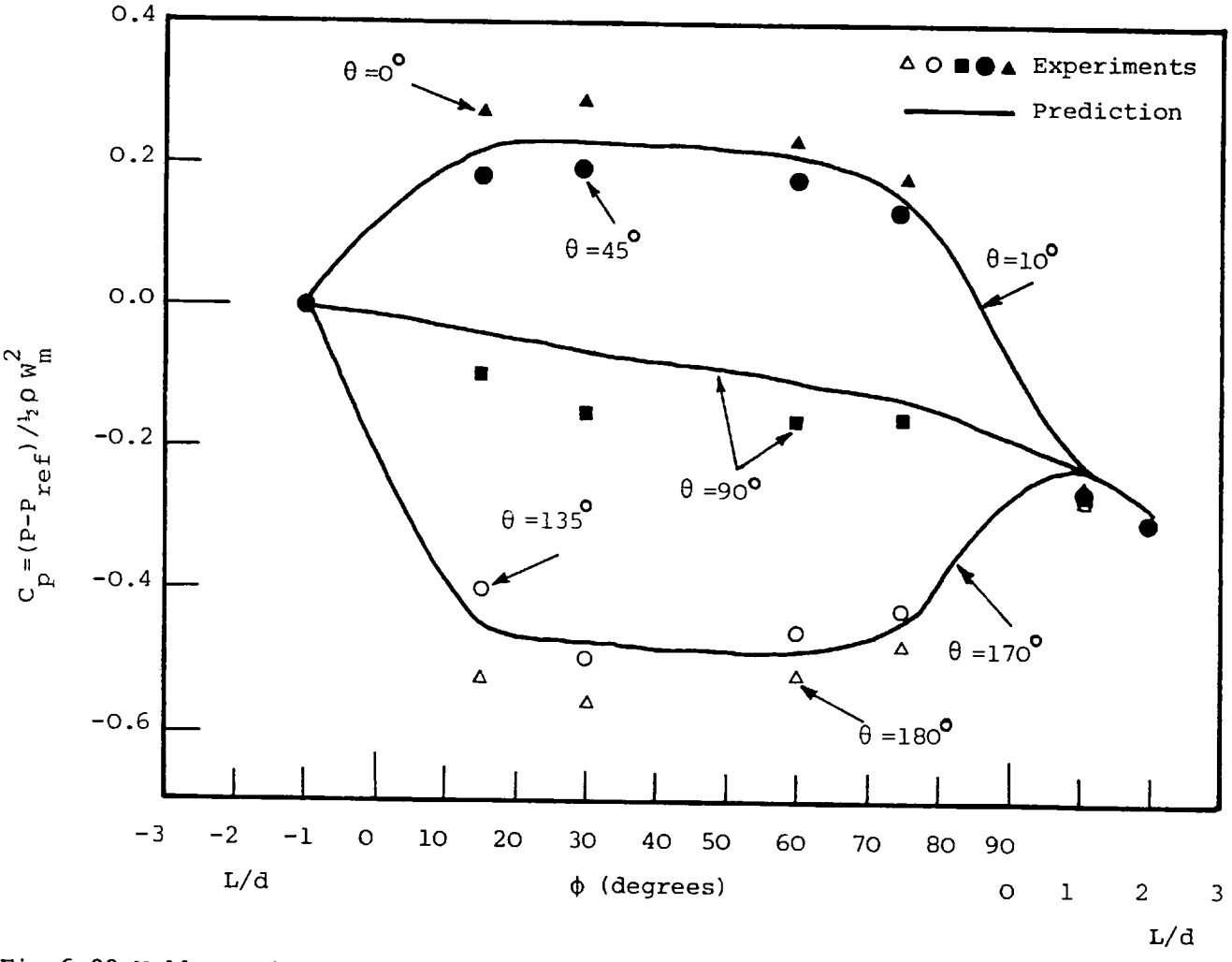


Fig.6.22 Wall static pressure variation for turbulent flow, Re=43 000, R/r_o=5.6, K=18171.

possible to obtain more accurate results by programming fully-elliptic equations without approximation, but in this case all the variables must be stored in three-dimensional arrays and more iterations must be used at great expense on a fine grid. The partially-parabolic method is considered to be the most suitable for this type of the flow, with reasonable computational time and storage space. Some discrepancies between the predicted and measured values for turbulent flow are probably due to the limitations of the k-ε turbulence model used. It appears from the present calculations that turbulence models based on the eddy viscosity concept do not completely represent the turbulence structure in curved ducts. It is necessary to develop either more-complex turbulence-models based on the stress transport equations or to devise empirical modifications to the k-ε turbulence model. Both these refinements to the turbulence model will need more experimental information on the turbulence structure in curved ducts which, at the moment is lacking.

Turbulent shear flows in practical engineering may be subjected to complicating influence such as the effects of body forces due to buoyancy (e.g. in asymmetrically heated pipe flows), rotation (e.g. in parallel rotating pipe flows, mentioned in Chapter 5) or curvature (e.g. in bend flows, mentioned in this chapter). The same type of secondary flows are observed in these complex types of flows. The failure of the calculation methods based on the simple eddy viscosity concept (e.g. k-ε turbulence model) to predict the exact observed response of the turbulence structure effects, unless modified fairly severly in some respect, draws attention to the importance of including anisotropy effects in turbulence models. Most of the turbulence models which are used to predict these complex flows

include the Corilis and centrifugal forces in the momentum equations but not in the turbulent energy and dissipation rate equations. Better predicted results have been obtained, by Brodynuik et al (1980), when the effects of Coriolis force were included in the turbulent energy and dissipation rate equations for the flows in radial rotating channels. Samaraweera (1978) also concluded that the weak point in his work of the numerical study of turbulent heat and mass transport processes in two- and three-dimensional flows seemed to lie in the modelling of the dissipation rate.

CHAPTER 7

CONCLUSIONS AND SUGGESTIONS FOR FUTURE RESEARCH

7.1 Conclusions

The main conclusions that can be drawn from the present study are as follows:

1) The study has shown that calculations of rotating and curved pipe flows are practicable. The computed detailed distributions of mean velocities, lateral velocities, static pressure and temperature facilitate understanding of the response of the flows to body forces. Fairly good agreement with the experimental data has been obtained.

2) Data from rotating pipe flows are insufficiently detailed to test thoroughly the turbulence model predictions. The analogous case of bend flow provides such a test for the velocity field.

3) The calculations draw attention to the defects in simple eddy viscosity modelling. Predictions for turbulent flow and heat transfer in parallel rotating ducts agree reasonably well with the experimental data. Modifications to account for the effects of the secondary flow on the turbulence-structure have been made using an algebraic Reynolds stress and heat flux model, to obtain better agreement with experiment. For a strongly-curved duct, the results obtained using the k-ε model did not agree too well with the data, although the general trend of the flow was predicted.

4) The main result is a series of computer codes for the

numerical solution of the laminar and turbulent flows in bends and rotating tubes. A parabolic calculation procedure has been applied to predict laminar flow in mildly-curved circular ducts, and laminar and turbulent flow in parallel rotating circular ducts. A partially-parabolic procedure has been applied to the calculation of laminar and turbulent flow in strongly-curved ducts in order to take into consideration the influence of downstream pressure which travels upstream.

5) The experimental study provides a useful addition to the data available for testing calculation methods. An experimental program has been successfully completed; measurements have been made of the contours of the developing axial velocity in 90^{o} bends for laminar and turbulent flows using non-intrusive laser Doppler methods.

6) The measurement technique used covered all the circular cross-section, a simple method has been deviced to calculate the position of the measuring point in the flow domain. Also a correction method of taking into account the effects of curvature on the beam path, has been applied to the measured axial velocity at every point.

7.2 Suggestions For Future Work:

The present work suggests a few areas where future research is needed to improve the present capabilities to investigate flows in curved ducts and parallel rotating ducts; these areas are as follows:

1) The use of finer grids with more nodes in the cross section of the duct to study the effects of grid size on the different

predictions, and improvements in the solution procedure so as to be able to use these grids within the computer time limitations.

2) Improvements in the k-ε model of turbulence, first in eddy viscosity changes based on the algebraic Reynolds stress model, and second in curvature and rotation modifications in the ε equation.

3) The incorporation of Reynolds stress models known to give good results in curved duct flows.

4) The development of new ideas in turbulent heat flux modelling. Further research is required to be directed particularly to modelling the pressure term interactions, turbulent diffusion and the temperature variance dissipation rate.

5) Experiment on heat transfer in laminar and turbulent flows in curved and rotating ducts for different test-sections with different geometeries to obtain the effects of the body forces on the flow structure (e.g. turbulence structure).

LIST OF REFERENCES

AGRAWAL, Y., GONG, K. and TALBOT, L. (1978): "Laser anemometer study of flow development in curved circular pipes". J. of Fluid Mech., 85, 3, 491-518.

AKIAMA, M. and CHENG, K.C. (1971): "Boundary vorticity method for laminar forced convection heat transfer in curved pipes". Int. J. Heat Mass Transfer, 14, 1659-1675.

AKIAMA, M., CHENG, K.C. and NAKAYAMA, J. (1979): "Effect of finite and infinite aspect ratios on flow pattern in curved rectangular channels". Flow visualization, (ed. T. Asanuma), McGraw Hill.

ANON (1968): "Debut of the water-cooled rotor". Engineering, January 1968, 58-60.

AUSTIN, L.R. (1971): "The development of viscous flow within helical coils". Ph.D. Thesis, University of Utah.

AUSTIN, L.R. and SEADER, J.D. (1973): "Fully-developed viscous flow in coiled circular pipes". AICHE J., 19, 1, 85-94.

BARROW, H., HUMPHREY, J.F. and MORRIS, W.D. (1967): "Convection heat transfer in the entry region of a tube which revolves about an axis parallel to itself". Int. J. Heat Mass Transfer, 10, 333-347.

BARUA, S.N. (1963): "On secondary flow in stationary curved pipes". Quart. J. Mech. App. Math., 16, 61-77.

BICEN, A.F. and WHITELAW, J.H. (1981): "Refraction correction for LDA measurements in flows with curved optical boundaries". Imperial College, Mech. Eng. Dept., London SW7, Report FS/81/17.

BOADWAY, J.D. and KARAHAN, E. (1981): "Correction of LDA readings for refraction at cylindrical interfaces". DISA Information, No.26, 4-6.

BORDYNUIK, R.M., HOWARD, J.H.G. and PATANKAR, S.V. (1980): "Flow prediction in rotating ducts using Coriolis-modified turbulence models". Trans. ASME, 102, 456-461.

BRADSHAW, P. (1972): "The understanding and prediction of turbulent flow". Aero. J., 76 , 403-418

BRADSHAW, P. (1973): "Effect of streamline curvature on turbulent flow". AGARD-AG-169.

BRAIN, P.L.T., DRAVID, A.N., MERRILL, E.W. and SMITH, K.A. (1971): "Effect of secondary fluid motion on laminar flow heat transfer in helically coiled tubes". AICHE J., 17, 5, 1114-1122.

BREMHORST, K. and BULLOCK, K.J. (1970): "Spectral measurements of temperature and longitudinal velocity fluctuations in fully-developed pipe flow". Int. J. Heat Mass Transfer, 13, 1313-1329.

BREMHORST, K., KREBS, L. and MULLER, U. (1981): "Measurements and prediction of the mean and fluctuating temperature field downstream of a multi-bare jet block in which one jet is heated". Int. J. Heat Mass Transfer, 24, 8, 1305-1312.

CHAMPAGNE, F.H., CORRSIN, S. and HARRIS, V.G. (1970): "Experiments on nearly homogeneous turbulent shear flow". J. Fluid Mech., 41, 1, 81-139.

CHIENG, C.C. and LAUNDER, B.E. (1979): "On the calculation of turbulent transport in flow through an asymmetrically heated pipe". Numerical Heat Transfer, 2, 359-371.

CHOU, P.Y. (1945): "On velocity correlations and solutions of the equations of turbulent fluctuation". Quart. Appl. Math., 3, 38-54.

CLAUSER, F.H. (1956): "The turbulent boundary layer". Advances in Applied Mechanics, 4, 1-51. Academic Press.

DEAN, W.R. (1927): "Note on the motion of fluid in a curved pipe". The London, Edinburgh _ Dublin Phil. Mag. and J. Science, 4, 208-223.

DEAN, W.R. (1929): "Stream-line flow through curved pipe". Proc. Roy. Soc., A, 123, 645-663.

DURST, F., MELLING, A. and WHITELAW, J.H. (1976): "Principles and practice of laser-Doppler anemometry". Academic Press, London.

ENAYET, M.M., GIBSON, M.M., TAYLOR, A.M.K.P. and YIANNESKIS, M. (1981): "Laser Doppler measurements of laminar and turbulent flow in a pipe bend". Imperial College, Mech. Eng. Dept., London SW7, Report FS/81/7. (also: NASA CR-3551-1982).

GHIA, K.N. and SOKHEY, J.S. (1977): "Laminar incompressible viscous flow in curved ducts of regular cross-sections". Trans. ASME, J. Fluids Eng., 99, 4, 640-648.

GIBSON, M.M. (1978): "An algebraic stress and heat-flux model for turbulent shear flow with streamline curvature". Int. J. Heat Mass Transfer, 21, 1609-1617.

GIBSON, M.M., JONES, W.P. and YOUNIS, B.A. (1981): "Calculation of turbulent boundary layers on curved surfaces". Phys. Fluids, 24, 3, 386-395.

GIBSON, M.M. and LAUNDER, B.E. (1976): "On the calculation of horizontal, turbulent, free shear flows under gravitational influence". Trans. ASME, Ser. C, 98, 81-86.

GIBSON, M.M. and LAUNDER, B.E. (1978): "Ground effects on pressure fluctuations on the atmospheric boundary layer". J. Fluid Mech., 86, 3, 491-511.

GIBSON, M.M. and RODI, W. (1981): "A Reynolds-stress closure model of turbulence applied to the calculation of a highly curved mixing layer". J. Fluid Mech., 103, 161-182.

GREENSPAN, D. (1973): "Secondary flow in a curved tube". J. Fluid Mech., 57, 1, 167-176.

HINZE, J.O. (1959): "Turbulence: An introduction to its mechanism and theory". McGraw Hill.

HUMMEL, R.L., KACZINSKY, J. and SMITH, J.W. (1975): "Laminar flow in the central plane of a curved circular pipe". Can. J. Chem. Eng., 53, 221-224.

HUMPHREY, J.F. (1968): "Heat transfer in a tube revolving about a displaced axis". A.R.C. C.P. No.1069.

HUMPHREY, J.A.C. (1977): "Flow in ducts with curvature and roughness". Ph.D. Thesis, June 1977, University of London, Imperial College, Mech. Eng. Dept.

HUMPHREY, J.A.C. (1978): "Numerical calculation of developig lamiar flow in pipes of arbitrary curvature radius". Can. J. Chem. Eng., 56, 151-164.

HUMPHREY, J.A.C., TAYLOR, A.M.K. and WHITELAW, J.H. (1977): "Laminar flow in a square duct of strong curvature". J. Fluid Mech., 83, 509-527.

HUMPHREY, J.A.C. and Whitelaw, J.H. (1978): "Measurements of turbulent flow properties in a square duct with strong curvature". Imperial College, Mech. Eng. Dept., Report FS/78/15.

HUMPHREY, J.A.C., WHITELAW, J.H. and YEE, G. (1981): "Turbulent flow in a square duct with strong curvature". J. Fluid Mech., 103, 443-463.

HUMPHREY, J.A.C. and YEE, G. (1979): "Developing laminar flow and heat transfer in strongly curved ducts of rectangular cross-section". ASME paper 79-WA/m-10.

IDERIAH, F.J.K. and GOSMAN, A.D. (1976): "TEACH-T: a general computer program for 2-D, turbulent, recirculating flows". Imperial College, Mech. Eng. Dept., London SW7.

ITO, H. (1959): "Friction factors for turbulent flow in curved pipes". J. Basic Eng. Trans. ASME, 81, Ser. D, 123-134.

ITO, H. (1969): "Laminar flow in curved pipes". Report No.224 of the Institute of High Speed Mechanics, Tohoku University. Published in Z. angew. Math. Mech., Bd.49(1969). Helft11, S.653/663.

JAYATILLAKA, C.L.V. (1966): "The influence of Prandtl number and surface roughness on the resistance of the laminar sub-layer to momentum and heat transfer". Imperial College, Mech. Eng. Dept., Report TWF/R/2.

KALB, C.E. and SEADER, J.D. (1972): "Heat and mass transfer phenomena for viscous flow in curved circular tube". Int. J. Heat Mass Transfer, 15, 801-817.

KALB, C.E. and SEADER, J.D. (1974): "Fully-developed viscous flow and heat transfer in curved circular tubes with uniform wall temperature". AICHE J., 20, 340-346.

KOLMOGOROV, A.N. (1968): "Equations of turbulent motion of an incompressible fluid". Translation by SPALDING, D.B., Imperial College, Mech. Eng. Dept., Report ON/6 November 1968.

LAUFER, J. (1953): "The structure of turbulence in fully-developed pipe flow". NACA TN2954, Report 1174.

LAUNDER, B.E. (1971): "An improved algebraic modelling of the Reynolds stresses". Imperial College, Mech. Eng. Dept., Report TM/TN/A/9.

LAUNDER, B.E. (1973): "Scalar property transport by turbulence". Imperial College, Mech. Eng. Dept., Report HTS/73/26.

LAUNDER, B.E. (1975): "On the effects of a gravitational field on the turbulent transport of heat and momentum". J. Fluid Mech., 67, 3, 569-581.

LAUNDER, B.E. (1976): "Heat and mass transport". in Turbulence, Chapter 6, edited by BRADSHAW, Springer, Berlin.

LAUNDER, B.E., MORSE, A., RODI, W. and SPALDING, D.B. (1972): "The prediction of free shear flows -a comparison of the performance of six turbulence models". N.A.S.A. SP-311, p.361. (Also: Imperial College, Mech. Eng. Dept., Report TM/TN/B/19).

LAUNDER, B.E., REECE, G.J. and RODI, W. (1973): "Progress in the development of a Reynolds stress turbulence closure". Imperial College, Mech. Eng. Dept., Report HTS/73/31. (also: J. Fluid Mech. 68, 3, 537-566, 1975).

LAUNDER, B.E. and SPALDING, D.B. (1972): "Mathematical models of turbulence". Academic press, London.

LAUNDER, B.E. and SPALDING, D.B. (1974): "The numerical computation of turbulent flows". Computer Methods in Applied Mechanics and Engineering, 3, 269-289.

LAUNDER, B.E. and YING, W.M. (1973): "Prediction of flow and heat transfer in ducts of square cross-section". Proc. I. Mech. E., 187, 455-461.

LAWN, C.J. (1971): "The determination of the rate of dissipation in turbulent pipe flow". J. Fluid Mech., 48, 3, 477-505.

McLAUGHIN, E.F. and SEBAN, R.A. (1963): "Heat transfer in tube coils with laminar and turbulent flow". Int. J. Heat Mass Transfer, 6, 387-395.

MAJUMDAR, A.K., MORRIS, W.D., SKIADARESSIS, D. and SPALDING, D.B. (1976): "Heat transfer in rotating ducts". Imperial College, Mech. Eng. Dept., Report HTS/76/5.

MAJUMDAR, A.K. and SPALDING, D.B. (1976): "A numerical investigation of 3-D flows in a rotating duct by partially-parabolic procedure". Imperial College, Mech. Eng. Dept., Report HTS/76/26.

MEGAHED, I.E.A. (1979): "The prediction of three-dimensional gas fired combustion chamber flows". Ph.D. Thesis, Imperial College, Mech. Eng. Dept., March 1979.

MELLING, A. and WHITELAW, J.H. (1976): "Turbulent flow in a rectangular duct". J. Fluid Mech., 78, 2, 289-315.

MORI, Y. and NAKAYAMA, W. (1965): "Study of forced convective heat transfer in curved pipes". (1st report, laminar region). Int. J. Heat Mass Transfer, 8, 67-82.

MORI, Y. and NAKAYAMA, W. (1967a): "Study of forced convective heat transfer in curved pipes". (2nd report, turbulent region). Int. J. Heat Mass Transfer, 10, 37-59.

MORI, Y. and NAKAYAMA, W. (1967b): "Forced convective heat transfer in a straight pipe rotating around a parallel axis". (1st report, laminar region). Int. J. Heat Mass Transfer, 10, 1179-1193.

MORI, Y., UCHIDA, Y. and UKON, T. (1971): "Forced convective heat transfer in a curved channel with square cross-section". Int. J. Heat Mass Transfer, 14, 1787-1805.

MORRIS, W.D. (1964): "Heat transfer characteristics of a rotating thermosyphon". Ph.D. Thesis, University of Wales.

MORRIS, W.D. (1965a): "A theoretical analysis of the influence of rotation on flow in a tube rotating about a parallel axis with uniform angular velocity". J. Roy. Aero. Soc., 69, 201-202. (also: "Heat transfer and fluid flow in rotating coolant channels". Research Studies Press, 1981).

MORRIS, W.D. (1965b): "Laminar convection in a heated vertical tube rotating about a parallel axis". J. Fluid Mech., 21, 3, 453-464.

MORRIS, W.D. (1968): "An experimental investigation of laminar heat transfer in a uniformly heated tube rotating about a parallel axis". A.R.C. C.P. 1055.

MORRIS, W.D. (1969): "Some observations on the heat transfer characteristics of a rotating mixed convection thermosyphon". A.R.C. C.P. No.1115.

MORRIS, W.D. (1981): "Heat transfer and fluid flow in rotating coolant channels". Research Studies Press.

MORRIS, W.D. and WOODS, J.L. (1971): "A numerical analysis of laminar heat transfer and flow resistance in a tube rotating about an axis parallel to itself". Mech. Eng. Dept., School of Applied Science, University of Sussex.

MORRIS, W.D. and WOODS, J.L. (1974): "An investigation of laminar flow in the rotor windings of directly cooled electrical machines". J. Mech. Eng. Sci., 16, 6, 408-417.

MORRIS, W.D. and WOODS, J.L. (1977): "Heat transfer in the entrance region of tubes which rotate about a parallel axis". School of Applied Science, University of Sussex, Report 77/ME/92. (also: J. Mech. Eng. Sci., 20, 6, 319, 1978).

NAKAYAMA, W. (1968): "Forced convective heat transfer in a straight pipe rotating around a parallel axis". (2nd report, turbulent region). Int. J. Heat Mass Transfer, 11, 1185-1201.

NIKURADSE, J. (1932): VDI Forschungsheft, 356.

PATANKAR, S.V., PRATAP, V.S. and SPALDING ,D.B. (1974): "Prediction of laminar flow and heat transfer in helically coiled pipes". J. Fluid Mech., 62, 3, 539-551.

PATANKAR, S.V., PRATAP, V.S. and SPALDING, D.B. (1975): "Prediction of turbulent flow in curved pipes". J. Fluid Mech., 67, 3, 583-595.

PATANKAR, S.V. and SPALDING, D.B. (1972): "A calculation procedure for heat, mass and momentum transfer in three-dimensional parabolic flows". Int. J. Heat Mass Transfer, 15, 1787-1806.

PRATAP, V.S. (1975): "Flow and heat transfer in curved ducts". Ph.D. Thesis, Imperial College, Mech. Eng. Dept. (Also: report HTS/75/25).

QUARMBY, A. and QUIRK, R. (1972): "Measurements of the radial and tangential eddy diffusivities of heat and mass in turbulent flow in a plain tube". Int. J. Heat Mass Transfer, 15, 2309-2327.

QUARMBY, A. and QUIRK, R. (1974): "Axisymmetric and non-axisymmetric turbulent diffusion in a plain circular tube at high schmidt number". Int. J. Heat Mass Transfer, 17, 143-147.

REYNOLDS, W.C. (1963): "Turbulent heat transfer in a circular tube with variable circumferential heat flux". Int. J. Heat Mass Transfer, 6, 445-454.

REYNOLDS, W.C. (1976): "Computation of turbulent flows". Ann. Rev. Fluid Mech., 8, 183-208.

ROWE, M. (1970): "Measurements and computations of flow in pipe bends". J. Fluid Mech., 43, 771-783.

RODI, W. (1972): "The prediction of free turbulent boundary layer by use of two-equation model of turbulence". Ph.D. Thesis, University of London, Imperial College, Mech. Eng. Dept.

RODI, W. (1976): "A new algebraic relation for calculating the Reynolds-stresses". Z. Ang. Math. Mech., 56, 219-221.

RODI, W. (1980): "Turbulence models and their application in hydraulics". International Association For Hydraulic Research (IAHR) -Section on Fundamentals of Division II: Experimental and Mathematical Fluid Dynamics.

ROTTA, J. (1951a): "Statistical theory of non-homogeneous turbulence". paper 1, Z. fur Physick, 129, 547-572. (Also: Translation by RODI, W., Imperial College, Mech. Eng. Dept., Report TWF/TN/39, March 1968).

ROTTA, J. (1951b): "Statistical theory of non-homogeneous turbulence". paper 2, Z. Phys., 131, 51-77. (Also: Translation by RODI, W., Imperial College, Mech. Eng. Dept., Report TWF/TN/38, Feb.1968).

SAMARAWEERA, D.S.A. (1978): "Turbulent heat transport in two- and three-dimensional temperature field". Ph.D. Thesis, University of London, Imperial College, Mech. Eng. Dept.

SHIR, C.C. (1973): "A preliminary numerical study of atmospheric turbulent flow in the idealized planetary boundary layer". J. Atoms. Sci., 30, 1327-1339.

SKIADARESSIS, D. and SPALDING, D.B. (1976): "Laminar heat transfer in a pipe rotating about a parallel axis". Imperial College, Mech. Eng. Dept., Report HTS/76/23.

SPALDING, D.B. (1974): "Numerical computation of steady boundary layers- A survey". Imperial College, Mech. Eng. Dept., Report HTS/74/27.

SPLDING, D.B. (1975): "Calculation procedures for 3-D parabolic and partially-parabolic flows". Imperial College, Mech. Eng. Dept., Report HTS/75/5.

STEPHENSON, P.L. (1982): "An experimental study of flow and heat transfer in a duct rotating about a parallel axis". XIV Int. Confre. for Heat and Mass Transfer Symposium on "Heat and mass transfer in rotating machinery", Dubrovnik, Yougoslavia, 30Aug.-3Sept. 1982.

TAYLOR, A.M.K.P., WHITELAW, J.H. and YIANNESKIS, M. (1980): "Measurements of laminar and turbulent flow in a curved duct with thin inlet boundary layer". Imperial Collerge, Mech. Eng. Dept., Report FS/80/29.

TAYLOR, A.M.K.P., WHITELAW, J.H. and YIANNESKIS, M. (1981): "Developing flow in S-shaped ducts: Square cross-section duct". Imperial College, Mech. Eng. Dept., Report FS/81/22.

NOMENCLATURE

Sympol	Meaning	Location of first occurence
A	constant	Eqn.(1.7)
	surface area	Eqn.(3.1)
A_i	coefficient in the finite-difference eqn.	Eqn.(3.5)
a	duct width	Fig.1.21
	area	Eqn.(3.9)
B	constant in the logarithmic wall function	Eqn.(2.19)
b	duct height	Fig.1.21
C_f	resistance coefficient ($\tau_w/\frac{1}{2}\rho W_m^2$)	Sec.(1.2.1)
	correction factor	Eqn.(4.10)
C_p	specific heat at constant pressure	Eqn.(2.26)
	dimensionless pressure	Fig.4.20
C_T	overall pressure loss coefficient	Eqn.(1.14)
C_T'	constant in the turbulence model	Eqn.(2.42)
C_1, C_2	constants in the turbulence model	Eqn.(2.17)
C_1, C_2	constants in the turbulence model	Eqns.(2.30) and (2.31)
C_{1T}, C_{2T}	constants in the turbulence model	Eqn.(2.37)
C_μ	constant in the turbulence model	Eqn.(2.14)
D	coefficients of pressure gradient terms	Eqns.(3.6-3.8)
	diameter	Eqn.(4.8)
d	diameter	Eqn.(1.15)
E	constant in the logarithmic law	Eqn.(2.19)
f	wall-damping function	Eqn.(2.32)
	focal length	Fig.4.7
g	gravitational acceleration	Eqn.(1.9)

Sympol	Meaning	Location of first occurence
Gr_r	rotational Grashof number	Eqn.(1.17)
H	radius of rotation	Fig.1.1
J	rotational Reynolds number	Eqn.(1.11)
K	Dean number	Eqn.(1.20)
	constant	Eqn.(4.7)
k	kinetic energy of turbulence	Eqn.(2.9)
L	pipe length	Fig.1.5
l	length scale	Eqn.(2.13)
M	lens magnification	Eqn.(4.8)
m	constant	Sec.(1.2.1)
$\dot{m}$	mass flow rate	Table (4.1)
N_{fr}	number of fringes	Eqn.(4.9)
Nu	Nusselt number	Fig.1.3
n_f	refraction index of the fluid	Eqn.(4.10)
n_i	unit vector normal to the surface	Eqn.(2.32)
n_w	refraction index of the wall	Eqn.(4.10)
P	local mean pressure	Eqn.(1.1)
	production rate of turbulence energy	Sec.(2.3.2)
P_{ij}	production rate of $\overline{u_i u_j}$	Eqn.(2.29)
P_{iT}	production rate of $\overline{u_i t}$ contains mean strain	Eqn.(2.37)
Pr	Prandtl number	Fig.1.4
p	local fluctuating pressure	Eqn.(2.29)
$\dot{q}''_w$	wall heat transfer rate per unit area	Eqn.(2.26)
R	radius ratio r/r_c	Sec.(1.2.1)
	radius of curvature	Eqn.(1.20)
Ra_g	gravitational Rayleigh number	Eqn.(1.9)
Ra_r	rotational Rayleigh number	Eqn.(1.8)

Sympol	Meaning	Location of first occurence
Re	Reynolds number	Eqn.(1.10)
Ro	Rosby number	Eqn.(1.13)
r	coordinate in the cylinderical polar system	Eqn.(1.1)
r_i	position vector	Eqn.(2.32)
r_o	pipe radius	Eqn.(1.8)
S_{iT}	surface integration includes wall effect	Eqn.(2.37)
Sp,Su	linearlisation terms	Eqn.(3.2)
Sw	swirl number	Eqn.(1.16)
S_ϕ	generation of Φ per unit volume	Eqn.(2.3)
T	local mean temperature	Fig.1.2
T^+	dimensinless temperature	Eqn.(2.25)
t	time	Eqn.(2.2)
	fluctuating temperature	Eqn.(2.36)
$\hat{U}_i$	instantaneous velocity	Eqn.(2.1)
U_i	local mean velocitty components	Eqn.(2.4)
U,V,W	local mean velocity components	Fig.1.1
u^+	local mean velocity/friction velocity	Eqn.(2.19)
u_i	fluctuating velocity components	Eqn.(2.4)
u,v,w	fluctuating velocity components	Sec.(5.2.1)
u_τ	friction velocity	Eqn.(2.20)
X_j	general coordinates	Eqn.(2.1)
x	coordinate in the cartesian system	Fig.1.21
y	distance from the wall	Eqn.(2.21)
	coordinate in the cartesian system	Fig.1.21
y^+	dimensionless distance	Eqn.(2.19)
z	coordinate in the culinderical polar system	Eqn.(1.1)

Greek letters:

symbol	Meaning	Location of first occurence
α	thermal diffusivity	Eqn.(1.8)
β	coefficient of expansion	Eqn.(1.8)
	eddy-viscosity coefficient	Eqn.(2.46)
γ	axial pressure gradient	Eqn.(1.6)
δ_{ij}	kronecker delta (=1 for i=j, =0 for i≠j)	Eqn.(2.9)
Δ	difference of	Sec.(1.2.1)
ε	eccentricity parameter	Eqn.(1.18)
	dissipation rate of turbulence K.E.	Sec.(1.2.3)
Γ	ratio of inertia force to body force	Sec.(1.2.1)
	exchange coefficient	Eqn.(2.3)
ρ	fluid density	Eqn.(1.1)
η	eddy-diffusivity coefficient	Eqn.(2.47)
θ	coordinate in the cylinderical-polar system	Eqn.(1.1)
κ	Von Karman constant	Eqn.(2.19)
ν	kinematic viscosity	Eqn.(1.1)
	frequency	Eqn.(4.1)
λ	wave length	Eqn.(4.1)
Φ	local mean scalar property	Eqn.(2.5)
Φ_{ij}	pressure-strain correlation	Eqn.(2.30)
Φ_{iT}	pressure-temperature gradient correlation	Eqn.(2.37)
ϕ	coordinate in the toroidal system (r,θ,ϕ)	Fig.1.13
	scalar property fluctuation	Eqn.(2.5)
Ψ	dimenssionless stream-function	Eqn.(1.5)
	angle	Eqn.(4.1)
τ	axial temperature gradient	Eqn.(1.8)
	shear stress	Eqn.(2.20)

symbol	Meaning	Location of first occurence
σ	Prandtl or Schmidt number	Eqn.(2.11)
Ω	rotational speed	Eqn.(1.1)

Subscripts:

c	curved	Eqn.(A1.10)
CL	centre line value	Fig.1.20
corr	corrected value	Eqn.(4.12)
D	downstream	Eqn.(3.8)
	Doppler	Eqn.(4.1)
E	east grid node	Eqn.(3.9)
e	east interface	Eqn.(3.9)
eff	effective	Eqn.(2.16)
k	kinetic energy of turbulence	Eqn.(2.16)
m	mean value	Sec.(1.2.1)
max	maximum value	Fig.A4.1
N	north grid node	Eqn.(3.9)
n	north interface	Eqn.(3.9)
o	reference datum	Eqn.(1.21)
?	stationary pipe flow	Sec.(1.2.1)
P	at point P	Eqn.(3.2)
ph	pinhole	Eqn.(4.8)
ref	reference	Fig.4.20
S	south grid node	Eqn.(3.7)
s	south interface	Eqn.(3.9)
t	turbulent	Eqn.(2.9)
U	upstream	Eqn.(3.9)
W	west grid node	Eqn.(3.6)

Symbol	Meanig	Location of first occurence
w	wall value	Fig.1.2
W	west interface	Eqn.(3.9)
ε	dissipation rate of turbulence K.E.	Eqn.(2.17)

Superscripts:

u,v,w	velocity components	Eqn.(3.6 - 3.8)
'	correction	Eqn.(3.15)

APPENDIX A1

THE GOVERNING DIFFERENTIAL EQUATIONS

A1.1 Introduction

In this appendix, the partial-differential equations governing the steady, three-dimmential incompressible flow and heat transfer phenomena in circular ducts rotating about an axis parallel to itself, as well as the flow in curved ducts are described in their full form. The equations are expressed in the two coordinate systems mentioned before, namely the (r, θ, z) coordinates for rotating ducts and (r, θ, ϕ) coordinates for bends. The equations stated here are identical for laminar and turbulent flows except that for turbulent flow, the shear stresses are calculated from an "effective" exchange-coefficient which is the sum of the laminar and turbulent exchange coefficients, as mentioned in Chapter 2 for the k-ε model of turbulence. The k-ε turbulence model is introduced in this appendix; the algebraic Reynolds stresses and heat flux models will be described in the Appendices number A2, A3 and A4.

A1.2 The (r,θ,z) Coordinate System

The partial-differential equations governing flow and heat transfer phenomena in a rotating pipe flow, as shown in Fig.1.1, are as follwing:

Continuity

$$\partial(rV)/\partial r + \partial U/\partial\theta + \partial(rW)/\partial z = 0 \qquad (A1.1)$$

Radial momentum

$$\rho\,(V.\ \partial V/\partial r + U.\ \partial V/r\partial\theta + W.\ \partial V/\partial z - U^2/r) = -\partial p/\partial r + \partial(r.\tau_{rr})/r\partial r + \partial\tau_{r\theta}/r\partial\theta - \tau_{\theta\theta}/r + 2U.\ \rho.\Omega + (r+H.\cos\theta).\rho.\Omega^2 \qquad (A1.2)$$

Tangential momentum

$$\rho\,(V.\ \partial U/\partial r + U.\ \partial U/r\partial\theta + W.\ \partial U/\partial z + U.V/r) = -\partial p/r\partial\theta + \partial(r.\tau_{r\theta})/r\partial r + \partial\tau_{\theta\theta}/r\partial\theta + \tau_{r\theta}/r - 2U.\ \rho.\Omega + H.\ \rho.\ \Omega^2.\sin\theta \qquad (A1.3)$$

Axial momentum

$$\rho\,(V.\ \partial W/\partial r + U.\ \partial W/r\partial\theta + W.\ \partial W/\partial z) = -\partial p/\partial z + \partial(r.\tau_{rz})/r\partial r + \partial\tau_{\theta z}/r\partial\theta \qquad (A1.4)$$

Kinetic energy of turbulence

$$V.\ \partial k/\partial r + U.\ \partial k/r\partial\theta + W.\ \partial k/\partial z = \partial(\nu_{eff}/\sigma_k\ .r.\partial k/\partial r)/r\partial r + \partial(\nu_{eff}/\sigma_k\ .\partial k/r\partial\theta\ )/r\partial\theta + P - \varepsilon \qquad (A1.4)$$

Dissipation rate of kinetic energy of turbulence

$$V.\ \partial\varepsilon/\partial r + U.\ \partial\varepsilon/r\partial\theta + W.\ \partial\varepsilon/\partial z = \partial(\nu_{eff}/\sigma_\varepsilon\ .r.\partial\varepsilon/\partial r)/r\partial r + \partial(\nu_{eff}/\sigma_\varepsilon\ .\partial\varepsilon/r\partial\theta\ )/r\partial\theta + C_{\varepsilon1}.P.\ \varepsilon/k - C_{\varepsilon2}.\varepsilon^2/k \qquad (A1.5)$$

Energy

$$V.\ \partial T/\partial r + U.\ \partial T/r\partial\theta + W.\ \partial T/\partial z = \partial(r.\nu_{eff}/\sigma_t.\ \partial T/\partial r)/r\partial r + \partial(\nu_{eff}/\sigma_t.\ \partial T/r\partial\theta\ )/r\partial\theta + S_T \qquad (A1.6)$$

The shear stresses are expressed below, after they have been simplified by the neglect of gradients in axial direction:

$$\left.\begin{aligned}
\tau_{rr}/\rho &= 2\nu_{eff}\cdot\ \partial V/\partial r \\
\tau_{\theta\theta}/\rho &= 2\nu_{eff}(\ \partial U/r\partial\theta + V/r) \\
\tau_{r\theta}/\rho &= \tau_{\theta r}/\rho = \nu_{eff}(\ \partial U/\partial r + \partial V/r\partial\theta - U/r) \\
\tau_{\theta z}/\rho &= \tau_{z\theta}/\rho = \nu_{eff}(\ \partial W/r\partial\theta + \partial U/\partial z) \\
\tau_{rz}/\rho &= \tau_{zr}/\rho = \nu_{eff}(\ \partial V/\partial z + \partial W/\partial r)
\end{aligned}\right\} \qquad \text{(A1.7)}$$

where:

$\nu_{eff} = \nu$ for laminar flow

$\nu_{eff} = (\nu + \nu_t)$ for turbulent flow

$\nu_t = C_\mu \cdot k^2/\varepsilon$

Production of the kinetic energy of turbulence, for three-dimensional flow, is expressed as follows: (see MEGAHED, 1979 for detail)

$$P=\{(\tau_{rr}/\rho)^2+(\tau_{\theta\theta}/\rho)^2+2(\tau_{r\theta}/\rho)^2+2(\tau_{\theta z}/\rho)^2+2(\tau_{zr}/\rho)^2\}/(2\nu_t) \qquad \text{(A1.8)}$$

From equations (A1.7) and (A1.8) we get:

$$P = \nu_t\{2(\partial V/\partial r)^2+2(\partial U/r\partial\theta)^2+2(V/r)^2+(U/r)^2+4(V/r)(\partial U/r\partial\theta) -2(U/r)(\partial V/r\partial\theta+\partial U/\partial r)+(\partial U/\partial r+\partial V/r\partial\theta)^2+(\partial W/\partial r)^2+(\partial W/r\theta\,\theta)^2\}$$

The fluid density ρ was considered invariant with exception of that included in the body force terms in equations (A1.2 - A1.3) which expressed as:

$$\rho/\rho_o = 1 + \beta(T_w - T) \qquad \text{(A1.9)}$$

where β is a function of temperature and is taken as $1/T$ for gas flow. The results obtained using this coordinate system are shown in Chapter 5.

A1.3 The (r,θ,φ) Coordinate System

The governing differential equations for the (r,θ,ϕ) coordinate system used for the flow in bends are as follows:

Continuity

$$\partial(r.V)/r\partial r + \partial U/r\partial\theta + \partial W/R_c\,\partial\phi + (V.\cos\theta - U.\sin\theta)/R_c = 0 \qquad (A1.10)$$

where:

$$R_c^2 = r^2 + R^2 + 2.r.R.\cos\theta \qquad (A1.11)$$

Radial momentum

$$\begin{aligned}\rho(V.\partial V/\partial r + U.\partial V/r\partial\theta + W.\partial V/R_c\partial\phi - U^2/r - W^2.\cos\theta/R_c &= -\partial p/\partial r\\ + \partial(r.\tau_{rr})/r\partial r + \partial\tau_{r\theta}/r\partial\theta - \tau_{\theta\theta}/r&\\ + \tau_{rr}.\cos\theta/R_c - \tau_{r\theta}.\sin\theta/R_c &\end{aligned} \qquad (A1.12)$$

Tangential monentum

$$\begin{aligned}\rho(V.\partial U/\partial r + U.\partial U/r\partial\theta + W.\partial U/R_c\partial\phi + U.V/r + W^2.\sin\theta/R_c &= -\partial p/r\partial\theta\\ + \partial(r.\tau_{r\theta})/r\partial r + \partial\tau_{\theta\theta}/r\partial\theta + \tau_{r\theta}/r&\\ + \tau_{\theta r}.\cos\theta/R_c - \tau_{\theta\theta}.\sin\theta/R_c &.\end{aligned} \qquad (A1.13)$$

Axial momentum

$$\begin{aligned}\rho(V.\partial W/\partial r + U.\partial W/r\partial\theta + W.\partial W/R_c\partial\phi + W.V.\cos\theta/R_c - W.U.\sin\theta/R_c &=\\ -\partial p/R_c\partial\phi + \partial(r.\tau_{\phi r})/r\partial r + \partial\tau_{\phi\theta}/r\partial\theta&\\ + \tau_{\phi r}.\cos\theta/R_c - \tau_{\phi\theta}.\sin\theta/R_c &\end{aligned} \qquad (A1.14)$$

Kinetic energy of turbulence

$$V.\partial k/\partial r + U.\partial k/r\partial\theta + W.\partial k/R_c\partial\phi = \partial(r.\nu_{eff}/\sigma_k.\partial k/\partial r)/r\partial r + \partial(\nu_{eff}/\sigma_k.\partial k/r\partial\theta)/r\partial\theta + (\nu_{eff}/\sigma_k)(\cos\theta.\partial k/\partial r - \sin\theta.\partial k/r\partial\theta)/R_c + P - \varepsilon \quad (A1.15)$$

Dissipation rate of the kinetic energy of turbulence

$$V.\partial\varepsilon/\partial r + U.\partial\varepsilon/r\partial\theta + W.\partial\varepsilon/R_c\partial\phi = \partial(r.\nu_{eff}/\sigma_\varepsilon.\partial\varepsilon/\partial r)/r\partial r + \partial(\nu_{eff}/\sigma_\varepsilon.\partial\varepsilon/r\partial\theta)/r\partial\theta + (\nu_{eff}/\sigma_\varepsilon)(\cos\theta.\partial\varepsilon/\partial r - \sin\theta.\partial\varepsilon/r\partial\theta)/R_c + C_{\varepsilon1}.P.\varepsilon/k - C_{\varepsilon2}.\varepsilon^2/k \quad (A1.16)$$

Energy

$$V.\partial T/\partial r + U.\partial T/r\partial\theta + W.\partial T/R_c\partial\phi = \partial(r.\nu_{eff}/\sigma_t.\partial T/\partial r)/r\partial r + \partial(\nu_{eff}/\sigma_t.\partial T/r\partial\theta)/r\partial\theta + (\nu_{eff}/\sigma_t)(\cos\theta.\partial T/\partial r - \sin\theta.\partial T/r\partial\theta)/R_c + S_T \quad (A1.17)$$

The shear stresses are expressed below, after they had been simplified by neglecting the gradients in the axial direction:

$$\left.\begin{aligned}
\tau_{rr}/\rho &= 2.\nu_{eff}.\partial V/\partial r \\
\tau_{\theta\theta}/\rho &= 2.\nu_{eff}\,(\partial U/r\partial\theta + V/r) \\
\tau_{r\theta}/\rho &= \tau_{\theta r}/\rho = \nu_{eff}(\partial U/\partial r + \partial V/r\partial\theta - U/r) \\
\tau_{r\phi}/\rho &= \tau_{\phi r}/\rho = \nu_{eff}(\partial W/\partial r - W.\cos\theta/R_c) \\
\tau_{\theta\phi}/\rho &= \tau_{\phi\theta}/\rho = \nu_{eff}(\partial W/r\partial\theta + W.\sin\theta/R_c)
\end{aligned}\right\} \quad (A1.18)$$

The production of the kinetic energy of turbulence can be obtained from equation (A1.8) and (A1.18) as following:

$$P = \nu_t\{2(\partial V/\partial r)^2+2(\partial U/r\partial\theta)^2+2(V/r)^2+(U/r)^2+4(V/r)(\partial U/r\partial\theta)$$
$$-2(U/r)(\partial V/r\partial\theta+\partial U/\partial r)+(\partial U/\partial r+\partial V/r\partial\theta)^2+(\partial W/\partial r)^2+(\partial W/r\partial\theta)^2$$
$$+(W/R_c)^2+2.W(\sin\theta.\partial W/r\partial\theta-\cos\theta.\partial W/\partial r)/R_c\}$$

The results of the curved ducts using this (r,θ,ϕ) coordinate system are shown in Chapter 6.

APPENDIX A2

ALGEBRAIC REYNOLDS STRESS AND HEAT FLUX MODEL EQUATIONS FOR THE FLOW IN PARALLEL ROTATING PIPES

The transport equations for the Reynolds sresses in the flow in a tube rotating about a parallel axis may be obtained in the usual way from Navier-Stokes equations by multiplying the (U_i+u_i) equation by u_j and averaging. U, V and W are the components of the local mean velocity in tangential, radial and axial directions respectively as shown in Fig.1.1. The corresponding fluctuating components are u, v and w. After some manipulations and ignoring triple correlations the transport equations may be written as follows:

$$T_{\overline{uu}} = -2.\overline{uu}.V/r - 2.\overline{uu_j}(\partial U/\partial X_j) - 2.\overline{uv}.U/r - 4.\overline{uv}.\Omega - 2.\varepsilon/3 + \Phi_{11} \qquad (A2.1)$$

$$T_{\overline{vv}} = -2.\overline{u_j v}(\partial V/\partial X_j) + 4.\overline{uv}.U/r + 4.\overline{uv}.\Omega - 2.\varepsilon/3 + \Phi_{22} \qquad (A2.2)$$

$$T_{\overline{ww}} = -2.\overline{u_j w}(\partial W/\partial X_j) - 2.\varepsilon/3 + \Phi_{33} \qquad (A2.3)$$

$$T_{\overline{vw}} = 2.\overline{uw}.U/r - \overline{u_j w}(\partial V/\partial X_j) - \overline{u_j v}(\partial W/\partial X_j) + 2.\overline{uw}.\Omega + \Phi_{23} \qquad (A2.4)$$

$$T_{\overline{uv}} = -\overline{u_j u}(\partial V/\partial X_j) - \overline{u_j v}(\partial U/\partial X_j) + (2.\overline{uu}-\overline{vv}).U/r - \overline{vu}.V/r - 2(\overline{vv}-\overline{uu}).\Omega + \Phi_{12} \qquad (A2.5)$$

$$T_{\overline{uw}} = -\overline{u_j w}(\partial U/\partial X_j) - \overline{u_j u}(\partial W/\partial X_j) - \overline{vw}.U/r - \overline{uw}.V/r - 2.\overline{vw}.\Omega + \Phi_{13} \qquad (A2.6)$$

The transport (convection + diffusion) terms are denoted by T and the ϕ's represent the pressure strain correlations. The transport equation for general Reynolds stress $\overline{u_i u_j}$ can be put in the form:

$$T_{\overline{u_i u_j}} = P_{ij} + \Phi_{ij} - 2.\delta_{ij}.\varepsilon/3 \qquad \text{(A2.7)}$$

The k equation is obtained as one half the sum of equations A2.1-A2.3:

$$T_k = P - \varepsilon = -\overline{u_i u_j}(\partial U_j/\partial X_j) - \overline{uu}.V/r + \overline{uv}.U/r - \varepsilon \qquad \text{(A2.8)}$$

It is noticed that the stress equations contain contributions from the Coriolis terms but that the centripital components (which contain H) formally do not appear.

Using Rodi's proposal mentioned in equation (2.39) the algebraic Reynolds stress equations can be obtained as follows:

$$T_{\overline{u_i u_j}} = T_k(\overline{u_i u_j}/k) = \overline{u_i u_j}.(P/\varepsilon - 1).\varepsilon/k \qquad \text{(A2.9)}$$

from equations (A2.8) and (A2.9) we obtain:

$$\overline{u_i u_j}.(P/\varepsilon - 1).\varepsilon/k = P_{ij} - 2.\delta_{ij}.\varepsilon/3 + \Phi_{ij} \qquad \text{(A2.10)}$$

where:

$$\Phi_{ij} = \Phi_{ij1} + \Phi_{ij2} + \Phi_{ij1w} + \Phi_{ij2w} \qquad \text{(A2.11)}$$

For tube flow the Gibson-Launder model with wall damping applied to the v component, as shown in equations 2.31, 2.32, 2.33 and 2.35, will be as follows:

$$\left.\begin{aligned}
\Phi_{ij1} &= -C_1.\overline{u_i u_j}(\varepsilon/k) + 2.C_1.\delta_{ij}.\varepsilon/3 \\
\Phi_{ij2} &= -C_2.P_{ij} + 2C_2.\delta_{ij}.P/3 \\
\Phi_{ij1w} &= \{\overline{vv}.\delta_{ij} - 3\overline{vu_j}.(n_2.n_j)/2 - 3\overline{u_j v}.(n_2.n_i)\}.C_{1w}.f.\varepsilon/k \\
\Phi_{ij2w} &= \{\Phi_{222}.\delta_{ij} - 3.\Phi_{i22}.(n_2.n_j)/2 - 3\Phi_{j22}.(n_2.n_i)/2\}.C_{2w}.f
\end{aligned}\right\} \qquad \text{(A2.12)}$$

where:

$u_1=u$, $u_2=v$, $u_3=w$, $n_i.n_j=1$ for $i=j$ and $n_i.n_j=0$ for $i\neq j$.

Simplifying the transport equations (A2.1-A2.6) by considering only gradients in radial direction to be significant and neglecting

production terms containing secondary-flow components U and V will lead to:

$$T_{\overline{uu}} = -4.\overline{uv}.\Omega + -2.\varepsilon/3 + \Phi_{11} \qquad \text{(A2.13)}$$

$$T_{\overline{vv}} = -2.\overline{vv}(\partial V/\partial r) + 4.\overline{uv}.\Omega - 2.\varepsilon/3 + \Phi_{22}$$

$$= 2.P + 2.\overline{vw}(\partial W/\partial r) + 4.\overline{uv}.\Omega - 2.\varepsilon/3 + \Phi_{22} \qquad \text{(A2.14)}$$

$$T_{\overline{ww}} = -2.\overline{vw}(\partial W/\partial r) - 2.\varepsilon/3 + \Phi_{33} \qquad \text{(A2.15)}$$

$$T_{\overline{vw}} = -\overline{vw}(\partial V/\partial r) - \overline{vv}(\partial W/\partial r) + 2.\overline{uw}.\Omega + \Phi_{23} \qquad \text{(A2.16)}$$

$$T_{\overline{uv}} = -\overline{vv}.(2.\Omega + \partial U/\partial r) + 2.\overline{uu}.\Omega + \Phi_{12} \qquad \text{(A2.17)}$$

$$T_{\overline{wu}} = -\overline{vw}.(2.\Omega + \partial U/\partial r) - \overline{uv}(\partial W/\partial r) + \Phi_{13} \qquad \text{(A2.18)}$$

where:

$$\Phi_{111} = 2C_1.\varepsilon/3 - C_1.\overline{uu}.\varepsilon/k$$

$$\Phi_{221} = 2C_1.\varepsilon/3 - C_1.\overline{vv}.\varepsilon/k$$

$$\Phi_{331} = 2C_1.\varepsilon/3 - C_1.\overline{ww}.\varepsilon/k$$

$$\Phi_{121} = -C_1.\overline{uv}.\varepsilon/k$$

$$\Phi_{231} = -C_1.\overline{vw}.\varepsilon/k$$

$$\Phi_{131} = -C_1.\overline{uw}.\varepsilon/k$$

$$\Phi_{112} = 4.\overline{uv}.C_2.\Omega + 2C_2.P/3$$

$$\Phi_{222} = -2C_2.\overline{vw}(\partial W/\partial r) - 4C_2.\overline{uv}.\Omega - 4C_2.P/3$$

$$\Phi_{332} = 2C_2.\overline{vw}(\partial W/\partial r) + 2C_2.P/3$$

$$\Phi_{122} = C_2.\overline{vv}(2\Omega + \partial U/\partial r) - 2C_2.\overline{uu}.\Omega$$

$$\Phi_{232} = C_2.\overline{vw}(\partial V/\partial r) + C_2.\overline{vv}(\partial W/\partial r) - 2C_2.\overline{uw}.\Omega$$

$$\Phi_{132} = C_2.\overline{vw}(2\Omega + \partial U/\partial r) + C_2.\overline{vu}(\partial W/\partial r)$$

$$\Phi_{111w} = C_{1w}.f.\overline{vv}.\varepsilon/k$$

$$\Phi_{221w} = -2C_{1w}.f.\overline{vv}.\varepsilon/k$$

$$\Phi_{331w} = C_{1w}.f.\overline{vv}.\varepsilon/k$$

$$\Phi_{121w} = -(3/2).C_{1w}.f.\overline{uv}.\varepsilon/k$$

$$\Phi_{231w} = -(3/2).C_{1w}.f.\overline{vw}.\varepsilon/k$$

$$\Phi_{131w} = C_{1w}.f.(0).\varepsilon/k = 0$$

$$\Phi_{112w} = C_{2w}.f.(\Phi_{222})$$
$$= -2.C_2.C_{2w}.f.\overline{vw}(\partial W/\partial r) - 4.C_2.C_{2w}.f.\overline{uv}.\Omega - 4C_2.C_{2w}.f.P/3$$

$$\Phi_{222w} = C_{2w}.f.(-2\Phi_{222})$$
$$= 4.C_2.C_{2w}.f.\overline{vw}(\partial W/\partial r) + 8.C_2.C_{2w}.f.\overline{uv}.\Omega + 8C_2.C_{2w}.f.P/3$$

$$\Phi_{332w} = C_{2w}.f.(\Phi_{222})$$
$$= -2.C_2.C_{2w}.f.\overline{vw}(\partial W/\partial r) - 4.C_2.C_{2w}.f.\overline{uv}.\Omega - 4C_2.C_{2w}.f.P/3$$

$$\Phi_{122w} = C_{2w}.f.(-3.\Phi_{122}/2)$$
$$= -3C_2.C_{2w}.f.\overline{vv}.(1+2\Omega)/2 + 3.C_2.C_{2w}.f.\overline{uu}.\Omega$$

$$\Phi_{232w} = C_{2w}.f.(-3.\Phi_{232}/2)$$
$$= -3C_2.C_{2w}.f.\overline{vw}(\partial V/\partial r)/2 - 3C_2.C_{2w}.f.\overline{vv}(\partial W/\partial r)/2 - 3C_2.C_{2w}.f.\overline{uw}.\Omega$$

$$\Phi_{132w} = 0$$

Substituting in equation (A2.10) we get the required algebraic Reynolds stress equations, as function of P/ε and f, as shown below:

$$\overline{uu}.(P/\varepsilon - 1 + C_1)/k = C_{1w}.f.\overline{vv}/k - 2C_2.C_{2w}.f.\overline{vw}.(\partial W/\partial r)/\varepsilon$$
$$+ 2\{C_2(1-2C_{2w}.f).P/\varepsilon + C_1 - 1\}/3$$
$$- 4.\Omega.\overline{uv}(1 - C_2 + C_2.C_{2w}.f)/\varepsilon \qquad \text{(A2.19)}$$

$$\overline{vv}.(P/\varepsilon -1+C_1-2C_{1w}.f)/k = 2.\overline{vw}.(\partial W/\partial r)(1-C_2+2C_2.C_{2w}.f) +4.\overline{uv}.\Omega\ (1-C_2+2C_2.C_{2w}.f) +2\{C_1-1+(1-2C_2-4C_2.C_{2w}.f).P/\varepsilon\}/3 \qquad (A2.20)$$

$$\overline{ww}.(P/\varepsilon -1+C_1)/k = C_{1w}.f.\overline{vv}/k +2.\overline{vw}.(\partial W/\partial r)(C_2-1-C_2.C_{2w}.f) -4C_2.C_{2w}.f.\ \Omega.\overline{uv}/\varepsilon + 2\{C_1-1+C_2.(1-2C_{2w}.f).P/\varepsilon\}/3 \qquad (A2.21)$$

$$\overline{-vw}\{P/\varepsilon -1+C_1+3C_{1w}.f/2+(\partial V/\partial r)(1-C_2+3C_2.C_{2w}.f/2).k/\varepsilon\} = +\overline{vv}.(\partial W/\partial r)(1-C_2+3C_2.C_{2w}.f/2).k/\varepsilon -2.\overline{uw}.k.\ \Omega(1-C_2+3C_2.C_{2w}.f/2)/\varepsilon \qquad (A2.22)$$

$$-\overline{uv}.(P/\varepsilon -1+C_1+3C_{1w}.f/2) = +\overline{vv}.(2\ \Omega+\ \partial U/\partial r)(1-C_2+3C_2.C_{2w}.f/2).k/\varepsilon -2.\overline{uu}.\ \Omega.k(1-C_2+3C_2.C_{2w}.f/2)/\varepsilon \qquad (A2.23)$$

$$-\overline{uw}.(P/\varepsilon -1+C_1) = \overline{vw}.(2\Omega +\partial U/\partial r)(1-C_2).k/\varepsilon + \overline{uv}.(1-C_2)(\partial W/\partial r).k/\varepsilon \qquad (A2.24)$$

The equation (A2.22) can be put in the following expression:

$$-\overline{vw} = \beta.\overline{vv}.(\partial W/\partial r).k/\varepsilon = \nu_t.(\partial W/\partial r) \qquad (A2.25)$$

where:

$$\beta = \left[\frac{(1-C_2+3C_2.C_2\ .f/2)\{1-2(\overline{uw}/\overline{vv}).\Omega\ /(\partial W/\partial r)\}}{C_1+3C_{1w}.f/2\ +P/\varepsilon\ -1\ +(\partial V/\partial r)(1-C_2+3C_2.C_{2w}.f/2).k/\varepsilon}\right] \qquad (A2.26)$$

and ν_t is the turbulent viscosity defined in equation (2.15) as:

$\nu_t = C_\mu.k^2/\varepsilon$

thus:

$$C_\mu = \beta.\overline{vv}/k \qquad (A2.27)$$

The algebraic Reynolds srtress model is now complete and the solution of U, V, W, p, k and ε equations is as normal but with the original constant C replaced by the function of P/ε and f as shown in equation (A2.27). Then the different Reynolds stresses can be found easily from the solution of the algebraic set of equations (A2.19-A2.24).

For the heat flux model, the transport equations can be obtained by multiplying the (U_j+u_j) equation by fluctuating temperature t and the instantaneous temperature equation of (T+t) by u_j and averaging, the results will be as follows:

$$T_{\overline{ut}} = -\overline{u_j u}(\partial T/\partial X_j) - \overline{u_j t}(\partial U/\partial X_j) - \overline{ut}.V/r - \overline{vt}.U/r - 2.\overline{vt}.\Omega + \Phi_{1T} \quad \text{(A2.28)}$$

$$T_{\overline{vt}} = -\overline{u_j v}(\partial T/\partial X_j) - \overline{u_j t}(\partial V/\partial X_j) + 2\overline{ut}.U/r + 2.\overline{ut}.\Omega + \Phi_{2T} \quad \text{(A2.29)}$$

$$T_{\overline{wt}} = -\overline{u_j w}(\partial T/\partial X_j) - \overline{u_j t}(\partial W/\partial X_j) + \Phi_{3T} \quad \text{(A2.30)}$$

The general heat flux equation can be put as following:

$$T_{\overline{u_i t}} = -\overline{u_i u_j}(\partial T/\partial X_j) + P_{iT} + \Phi_{it} \quad \text{(A2.31)}$$

Using Gibson-Launder approximation as shown in equation (2.43 and 2.46) the following algebraic equation of heat flux $\overline{u_i t}$ can be obtained:

$$\overline{u_i t}.(P/\varepsilon - 1).\varepsilon/(2k) = \overline{-u_i u_j}(\partial T/\partial X_j) + P_{iT} + \Phi_{iT} \quad \text{(A2.32)}$$

where:

$$\Phi_{iT} = \Phi_{iT1} + \Phi_{iT2} + \Phi_{iT1w} + \Phi_{iT2w}$$

For tube flow with wall damping applied to the v component, as shown in equations (2.37 and 2.39), and with C_{2Tw} is assumed to be

zero as suggested by Gibson (1978), the Φ's will be as following:

$$\Phi_{iT1} = -C_{1T}.\overline{u_i t}.\varepsilon/k$$
$$\Phi_{iT2} = -C_{2T}.P_{iT} \qquad \text{(A2.33)}$$
$$\Phi_{iT1w} = -C_{1Tw}.\overline{vt}.(n_i.n_2).f.\varepsilon/k$$
$$\Phi_{iT2w} = 0$$

Substituting in the equation (A2.32), we get the following equations:

$$\overline{ut}\{C_{1T}-(1-C_{2T})(V/r-\partial U/r\partial\theta)+(P/\varepsilon-1)/2\} = -\overline{uu_j}.(\partial T/\partial X_j).k/\varepsilon - \overline{vt}.(1-C_{2T}).(\partial U/\partial r-U/r-2\Omega).k/\varepsilon \qquad \text{(A2.34)}$$

$$\overline{vt}\{C_{1T}+(P/\varepsilon-1)/2 +C_{1Tw}.f +(\partial V/\partial r)(1-C_{2T}).k/\varepsilon\} = \overline{-vu_j}(\partial T/\partial X_j).k/\varepsilon +(2\Omega+U/r-\partial V/r\partial\theta)(1-C_{2T}).\overline{ut}.k/\varepsilon \qquad \text{(A2.35)}$$

$$\overline{wt}\{C_{1T}+(P/\varepsilon-1)/2\} = \overline{-u_j w}(\partial T/\partial X_j).k/\varepsilon\ \overline{-vt}(1-C_{2T})(\partial W/\partial r).k/\varepsilon \overline{-ut}(1-C_{2T})(\partial W/r\partial\theta).k/\varepsilon \qquad \text{(A2.36)}$$

solving the three equations (A2.34 to A2.36) simultaneously will lead to the three components of the heat flux required.

From equation (2.44), the temperature fluctuation can be obtained as follows:

$$\overline{t^2} = -C_T'\{\overline{ut}(\partial T/r\partial\theta) +\overline{vt}(\partial T/\partial r) +\overline{wt}(\partial T/\partial z)\}.k/\varepsilon \qquad \text{(A2.37)}$$

Tangential and radial heat flux components $\overline{ut}$ and $\overline{vt}$ can be put in the form:

$$\overline{ut} = -\Gamma_{T\theta}.(\partial T/r\partial\theta) \qquad \text{(A2.38)}$$

$$\overline{vt} = -\Gamma_{Tr}.(\partial T/\partial r) \qquad (A2.39)$$

where $\Gamma_{T\theta}$ and Γ_{Tr} are the diffusivity of heat in tangential and radial directions respectively. Its ratio is required to see the effect of body force on heat transfer in different directions in the flow as discused in Chapter 5 with the other results of algebraic Reynolds stress snd heat flux models applied to rotating pipe flow.

APPENDIX A3

ALGEBRAIC REYNOLDS STRESS AND HEAT FLUX MODEL EQUATIONS FOR THE FLOW IN BENDS

The transport equations for the Reynolds stresses for the flow in bends can be written as:

$$T_{\overline{uu}} = -2\overline{uu_j}(\partial U/\partial X_j) - 2\overline{vu}.U/r - 2\overline{uu}.V/r - 4\overline{uw}.W.\sin\theta/R_c - 2\varepsilon/3 + \Phi_{11} \quad (A3.1)$$

$$T_{\overline{vv}} = -2\overline{vu_j}(\partial V/\partial X_j) + 4\overline{uv}.U/r + 4\overline{vw}.W.\cos\theta/R_c - 2\varepsilon/3 + \Phi_{22} \quad (A3.2)$$

$$T_{\overline{ww}} = -2\overline{wu_j}(\partial W/\partial X_j) - 2\overline{ww}(V.\cos\theta - U.\sin\theta)/R_c - 2\overline{vw}.W.\cos\theta/R_c + 2\overline{uw}.W.\sin\theta/R_c - 2\varepsilon/3 + \Phi_{33} \quad (A3.3)$$

$$T_{\overline{uv}} = -\overline{uu_j}(\partial V/\partial X_j) - \overline{vu_j}(\partial U/\partial X_j) + 2\overline{uu}.U/r - \overline{uv}.V/r - \overline{vv}.U/r + 2\overline{uw}.W.\cos\theta/R_c - 2\overline{vw}.W.\sin\theta/R_c + \Phi_{12} \quad (A3.4)$$

$$T_{\overline{vw}} = -\overline{vu_j}(\partial W/\partial X_j) - \overline{wu_j}(\partial V/\partial X_j) - \overline{vw}(V.\cos\theta - U.\sin\theta)/R_c + 2\overline{uw}.U/r + \overline{uv}.W.\sin\theta/R_c + (2\overline{ww} - \overline{vv}).W.\cos\theta/R_c + \Phi_{23} \quad (A3.5)$$

$$T_{\overline{uw}} = -\overline{uu_j}(\partial W/\partial X_j) - \overline{wu_j}(\partial U/\partial X_j) - \overline{uw}\{(V/r) + (V.\cos\theta - U.\sin\theta)/R_c\} - \overline{vw}.U/r - \overline{uv}.W.\cos\theta/R_c + (\overline{uu} - 2\overline{ww}).W.\sin\theta/R_c + \Phi_{13} \quad (A3.6)$$

The general Reynolds stress equation can be written as:

$$T_{\overline{u_i u_j}} = P_{ij} - 2.\delta_{ij}.\varepsilon/3 + \Phi_{ij} \quad (A3.7)$$

The k equation is obtained as on half the sum of equations (A3.1 - A3.2) as following:

$$T_k = P - \varepsilon = -\overline{u_i u_j}(\partial U/\partial X_j) + \overline{uv}.U/r - \overline{uu}.V/r - \overline{ww}(V.\cos\theta - U.\sin\theta)/R_c + \overline{vw}.W.\cos\theta/R_c - \overline{uw}.W.\sin\theta/R_c - \varepsilon \quad (A3.8)$$

As an approximation, one can ignore all production terms containing secondary flow components U and V and consider only gradients in the radial direction to be significant. The transport equations will reduce to:

$$T_{\overline{uu}} = -4\overline{uw}.W.\sin\theta/R_c - 2\varepsilon/3 + \Phi_{11} \quad (A3.9)$$

$$T_{\overline{vv}} = 4\overline{vw}.W.\cos\theta/R_c - 2\varepsilon/3 + \Phi_{22} \quad (A3.10)$$

$$T_{\overline{ww}} = -2\overline{vw}\{(\partial W/\partial r) + W.\cos\theta/R_c\} + 2\overline{uw}.W.\sin\theta/R_c - 2\varepsilon/3 + \Phi_{33}$$
$$= -4\overline{vw}(\partial W/\partial r) - 2P - 2\varepsilon/3 + \Phi_{33} \quad (A3.11)$$

$$T_{\overline{uv}} = 2\overline{uw}.W.\cos\theta/R_c - 2\overline{vw}.W.\sin\theta/R_c + \Phi_{12} \quad (A3.12)$$

$$T_{\overline{vw}} = -\overline{vv}\{(\partial W/\partial r) + W.\cos\theta/R_c\} + 2\overline{ww}.W.\cos\theta/R_c + \overline{uv}.W.\sin\theta/R_c + \Phi_{23} \quad (A3.13)$$

$$T_{\overline{uw}} = -\overline{uv}\{(\partial W/\partial r) + W.\cos\theta/R_c\} + (\overline{uu}-2\overline{ww}).W.\sin\theta/R_c + \Phi_{13} \quad (A3.14)$$

where Φ_{ij} is the pressure-strain correlations given in detail by equations (A2.11) and (A2.12):

$$\Phi_{111} = -C_1.\overline{uu}.\varepsilon/k + 2C_1.\varepsilon/3$$

$$\Phi_{221} = -C_1.\overline{vv}.\varepsilon/k + 2C_1.\varepsilon/3$$

$$\Phi 331 = -C_1.\overline{ww}.\varepsilon/k + 2C_1.\varepsilon/3$$

$$\Phi_{121} = -C_1.\overline{uv}.\varepsilon/k$$

$$\Phi_{231} = -C_1.\overline{vw}.\varepsilon/k$$

$$\Phi_{131} = -C_1.\overline{uw}.\varepsilon/k$$

$$\Phi_{112} = 2C_2.P/3 + 4C_2.\overline{uw}.W.\sin\theta/R_c$$

$$\Phi_{222} = 2C_2.P/3 - 4C_2.\overline{vw}.W.\cos\theta/R_c$$

$$\Phi_{332} = 8C_2.P/3 + 4C_2.\overline{vw}(\partial W/\partial r)$$

$$\Phi_{122} = 2C_2.\overline{vw}.W.\sin\theta/R_c - 2C_2.\overline{uw}.W.\cos\theta/R_c$$

$$\Phi_{232} = C_2.\overline{vv}\{(\partial W/\partial r) + W.\cos\theta/R_c\} - 2C_2.\overline{ww}.W.\cos\theta/R_c - C_2.\overline{uv}.W.\sin\theta/R_c$$

$$\Phi_{132} = C_2.\overline{uv}\{(\partial W/\partial r) + W.\cos\theta/R_c\} + (2\overline{ww}-\overline{uu}).C_2.W.\sin\theta/R_c$$

$$\Phi_{111w} = C_{1w}.f.\overline{vv}.\varepsilon/k$$

$$\Phi_{221w} = -2C_{1w}.f.\overline{vv}.\varepsilon/k$$

$$\Phi_{331w} = C_{1w}.f.\overline{vv}.\varepsilon/k$$

$$\Phi_{121w} = -3C_{1w}.f.\overline{uv}.(\varepsilon/k)/2$$

$$\Phi_{231w} = -3C_{1w}.f.\overline{vw}.(\varepsilon/k)/2$$

$$\Phi_{131w} = 0$$

$$\Phi_{112w} = 2C_2.C_{2w}.f.P - 4C_2.C_{2w}.f.\overline{vw}.W.\cos\theta/R_c$$

$$\Phi_{222w} = -4C_2.C_{2w}.f.P/3 + 8C_2.C_{2w}.f.\overline{vw}.W.\cos\theta/R_c$$

$$\Phi_{332w} = 2C_2.C_{2w}.f.P/3 - 4C_2.C_{2w}.f.\overline{vw}.W.\cos\theta/R_c$$

$$\Phi_{122w} = -3C_2.C_{2w}.f.\overline{vw}.W.\sin\theta/R_c + 3C_2.C_{2w}.f.\overline{uw}.W.\cos\theta/R_c$$

$$\Phi_{232w} = -3C_2.C_{2w}.f.\overline{vv}\{(\partial W/\partial r) + W.\cos\theta/R_c\}/2 + 3C_2.\overline{ww}.W.\cos\theta/R_c + 3C_2.C_{2w}.f.\overline{uv}.W.\sin\theta/R_c$$

$$\Phi_{132w} = 0$$

Substituting in equation (A2.10) the Reynolds stresses required can be obtained as:

$$\overline{uu}(P/\varepsilon - 1 + C_1)/k = C_{1w}.f.\overline{vv}/k + 2\{C_2(1+C_{2w}.f).P/\varepsilon + C_1 - 1\}/3 - 4C_2.C_{2w}.f.\overline{vw}.W.\cos\theta/(\varepsilon.R_c) - 4(1-C_2).\overline{uw}.W.\sin\theta/R_c \qquad (A3.15)$$

$$\overline{vv}(P/\varepsilon -1+C_1+2C_{1w}.f)/k = 4(1-C_2+8C_2.C_{2w}.f).\overline{vw}.W.\cos\theta/(\varepsilon.R_c) \\ 2\{C_2(1-2C_{2w}.f).P/\varepsilon +C_1-1\}/3 \qquad (A3.16)$$

$$\overline{ww}(P/\varepsilon -1+C_1)/k = 4\overline{vw}\{(\partial W/\partial r)(C_2-1) -C_2.C_{2w}.f.W.\cos\theta/R_c\}/\varepsilon \\ -C_{1w}.f.\overline{vv}/k + 2\{(4C_2-3+C_2.C_{2w}.f).P/\varepsilon +C_1-1\}/3 \qquad (A3.17)$$

$$-\overline{uv}(P/\varepsilon -1+C_1+3C_{1w}.f/2)\frac{\varepsilon}{k} = -2(1-C_2+3C_2.C_{2w}.f/2).\overline{uw}.W.\cos\theta/R_c \\ +2(1-C_2+3C_2.C_{2w}.f/2).\overline{vw}.W.\sin\theta/R_c \qquad (A3.18)$$

$$-\overline{vw}(P/\varepsilon -1+C_1+3C_{1w}.f/2) = \overline{vv}\{(\partial W/\partial r)+W.\cos\theta/R_c\}(1-C_2+3C_2.C_{2w}.f/2).k/\varepsilon \\ -2(1-C_2+3C_2.C_{2w}.f/2)(k/\varepsilon).\overline{ww}.W.\cos\theta/R_c \\ -\overline{uv}(k/\varepsilon)(1-C_2+3C_2.C_{2w}.f/2).W.\sin\theta/R_c \qquad (A3.19)$$

$$-\overline{uw}(P/\varepsilon -1+C_1)\frac{\varepsilon}{k} = \overline{uv}\{(\partial W/\partial r)+W.\cos\theta/R_c\}(1-C_2) \\ +(2\overline{ww}-\overline{uu})(1-C_2).W.\sin\theta/R_c \qquad (A3.20)$$

The equation (A3.19) can be put in the following form:

$$-\overline{vw} = \beta.(k/\varepsilon)(\partial W/\partial r).\overline{vv} = \nu_t\ (\partial W/\partial r)$$

where

$$\beta = (1 +a1 +a2 +a3)(1-C_2+3C_2.C_{2w}.f/2) \ /\ (P/\varepsilon -1+C_1+3C_{1w}.f/2)$$

and

$$a1 = (W.\cos\theta/R_c) \ /\ (\partial W/\partial r)$$

$$a2 = -2(\overline{ww}/\overline{vv})(W.\cos\theta/R_c) \ /\ (\partial W/\partial r)$$

$$a3 = -(\overline{uv}/\overline{vv})(W.\sin\theta/R_c) \ /\ (\partial W/\partial r)$$

Thus the coefficient C_μ can be put as:

$$C_\mu = \beta.\overline{vv}/k$$

For heat flux model the transport equations for different heat flux componenets are:

$$T_{\overline{ut}} = -\overline{uu_j}(\partial T/\partial X_j) - \overline{u_j t}(\partial U/\partial X_j) - 2\overline{wt}.W.\sin\theta/R_c + \Phi_{1T} \qquad (A3.21)$$

$$T_{\overline{vt}} = -\overline{vu_j}(\partial T/\partial X_j) - \overline{u_j t}(\partial V/\partial X_j) + 2\overline{wt}.W.\cos\theta/R_c + \Phi_{2T} \qquad (A3.22)$$

$$T_{\overline{wt}} = -\overline{wu_j}(\partial T/\partial X_j) - \overline{u_j t}(\partial W/\partial X_j) + (\overline{ut}-\overline{vt}).W.\cos\theta/R_c + \Phi_{3T} \qquad (A3.23)$$

where Φ's are the pressure-temperature gradients given by equation (A2.33) as:

$$\Phi_{1T1} = -C_{1T}.\overline{ut}.\varepsilon/k$$
$$\Phi_{2T1} = -C_{1T}.\overline{vt}.\varepsilon/k$$
$$\Phi_{3T1} = -C_{1T}.\overline{wt}.\varepsilon/k$$

$$\Phi_{1T2} = C_{2T}.\overline{vt}(\partial U/\partial r) + 2C_{2T}.\overline{wt}.W.\sin\theta/R_c$$
$$\Phi_{2T2} = C_{2T}.\overline{vt}(\partial V/\partial r) - 2C_{2T}.\overline{wt}.W.\cos\theta/R_c$$
$$\Phi_{3T2} = C_{2T}.\overline{vt}(\partial W/\partial r) + C_{2T}(\overline{vt}-\overline{ut}).W.\cos\theta/R_c$$

$$\Phi_{1T1w} = 0$$
$$\Phi_{2T1w} = -C_{1Tw}.\overline{vt}.f.\varepsilon/k$$
$$\Phi_{3T1w} = 0$$

Substituting in equation (A2.32) we get the required heat flux equations:

$$\overline{ut}\{(P/\varepsilon-1)/2 + C_{1T}\} = -\overline{uu_j}(\partial T/\partial X_j) - \overline{vt}(\partial U/\partial r)(1-C_{2T}).k/\varepsilon$$
$$-2(1-C_{2T})(k/\varepsilon).\overline{wt}.W.\sin\theta/R_c \qquad (A3.24)$$

$$\overline{vt}\{(P/\varepsilon-1)/2 + C_{1T} + (1-C_{2T})(\partial V/\partial r) + C_{1T}.f\} = -\overline{vu_j}(\partial T/\partial X_j).k/\varepsilon + 2(1-C_{2T}).\overline{wt}.W.\cos\theta/R_c \qquad (A3.25)$$

$$\overline{wt}\{(P/\varepsilon-1)/2 + C_{1T}\} = -\overline{wu_j}(\partial T/\partial X_j).k/\varepsilon + \overline{ut}(1-C_{2T})(k/\varepsilon).W.\cos\theta/R_c - \overline{vt}(1-C_{2T})\{(\partial W/\partial r)+W.\cos\theta/R_c\}(k/\varepsilon) \qquad (A3.26)$$

The algebraic and heat flux models mentioned in this appendix are needed to be put in a program to solve numerically the flow in bends. Due to lack of time, this has not been done in the thesis, and it is left as a suggestion for future work. It is iteresting to see the comparison between the solution using k-ε model and the solution using these more advanced models for this type of complex flow.

APPENDIX A4

ALGEBRAIC REYNOLDS STRESS AND HEAT FLUX MODELS APPLIED TO STATIONARY PIPE FLOW

As a preliminary calculation, the algebraic and heat flux model have been applied to fully-developed stationary pipe flow. Comparison with the measurements and with the k-ε model prediction has been performed to check the computer code used for complex rotating pipe flow.

Taking into consideration that for symmetrical fully-developed pipe flow in which the lateral velocity components U and V and axial and tangential velocity grdients are equal to zero, the transport equations of the Reynolds stresses can be written as follows:

$$\left.\begin{aligned}
T_{\overline{uu}} &= \Phi_{11} - 2\varepsilon/3 \\
T_{\overline{vv}} &= \Phi_{22} - 2\varepsilon/3 \\
T_{\overline{ww}} &= -2\overline{vw}.(\partial W/\partial r) + \Phi_{33} - 2\varepsilon/3 \\
T_{\overline{vw}} &= -\overline{vv}.(\partial W/\partial r) + 2\overline{uw} + \Phi_{23} \\
T_{\overline{uv}} &= \Phi_{12} \\
T_{\overline{uw}} &= -\overline{vu}.(\partial W/\partial r) + \Phi_{13}
\end{aligned}\right\} \quad (A4.1)$$

The equation of the kinetic energy of turbulence is obtained as:

$$T_k = P - \varepsilon = -\overline{vw}.(\partial W/\partial r) - \varepsilon \qquad (A4.2)$$

Φ's can be obtained using equations (2.31) - (2.34) as follows:

$$\Phi_{111} = -(\overline{uu}-2k/3).C_1.\varepsilon/k$$

$$\Phi_{221} = -(\overline{vv}-2k/3).C_1.\varepsilon/k$$

$$\Phi_{331} = -(\overline{ww}-2k/3).C_1.\varepsilon/k$$

$$\Phi_{121} = -\overline{uv}.C_1.\varepsilon/k$$

$$\Phi_{231} = -\overline{vw}.C_1.\varepsilon/k$$

$$\Phi_{131} = -\overline{uw}.C_1.\varepsilon/k$$

$$\Phi_{112} = 2C_2.P/3$$

$$\Phi_{222} = 2C_2.P/3$$

$$\Phi_{332} = -2C_2.\overline{vw}.(\partial W/\partial r) + 2C_2.P/3 = -4C_2.P/3$$

$$\Phi_{122} = -C_2(0)=0$$

$$\Phi_{232} = C_2.\overline{vw}.(\partial W/\partial r) - 2C_2.\overline{uw}$$

$$\Phi_{132} = C_2.\overline{vu}.(\partial W/\partial r)$$

$$\Phi_{111w} = C_{1w}(\overline{vv})\varepsilon.f/k$$

$$\Phi_{221w} = C_{1w}(\overline{vv}-3\overline{vv})\varepsilon.f/k = -C_{1w}(2\overline{vv})\varepsilon.f/k$$

$$\Phi_{331w} = C_{1w}(\overline{vv})\varepsilon.f/k$$

$$\Phi_{121w} = C_{1w}(-3\overline{uv}/2)\varepsilon.f/k$$

$$\Phi_{231w} = C_{1w}(-3\overline{vw}/2)\varepsilon.f/k$$

$$\Phi_{131w} = C_{1w}(0)\varepsilon.f/k= 0$$

$$\Phi_{112w} = C_{2w}(\Phi_{222}).f$$

$$\Phi_{222w} = C_{2w}(-2\Phi_{222}).f$$

$$\Phi_{332w} = C_{2w}(\Phi_{222}).f$$

$$\Phi_{122w} = C_{2w}(-3\Phi_{122}/2).f$$

$$\Phi_{232w} = C_{2w}(-3\Phi_{232}/2).f$$

$$\Phi_{132w} = 0$$

With this simplifications, the algebraic Reynolds stress equations will be as follows:

$$\overline{uu}/k = [(2/3)\{C_1-1+C_2(1+C_{2w}.f).P/\varepsilon\}+C_{1w}.f.\overline{vv}/k]/(C_1-1+P/\varepsilon) \quad (A4.3)$$

$$\overline{vv}/k = (2/3)\{C_1-1+C_2(1-2C_{2w}.f).P/\varepsilon\}/(C_1-1+2C_{1w}.f+P/\varepsilon) \quad (A4.4)$$

$$\overline{ww}/k = [(2/3)\{C_1-1+(3-2C_2+C_2.C_{2w}.f).P/\varepsilon\}+C_{1w}.f.\overline{vv}/k]/(C_1-1+P/\varepsilon) \quad (A4.5)$$

$$\overline{vw} = \{(1-C_2+3C_2.C_{2w}.)/(C_1-1+3C_{1w}.f/2+P/\varepsilon)\}.(W/r).\overline{vv}.k/\varepsilon \quad (A4.6)$$

$$\overline{uw} = \overline{uv} = 0 \quad (A4.7)$$

In addition to these equations, relation (2.37) yeilds for the shear stress $-\overline{vw}$ a combination of the eddy viscosity concept (2.9) and the Kolmogorov-Prandtl formula (2.13) but with the original constant C_μ replaced by the following function of P/ε and f:

$$C_\mu = \left[\frac{(2/3)\{C_1-1+C_2(1-2C_{2w}.f).P/\varepsilon\}(1-C_2+3C_2.C_{2w}.f/2)}{(C_1-1+2.C_{1w}.f+P/\varepsilon)(C_1-1+3C_{1w}.f/2+P/\varepsilon)}\right] \quad (A4.8)$$

Using the relation (A4.8) of C_μ in the calculations instead of the constant value 0.09 used in the k-ε model, we can get the results shown in Figs.A4.1 to A4.4. These results agree reasonably well with the experimental data but are not noticeably superior in this respect to the k-ε predictions for this simple flow. The pipe flow does not discriminate between the local equilibrium model (energy production P = disspation ε) and the more general algebraic form where P/ε is allowed to vary.

For the heat flux mosdel:

$$\left.\begin{aligned} T_{\overline{ut}} &= -\overline{u_k u}.(\partial T/\partial X_k) + \Phi_{1T} \\ T_{\overline{vt}} &= -\overline{u_k v}.(\partial T/\partial X_k) + \Phi_{2T} \\ T_{\overline{wt}} &= -\overline{u_k w}.(\partial T/\partial X_k) - \overline{vt}.(\partial W/\partial r) + \Phi_{3T} \end{aligned}\right\} \quad (A4.9)$$

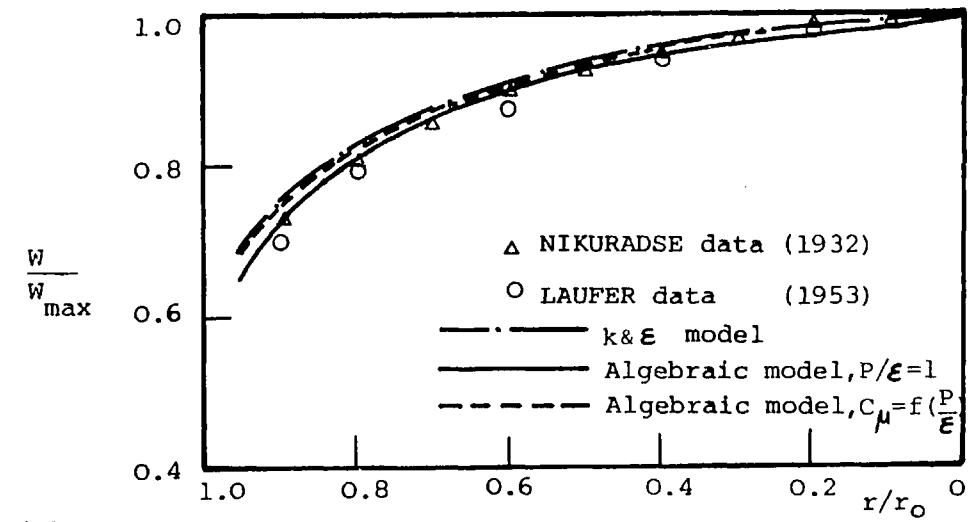


Fig.A4.1 Fully-developed mean axial velocity profile for stationary pipes for R_e= 50000.

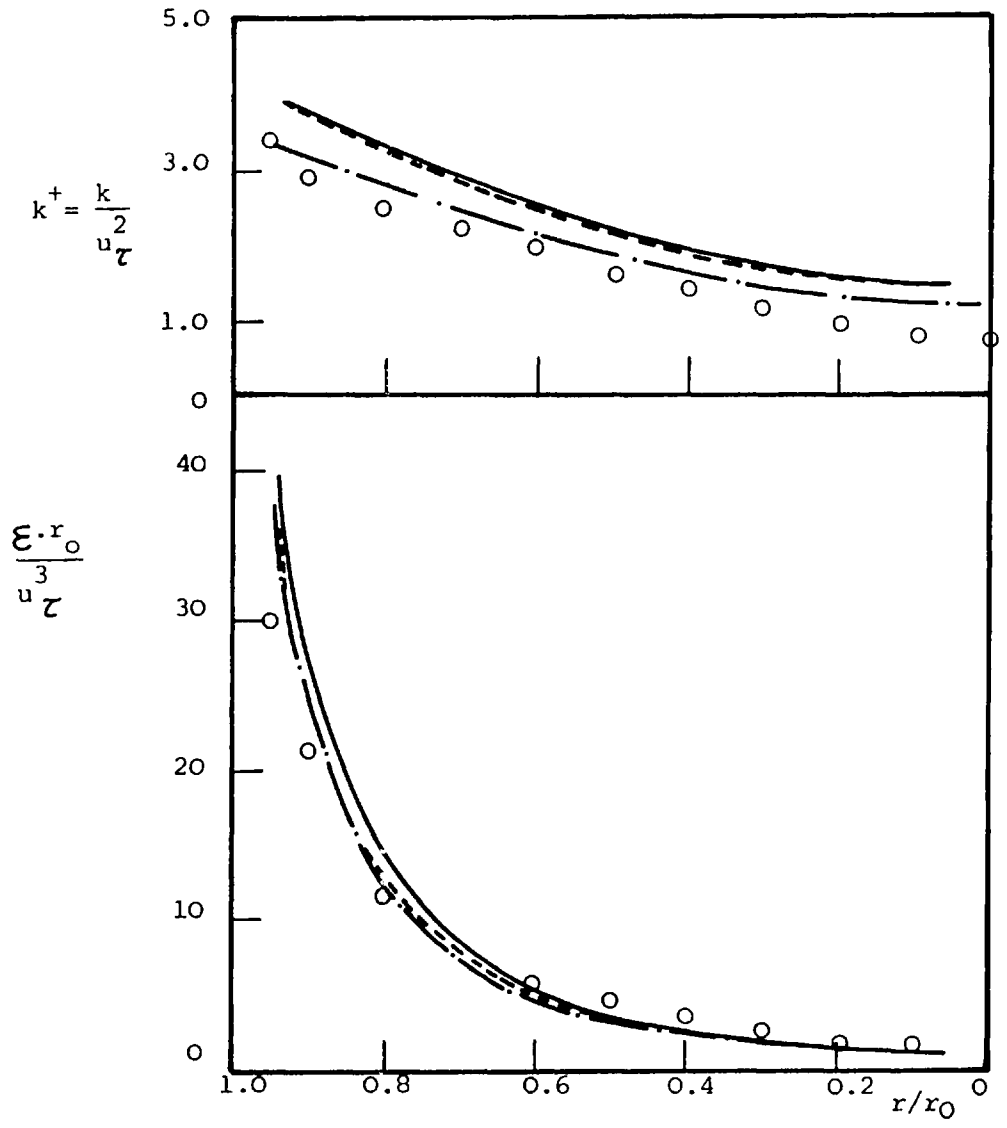


Fig.A4.2 Fully-developed kinetic energy and energy dissipation rate of turbulence for R_e=50000.

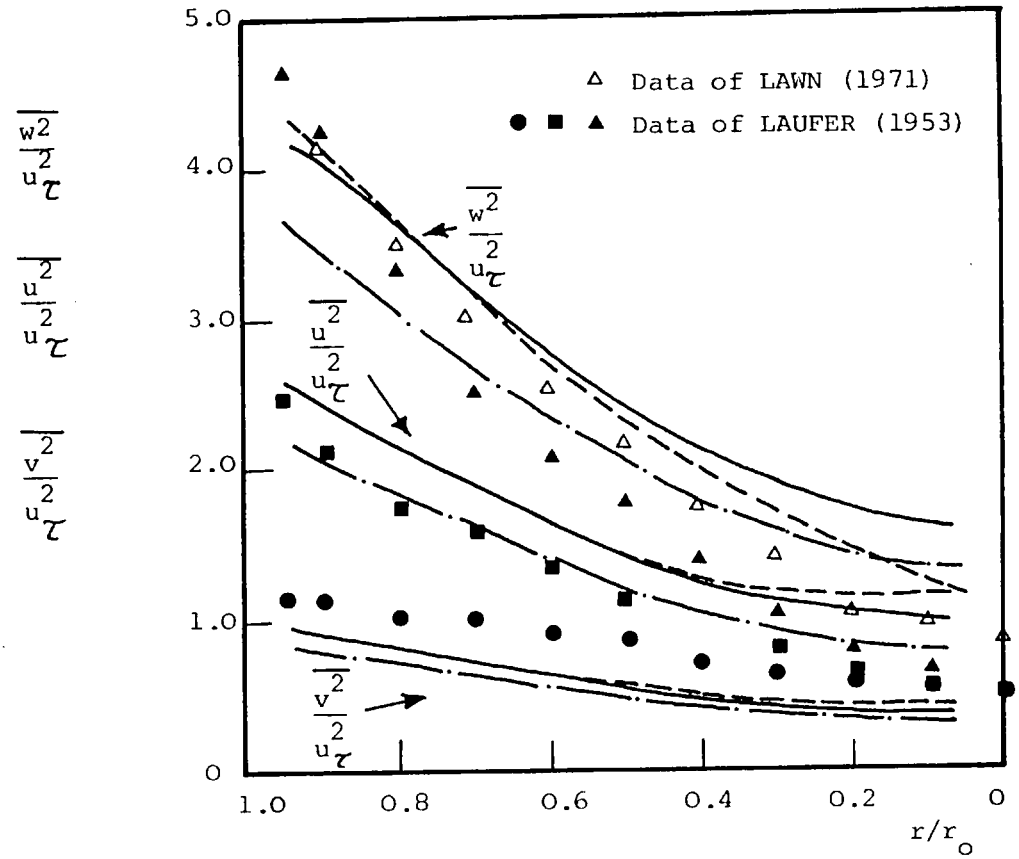


Fig.A4.3 Turbulence intensities for fully-developed pipe flow for Re=50000.

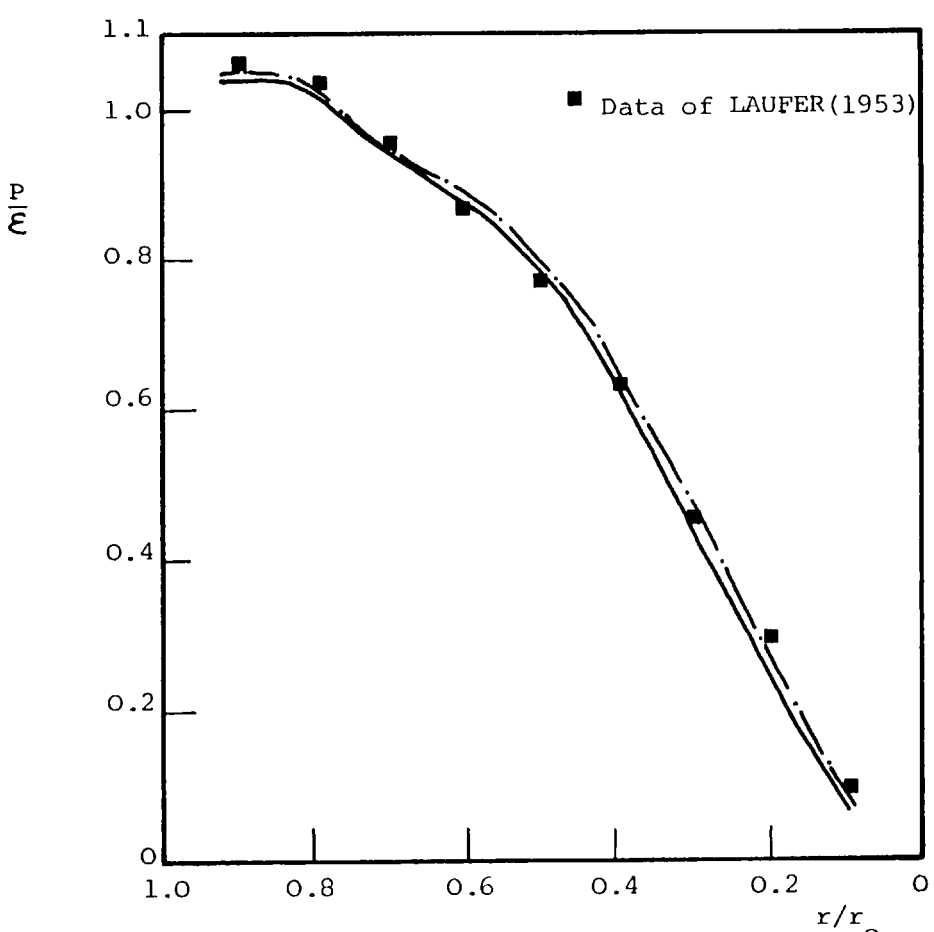


Fig.A4.4 (production/dissipation) of turbulence for fully-developed pipe flow for Re=50000.

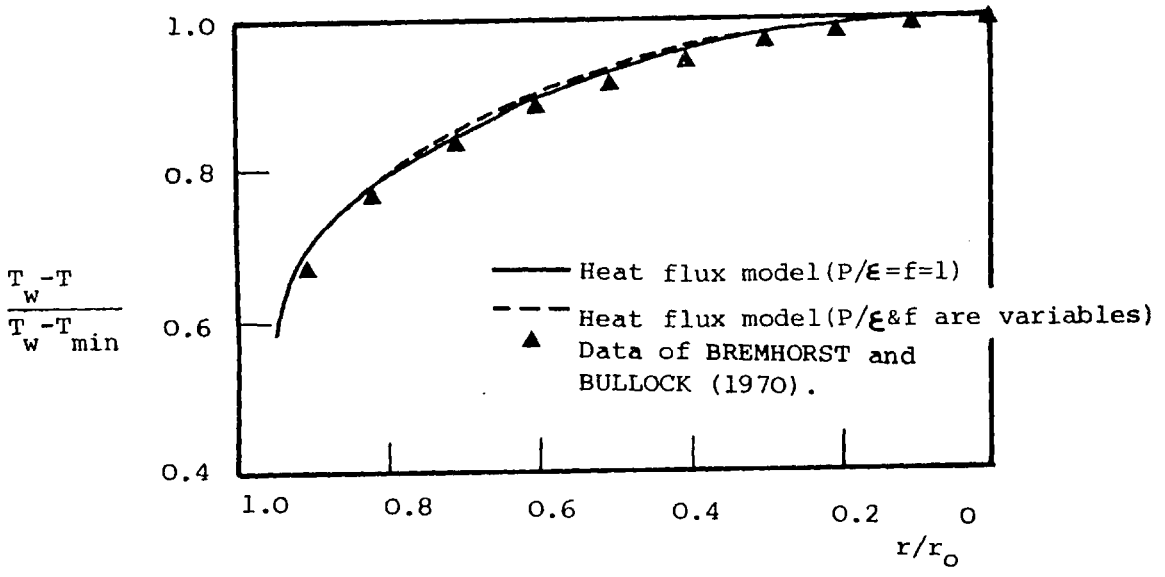


Fig.A4.5 Fully-developed pipe flow: Mean temperature profile.
(R_e=34700, $\dot{q}$=0.1767 KW/m^2)

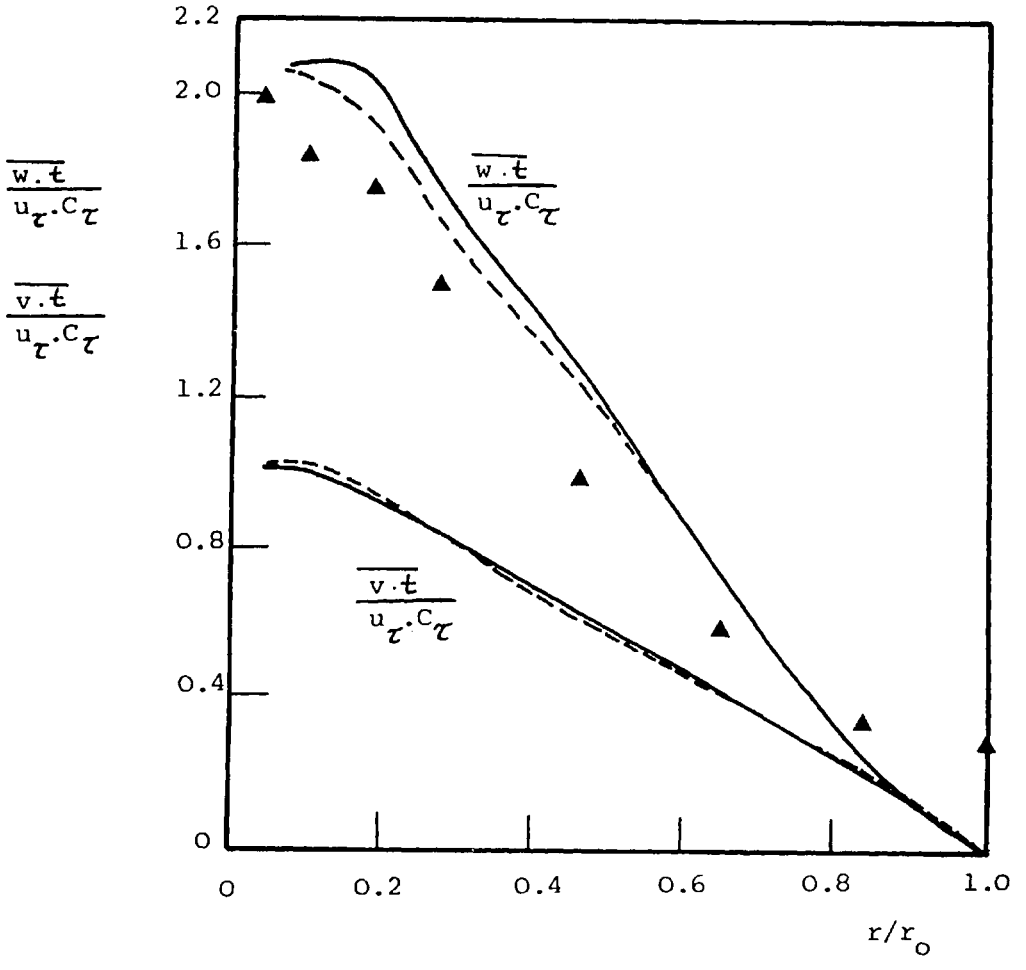


Fig.A4.6 Fully-developed pipe flow: radial and streamwise heat flux profiles. (Re=34700, $\dot{q}$=0.1767 KW/m^2).

Φ's can be obtained with reference to equations (2.39) and (2.41) as follows:

$$\Phi_{1t} = -\overline{ut}.C_{1T}.\varepsilon/k$$

$$\Phi_{2T} = -\overline{vt}.C_{1T}.\varepsilon/k - C_{1Tw}.\overline{vt}.f.\varepsilon/k$$

$$\Phi_{3T} = -\overline{wt}.C_{1T}.\varepsilon/k + C_{2T}\ \overline{vt}.(\partial W/\partial r)$$

For fully-developed symmetrical pipe flow the following equations can be obtained:

$$\overline{ut} = 0 \qquad \text{(A4.10)}$$

$$\overline{vt}=-(k/\varepsilon)\{\overline{vv}.(\partial T/\partial r)+\overline{vw}.(\partial T/\partial z)\}/\{C_{1T}+C_{1Tw}.f+(P/\varepsilon-1)/2\} \qquad \text{(A4.11)}$$

$$\overline{wt}=-(k/\varepsilon)\{\overline{vw}(\partial T/\partial r)+\overline{ww}(\partial T/\partial z)-(C_{2T}-1).\overline{vt}(\partial W/\partial r)\}/\{C_{1T}+(P/\varepsilon-1)/2\} \qquad \text{(A4.12)}$$

The model suggests that the ratio of tangential to radial thermal diffusivities in stationary pipe flow is proportional to $(\overline{uu}/\overline{vv})$ and reaches a value of around 3 close to the wall. This result is broadly in accord with observations in asymetrically heat pipes (see Launder, 1977) and is likely to be very important when heating asymetries are combined with secondary flow effects due to rotation. Figs.A4.5 and A4.6 show typical predictions of temperature and heat flux in stationary fully-developed pipe flow both in good agreement with the data. There is no considerable difference between the prediction which has been done using the local values of P/ε and f varies with radial distance, as suggested by Smaraweera (1978), and that prediction using the assumption that P/ε and f are to be unity throughout pipe flow. For fully-developed pipe flow, the effect of the wall reahes the centre line and it seems to be a reasonable assumption that f=1, and will be considered in the prediction of rotating tube.

APPENDIX A5

THE DETERMMINATION OF THE LASER BEAM BATH THROUGH A DUCT OF CIRCULAR CROSS-SECTION

The position of the measuring (scattering) volume of the laser Doppler velocimeter and the transfer function is affected by refraction of the laser beam at the Perspex/air and Perspex/water interfaces.

It is essential that we determine the position of the measuring volume as a function of the traverse co-ordinate Z^* and l^*. The origin of co-ordinates for Z^* and l^* is shown in Fig.A5.1. The first part in this appendix describes the calculation procedure used for bend cross-section. The second part describes the situation of the straight pipe cross-section.

A5.1 Bend Cross-Section

Fig.A5.1 shows a section in the circular bend in a plane whose normal is in the local streamwise direction and which contains the optical axis EDCG of the laser Doppler velocimeter. Fig.A5.2 shows the view along section J-J. The beam enters the Perspex bend at A and is refracted at B, the Perspex/water interface. The measuring volume is formed at point P. Three-dimensional analysis is shown in detail in Enayet et al (1981). In the present work more simplified method has been adopted.

Now let us direct our attention to the refraction of the laser beam in its path through the wall and the fluid. If a single beam passes through the bend cross-section, it will refract as shown in Fig.A5.3. The different angles required in the analysis are also

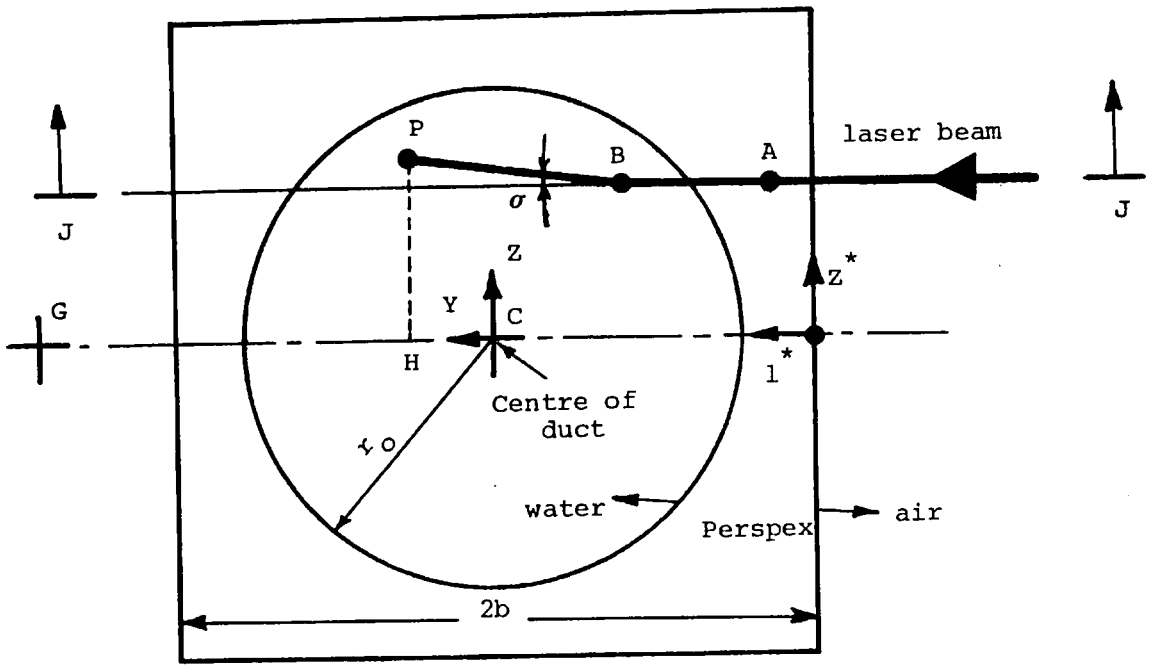


Fig.A5.1 Section along optical axis.

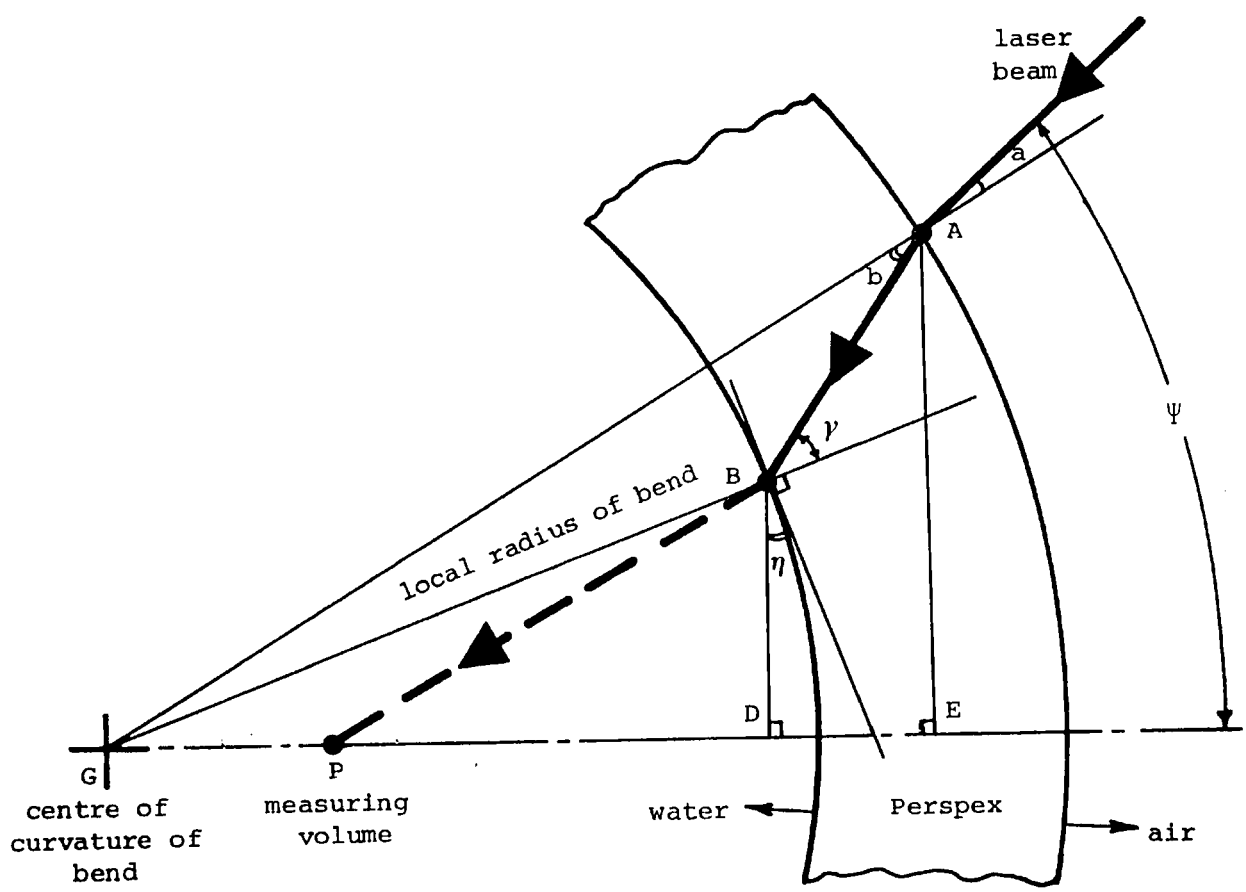


Fig.A5.2 Section on JJ of Fig.A5.1.

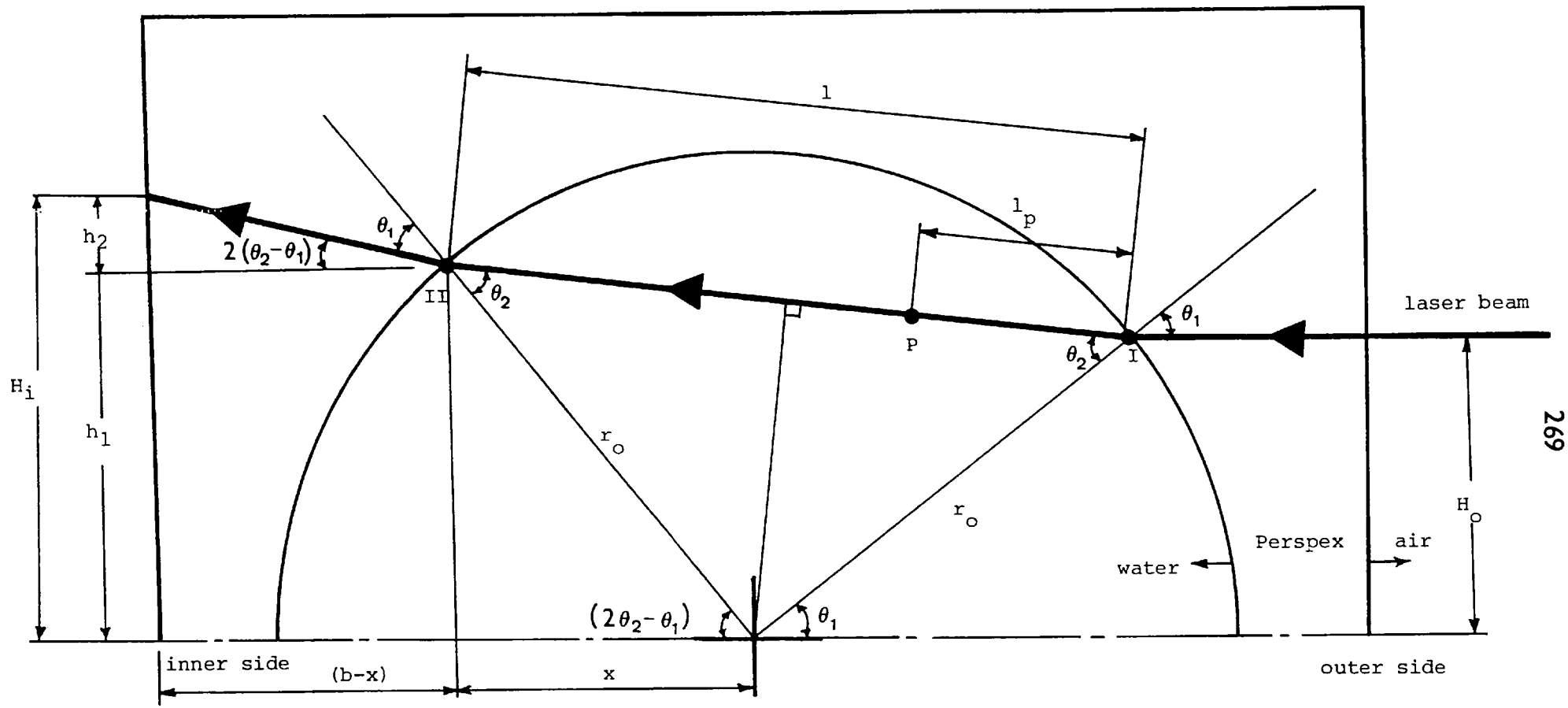


Fig.A5.3 Laser beam path details for bend cross-section.

shown in the same figure. Applying Snell's law at point I and II will give the following:

$$n_w.\sin\theta_1 = n_f.\sin\theta_2 \qquad (A5.1)$$

where n_w and n_f are the refractive indecis of water and Perspex respectively and are equal to 1.33 and 1.49.

The angle θ_1 can be determined from the relation:

$$\sin\theta_1 = H_o/r_o \qquad (A5.2)$$

where H_o is the outer height controlled by the traversing table and is considered as input data. From geometry the following relations are obtained:

$$h_1 = r_o.\sin(2\theta_2-\theta_1) \qquad (A5.3)$$

$$X = r_o.\cos(2\theta_2-\theta_1) \qquad (A5.4)$$

$$h_2 = (b-X).\tan(2\theta_2-2\theta_1) \qquad (A5.5)$$

where the inner height H_i is given by:

$$H_i = h_1 + h_2 \qquad (A5.6)$$

The length of the laser beam path through the fluid is given by:

$$l = 2r_o.\cos\theta_2 \qquad (A5.7)$$

Using test section geometry and the chosen hight H_o the height H_i can be obttained, and its calculated values are compared with the measured values $H_i)_{measured}$ as shown in Table(A5.1) which shows good agreement.

By using the previous method the path of the laser beam can be determined. Now let us locate the position of the measuring volume on the determined laser beam path. The position of the measuring point P is described by the length l measured from point of intersection of the laser beam with the inner surface. The reading of the traversing mechanism movement from the point of intersection with inner surface

is denoted as l_p^* and assumed to be proportional to the calculated one linearly as:

$$l/l_p = l^*/l_p^* \qquad (A5.8)$$

thus

$$l_p/r_o = (l/r_o).l_p^*/l^* \qquad (A5.9)$$

Thus we can locate the point P at different readings of the traversing mechanism at every line as shown in Table(A5.1) and Fig.4.13.

A5.2 Straight Pipe Cross-Section

Fig.A5.4 shows a cross-section in the straight pipe in the plane contains the optical axis, as mentioned before for bend cross-section. For this case, we must calculate the position of intersection of laser beam with inner interface twice as shown in the figure.

Applying Snell's law at the points I, II and III and using geometry relations will give the following:

$$\sin\theta_1 = H_o/r_{out} \qquad (A5.10)$$

$$n_a.\sin\theta_1 = n_w.\sin\theta_2 \qquad (A5.11)$$

where r_{out} is the average outer radius of the straight pipe and equal to 30.175 mm, and n_a is the refractive index of air and equal to unity.

From geometry the following relations can be obtained:

$$\phi_1 = \theta_2 + \Delta\theta \qquad (A5.12)$$

$$r_o/\sin\theta_2 = \Delta l/\sin(\Delta\theta) = r_{out}/\sin\phi_1 \qquad (A5.13)$$

Thus ϕ_1 and $\Delta\theta$ can be obtained, hence:

$$y = r_o.\sin(\Delta\theta + \phi_1) \qquad (A5.14)$$

$$n_w.\sin\phi_1 = n_f.\sin\phi_2 \qquad (A5.15)$$

H_o/r_o	θ_1°	θ_2°	h_1/r_o	H_i/r_o		l/r_o	l_p/r_o
				calculated	measured		
0	0	0	0	0	0	2.00	$l_p^*/20.80$
0.125	7.181	8.048	0.155	0.173	0.167	1.980	$l_p^*/20.66$
0.250	14.478	16.260	0.310	0.349	0.354	1.920	$l_p^*/20.83$
0.375	22.024	24.834	0.464	0.533	0.521	1.807	$l_p^*/20.81$
0.500	30.000	34.056	0.617	0.731	0.750	1.657	$l_p^*/20.94$
0.625	38.680	44.427	0.768	0.960	0.979	1.428	$l_p^*/20.80$
0.750	48.590	57.140	0.911	1.272	1.292	1.085	$l_p^*/19.91$
0.802	53.330	63.942	0.964	1.475	1.521	0.879	$l_p^*/19.92$

Table A5.1 Laser beam path details for bend cross-section.

H_o/r_o	θ_1°	θ_2°	ϕ_1°	ϕ_2°	y/r_o	z/r_o	l/r_o	l_p/r_o
0	0	0	0	0	0	0	2.0	$l_p^*/17.50$
0.208	9.538	6.38	8.04	9.01	0.194	0.119	1.975	$l_p^*/17.59$
0.417	19.350	12.83	16.24	18.26	0.387	0.238	1.899	$l_p^*/17.85$
0.625	29.810	19.49	24.80	28.03	0.575	0.357	1.765	$l_p^*/17.48$
0.833	41.514	26.41	34.00	38.79	0.756	0.477	1.559	$l_p^*/17.25$
1.042	55.950	33.78	44.35	51.55	0.917	0.596	1.244	$l_p^*/17.28$
1.208	73.960	40.17	54.19	65.30	1.000	0.677	0.835	$l_p^*/17.37$

Table A5.2 Laser beam path details for straight pipe cross-section.

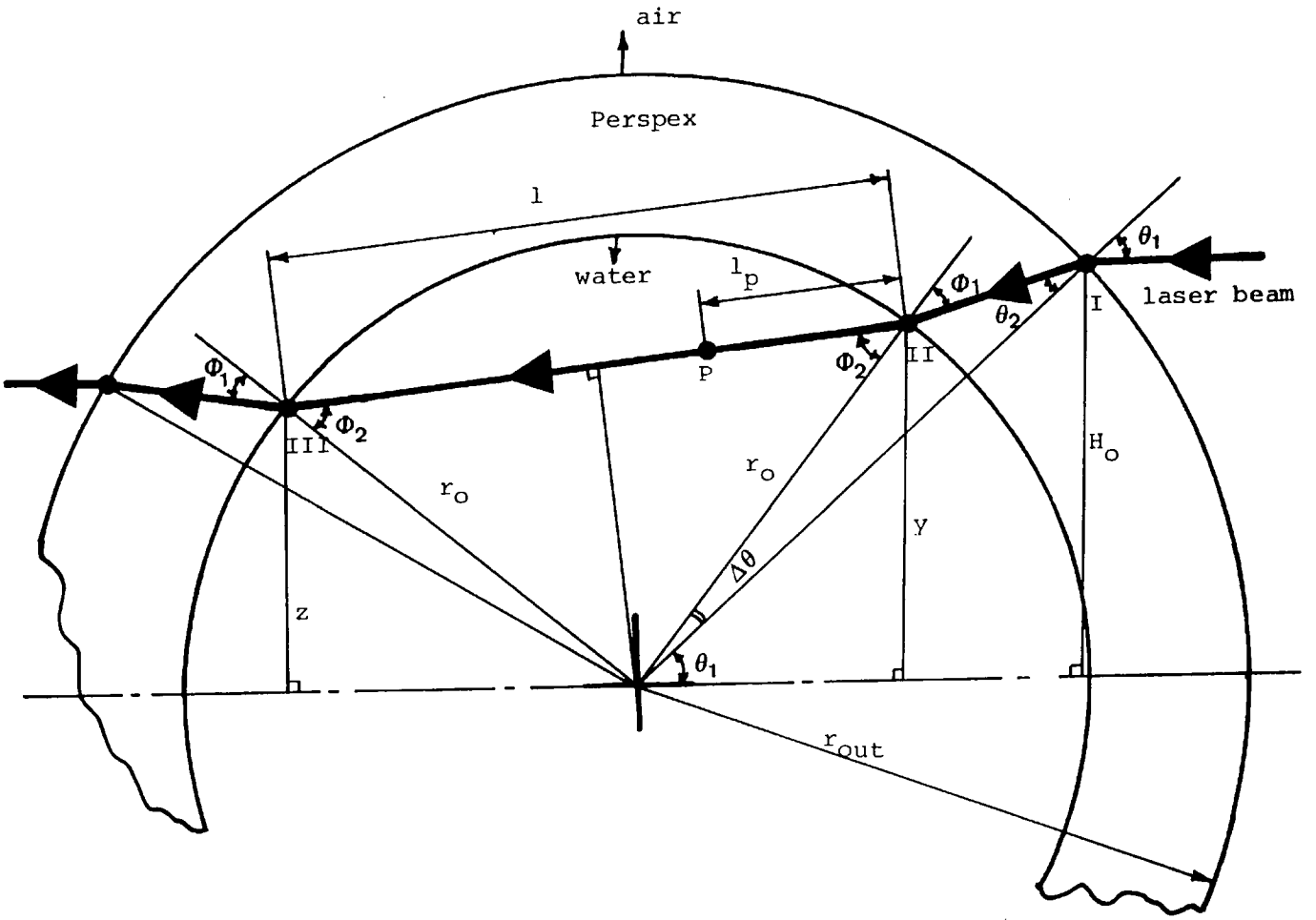


Fig.A5.4 Laser beam path details for straight pipe cross-section.

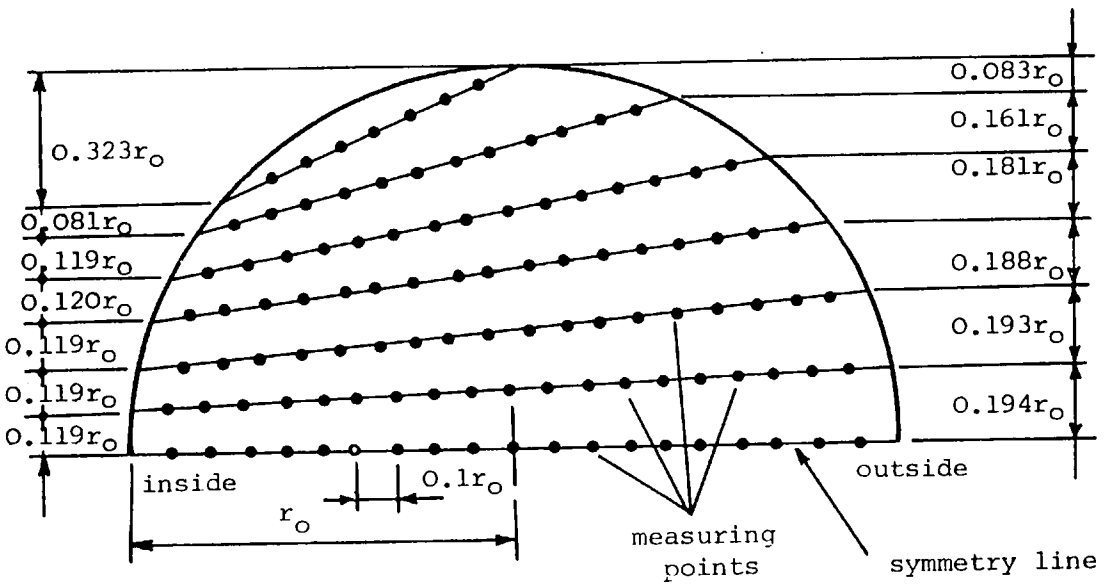


Fig.A5.5 Flow measuring domain for straight pipe cross-section.

thus ϕ_2 can be obtained, and

$$l = 2r_o.\cos\phi_2 \qquad (A5.16)$$

$$Z = r_o.\sin(2\phi_2 - \phi_1 - \theta_1 + \theta_2) \qquad (A5.17)$$

The different locations of the measuring points are shown in Fig.A5.5 and Table(A5.2). The previous results obtained for the bend cross-section show that this simple method agrees well with experiments, as shown from the comparison of H_i in Table(A5.1). So it is recommended to use this simple procedure rather than three dimensional analysis mentioned in Enayet et al (1981) which need verification before use.

APPENDIX A6

PUBLICATIONS

Laser–Doppler measurements of laminar and turbulent flow in a pipe bend

M. M. Enayet, M. M. Gibson, A. M. K. P. Taylor and M. Yianneskis*

Laser–Doppler measurements are reported for laminar and turbulent flow through a 90° bend of circular cross-section with mean radius of curvature equal to 2.8 times the diameter. The measurements were made in cross-stream planes 0.58 diameters upstream of the bend inlet plane, in 30, 60, and 75° planes in the bend and in planes one and six diameters downstream of the exit plane. Three sets of data were obtained: for laminar flow at Reynolds numbers of 500 and 1093 and for turbulent flow at the maximum obtainable Reynolds number of 43 000. The results show the development of strong pressure-driven secondary flows in the form of a pair of counter-rotating vortices in the streamwise direction. The strength and character of the secondary flows were found to depend on the thickness and nature of the inlet boundary layers, inlet conditions which could not be varied independently of Reynolds number. The quantitative anemometer measurements are supported by flow visualization studies. Refractive index matching at the fluid–wall interface was not used; the measurements consist, therefore, of streamwise components of mean and fluctuating velocities only, supplemented by wall pressure measurements for the turbulent flow. The displacement of the laser measurement volume due to refraction is allowed for in simple geometrical calculations. The results are intended for use as benchmark data for calibrating flow calculation methods.

Keywords: *flow measurement, turbulence, flow visualization, pipe bends*

As a fluid flows through a straight pipe or duct and into a bend the pressure, which in the straight section is uniform across the flow, must adjust in the bend to counter centrifugal forces. The pressure is greatest at the outer wall farthest from the centre of curvature and least at the inner wall nearest the centre of curvature and the cross-stream pressure gradient in the bend has two well known effects on the flow. At the bend inlet, the boundary layer on the outer wall experiences the effects of a positive streamwise pressure gradient which may in a tight bend be sufficiently strong to produce local separation; conversely, the inner wall boundary layer is accelerated. The reverse occurs at the pipe exit where local pressure gradients of the opposite sign appear as the flow adjusts to uniform pressure conditions downstream. Inside the bend, the presence of side wall boundary layers ensures that the conditions for radial equilibrium cannot be satisfied exactly over the entire field. The slow moving fluid in these layers is forced inwards towards the centre of curvature and continuity ensures that the high speed fluid near the axis is driven outwards. The result is a secondary flow superimposed on the main flow.

If the bend is of circular cross-section, or its height is not significantly greater than its width measured in the radial direction, the effect of the secondary flow is to displace the region of maximum velocity from the centre towards the outer wall. If, however, the boundary layers are thin and the secondary flow is weak, the velocity distribution in the inviscid central core will approximate to that of a free vortex with velocity increasing towards the centre of curvature. The effects of longitudinal curvature on the boundary layers on the inner and outer walls also tend to counteract the effects of pressure-driven secondary flow. In the inner boundary layer, the shear stress is reduced by curvature and the boundary layer grows relatively slowly. In the outer boundary layer the shear stress is increased and the layer is retarded and thickened. Thus, in the flow in a high narrow curved channel, where the secondary flows are weak and confined to the edge zones, the region of maximum velocity is found closer to the inner wall[1]. The effects of curvature on laminar boundary layers are weak in ducts of moderate aspect ratio and are masked by the secondary flow; the fractional change in shear stress is of order δ/R (where δ, boundary layer thickness and R, radius of curvature). The effects of curvature on the turbulence

* Fluids Section, Mechanical Engineering Department, Imperial College of Science and Technology, Exhibition Road, London, UK, SW7 2BX
Received 5 March 1982 and accepted for publication on 14 June 1982

in turbulent boundary layer flow are an order of magnitude greater[2] and may be sufficiently large to counteract the effects of secondary flow and to be significant in determining the flow structure.

The presence and origin of secondary flow in bends have long been known and understood although obvious measurement difficulties associated with probe explorations have hindered detailed investigation and have largely restricted experiments to flow visualization studies and measurements of overall pressure loss. The former[3] show that a laminar boundary layer in a 90° pipe bend is deflected through 45° while the deflection of a turbulent layer does not exceed 30°. Work carried out prior to 1970, which consists almost entirely of measurements of wall pressure and pressure probe surveys of the outlet plane, is summarized and reviewed by Ward-Smith[4]. These data provide a basis for empirical pressure decrease correlations but are necessarily too limited to be used for the validation of flow calculation methods. The development of these methods to the point where they can be used as standard design tools has, fortunately, been paralleled by the development of the laser–Doppler anemometer which, by obviating the need for probe insertion, has made possible more detailed measurement of complex flows including those in bends. Humphrey *et al*[5] report measurements of the longitudinal velocity component in laminar flow through a strongly curved duct of square cross-section. This work has been extended[6] to the measurement in turbulent flow of two components of mean velocity, two components of turbulent energy and one shear stress component; similar measurements also have been reported[7] for laminar and turbulent flow with thin inlet boundary layers.

The problem of flow in a round pipe, which is examined in this paper, presents additional measurement difficulties and has consequently received less attention. Rowe[8] reports total-pressure measurements in a mildly curved pipe bend while laser–Doppler measurements appear to be limited to the laminar flow experiment described by Agrawal *et al*[9]. The difficulties arise because in off-diameter planes, the laser beams are refracted at the fluid–wall interface unless care is taken to match the refractive indices. If this is not carried out, the measurements will be limited to longitudinal components of mean and fluctuating velocity. The measurement volume is displaced but to a position which can be located reasonably accurately by simple calculation[10].

In this paper, measurements are reported of laminar and turbulent flow in and downstream of a tight 90° pipe bend. The results, which complement and extend those of previous investigations[5–7] are seen as a useful contribution to the 'data bank' available for the further testing and development of numerical flow calculation methods.

Experimental

Test bend

The geometry and dimensions of the test bend are shown in Fig 1. The dimensions are similar to those of the square-sectioned bend used previously[6,7] with

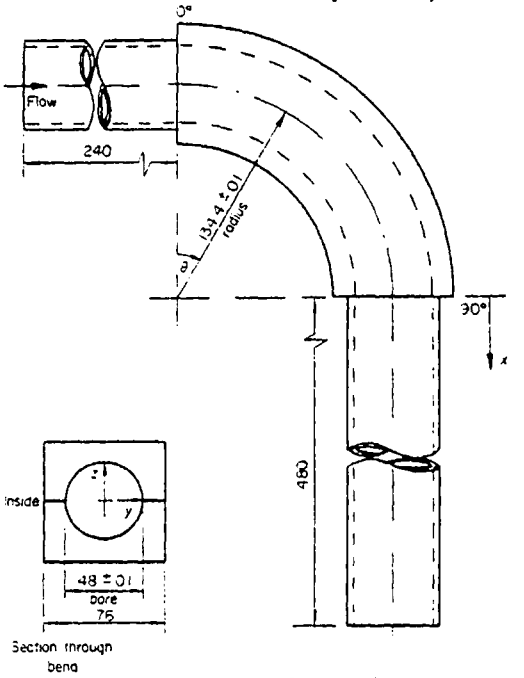


Fig 1 Bend dimensions and co-ordinate system (dimensions in mm)

Notation

C_p	Pressure coefficient (Fig 7)	u'	rms streamwise velocity fluctuation
d	Pipe diameter	x	Distance measured along the pipe and bend centreline
l	Distance of control volume from pipe wall along refracted beam path	y	Distance measured horizontally from centreline (Fig 1)
$\dot{m}$	Mass flow rate	z	Distance measured vertically from centreline (Fig 1)
p	Static pressure	β	half-angle of beam intersection
p_{ref}	Static pressure one diameter upstream of pipe bend	δ	Boundary layer thickness
R	Radius of curvature of the bend	θ	Bend angle (Fig 1)
r	Internal radius of pipe $= \frac{1}{2}d$	ϕ	Angle subtended at pipe centreline (Fig 7)
Re	Reynolds number $U_B d/\nu$	ν	Kinematic viscosity
U	Streamwise local mean velocity	ρ	Density
U_B	Bulk velocity $4\dot{m}/(\pi\rho d^2)$		

radius of curvature equal to 2.8 times the internal diameter. The bend was machined accurately from two halves of a rectangular perspex block, split in the plane of symmetry. It was thus possible to maintain a tolerance of ±0.1 mm on the internal diameter and to minimize refraction problems at the external, air–perspex interface by the retention of a rectangular external section. The bend was fixed in the horizontal plane downstream of a straight tube of the same diameter (48 mm) and 240 mm long; a second straight tube, 480 mm long, was fitted downstream.

The bend was fitted in a water flow rig identical to that described by Taylor *et al*[7]. The flow rate was constantly monitored using Fischer and Porter precision flowmeters. The maximum obtainable Reynolds number, $4\dot{m}/\pi\nu d$, was 43 000. For the turbulent flow measurements the water was seeded with minute quantities of milk to increase the scattering particle concentration and, consequently, the particle arrival rate[11].

Instrumentation and signal processing

The optical arrangement is similar to that described by Taylor *et al*[7]. The light beam generated by a 5 mW helium–neon laser is focussed on to a radial diffraction grating, collimated to reduce spherical aberration and then focussed to form the scattering volume at the point of measurement in the bend. Measurements in the vertical plane were made in the straight pipe sections at each end of the bend. For these the light beam was turned through 90° using a mirror which was optically flat to within one tenth of the wavelength of light. Forward scattered light collected by the objective lens is focussed on and passes through a pinhole to an EMI 9658 photomultiplier, the output from which is processed in a Cambridge Consultants CC01 frequency tracking demodulator. The principal characteristics of the laser–Doppler anemometer are given in Table 1.

Scope and accuracy of the measurements

Refraction of the laser beam at the water–perspex interface not only displaces the measurement volume by an amount which can be readily calculated but also, and more importantly, prevents the measurement of cross-section velocity components. The method used successfully for the latter in the rectangular bend experiments[6,7] fails for the round pipe because, unless the refractive indices of the fluid and pipe wall are equal, the twin laser beams entering the pipe in a plane at 45° to the axis cannot converge. Consideration has been given to the use of fluids other than water which would allow the indices to be equalized. Unfortunately, it appears that such fluids either possess highly unpleasant or toxic properties or are so viscous that it is difficult to realize Reynolds numbers high enough for turbulent flow. An example of this is given in the experiment described by Agrawal *et al*[9] where the use of a glycerine–water mixture to match the indices limited the investigation to laminar flow. As the main objective here is the study of turbulent bend flow, the limitation on the scope of the measurements to streamwise velocities only has had to be accepted at this stage.

There is no difficulty in measuring the streamwise velocities or in calculating the displaced position of the measurement volume. The measurements are made at points along the optical axis which is refracted at the pipe wall at an angle to the plane of symmetry to which it was originally parallel. A straightforward calculation produces the beam trajectories shown in Fig 2. The actual location of

Table 1 Optical characteristics of the laser–Doppler anemometer

Focal length of imaging lens	300 mm
Half-angle of beam intersection	9.11°
Fringe separation (line-pair spacing)	1.9 μm
Number of fringes in measuring volume	84
Intersection volume diameter calculated at $1/e^2$ intensity	0.167 mm
Intersection volume length calculated at $1/e^2$ intensity	1.391 mm
Photomultiplier pinhole diameter	0.50 mm
Transfer constant	0.500 MHz/ms

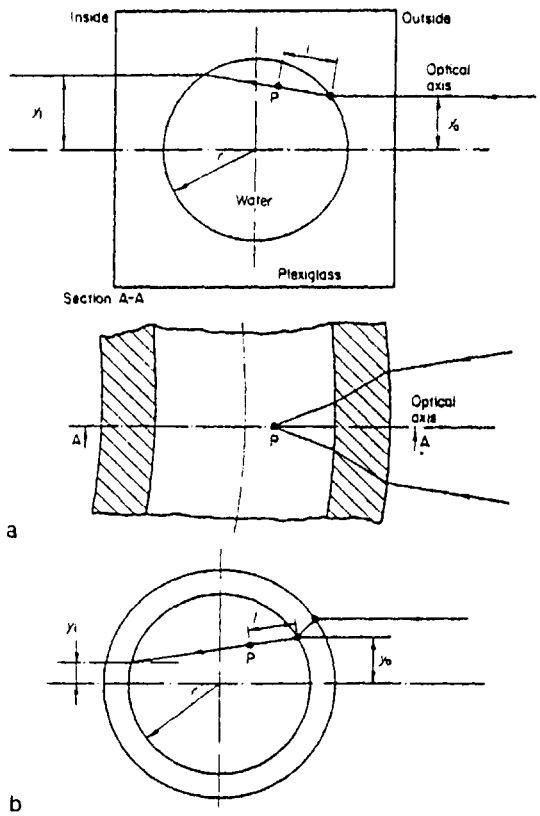


Fig 2 (a) Beam paths through test section. Bend section in θ–y plane. Point P marks location of scattering volume (b) Cross-section through upstream and downstream tangents

the measurement points along the optical axis is obtained by applying the correction described by Boadway and Karahan[10] for the effects of refraction due to the bend curvatures. These two corrections have been applied independently to the results presented here. It was also found that signal quality was only slightly impaired by refraction and that measurements were feasible for points in the flow distant more than one tenth of the radius from the wall in the vertical plane.

Estimated measurement errors are summarized in Table 2. Corrections were not applied for the effects of finite transit time and instrument noise broadening. Systematic errors of up to 2.5% are mainly associated with velocity gradient effects near the walls and have been included in the Table.

The measurements were made in cross-stream planes 0.58 diameters upstream of the bend inlet plane, in 30, 60, and 75° planes in the bend and in planes at one and six diameters downstream of the exit plane. Three sets of data were obtained: for laminar flow at Reynolds numbers of 500 and 1093 and for turbulent flow at the maximum obtainable Reynolds number of 43 000.

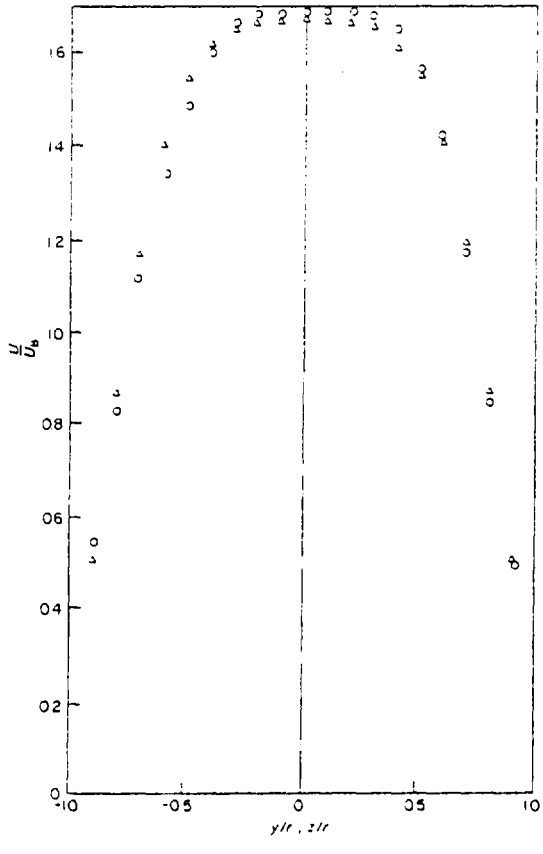


Fig 3 Horizontal, ○, and vertical, △, profiles of mean velocity in the laminar approach flow 0.58 diameters upstream of the inlet plane. Re = *500*

Results and discussion

Flow visualization

Observation of hydrogen bubble paths in low speed flow revealed no unusual features such as the local separation reported[5] for fully developed flow through the square-section bend. These observations were entirely consistent with large-scale secondary flow patterns detected by laser-Doppler anemometry.

Laminar flow measurements

The results of velocity measurements at a Reynolds number of 500, mean velocity 10·5 mm/s, are shown in Figs 3 and 4. Fig 3 shows the inlet conditions: horizontal and vertical velocity profiles 0.58 diameters upstream of the bend. The boundary layer thickness is $\approx 0.27\,d$ so that there is a significant potential core. The apparent, slight asymmetry shown in the results is within the estimated error band. Contours of the streamwise velocity in four cross-stream planes (Fig 4) show the effects of strong secondary flow which displaces the region of maximum velocity to the outside of the bend. The secondary flow develops gradually: in the 30° plane the only visible effect is a thickening of the shear layer on the inside of the bend. By 60° the secondary flow has become almost fully developed as is shown by the distortion of the contours. The fourth set of

Table 2 Measurement errors

Quantity	Systematic error	Random error
x	±0.5 mm	±0.02 mm
y, z	±0.2 mm	±0.02 mm
θ	±0.3°	±0.17°
β	±0.05°	nil
U_B (laminar)	±0.8%	±0.8%
U_B (turbulent)	±1.5%	±0.5%
U/U_B	up to 2.5%	±1.5%
u'/U_B	up to 3%	up to ±3%

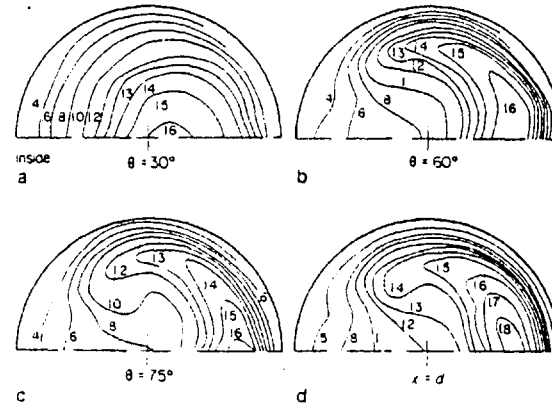


Fig 4 Contours of mean velocity U/U_B *in the bend, laminar flow* Re = *500*

contours, in the plane one diameter downstream, shows that the secondary motion persists without significant decay to this distance.

The effects of doubling the mean velocity and Reynolds number to 23 mm/s and 1093, respectively, are shown in Figs 5 and 6. The inlet boundary layers are reduced in thickness by ≈15% to 0.23 d, the transverse pressure gradient is increased and the secondary flow is intensified. The peak velocity in the 30° plane is displaced from the plane of symmetry but remains closer to the centreline. This displacement, which persists downstream, has also been observed in the flow in a square bend[7]. The shape of the contours near the outside of the bend reflect scatter in the data attributable mainly to difficulties in locating accurately the measurement volume near the wall and partly, perhaps, to slight asymmetry in the flow.

In neither case do the measurements show any unexpected feature: the secondary flow superposed on the main motion is essentially as described qualitatively elsewhere[1,3]; it develops gradually and persists downstream after the removal of the transverse pressure gradient responsible for its generation in the bend. The strength and location of the pressure-driven secondary flow depend on the inlet conditions and the Reynolds number which could not be varied independently in these experiments. The stronger secondary flow observed at $Re = 1093$ must be attributable mainly to the increased centrifugal forces and transverse pressure gradient rather than to the relatively small changes noted in the initial conditions. These quantitative data of velocity in the bend are considered to be sufficiently accurate to be useful in checking the numerical accuracy of flow prediction methods.

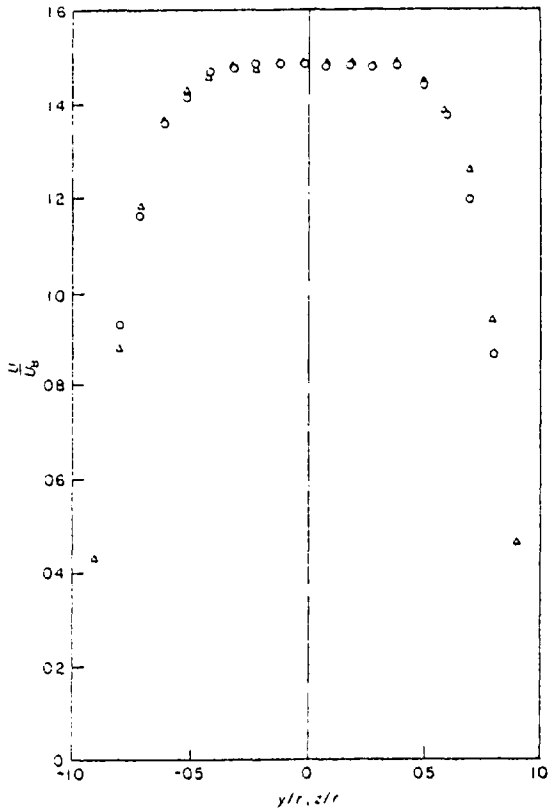


Fig 5 Horizontal, ○, and vertical, △, profiles of mean velocity in the laminar approach flow 0.58 diameters upstream of the inlet plane, Re = *1093*

Turbulent flow measurements

At the maximum flow velocity of 0.92 m/s, Reynolds number 43 000, the inlet boundary layers are turbulent. The static pressure variation on the bend wall is large enough to be measured accurately with the results shown in Fig 7. At the bend inlet, the negative pressure gradient on the inner wall is approximately twice the positive gradient on the outside. These initial gradients resulting from the change from straight to curved flow disappear at ≈25° so that in the mid-section of the bend ($25° < \theta < 75°$), a quasi-equilibrium condition is reached with approximately uniform pressure on the inner and outer walls. The transition to straight flow downstream is signalled by the appearance of strong gradients for $\theta > 75°$. The overall pressure decrease is about $0.3\rho U_B^2$.

Laser–Doppler measurements of the mean and rms fluctuation of the streamwise velocity at inlet are shown in Fig 8 and contours of these quantities at downstream stations in Figs 9 and 10. The inlet boundary layers of Fig 8 are much thinner, 0.09 d, than in the two laminar flows investigated and the presence of a large central region of uniform velocity flow influences significantly the development of secondary flow downstream. The mean velocity contours (Fig 9) show that by the 30° plane the potential

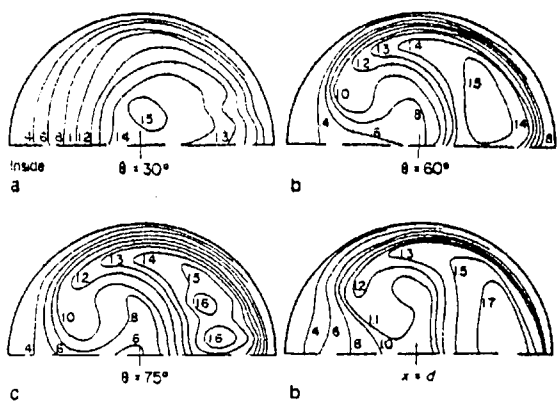


Fig 6 Contours of mean velocity U/U_B *in the bend, laminar flow,* Re = *1093*

core has adjusted to the cross-stream pressure gradient imposed by the bend and the region of maximum velocity has been displaced toward the inside. The results also differ from the corresponding laminar flow measurements in that the thickness of the outer wall boundary layer is increased relative to that on the inside of the bend due mainly to the effects of the potential flow adjustment and the wall

pressure gradients of opposite sign but also, quite possibly, to the effects of longitudinal curvature on the turbulence structure. In the 60° plane, distortion of the contours suggests the presence of strong secondary flow largely confined to the region of steep velocity gradients near the inner wall. This secondary flow grows with distance through the bend and by the 75° plane extends over and beyond the inner half of the section. The removal of the transverse pressure gradient in the straight flow downstream results in a shift of the velocity maximum toward the outside. A large secondary flow, similar to that observed in the laminar flow experiments, now extends over the entire flow area and persists in the plane six diameters downstream of the bend where, however, the transverse velocity gradients have decayed to approximately one half of their values one diameter downstream.

The contours of turbulence intensity (Fig 10) are consistent with those of the mean velocity. As expected, high values of the velocity fluctuation are associated with steep mean velocity gradients and with the distortion of the symmetrical inlet flow.

These results may be compared with the measurements made by Humphrey *et al*[6] in a tight

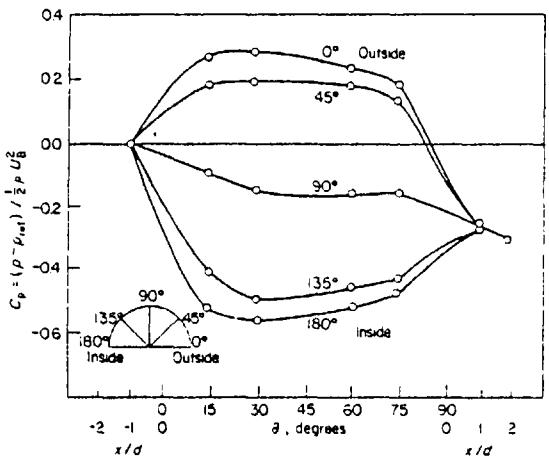


Fig 7 Wall static pressure variation. Turbulent flow Re = *43 000*

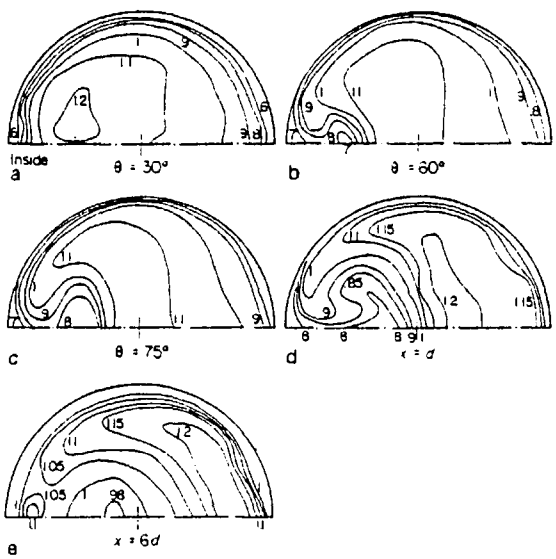


Fig 9 (a–c) Contours of mean velocity U/U_B *in the bend. (d–e) Contours of mean velocity* U/U_B *downstream of the bend. Turbulent flow,* Re = *43 000*

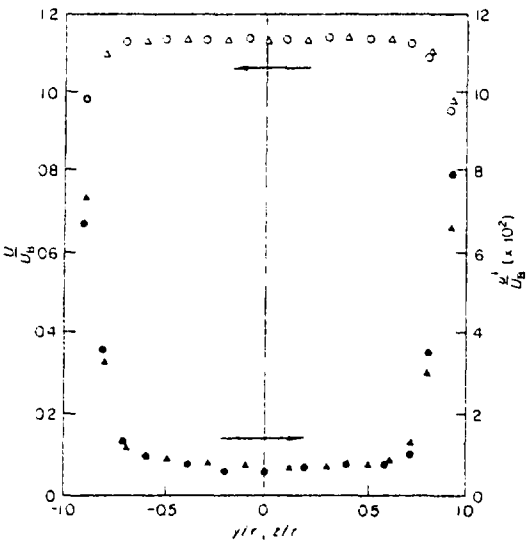


Fig 8 Profiles of mean velocity U/U_B *and turbulence intensity* U'/U_B *in the turbulent approach flow 0.58 diameters upstream of the bend.* ○ *horizontal,* △ *vertical,* Re = *43 000*

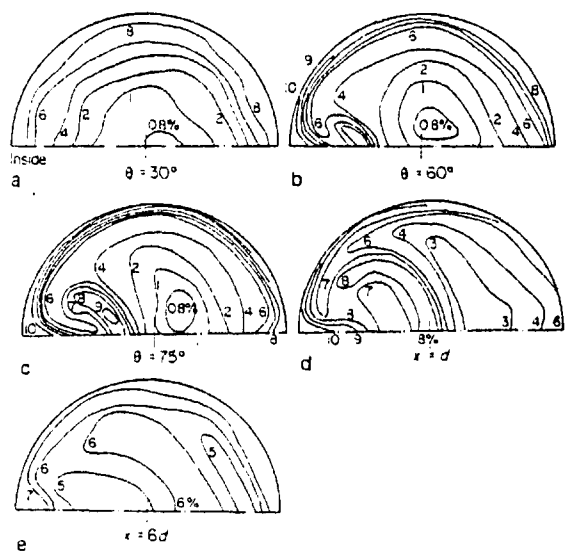


Fig 10(a–c) Contours of turbulence intensity (u'/U_B) *in the bend. (d–e) Contours of turbulence intensity* (u'/U_B) *downstream of the bend. Turbulent flow,* Re = *43 000*

bend of square cross-section. The inlet boundary layers of that flow were substantially thicker than the flow here and contained stress-driven secondary flows towards the corners. Consequently, the pressure-driven secondary flow was similar to those observed in the two laminar flows and extended over the entire flow area.

Conclusions

The measurements show, as expected, that in bend flow, strong cross-stream flows occur which are produced by the inward motion of slow moving fluid in a radial pressure gradient. The strength of the secondary flow is influenced by the initial inlet flow conditions: when the inlet boundary layers are thin, as in the turbulent flow case reported here, the initial flow adjustment is an inward shift of the velocity peak in the potential core. The secondary flow then develops initially in the inside of the bend. The secondary flow always takes some time to develop and its effects are still increasing by the exit and persist downstream.

The effects of refraction at the doubly-curved fluid–wall interface prevent the measurement of cross-stream velocity components. The investigation of flows in the round bend to the same level of detail that has been achieved previously in square bends, will require refractive index matching. For the streamwise velocity measurements reported here, simple geometrical corrections allow for the displacement of the measurement volume by refraction.

The laminar flow data may be used to check the numerical accuracy of flow prediction methods; the turbulent flow measurements provide the additional information needed to validate mathematical models of turbulence.

Acknowledgements

This research was supported principally by a research contract from the CEGB Central Electricity Research Laboratories, UK. A. Taylor and M. Yianneskis received financial support from NASA Lewis Research Center, USA. Professor J. H. Whitelaw contributed valuable advice in numerous discussions. Mr O. Vis made the test bend, Mr M. Roper the water channel and Miss K. Maxwell prepared the typescript.

References

1. Goldstein S. (ed). Modern developments in fluid dynamics. *Oxford, 1938*
2. Bradshaw P. Effects of streamline curvature on turbulent flow. *AGARDograph 169, 1973*
3. Prandtl L. Essentials of fluid dynamics. *Blackie, London, 1952*
4. Ward-Smith A. J. Pressure losses in ducted flows. *Butterworth, London, 1971*
5. Humphrey J. A. C., Taylor A. M. K. P. and Whitelaw J. H. Laminar flow in a square duct of strong curvature. *J. Fluid Mech. 1977, 83, 509*
6. Humphrey J. A. C., Whitelaw J. H. and Yee G. Turbulent flow in a square duct with strong curvature. *J. Fluid Mech., 1981, 103, 443*
7. Taylor A. M. K. P., Whitelaw J. H. and Yianneskis M. Measurements of laminar and turbulent flow in a curved duct with thin inlet boundary layers. *NASA Contractor Rep. 3367, 1981*
8. Rowe M. Measurements and computations of flow in pipes. *J. Fluid Mech., 1970, 43, 771*
9. Agrawal Y., Talbot L. and Gong K. Laser anemometry study of flow development in curved circular pipes. *J. Fluid Mech., 1978, 85, 497*
10. Boadway J. D. and Karahan E. Correction of laser Doppler anemometer readings for refraction at cylindrical interfaces. *DISA Information 26, 1981*
11. Durst F., Melling A. and Whitelaw J. H. Principles and practice of Laser–Doppler anemometry. *Academic Press, London, 1976*

TECHNICAL NOTE

Measurements of turbulent developing flow in a moderately curved square duct

M. M. Enayet, M. M. Gibson and M. Yianneskis*

Laser–Doppler measurements in the turbulent flow in a right-angled bend of square cross-section, radius/duct-width ratio 7.0, are presented and show the development of secondary circulation in cross-stream planes. Distributions of the streamwise and radial components of the mean velocity and turbulence intensity, and the corresponding Reynolds shear stress, are presented as contour plots and are intended for use in the further development of numerical flow prediction methods

Key words: *flow measurement, turbulence, ducting*

This note is a postscript to the longer and more detailed account of laser–Doppler measurements of laminar and turbulent flow in a strongly curved pipe bend[1]. Measurements are reported here of turbulent flow in a more moderately curved bend of square cross-section which were made using the same experimental arrangements and instrumentation as previously[1]. A principal objective of this research has been the recording of basic data suitable for testing numerical calculation methods; in addition, the flow exhibits a number of interesting features.

Detailed measurements of the flow in strongly curved bends[1–4] show that the main secondary motion develops over an appreciable distance and that it is more complicated than originally expected or suggested by the idealized diagrams of the textbooks. Investigations of laminar and turbulent flow in right-angled bends of square section have been carried out[2–4], and the effects of changes in inlet conditions have been established[4]. Details of the flow in an equivalent round bend have been published[1] and these studies recently have been extended to flow in an S-bend of moderate curvature[5]. This note contains the results of similar measurements in turbulent flow in a right-angled square bend of lesser curvature, with a radius/duct-width ratio of 7.0 compared to that of 2.3 in the previous experiments.

Experimental

The geometry and dimensions of the test bend are shown in Fig 1. It was manufactured from 20 mm thick perspex with a cross-section of $40 \times 40\ mm^2$. The curved surfaces were machined from solid perspex to radii of 260 and 300 mm. The tolerance on each of these dimensions was ±0.1 mm. The bend was fixed in the horizontal plane at the end of a straight duct 300 mm long and discharged into another straight duct 200 mm long. The complete assembly was attached to the water flow rig described previously[1]. The bulk velocity was 0.88 m/s giving a Reynolds number based on the bulk velocity and duct width of 35 200. The boundary layers in the bend inlet plane were turbulent and ≈0.14 duct widths thick. Measurements were made in the 45°

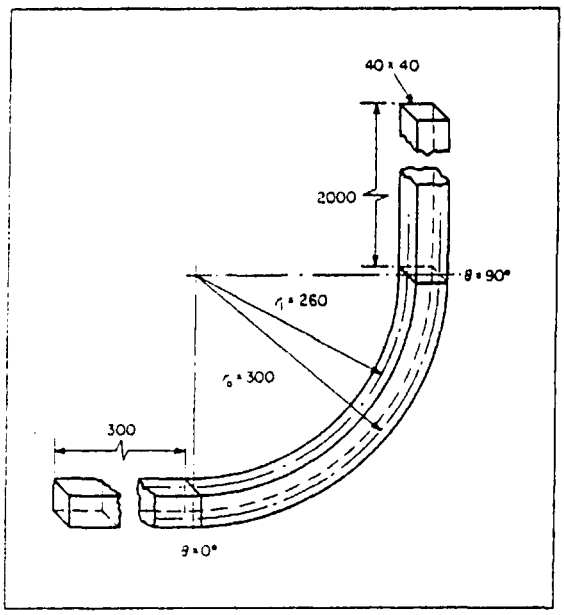


Fig 1 Duct bend geometry (dimensions in mm)

* Mechanical Engineering Department, Imperial College of Science and Technology, Exhibition Road, London, UK, SW7 2BX
Received 5 March 1982 and accepted for publication on 14 June 1982

Notation

r_i	Inside radius of curvature of bend	U_B	Bulk viscosity
r_o	Outside radius of curvature of bend	V	Radial component of mean velocity
U	Circumferential component of mean velocity	u', v'	rms fluctuating velocity components
		$\overline{uv}$	Reynolds shear stress
		θ	Angle subtended at centre of curvature

and exit (90°) planes, the optical axis being vertical. Measurements in the inlet plane were made with an 'S'-bend fitted to the rig as reported previously[5]. The laser–Doppler anemometer system and associated equipment have been fully described elsewhere[1].

Results and discussion

The results consist of the streamwise and radial mean velocity components U and V, the corresponding turbulence intensities u' and v' and the Reynolds shear stress $\overline{uv}$. Measurements in the inlet plane for a Reynolds number of 40 000 were made by Taylor *et al*[5] when an 'S'-bend was fitted to the water rig. It is assumed that the inlet conditions do not differ significantly in the present bend flow and the data from Taylor *et al*[5] are reproduced in Fig 2. These show reasonably uniform inlet boundary layers with an appreciable potential core. The radial component of the mean velocity, which is not presented, never exceeded $0.07U_B$ and the shear stress levels, also not presented, appear to be consistent with the intensities, but the boundary layers were too thin for more detailed measurements of the cross-correlation in the high shear regions adjacent to the walls. The measurements in the 45° and exit planes (Figs 3–7) may usefully be compared with the equivalent data[3,4] from the more strongly curved bend. As in these previous experiments, the flow responds in two ways to the imposition by the bend of a radial pressure gradient. Initially, the peak velocity in the core moves towards the inside of the bend as required for radial equilibrium in the centre, but further downstream the development of secondary flows results in a shift of this peak to the outside region. Both these effects are very evident in the tight bend flow[3,4] but the former is not apparent in the measurements made here where the transverse pressure gradients are considerably smaller and less influential. The secondary flows, the presence of which is evident in the mean velocity contours at 45°, effectively displace the velocity maximum to the outside of the bend and result in an accumulation

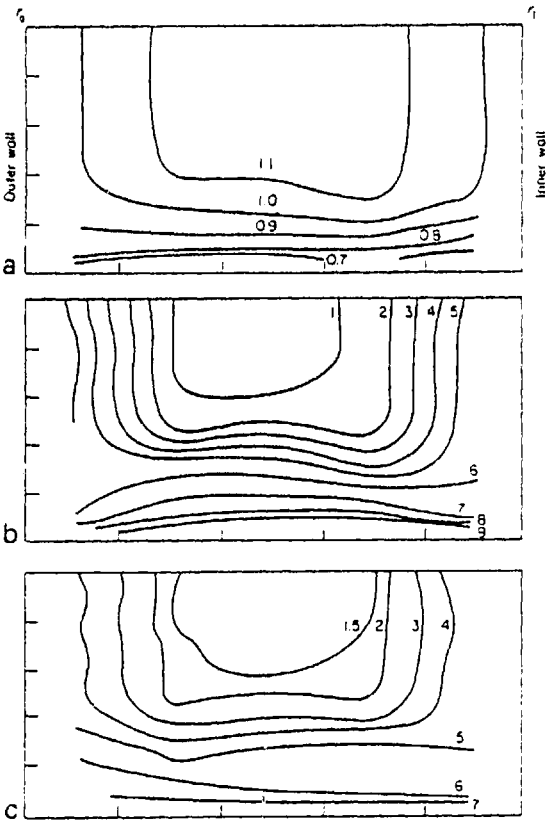


Fig 2 Contours of mean velocity and rms turbulence intensity in the inlet plane: (a) U/U_B (b) $u'/U_B \times 10^2$ (c) $v'/U_B \times 10^2$. (Data from Taylor et al[5]. Re = 40 000)

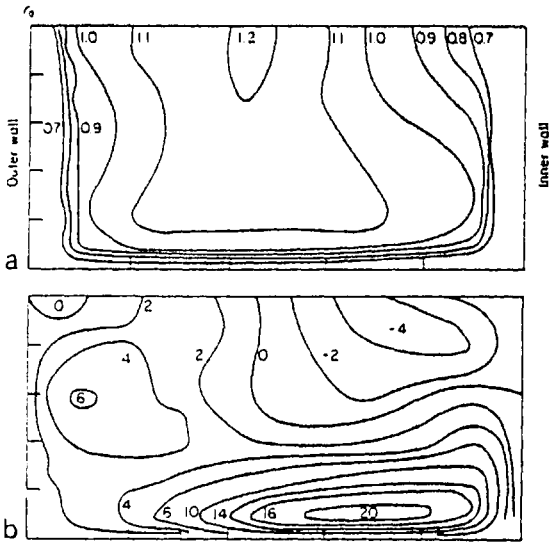


Fig 3 Contours of mean velocity in the 45° plane: (a) U/U_B (b) $V/U_B \times 10^2$

of slow moving fluid on the inner wall. The inward flows at the side-walls ensure that the boundary layers there remain thin. As the flow approaches the bend exit it is accelerated on the outer wall and retarded on the inner one. The adjustment to rectilinear flow is rapid: the measurements in Fig 4 show that in the exit plane the transverse mean velocities have decreased to approximately half their values at 45° while the much distorted contours of U simply record the history of the flow. Profiles of the transverse component V, plotted in Fig 5, show strong inward flow in the inner part of the duct and also suggest the presence of a weak secondary circulation of the opposite sense in the outer part of the duct. These circulations presumably arise from the destabilizing action of concave curvature on the outer wall boundary layer and persist because the curvature is sufficiently mild for it not to be swept into the main pressure-driven secondary motion of the opposite sense.

Contours of the rms turbulence intensities u' and v' and the Reynolds shear stress $\overline{uv}$ are plotted in Figs 6 and 7. The distortion of the nearly symmetrical inlet contours, Fig 2, is very evident and generally consistent with the development of local high shear zones in the mean flow. The high levels of v' measured near the inner corner in the exit plane are rather surprising and in contrast with the strong curvature results[3,4] where peak values of v', of the same order as u', were distributed in the outer part of the exit plane. The shear stress plots contain less detail but generally show higher levels near the inside of the bend consistent with high shear and turbulence activity there. There appears to be no evidence of significant damping or amplification of turbulence due to longitudinal curvature as observed in the strongly-curved bend[3] and the position of zero shear stress coincides approximately with that of the maximum mean velocity.

Conclusions

The measurements show the development and decay of cross-stream flows in a 90° moderately curved bend. The flow behaviour is consistent with that previously observed in more strongly curved bends and differences in the details of the two flows are accounted for by the differences in curvature: here, the secondary cross-stream velocities are only one half of those measured in the strongly curved bend. The results are seen as a contribution to the data base available to developers of turbulence models and computer flow prediction methods.

Acknowledgement

Financial support from the CEGB Central Electricity Research Laboratories and NASA Lewis Research Center is gratefully acknowledged.

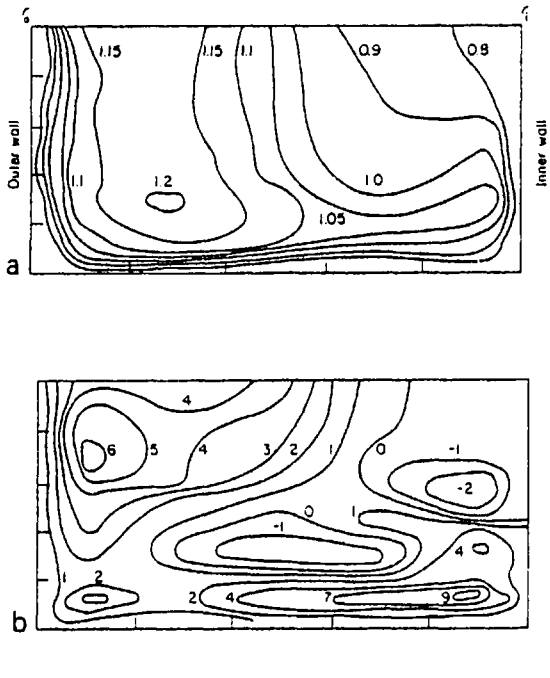


Fig 4 Contours of mean velocity in the exit plane, $\theta = 90°$: (a) U/U_B (b) $V/U_B \times 10^2$

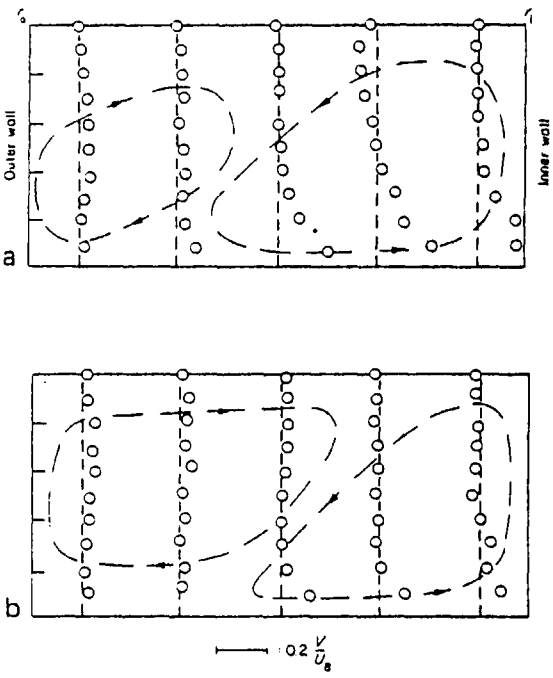


Fig 5 Profiles of radial velocity V/U_B: (a) $\theta = 45°$ (b) $\theta = 90°$

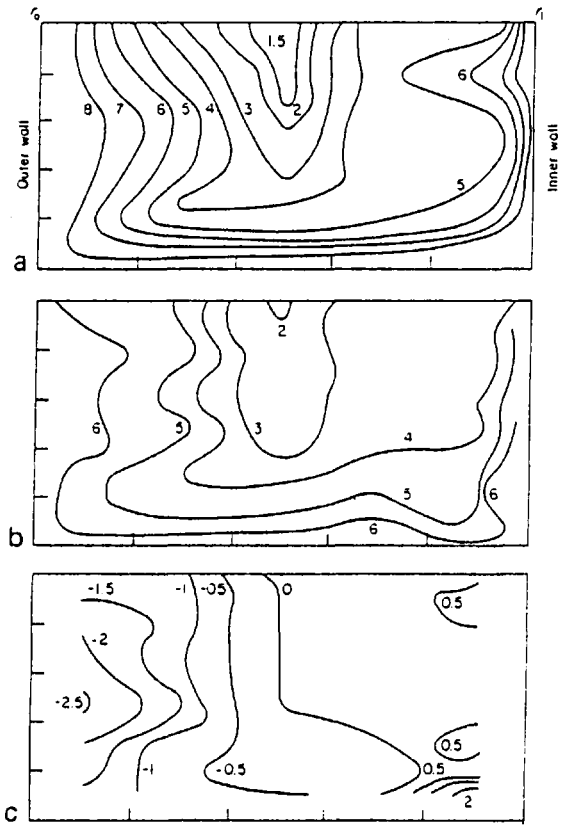


Fig 6 Turbulence measurements in the 45° plane: contours of (a) $u'/U_B \times 10^2$ (b) $v'/U_B \times 10^2$ (c) $\overline{uv}/U_B^2 \times 10^3$

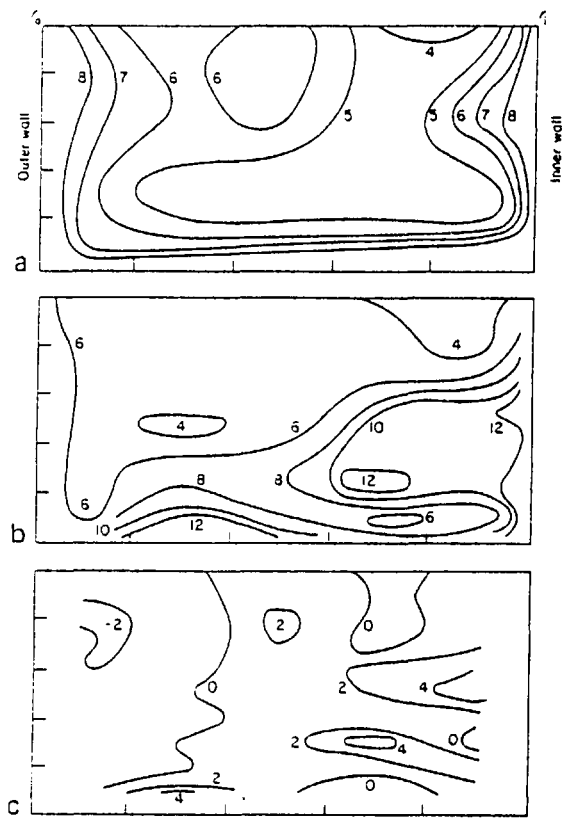


Fig 7 Turbulence measurements in the exit plane: contours of (a) $u'/U_B \times 10^2$ (b) $v'/U_B \times 10^2$ (c) $\overline{uv}/U_B^2 \times 10^3$

References

1. **Enayet, M. M., Gibson, M. M., Taylor, A. M. K. P. and Yianneskis, M.** Laser Doppler measurements of laminar and turbulent flow in a pipe bend. *Int. J. Heat and Fluid Flow, 1982, 3, 211–217*

2. **Humphrey, J. A. C., Taylor, A. M. K. P. and Whitelaw, J. H.** Laminar flow in a square duct of strong curvature. *J. Fluid Mech. 1977, 83, 509*

3. **Humphrey, J. A. C., Whitelaw, J. H. and Yee, G.** Turbulent flow in a square duct with strong curvature *J. Fluid Mech. 1981, 103, 443*

4. **Taylor, A. M. K. P., Whitelaw, J. H. and Yianneskis, M.** Measurements of laminar and turbulent flow in a curved duct with thin inlet boundary layers. *NASA Contractor Rep. 3367, 1981*

5. **Taylor, A. M. K. P., Whitelaw, J. H. and Yianneskis, M.** Developing flow in S-shaped ducts I: Square cross-section duct. *Imperial College MED rep. FS/81/22, 1981*